UNIVERSITY OF SOUTHAMPTON
FACULTY OF PHYSICAL SCIENCES AND ENGINEERING
SCHOOL OF ELECTRONICS AND COMPUTER SCIENCE

Distributed Joint Source-Channel Coding and Modulation for Wireless Communications

by

Abdulah Jeza Aljohani
B.Sc.(Eng.), MSc.

A doctoral thesis report submitted in partial fulfilment of
the requirements for the award of Doctor of Philosophy
at the University of Southampton

December 2015

SUPERVISORS:
Dr. Soon Xin Ng
PhD, SMIEEE, MIET, CEng, FHEA
and
Professor Lajos Hanzo
FREng, FIEEE, FIEE, DSc, EIC IEEE Press
Chair of Southampton Wireless Group
Department of Electronics and Computer Science
University of Southampton
Southampton SO17 1BJ
United Kingdom

Dedicated to my family and friends

UNIVERSITY OF SOUTHAMPTON

ABSTRACT

FACULTY OF PHYSICAL SCIENCES AND ENGINEERING
SCHOOL OF ELECTRONICS AND COMPUTER SCIENCE

Doctor of Philosophy

Distributed Joint Source-Channel Coding and Modulation for Wireless Communications

by Abdulah Aljohani

Distributed Source Coding (DSC) schemes rely on separate encoding but joint decoding of statistically dependent sources, which exhibit correlation. DSC has numerous promising applications ranging from reduced-complexity handheld video communications to onboard hyperspectral image coding under computational limitations. The concept of separate encoding at the first sight compromises the attainable encoding performance. However, DSC theory proves that independent encoding can in fact be designed as efficiently as joint encoding, as long as joint decoding is allowed. More specifically, Distributed Joint Source-Channel coding (DJSC) is associated with the scenario, where the correlated source signals are transmitted through a noisy channel. A series of Turbo Trellis-Coded Modulation (TTCM) aided DJSC-based cooperative transmission schemes are proposed.

An iterative Joint Source-coding, Channel-coding and Modulation (JSCM) scheme relying on the intrinsic amalgamation of Variable Length Code (VLC) and TTCM was proposed for two-way-aided transmission. The system advocated was designed for improving the attainable throughput, reliability and coverage area compared to that of conventional one-way relaying. Briefly, a pair of users exchange their information with the aid of a twin-antenna aided Relay Node (RN). We quantify the Discrete-input Continuous-output Memoryless Channel (DCMC) capacity of the corresponding two-way relay channel. The semi-analytical EXtrinsic Information Transfer Characteristics (EXIT) charts are employed for investigating the decoding convergence of the joint source and channel decoder as well as for assisting the overall system design. Furthermore, our iterative scheme employs a novel low-complexity source coding technique that significantly reduces the number of states in the bit-based trellis before invoking it for robust image and video transmission.

Then, an adaptive DJSC scheme is conceived for the transmission of a pair of correlated sources to a Destination Node (DN). The first source sequence is TTCM encoded and then it is compressed before it is transmitted both over a Rayleigh fading and Nakagami-m fading channels, where the second source signal is assumed to be perfectly decoded side-information at the DN for the sake of improving the achievable decoding performance of the first source. The proposed scheme is capable of performing reliable communications for various levels of correlation near to the theoretical Slepian-Wolf/Shannon (SW/S) limit. Additionally, its encoder is capable of accommodating arbitrary time-variant short-term correlation between the two sources.

Pursuing our objective of designing practical DJSC schemes, we further extended the above-

mentioned arrangement to a more realistic cooperative communication system, where the pair of correlated sources are transmitted to a DN with the aid of a RN. Explicitly, the two correlated source sequences are TTCM encoded and compressed before transmission over a Rayleigh fading Multiple Access Channel (MAC). The RN transmits both users' signal with the aid of a powerful SuperPosition Modulation (SPM) technique that judiciously allocates the transmit power between the two signals. The correlation is beneficially exploited at both the RN and the DN using our powerful iterative joint decoder, which is optimised using EXIT charts. We further conceive a so-called Block Syndrome Decoding (BSD) approach for our DJSC scheme, which reduces the decoding complexity, whilst additionally providing an accurate correlation estimate.

As a further new cooperative technique, our DJSC scheme invokes RN-aided Network Coding (NC) which is capable of improving the overall throughput without increasing the energy dissipation. To investigate our DJSC in the context of diverse environments, our NC-based schemes are also appraised in the context of slow fading effects that might be imposed by obstacles blocking the line-of-sight transmission links. Our proposed scheme is shown to achieve substantial performance gains over its conventional non-cooperative counterpart.

Declaration of Authorship

I, **Abdulah Jeza Aljohani**, declare that the thesis entitled **Distributed Joint Source-Channel Coding and Modulation for Wireless Communications** and the work presented in it are my own and has been generated by me as the result of my own original research. I confirm that:

- This work was done wholly or mainly while in candidature for a research degree at this University;
- Where any part of this thesis has previously been submitted for a degree or any other qualification at this University or any other institution, this has been clearly stated;
- Where I have consulted the published work of others, this is always clearly attributed;
- Where I have quoted from the work of others, the source is always given. With the exception of such quotations, this thesis is entirely my own work;
- I have acknowledged all main sources of help;
- Where the thesis is based on work done by myself jointly with others, I have made clear exactly what was done by others and what I have contributed myself;
- Parts of this work have been published.

Signed: ..... Date: .....

Acknowledgements

I wish to express my heartfelt gratitude to my supervisors Dr. Soon Xin Ng and Professor Lajos Hanzo for their excellent guidance and support throughout my research. I sincerely thank Dr. Ng for the countless research ideas and tools I have learned from him. Without his support and great patience my research would not approach this level.

I would also like to thank Prof. Hanzo for his outstanding guidance and inspiration. His patience, enthusiasm and encouragement have been highly supportive to me. Many thanks to the staff and my colleagues of Southampton Wireless Group, particularly Prof. Sheng Chen, Prof. Lie-Liang Yang, Dr. Rob Maunder, Dr. Mohammed El-Hajjar, Dr. Rong Zhang, Dr. Halil Yetgin, Dr. Hung Viet Nguyen, Dr. Zunaira Babar and Dr. Hua Sun, for their invaluable technical support and collaborative works.

I would also like to express my sincere gratitude to my beloved family, my parents: Jeza Aljohani and Muznah Aljohani, my parents-in-law: Mohammed Alzahrani and Fatimah Alzahrani, my brothers: Captain. Khalid and Dr. Naif, my sisters: Nashmia, Dr. Nouf, Dr. Kholud and Sara. Last but not least heartfelt thanks to my lovely wife Ebtesam Alzahrani and my son Amr (Amoori) for their love, support and care for me.

List of Publications

Journals:

1. **A. J. Aljohani**, S. X. Ng, R. G. Maunder and L. Hanzo,"EXIT-chart Aided Joint Source-Coding, Channel-Coding and Modulation Design for Two-Way Relaying", IEEE Transactions on Vehicular Technology, vol. 62, no. 6, pp. 2496-2506, July 2013.

2. **A. J. Aljohani**, S. X. Ng and L. Hanzo, "TTCM-Aided Rate-Adaptive Distributed Source Coding for Rayleigh Fading Channels", IEEE Transactions on Vehicular Technology, vol. 63, no.3, pp. 126-134, March 2014.

3. **A. J. Aljohani**, H. Sun, S. X. Ng and L. Hanzo, "Distributed Source and Turbo Trellis Coded Modulation Aided Superposition Modulation", (*to be submitted*).

4. **A. J. Aljohani**, H. Nguyen, S. X. Ng and L. Hanzo, "TTCM-Aided Distributed Joint Source-Channel coding based Adaptive Dynamic Network Coding", (*to be submitted*).

5. **A. J. Aljohani**, Z. Babar, S. X. Ng and L. Hanzo, "Distributed Joint Source-Channel coding Using Reduced-Complexity Syndrome-Based TTCM", (*to be submitted*).

Conferences:

6. **A. J. Aljohani**, S. X. Ng, R. G. Maunder and L. Hanzo, "Joint TTCM-VLC-Aided SDMA for Two-Way Relaying Aided Wireless Video Transmission", IEEE Vehicular Technology Conference (VTC2013-Fall) 2013.

7. **A. J. Aljohani**, H. Sun, S. X. Ng, and L. Hanzo, "Joint Source and Turbo Trellis Coded Hierarchical Modulation for Context-aware Medical Image Transmission", IEEE HEALTHCOM 2013 - The 1st International Workshop on Service Science for e-Health 2013.

8. **A. J. Aljohani**, S. X. Ng, and L. Hanzo, "TTCM-Assisted Distributed Source-Channel Coding for Nakagami-m Fading Channels", IEEE Vehicular Technology Conference (VTC2014-Fall) 2014.

Poster Presentation:

9. **A. J. Aljohani**, S. X. Ng, and L. Hanzo, "Adaptive Turbo Trellis Coded Modulation For Slepian-Wolf Coding Over A Rayleigh Fading Channel", the 8th Saudi Student Conference, Imperial College London, UK, 31 Jan - 01 Feb 2015.

Contents

Glossary

A-DJSTTCM	Adaptive Distributed Joint Turbo Trellis-Coded Modulation
ADNC	Adaptive Dynamic Network Coding
AWGN	Additive White Gaussian Noise
BCH	Bose-Chaudhuri-Hocquenghem
BER	Bit Error Ratio
BICM	Bit-Interleaved Coded Modulation
BP	Broadcast Phase
BPP	Bits Per Pixel
BSC	Binary Symmetric Channel
BSD	Block Syndrome Decoding
CCMC	Continuous-input Continuous-output Memoryless Channel
CE	Correlation Estimation
CM	Coded Modulation
CP	Cooperative Phase
CS	Cooperative System
CSC	Coded-Stream Compression
CSI	Channel State Information
DAC	Distributed Audio Coding
DCMC	Discrete-input Continuous-output Memoryless Channel
DF	Decode-and-forward
DJSC	Distributed Joint Source-Channel coding
DJSCN	Distributed Joint Source-Channel coding-aided Network-coding
DJSTTCM	Distributed Joint Source TTCM
DN	Destination Node
DNC	Dynamic Network Coding
DSC	Distributed Source Coding
DVC	Distributed Video Coding
EXIT charts	EXtrinsic Information Transfer
FEC	Forward Error Correction

FED	Free Euclidean Distance
FER	Frame Error Ratio
GF	Galois Fields
IFs	Information Frames
JSCC	Joint Source-coding and Channel-coding
JSCM	Joint Source-coding, Channel-coding and Modulation
LDPC	Low-Density Parity-Check
LLR	Logarithmic-Likelihood Ratios
LNC	Liner Network Coding
MAC	Multiple Access Channel
MAP	Maximum A-Posteriori
MDS	Maximum Distance Separable
MI	Mutual Information
MIMO	Multiple-Input Multiple-Output
ML	Maximum Likelihood
MMSE-IC	Minimum Mean-Square Error-assisted Interference Cancellation
MMSE-SIC	Minimum Mean-Square Error-assisted Successive Interference Cancellation
MSP	Mode of Selection Probability
MT	MultiTerminal
MUD	Multi-User Detector
NC	Network Coding
NLNC	Non-Linear Network Coding
PDF	Probability Density Function
PFs	Parity Frames
PS	Power Sharing
PSAM	Pilot Symbol Assisted Modulation
PSNR	Peak Signal to Noise Ratio
Phase-I	Source to Relay Transmission SR
Phase-II	Relay to Destination Transmission RD
RA	Rate-Adaptive
RC	Reduced-Complexity
RN	Relay Node
RS	Reed Solomon
RSC	Recursive Systematic Code
RVLC	Reversible Variable Length Code
SDMA	Space-Division Multiple Access
SER	Symbol Error Ratio
SN	Source Node
SNR	Signal-to-Noise Ratio

SNs	Source Nodes
SP	Set Partitioning
SPM	SuperPosition Modulation
STEREO	Solar Terrestrial Relations Observatory
SW/S limit	Slepian-Wolf Shannon limit
SWC	Slepian-Wolf Coding
TCM	Trellis-Coded Modulation
TDMA	Time-Division Multiple Access
TTCM	Turbo Trellis-Coded Modulation
UEC	Unary Error Correction
URC	Unity Rate Coding
VLC	Variable Length Code
WZC	Wyner-Ziv Coding
ZF	Zero Forcing

List of Symbols

Special Symbols

APP	The A Posteriori Probability.
$\{b\}$	The source sequence.
C_{CCMC}	Capacity of Continuous-input Continuous-output Memoryless Channel.
C_{DCMC}	Capacity of Discrete-input Continuous-output Memoryless Channel.
D	The shift register delay unit.
D_{NC}	Network coding diversity order.
$\mathcal{D}$	The difference between the current and the predicted pixels
$\mathbb{D}$	The maximum acceptable distortion level.
d_H	The Hamming distance.
d_{ab}	The geographical distance between node a and node b.
E_b/N_0	The SNR per bit.
e_i	The independent error binary random variable.
f_c	The Jacobian logarithm correction factor.
G	The reduced-pathloss-induced geometrical gain.
$\boldsymbol{G}$	Network coding transfer matrix.
$\boldsymbol{G}'$	Modified Network Coding transfer matrix.
$\mathbf{G}(D)$	The code generator polynomial/matrix.
$g(\cdot,\cdot)$	The Jacobian logarithm.

Special symbols (Cont.)

$g \in \{0,1\}$	The connection status between $\mathbf{G}(D)$ coefficients.
$\mathbf{H}$	The MIMO channel matrix.
$\mathbb{H}$	The syndrome former.
$H(\cdot\|\cdot)$	The conditional entropy.
$H(\cdot,\cdot)$	The joint entropy.
$H(\cdot)$	The entropy.
$h(t,x)$	The space and time invariant filter.
I	The number of the TTCM decoder iterations.
I_{out}	The number of outer iteration.
I_{in}	The number of inner iteration.
L_s	The VLC associated entropy.
L_{vlc}	The average VLC codeword length.
Nakagami-m	Nakagami channel fading parameter.
$\widetilde{\mathrm{m}}$	The CM code memory.
N_0	The power spectral density of AWGN.
N_s	The number of transmitted symbol per frame.
p_e	The cross-over probability.
$\widehat{p}_e$	The estimated cross-over probability.
R_{cm}	The TCM/TTCM coding rate.
R_{vlc}	The VLC coding rate.
(r_1, r_2)	The 16QAM-SPM weighting factor pair.
$U(x,t)$	The spatio-temporal source sound field.
$V(x,t)$	The spatio-temporal channel-induced sound field.

Special symbols (Cont.)

α	The path-loss exponent.
$\alpha_k(s)$	The forward recursive coefficient of a MAP decoder.
$\beta_k(\grave{s})$	The backward recursive coefficient of a MAP decoder.
η	The effective throughput of the corresponding system.
$\eta_k(\grave{s}, s)$	The transmission probability from state $\grave{s}$ to s of a MAP decoder.
Γ_T	The transmitted SNR in [dB].
Γ_R	The received SNR in [dB].
Γ_{lim}	The SNR limit corresponding to the associated capacity in [dB].
$\overline{\Gamma}_R$	The average receive SNR in [dB].
$\Gamma_{10^{-6}}$	The SNR values associated with BER level 10^{-6}.
γ_r	The Near-instantaneous SNR **Chapter 4**.
$\mu(\cdot)$	The QAM/PSK mapping function.
π	The interleaver.
π_s^{-1}	The de-interleaver.
ρ	The correlation coefficient.

Special Operations

$(\cdot)^H$	The Hermitian transpose of a matrix.
$(\cdot)^T$	The transpose of a matrix.
$\sum$	The summation of all elements.
$\prod$	The product of all elements.
$\int$	The integration function.
$e^{(\cdot)}$ / $\exp(\cdot)$	The natural exponentiation of the elements.
$\ln(\cdot)$	The natural logarithm of the elements.
$\log_a b$	The logarithm of b to base a.
$\mathbb{U}((\cdot))$	The update function.

Chapter 1

Introduction

1.1 Motivation

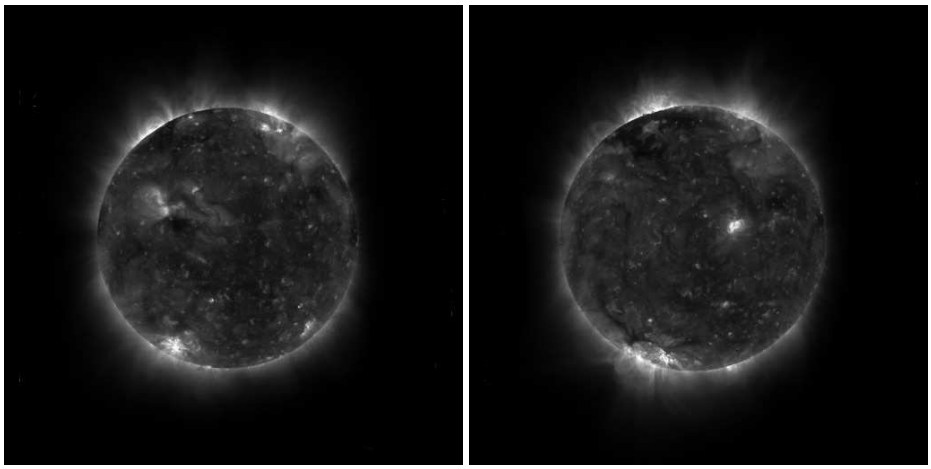

(a) STEREO **A**head solar image. (b) STEREO **B**ehind solar image.

Figure 1.1: Stereographic solar images taking by NASA's both STEREO satellites Ahead and Behind ©NASA [1].

Let us commence by considering the stereographic images of the Sun in Figure 1.1, which were captured using a pair of satellites that are part of NASA's Solar Terrestrial Relations Observatory (STEREO) project[1]. The location of both satellites, which are referred to as STEREO **A**head and STEREO **B**ehind, is shown in Figure 1.2. On the 20th of September 2013 they were more than 50 million km away from each other. In such a scenario, is it not readily feasible for them to communicate with each other. Similarly, each satellite has very limited communications with planet Earth [1, 3]. Thus, the employment of source compression is desirable, but the encoding of images has to be carried out separately at the satellites, while decoding may be carried out jointly at the Earth station, where both the power and computational constraints are relaxed. Intuitively, sep-

[1]The STEREO project aims for providing revolutionary stereoscopic imaging of the sun in order to reveal the solar surface activities, such as the Coronal Mass Ejection (CME) [1, 2].

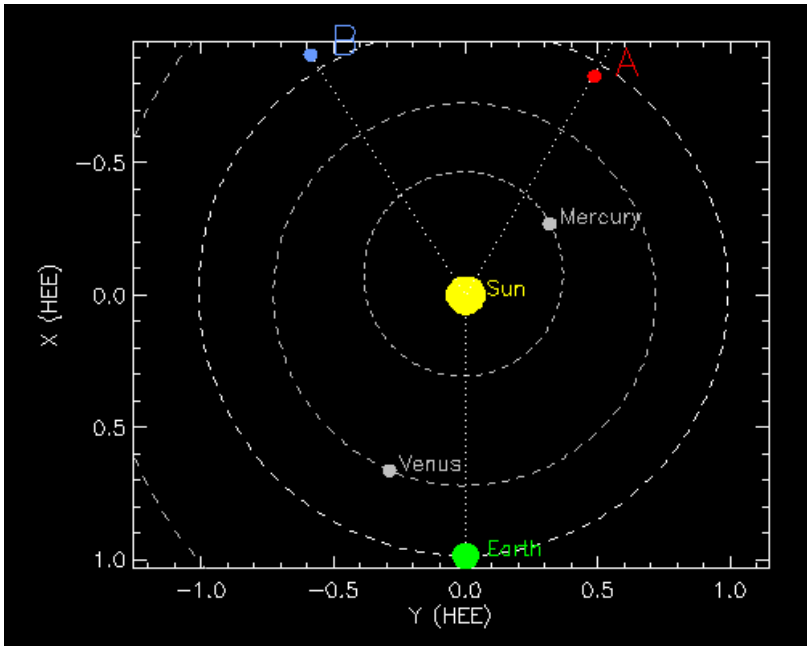

Figure 1.2: Positions of both STEREO satellites **A**head and **B**ehind recorded on the 20th September 2013 ©NASA [1].

arate encoding would only allow separate compression of the images of the distant satellites even though there is substantial correlation between their images. However, the Distributed Source Coding (DSC) theorem of [4] states that separate encoding may be invoked instead of joint encoding without any loss of compression efficiency as long as the correlation among the sources is preserved through out their transmission to the receiver, provided that they are jointly decoded [4,5,6].

To offer a glimpse on the benefits of applying the DSC technique, we have separately encoded both satellite views of Figure 1.1 before their transmission over a uncorrelated Rayleigh fading channel[2]. As Figure 1.3 illustrates, when joint decoding is activated by invoking our decoder of Section 5.3.2, no higher than 1.0 dB Signal-to-Noise Ratio (SNR) is required for attaining perfect images recovery. By contrast, for the same amount of transmit power, both the Ahead and Behind images were severely corrupted upon using exactly the same coding scheme dispensing with joint decoding. Thus, exploiting the correlation between the images by jointly decoding them has lead to a significant power reduction, while maintaining reliable communication. This room for improvement can be also utilised for further source sequence compression, as it is going to be illustrated in the subsequent chapters.

1.2 Distributed Source Coding

DSC refers to the problem of compressing several physically separated, but correlated sources, which are unable to communicate with each other by exploiting that the receiver can perform joint

[2]Both images were encoded separately using $1/2$-rate Turbo Trellis-Coded Modulation (TTCM) and decoded jointly using the decoder of Section 5.3 which is illustrated in Figure 5.3, readers can have a quick look at Table 5.2 for main simulations parameters summary.

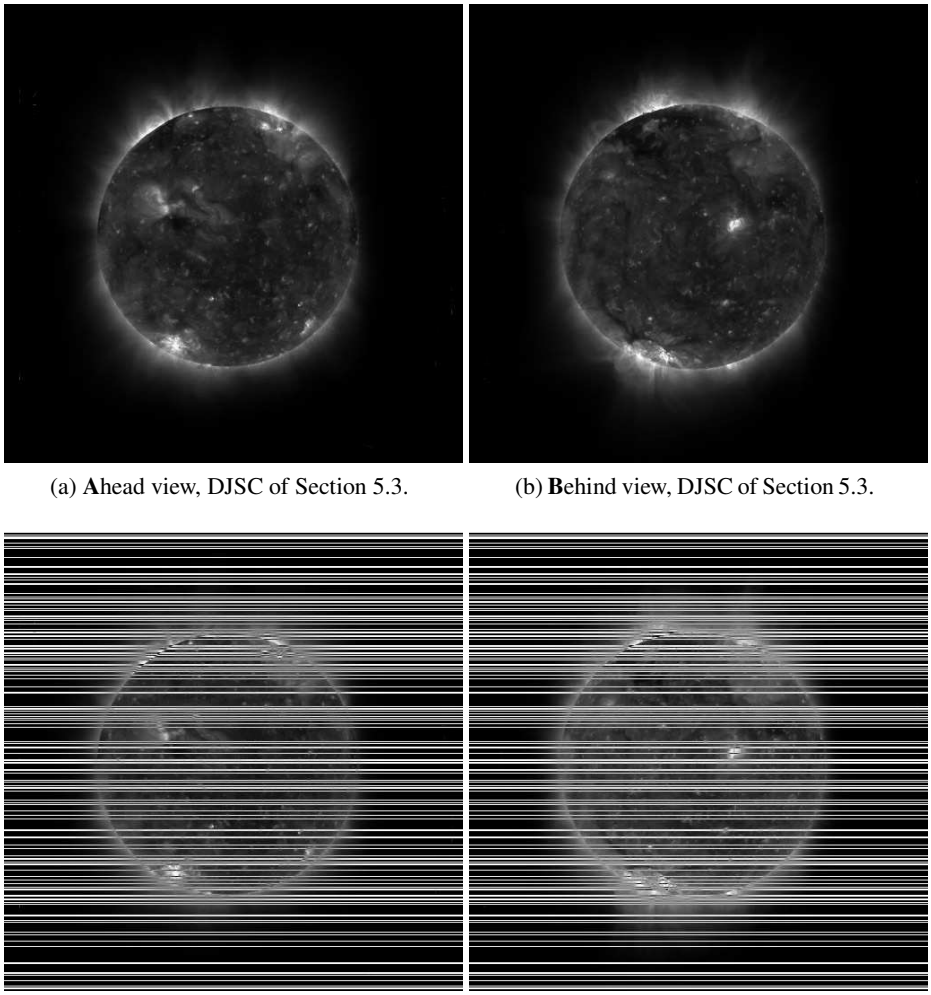

(a) **A**head view, DJSC of Section 5.3.

(b) **B**ehind view, DJSC of Section 5.3.

(c) **A**head view, non-DJSC benchmark of Section 5.3.

(d) **B**ehind view, non-DJSC benchmark of Section 5.3.

Figure 1.3: Decoded stereographic images of Figure 1.1 after transmission over uncorrelated Rayleigh fading channels at $\mathbf{SNR} = \mathbf{1.0}$ dB.

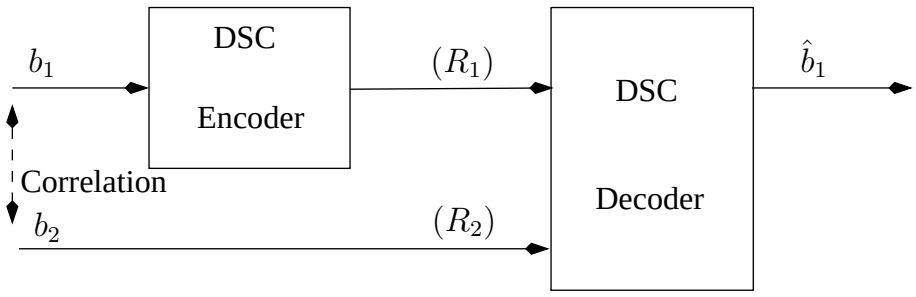

Figure 1.4: Schematic diagram of relying on perfect side-information DSC.

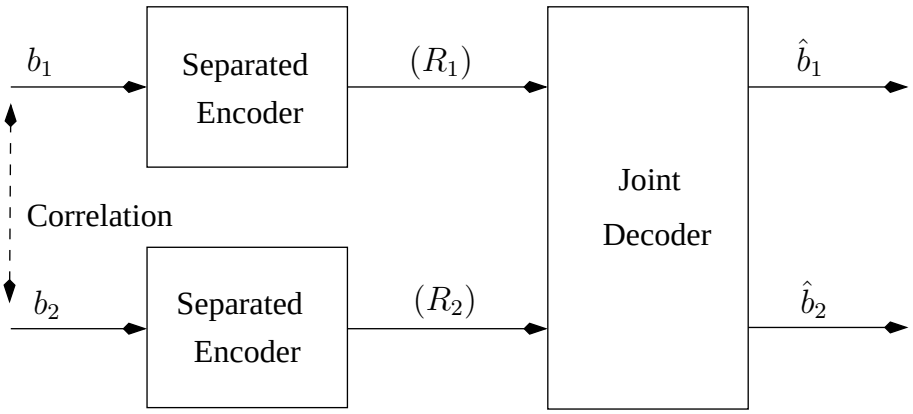

Figure 1.5: Schematic diagram of dispensing with perfect side-information DSC.

decoding of the encoded signals [3, 4, 7, 8, 9]. However, Distributed Joint Source-Channel coding (DJSC) is specific to the case, when the correlated sources signals are transmitted over noisy channels [8, 10, 11]. For both DSC and DJSC schemes the ultimate goal is to exploit the existing correlation for the sake of minimising the transmission energy required by the sources, while maintaining reliable communication. From an architectural perspective, distributed techniques may be categorised into two main families [3, 10, 12], namely the class of operating in the presence of perfect side-information and in the absence of perfect side-information schemes. The schematic of the former [3, 9, 12] is shown in Figure 1.4, where the source sequence $\{b_1\}$ is compressed before its transmission, while the correlated source signal $\{b_2\}$ is assumed to be flawlessly available at the decoder, but not at the source $\{b_1\}$. By contrast, in the scenario dispensing with perfect side-information both sources are compressed at a rate lower than their corresponding entropy rates, in which any point between the locations A and B of Figure 1.6 can be reached. A special case of the latter scenario, when both users are compressed at the same rate, represented by point C in Figure 1.6. The encoder has to compress $\{b_1\}$ without knowing $\{b_2\}$, yet the decoder is capable of exploiting the knowledge of $\{b_2\}$ for recovering $\{b_1\}$.

1.2.1 Slepian-Wolf Theory

The Slepian-Wolf (SW) theorem [4] has laid down the theoretical foundations of DSC through specifying the achievable rate regions of the compressed correlated sources. Let us consider the arrangement of Figure 1.5, where both $\{b_1\}$ and $\{b_2\}$ are random sequences of independent and identically distributed, i.i.d, samples. Upon their separate encoding and joint decoding, the SW theorem [4] states the rate region as:

$$R_1 \geq H(b_1|b_2)\,, \tag{1.1}$$

$$R_2 \geq H(b_2|b_1)\,, \tag{1.2}$$

$$R_1 + R_2 \geq H(b_1, b_2)\,, \tag{1.3}$$

where $H(b_1|b_2)$ and $H(b_1, b_2)$ denote the conditional and joint entropies, respectively. Remarkably, and as shown in Figure 1.6 this bound is identical, regardless whether joint encoding is used, i.e. regardless of where the joint processing takes place. Note that at the corner points shown in Figure 1.6, namely A and B, the Slepian-Wolf Coding (SWC) problem would be reduced to the scenario relying on perfect side-information, as shown in Figure 1.4. Using conventional lossless coding at rate of $R_2 = H(b_2)$, for example, will make $\{b_2\}$ available at the joint decoder, thus approaching point A.

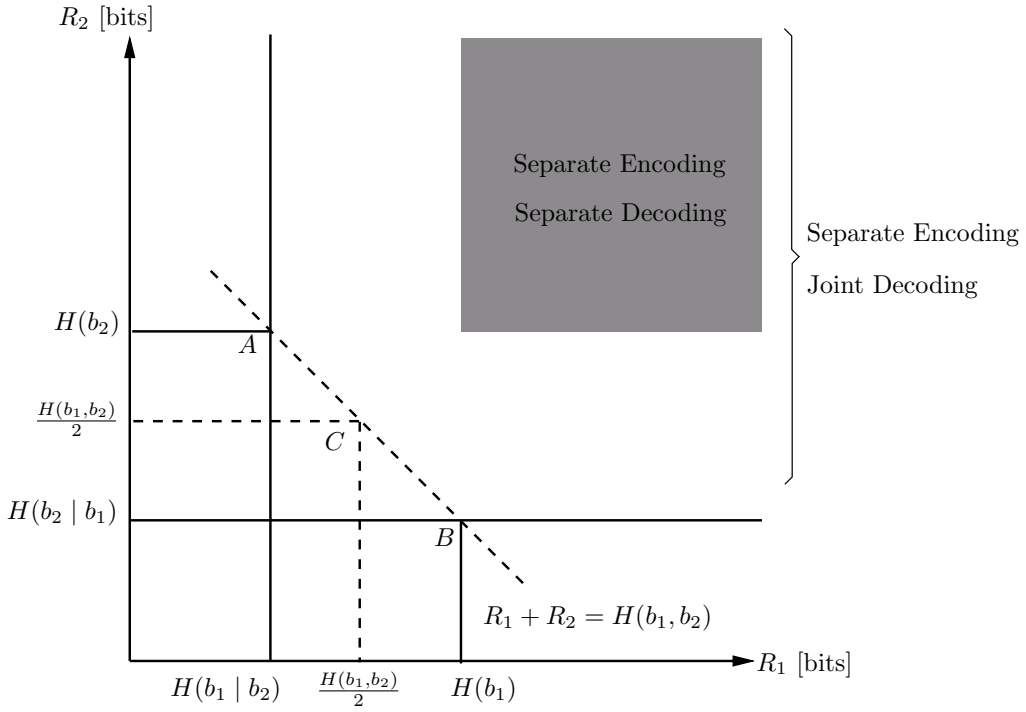

Figure 1.6: Graphical representation of SW bound, using Equations (1.1)-(1.3).

In 1976, the aforementioned lossless SWC problem of [4] was extended to a lossy source coding problem relying on side-information at the decoder [5], which is widely known as the Wyner-Ziv Coding (WZC) problem [7, 10, 13]. More explicitly, the WZC problem asks the question of how many bits are required for encoding $\{b_1\}$, when the side-information $\{b_2\}$ is perfectly known at the decoder, while maintaining a specific level of distortion concerning $\{b_1\}$ at the receiver. These promising theoretical results have led to intense research activities from both theoretical as well as from practical perspectives. Figure 1.7 summaries the main milestones of DSC, where each of these seminal contributions is linked to the corresponding section of this chapter.

1.2.1.1 Lossless Coding

Cover [14] generalised the SWC problem by deriving the rate region bounds for more than two users, and showed that the SW theorem can also be applied to non-binary ergodic sources. It was stated in [16] that to optimise the overall performance, it is necessary to design the source's

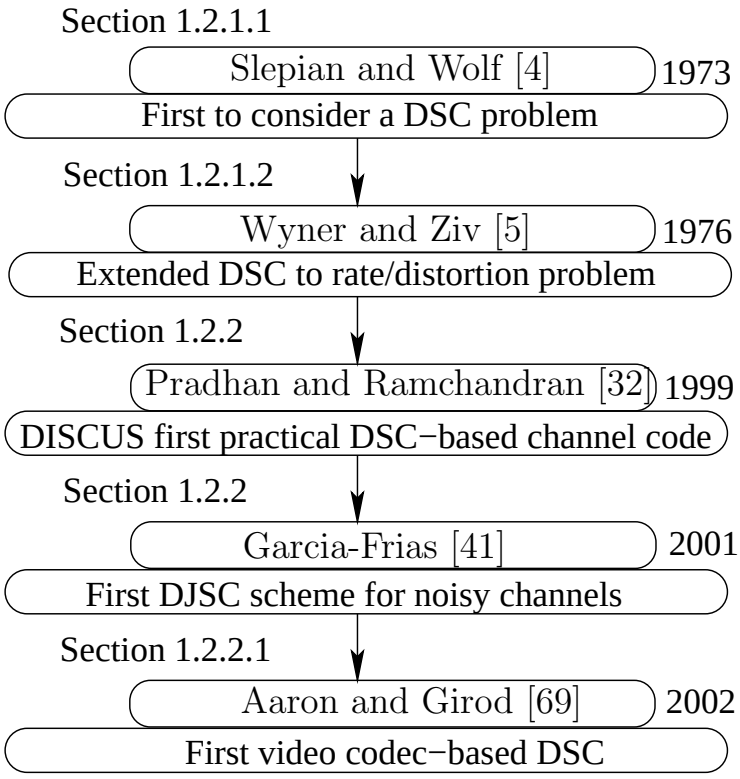

Figure 1.7: Major milestones in the history of DSC and their applications.

codewords having in mind the existence of the correlation. Additionally, it was stated in [16] that although the source and channel coding separation is indeed optimal for point-to-point communication, as shown by Shannon, it will lead to a catastrophic error propagation in realistic Multiple Access Channel (MAC) scenarios. In [17] Cristescu *et al.* considered the scenario of a large set of correlated sources communicating with a set of destinations, where the problem of finding the optimal transmission structure was studied and the optimal rate allocations were found with the aid of SWC. In order to maximise the throughput of such a system, according to [17], two steps have to be invoked; first the optimal network structure has to be found; then the optimal rate allocation can be determined by solving an optimisation problem under linear constraints that are constituted by the SW rate region. In [19] the outage probability of transmitting two correlated sources with the aid of a Relay Node (RN) was evaluated, where the signals of the users were combined with the aid of a simple network coding scheme by means of $\oplus$ operation. The major contributions made in the lossless DSC area are summarised in Table 1.1.

1.2.1.2 Lossy Coding

When considering lossy coding scenario, the WZ problem [5] asks the question of how many bits are necessary for encoding the source $\{b_1\}$, provided that the side-information $\{b_2\}$ is flawlessly known at the decoder. Thus, with the aid of Figure 1.4, the WZ problem can be characterised by

Year	Author(s)	Contribution
1973	Slepian and Wolf [4]	Determined the maximum achievable compression rates, where it was shown that, there is no loss of coding efficiency upon comparing separate encoding with joint encoding, as long as joint decoding is implemented.
1974	Cover [14]	Generalised the SW problem to more than two sources, additionally showing that the SW theorem can be applied to jointly decoding ergodic sources.
1975	Ahlswede *et al.* [15]	Determined the rate region of the side-information sequence $\{b_2\}$ by observing $\{b_2\} \oplus \{b_2\}$, where $\oplus$ is the modulo 2.
1980	Cover *et al*. [16]	Considered the Multiple Access Channel (MAC) of the SW problem, showing that designing the source and channel coding in a separate manner is not optimal.
2005	Cristescu *et al*. [17]	Solved the problem of supporting the communication of a large set of correlated sources with a set of destinations.
2006	Barros *et al*. [18]	Considered the problem multicasting correlated sources to a single destination, where only limited inter-user communication was allowed.
2015	Lu *et al*. [19]	The outage probability of Multiple Access Relay Channel (MARC) was derived for correlated sources-assisted by relay-aided transmission.

Table 1.1: Summary of major contributions on the theoretical fundamentals of lossless DSC.

the average distortion expression of:

$$\mathrm{E}\left[d(b_1, \widehat{b}_1)\right] \leq \mathbb{D}\,, \tag{1.4}$$

where $\mathrm{E}[\cdot]$ is the expectation operation, $\mathbb{D}$ is the maximum acceptable distortion level and $d(b_1, \widehat{b}_1)$ denotes the distortion function, which is widely chosen as the mean-squared error function $\left|b_1 - \widehat{b}_1\right|^2$ [13]. Accordingly, the maximum compression rate that is achieved for this problem can be formulated as [5]:

$$R_1(\mathbb{D}) = \inf I\left(b_1; Z \mid b_2\right)\,, \tag{1.5}$$

where inf is the mutual information infimum, i.e. the lower bound, which is calculated over all possible random variables of the set Z, in which the notation of $b_2 \rightarrow b_1 \rightarrow Z$ defines a Markov chain[3]. In 1985 [20], Heegard *et al*. have extended the WZ problem to more than two users. In his insightful tutorial [21], Zamir *et al*. proposed the employment of nested lattice quantization

[3]Further fundamental insights on lossy source coding can be found in [13, Chapter 1].

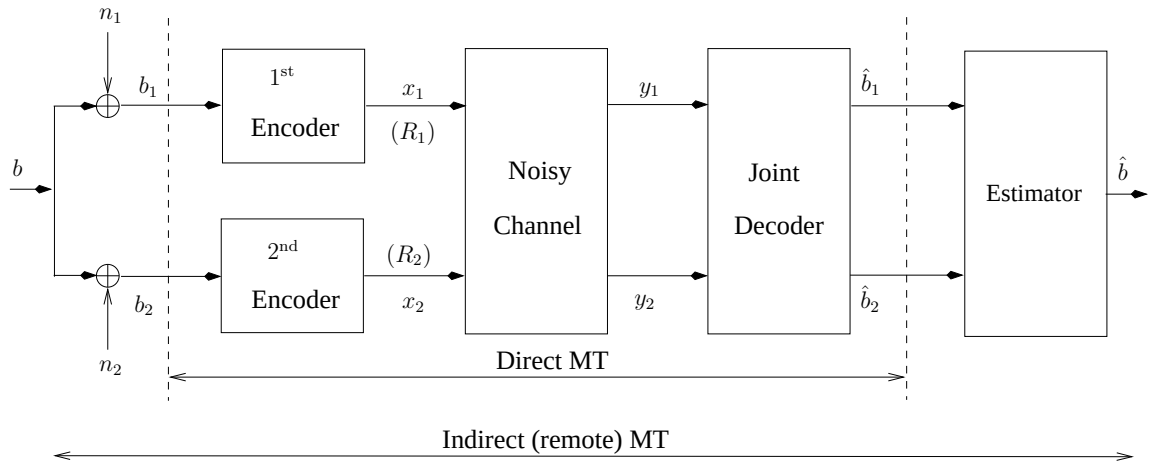

Figure 1.8: Schematic diagram illustrates the MultiTerminal (MT) coding problem.

for WZC. However, this lattice quantizer is only asymptotically optimal, as the size of the source dimensions tends to infinity, making it impractical to implement [10, 22]. Figure 1.8 illustrates a so-called MultiTerminal (MT) source coding problem, where the encoders only have access to a distorted imperfect version of the original sequences [10, 22]. As suggested by the figure, the problem may be categorised into two different classes. The first is the direct MT source coding problem when the sensors are interested in transmitting and estimating the noisy versions of the source directly [23, 24]. By contrast, in the second case the system has no direct access to noisy versions of the source, but it rather has to estimate them at the receiver [25, 26, 27]. The major works concerning the theoretical fundamentals of the lossy DSC are surveyed in Table 1.2.

1.2.2 Practical Issues

Applying DSC techniques in wireless sensor networks, for example, has led to a new processing paradigm, where the potential computational complexity has been moved from the battery-limited sources to the central decoder connected to the mains supply [3, 7, 8, 22]. As a consequence, the critical power constraint, which directly predetermines the operational life-span of a wireless node is satisfied [7, 8, 31]. The first practical SWC technique was proposed by Pradhan and Ramchandran [32], which was extended in [6], where both sources $\{b_1\}$ and $\{b_2\}$ are assumed to be emitting equiprobable codewords, but they exhibit a correlation, and $\{b_2\}$ is only known to the joint decoder but not to the encoder of $\{b_1\}$. Naturally, this assumption does not preclude that the codewords of $\{b_2\}$ are actually received from a remote source, but they must be first perfectly recovered in isolation, before they may be used by the joint decoder for recovering $\{b_1\}$. Then, all legitimate codewords of both sources are grouped into cosets, where the members of each coset are separated by the maximum possible Hamming distance. Given $\{b_2\}$ at the receiver, it is sufficient to transmit the index of the specific coset hosting the codewords of $\{b_1\}$. The decoder then estimates the transmitted codeword by opting for the one that is closest to the side-information constituted by $\{b_2\}$ of a given coset in terms of the Hamming distance d_H.

Year	Author(s)	Topic	Contribution
1976	Wyner and Ziv [5]	WZC	Extended the classic SW problem to lossy source coding relying on side-information.
1977	Berger [28]	MT	Introduced the MT coding problem for two physically separated sources.
1985	Heegard *et al.* [20]	MT	Extended the MT problem of [28] to more than two users.
1987	Flynn *et al.* [25]	Indirect MT	Considered The optimal fusion of information from the sensors involves both quantization and estimation.
1996	Zamir [29]	WZC	Determined the loss, when comparing the WZC to the separate decoding scenario.
1997	Oohama [23]	Direct MT	Considered the direct MT problem for quadratic Gaussian sources.
2002	Zamir *et al.* [21]	WZC	Proposed the use of nested lattice codes in the WZC problem.
2008	Yang*et al.* [24]	Direct/Indirect MT	Proposed SW-Coded quantization for direct and indirect MT.
2014	Oohama [30]	Indirect MT	The inner and outer bound of the rate distortion region were derived for the case of correlated sources.

Table 1.2: Summary of major contributions to the theoretical foundations of lossy DSC.

For example, consider the DSC scheme of Figure 1.4 relying on perfect side-information, where the correlated sources $\{b_1\}$ and $\{b_2\}$ are of 3-bit length, i.e. $\{b_1\}$ and $\{b_2\} \in \{000, 001, 010, 011, 100, 101, 110, 111\}$. Due to the sources' correlation, at a specific time instant i, $\{b_1^i\}$ and $\{b_2^i\}$ differ at most in one position, i.e. their Hamming distance obeys $d_H^i \leq 1$. Subsequently, the SW encoder groups all possible codewords into cosets, whose members are separated by the maximum possible Hamming distance, thus we have:

$$\mathbf{S} = [S_{00}, S_{01}, S_{10}, S_{11}] = [\{000, 111\}, \{001, 110\}, \{010, 101\}, \{100, 011\}] , \tag{1.6}$$

where each coset is colour coded similar to Figure 1.9. The encoder in this scenario would transmit the index of the coset containing $\{b_1^i\}$ using 2 bits rather than using 3 bits, while the decoder would recover $\{b_1^i\}$ correctly with the help of the side-information $\{b_2^i\}$. With reference to Figure 1.9, assume for example $\{b_1^i\} = 100$. Then, the index of the coset S_{11}, namely 11, will be transmitted. Now provided that we know if $\{b_2^i\} = 000$, the decoder will compare $\{b_2^i\}$ with each member of the coset S_{11} and then opts for the one having the lowest Hamming distance member from $\{b_2^i\}$. Hence, the decoder concludes that $\{b_1^i\} = 100$ was transmitted by exploiting the side-information knowledge of $\{b_2^i\}$ and its correlation with $\{b_1^i\}$.

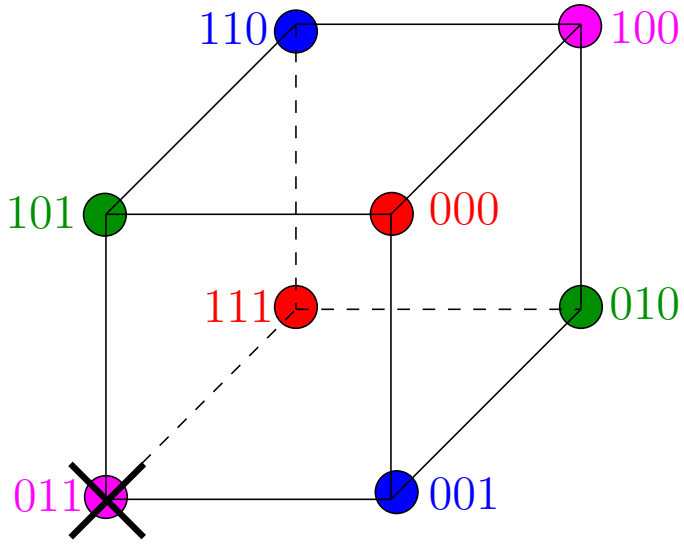

Figure 1.9: The geometric realisation of the cosets given in Equation (1.6).

Since the correlation between the sources may be interpreted as the ameliorating effect of a "virtual" channel, a good channel code having for example a maximum minimum Hamming distance is also expected to be a good SW code [10, 22, 33]. Thus, invoking powerful channel codes, such as turbo codes [34] and Low-Density Parity-Check (LDPC) [35] is capable of yielding a significant performance enhancement [7,8]. A DSC-aided syndrome bit-generation-based LDPC code relying on perfect side-information system was studied in [36,37,38,39], while a realistic imperfect side-information provision was investigated in [37, 39, 40].

As stated previously, when transmitting correlated sources over noisy channels, the DSC problem is converted into a DJSC one [8, 10, 3]. The first practical DJSC scheme was proposed by Garcia-Frias in [41]. Similar to the DSC philosophy, depending on the architecture considered, DJSC has been presented in the literature in the context of two different scenarios [8, 10]. The first one is perfect side-information case, when the side-information is constituted by the source $\{b_2\}$ is perfectly shown at the decoder and is used for assisting in the decoding of the source $\{b_1\}$ transmitted over the noisy channel. In this scenario, it was shown in [42] that the entropy of the source of $H(b_1)$ in a conventional point to point transmission should be replaced by $H(b_1 \mid b_2)$. Various schemes relying on perfect side-information-aided DJSC have been proposed in [9,43,44,45], where the channel codes, such as turbo and LDPC codes, can also be adapted similarly to the above-mentioned DSC designs.

In the second case, known as the MAC scenario, the correlated sources $\{b_1\}$ and $\{b_2\}$ are transmitted over a MAC, where the separation principle does not hold [16]. Practical DJSC schemes designed for the MAC transmission scenario have been proposed in [46,47,48,49,50]. Apart from the channel coding design, many other aspects have to be carefully considered when conceiving a DSC scheme. Figure 1.10 illustrates the main challenges to be circumvented, which can be summarised as [22, 31]:

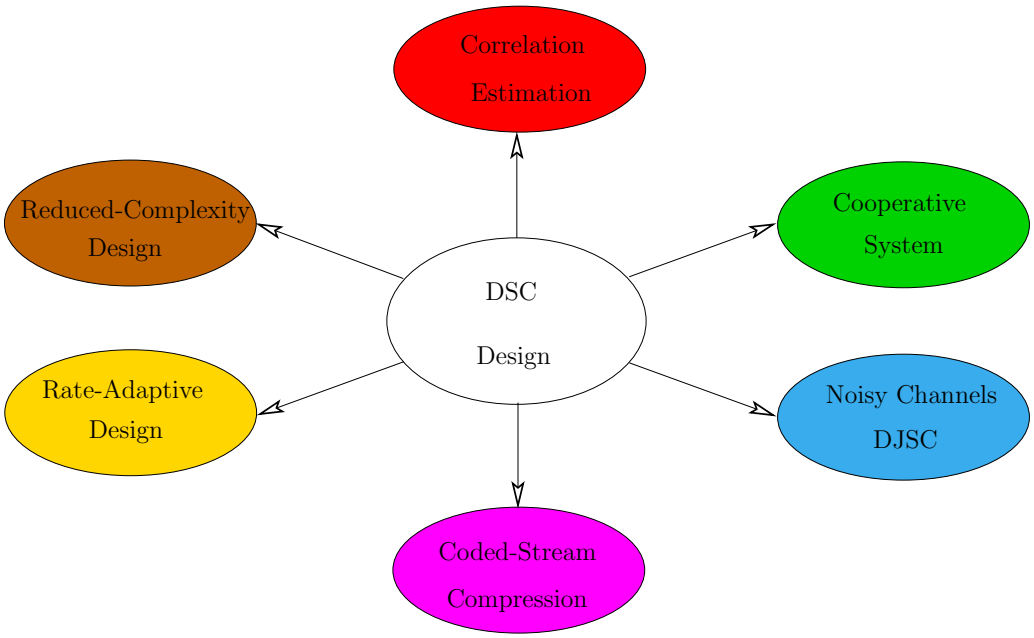

Figure 1.10: The main challenges when designing DSC schemes [22, 31].

- Correlation Estimation (CE): in practice the statistical dependence i.e. the correlation, between the sources varies in time, and typically the decoding process involves iterative information exchange between the constituent components of the joint decoder. This exchanged information has to be updated with the aid of an accurate correlation coefficient in order to avoid misleading the decoder [51, 52, 53, 54, 55].

- Reduced-Complexity (RC) design: the main goal of DSC-based schemes is to reduce the overall complexity, rather than only at the uplink transmitter side. For example, when considering a Distributed Video Coding (DVC) scheme for wireless transmission, real time decoding relaying on a low-complexity receiver is highly desirable [2, 39, 56, 57].

- Rate-Adaptive (RA) design: as stated in the first item, the correlation coefficient value varies in time. Additionally, the channel quality also fluctuates, when encountering a fading channel for example. Thus, schemes that are capable of adapting their coding rates and (or transmission rates) in response to these variables have to be found [3, 12, 38, 44, 58].

- DJSC: intuitively any practical scheme has to be evaluated for transmission over realistic imperfect channels [44, 47, 48, 50].

- Coded-Stream Compression (CSC): specially when considering realistic imperfect channels transmission, i.e. when considering DJSC schemes. Puncturing the coded sequences in these scenarios still remains a persistent challenge [10, 44, 47, 59].

- Cooperative System (CS) design: cooperative techniques are capable of either achieving a diversity gain or enhancing the overall scheme's throughput [60, 61, 62]. Given this rationale, several relay-aided DSC schemes were conceived in [49, 63, 64, 65, 66, 67, 68].

1.2.2.1 Other Selected Applications

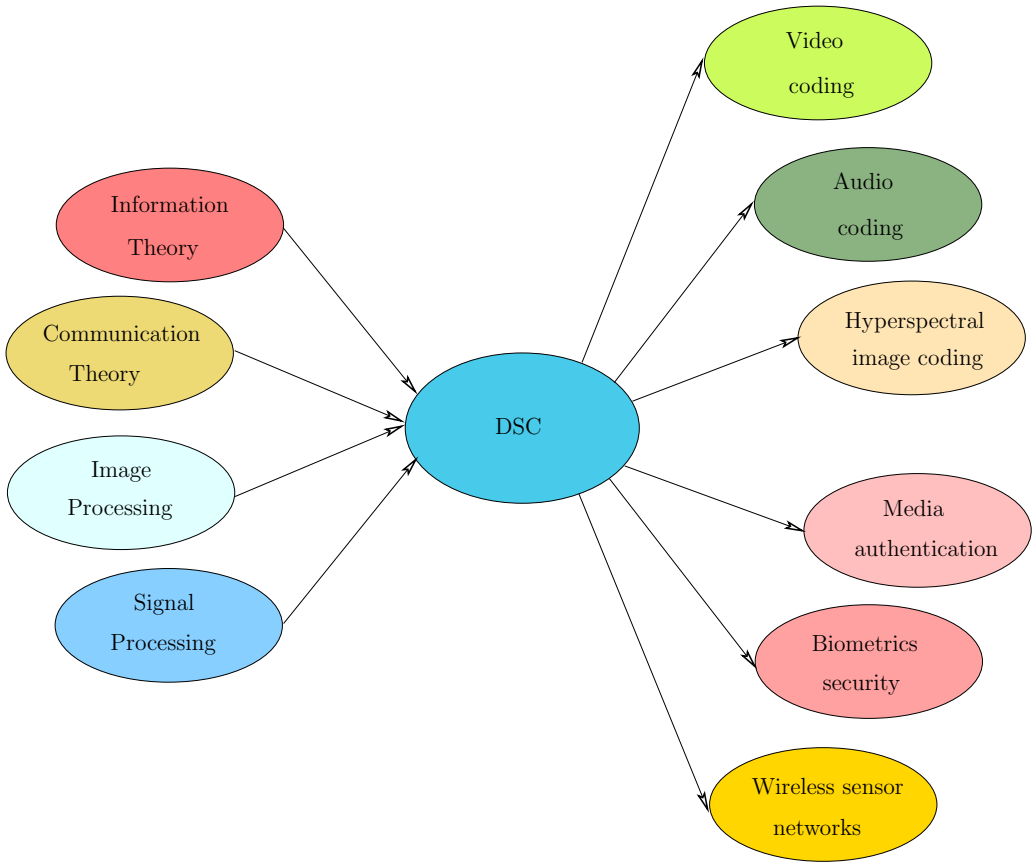

Figure 1.11: Stylised relationship of DSC to its theoretical foundations (left) and applications (right).

Although the DSC research was established in the realms of information theory, recently both communication theory and image processing have also contributed to this field, because DSC offers efficient solutions in diverse applications where the sources exhibit correlation. The stylised illustration of Figure 1.11 portrays the relationship of DSC to its theoretical background seen at the left of its diverse applications at the right [31].

The standard video codes including MPEG-2, H.263 and H.264 tend to have a high complexity encoder and a low complexity decoder [71]. More explicitly, in conventional video encoders a limited set of video frames, known as key frames, are encoded individually without involving other frames, which are referred to as intra-coded frames. The remaining predicted or intra-coded frames are encoded with reference to one or more previously encoded key frames, with the aid of motion-compensation, thus imposing a high-complexity at the encoder [3, 71]. This unequal distribution of complexity may be undesirable for emerging applications, such as wireless video sensor networks [7, 72], where both the energy and the computational complexity of the transmitter are constrained.

In this context, Distributed Video Coding (DVC), also known as WZ video coding, offers a new processing approach, where the high computational complexity of temporal redundancy reduction

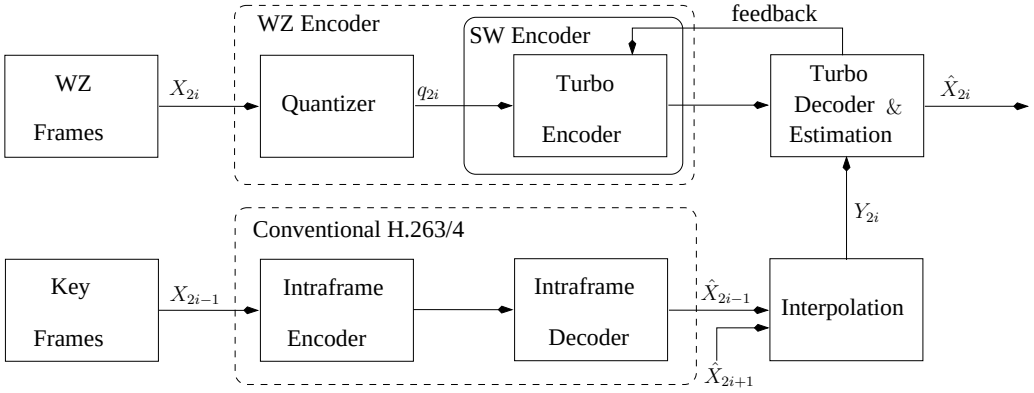

Figure 1.12: Schematic diagram illustrates the DVC proposed in [69, 70].

relying on motion-compensation is transferred from the encoder to the mains-powered decoder [3, 70, 73, 74]. To elaborate further, let us consider the DVC scheme of [69, 70] shown in Figure 1.12, where the WZ encoder is seen to consist of a SW encoder-based turbo encoder [34] following a quantization block, as justified below. The odd-indexed video frames X_{2i-1}, known as key frames, are intra-coded using a conventional video codec, such as the H.263/4 schemes of the lower branch in Figure 1.12. By contrast, the even frames X_{2i}, known in the DVC context as WZ frames, are encoded by the WZ codec seen in the upper branch of Figure 1.12. The WZ frames are being quantized for example to 8 bits/pixel and encoded using a turbo code, where only the parity bits are transmitted incrementally upon request by the feedback channel to the receiver. At the receiver, the side-information of the WZ frames will be estimated from their adjacent key frames using joint inter-frame decoding [69, 70]. By doing so, the encoder avoids the complexity of motion search and motion-compensation amongst the consecutive frames, while the decoder will assume the additional burden of constructing statistically dependent side-information frames Y_{2i}.

For the sake of avoiding provision of the aforementioned feedback channel which might preclude application of DVC in delay-sensitive services, an LDPC-based scheme was proposed in [38] which formed the basis of the so-called DIStributed COding for Video sERvices (DISCOVER) codec [74]. As further development, significant improvement were added to the DISCOVER codec by enhancing both the side-information construction [75, 76, 77] and by including an accurate correlation statistics estimation between the key and WZ frames [78, 79]. Table 1.3 illustrates briefly the major contributions to DVC research.

Distributed Audio Coding (DAC) addresses the problem of designing efficient compression schemes when dealing with the spatio-temporal sound field produced by an array of microphones for example [13, 86, 87]. More explicitly, DAC aims for designing distributed compression schemes for acoustic wireless sensor networks, where joint encoding cannot be readily performed. Consider the DAC system presented in [13], where the recording set-up is shown in Figure 1.13(a), which operates as follows [88]. Firstly, the sound sources create a spatio-temporal sound field $U(x,t)$, where x and t represent the space and time, respectively. Then, the received sound field $V(x,t)$ is recorded at a distance d, which is given by the convolution of $U(x,t)$ with the spatio-temporal

Year	Author(s)	Contribution
1976	Wyner and Ziv [5]	Stated the WZ theory of lossy source coding relying on side-information.
1980	Witsenhausen *et al*. [80]	Introduced the WZC technique into video coding.
2002/2003	Aaron, Girod *et al*. [9, 69]	Proposed an advanced DVC scheme using a WZC-based turbo code.
2002/2003	Puri and Ramchandran [81, 73]	Proposed a DVC scheme using WZC-based Bose-Chaudhuri-Hocquenghem (BCH) codes.
2006	Varodayan [38]	Proposed novel adaptive-rate LDPC codes for DSC.
2007	Artigas *et al*. [74]	Conceived a transform-domain-based DVC scheme using the LDPC of [38].
2008	Brites and Pereira [78]	Designed a realistic DVC scheme performing online correlation estimation between the key and WZ frames.
2009	Martins and Pereira *et al*. [82]	Proposed a novel method for refining the side-information of the DVC scheme.
2012	Wang *et al*. [83]	Combined particle filtering with an LDPC decoder for improving the correlation estimate in the DVC context.
	Skorupa *et al*. [84]	Proposed a reduced-delay-based DVC scheme relying on extrapolation techniques.
2013	Abou-Elailah *et al*. [85]	Introduced a novel method of combining both global and local motion estimation in DVC.

Table 1.3: Summary of major contributions on DVC schemes.

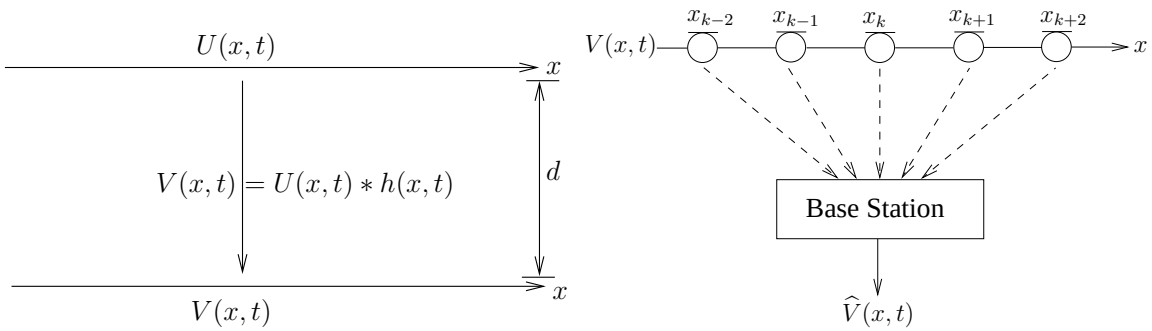

(a) Sound propagation.

(b) DAC set-up.

Figure 1.13: Schematic diagram illustrates the DAC sound propagation and DAC set-up [13, Chapter 14].

acoustic channels impulse response $h(t,x)$ [13]. The DAC scheme is illustrated in Figure 1.13(b), where the acoustic sensors, array of microphones for example, located on the upper line x generate samples of the channel-contaminated sound field $V(x,t)$, before transmitting their signals to the joint base station. The base station aims for estimating $\widehat{V}(x,t)$ representing the sound field $V(x,t)$ using the maximum achievable compression rate R, given the maximum acceptable distortion $\mathbb{D}$. This problem can be interpreted as a rate-distortion WZC problem, which was discussed in Section 1.2.1.2. Thus, several WZC techniques have been considered in the context of designing DAC schemes [13, 86, 87, 89, 90]. For example, a practical DAC based scheme was proposed in [86] which relied on DSC scheme of [32]. A novel wavelet-based DAC was introduced in [87] for wireless acoustic sensor networks.

Motivated by the above discussions, DSC techniques have been adopted in diverse applications. Albeit they are beyond the scope of this treatise, there is a significant number of related contributions in the context of hyperspectral image coding [2, 56, 57, 91, 92, 93], media authentication [94, 95, 96, 97, 98], securing biometric data [99, 100, 101, 102] and wireless sensor networks [7, 17, 49, 63, 65].

1.3 Joint Source-Coding and Channel-Coding

According to Shannon's separation theorem [118], reliable transmission can be attained by separate source coding using lossless entropy codes and channel coding, when communicating over Gaussian channel. However, the validity of this theorem hinges on a number of idealised assumptions, such as tolerating an infinite encoding/decoding complexity and delay. In reality, source coding typically fails to remove all the redundancy residing in the source [119]. Thus, Joint Source-coding and Channel-coding (JSCC) offers an alternative approach, in which the residual redundancy of the source-coded stream is exploited [119, 120]. More explicitly, JSCC techniques have been designed for realistic finite-delay, limited-complexity image/video systems communicating over wireless channels. Typically, JSCC schemes constitute a family of serially concatenated source encoders and channel encoders, which is capable of attaining substantial coding gains, while maintaining a realistic decoding complexity [105, 107, 108, 110, 121]. At the decoder, however, the extrinsic information is iteratively exchanged between the channel decoder and the source decoder, forming a so-called Joint Source-Channel Decoding (JSCD) mechanism. Thus, EXtrinsic Information Transfer (EXIT charts) charts can be employed for analysing the convergence behaviour of the iterative source/channel decoder pair [114, 119, 113, 122, 123][4]. Accordingly, diverse source-code and channel-code combinations have been considered. For example,a Variable Length Code (VLC) was combined with a Turbo Trellis-Coded Modulation (TTCM) scheme in [113, 123], while irregular VLCs were concatenated with Unity Rate Coding (URC) in [114, 119, 124]. The main contributions on the subject of JSCC are summarised in Table 1.4.

[4]More details on how the EXIT charts can be invoked to study the convergence behaviour will be provided in Section 2.5 and Section 3.3.1.

Year	Author(s)	Contribution
1991	Sayood and Borkenhagen [103]	A seminal JSCC design conceived for exploiting the residual redundancy of a fixed-length source encoded sequence.
1995	Hagenauer [104]	Proposed the first JSCD which exploited the residual redundancy exhibited after encoding a speech sequence.
1997	Balakirsky [105]	Proposed a novel trellis-based VLC and incorporated it into a JSCC scheme.
2000	Peng *et al*. [106]	Incorporated turbo codes into a JSCC designed for image transmission.
2001	Görtz [107]	Proposed the iterative JSCD philosophy employing a turbo-like decoder structure.
	Bauer and Hagenauer [108]	Adapted the powerful bit-level Maximum A-Posteriori (MAP) [34] algorithm for VLC decoding in the context of JSCC scheme.
	Garcia-Frias and Villasenor [109]	Applied JSCD for decoding hidden Markov sources.
2002	Kliewer and Thobaben [110]	Further developed the JSCC scheme of [108] decoding for correlated sources.
2005	Kliewer and Thobaben [111]	Introduced a modified MAP decoding algorithm for exploiting the inter-symbol correlation using a bit-level-based trellis VLC decoder [108].
2006	Kliewer *et al*. [112]	Proposed an efficient reduced-complexity method for computing non-binary EXIT charts.
2007	Ng *et al*. [113]	Intrinsically amalgamated Space Time Coded Modulation (STCM) with VLC to conceive a scheme that is capable of providing both multiplexing gain as well as coding gain.
2008	Maunder *et al*. [114]	Proposed a novel irregular VLC scheme for near-capacity JSCC.
2009	Zhang *et al*. [115]	Proposed a novel error-resilient JSCC video codec for the lossless DSC problem.
2014	Wang *et al*. [116]	Proposed a Unary Error Correction (UEC) code facilitating symbol values that are randomly selected from a set having an infinite cardinality for near-capacity JSCC.
2015	Zhang *et al*. [117]	Further investigated the JSCC scheme of [116] using EXIT charts for controlling the decoder activation order.

Table 1.4: Summary of major contributions on JSCC.

1.4 Network Coding

In their seminal work [125], Ahlswede *et al.* introduced Network Coding (NC) as an efficient data transport technique that is capable of increasing the overall achievable throughput of the system, while reducing both the energy required as well as the packet delay [126]. This is achieved by allowing Relay Nodes (RN)s in a communication network to combine multiple data packets received via the incoming links before transmitting them to the Destination Node (DN) [127]. Motivated by its benefits, NC has penetrated various fields, including; wireless communication, computer networks, cryptography, database management systems, optical networks and switching theory [126, 128].

In contrast to conventional cooperative communication, the RNs of NC schemes formulate specific combinations of the received signals, rather than simply forwarding their replicas of them [129]. More explicitly, the RNs of NC will combine multiple frames, known as Information Frames (IFs), received from the incoming links, before sending them to the DN [130]. According to the specific nature of the information combination process, NC may be categorised into Liner Network Coding (LNC) and Non-Linear Network Coding (NLNC) [126]. The algebraic linearity of LNC is beneficial because their exact mathematical foundations can been easily established [128, 126]. Furthermore, the coefficients used in the LNC can be found from a large finite set as detailed in [131, 132] or from parity-check matrices of channel codes, as discussed in [133, 134, 135]. Typically, these linear combining operations are defined over finite Galois Fields (GF) [134, 135, 136].

Later, the Dynamic Network Coding (DNC) concept was introduced in [137], where each of the RNs dynamically transmits its non-binary linear combinations to the DN. To elaborate further, each of the M users broadcasts his IFs to both the DN and to the RNs during their designated Broadcast Phase (BP). Next, after M BPs, each RN sends its Parity Frames (PFs) to the DN within the Cooperative Phase (CP)s, where each of these PFs is comprised of non-binary linear combinations of the successfully received IFs. In [135, 136], the concept of DNC techniques was extended, where each of the SNs and RNs is allowed to broadcast its IFs and PFs several times during the BPs and CPs rather than just once as in the baseline DNC counterpart scheme of [137]. In [135, 136], the NC problem was formulated as that of designing a linear Forward Error Correction (FEC) block code, where the diversity order achieved was evaluated in order to quantify the overall expected performance. The upper and lower Frame Error Ratio (FER) bounds as well as the outage probability of the NC systems was derived in [138].

Adaptive Dynamic Network Coding (ADNC) designs were proposed in [133, 139, 140], aiming for enhancing the average transmission rate without degrading the diversity gain of the scheme. A channel-quality feedback flag can be used to indicate, weather the IFs received at the DN were successfully or unsuccessfully decoded during the BPs [133, 139, 140]. As a consequence, the multiplexing gain and hence the attainable affective transmission rate was improved, as the number of PFs was reduced. In [133] an ADNC-based near-capacity irregular convolution code supporting multiple users was proposed, which exhibited an excellent performance in a hostile environment

imposing both uncorrelated Rayleigh fading and quasi-static shadow fading. A novel cooperative cognitive radio-aided ADNC regime was proposed in [139], where the cognitive users act as RNs that support the primary users, (or SNs in our case).

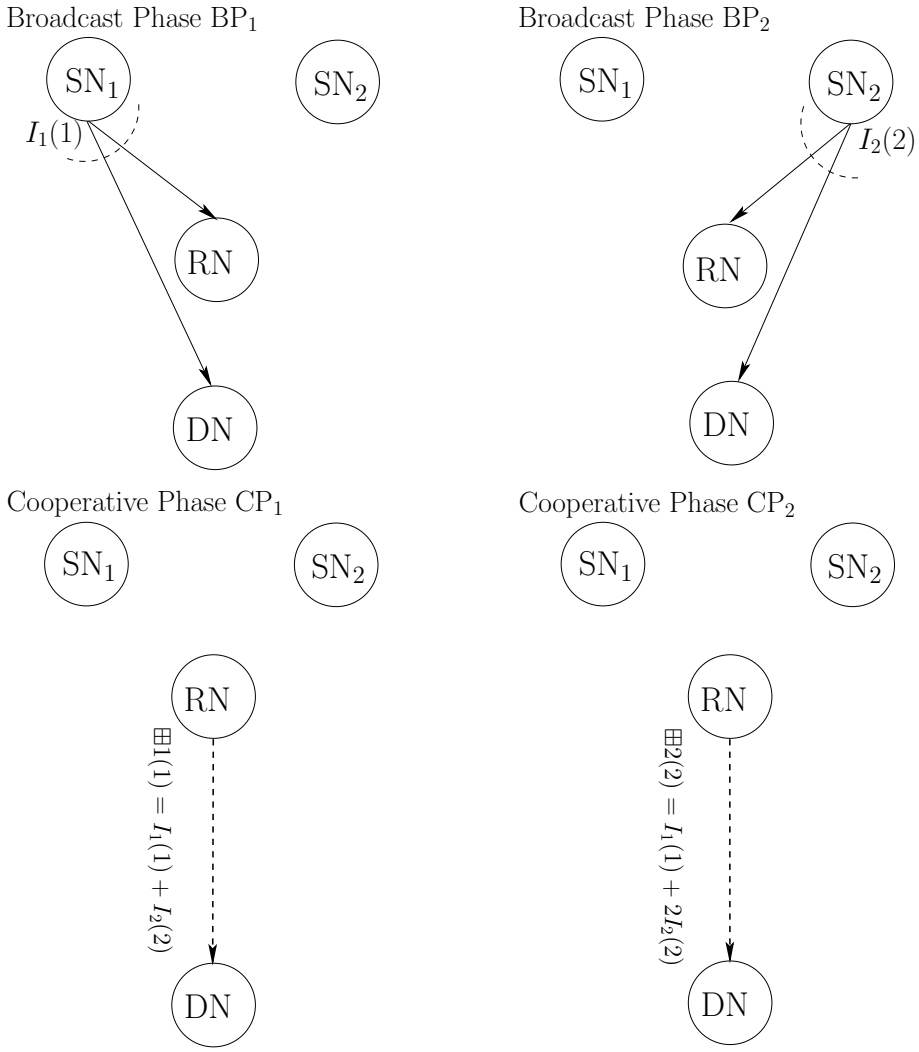

Figure 1.14: Schematic model of a NC-aided system having $M = 2$ SNs based on the generator transfer matrix $\boldsymbol{G}_{2\times 4}$ of Equation (1.11).

Let us now consider the specific example presented in Figure 1.14, where the system has $M = 2$ SNs, each of them broadcasting single IF during the corresponding BP. Then, during the CPs the RN transmits two PFs, as seen in Figure 1.14, hence the transmission phases can be summarised as follows:

$$(BP_1) : SN_1 \xrightarrow{I_1(1)} RN,\ SN_1 \xrightarrow{I_1(1)} DN\ , \tag{1.7}$$

$$(BP_2) : SN_2 \xrightarrow{I_2(2)} RN_1,\ SN_2 \xrightarrow{I_2(2)} DN\ , \tag{1.8}$$

$$(CP_1) : RN \xrightarrow{\boxplus 1(1)=I_1(1)+I_2(2)} DN\,, \tag{1.9}$$

$$(CP_2) : RN \xrightarrow{\boxplus 2(2)=I_1(1)+2\cdot I_2(2)} DN\,, \tag{1.10}$$

where the $\boxplus$ operation denotes the non-binary linear combinations performed over GF(4). In our example, if all the frames transmitted within all phases are successfully decoded, the NC protocol can be fully characterised using a (2×4)-element transfer matrix $\boldsymbol{G}_{2\times 4}$[5] that can be expressed as[6]:

$$\boldsymbol{G}_{2\times 4} = \left[\begin{array}{cc|cc} 1 & 0 & 1 & 1 \\ 0 & 1 & 1 & 2 \end{array}\right], \tag{1.11}$$

where the elements $\boldsymbol{G}_{2\times 4}(i,i) = 1$, $i = [1,2]$ represent the successful decoding of the IFs $I_i(i)$ transmitted by SN_i at the DN during the BP_i. Meanwhile, having $\boldsymbol{G}_{2\times 4}(1,3) = \text{“}1''$ or $(\boldsymbol{G}_{2\times 4}(2,4) = \text{“}2'')$ indicates that the PF transmitted by the RN during CP_1 or (CP_2) is successfully decoded at the DN corresponding to the element linear combining coefficient of the information frame $I_1(1)$ or $(I_2(2))$ in this parity frame has a value of “1″ or “2″. Furthermore, $\boldsymbol{G}_{2\times 4}(2,3) = \text{“}1''$ or $(\boldsymbol{G}_{2\times 4}(1,4) = \text{“}1'')$ indicates that the information frame $I_2(2)$ or $(I_1(1))$ is successfully decoded by RN during BP_2 or (BP_1), and the parity frame transmitted by RN during the cooperative phase CP_1 or CP_2 is successfully decoded at the DN.

1.5 Thesis Outline and Novel Contributions

Having discussed the motivation of employing DSC in Section 1.1, we have provided a brief summary of the history of DSC, JSCC and NC in Section 1.2, Section 1.3 and Section 1.4, respectively. Some of the surveyed contributions will be revisited in later chapters. Let us now present the outline of this treatise and highlight its novel contributions.

1.5.1 Thesis Outline

The characteristics of our system models considered in our main chapters are illustrated in Table 1.5. Figure 1.15 illustrates a bird-eye view of the thesis structure, showing the relationship of each chapter with the design challenges portrayed in Figure 1.11.

- In **Chapter 2** we commence with a concise historic background of the powerful Coded Modulation (CM) concept in Section 2.2, followed by our discussion of the main Trellis-Coded Modulation (TCM) principles in Section 2.3. More explicitly, Set Partitioning (SP) is the mapping technique that ensures maintaining a high Euclidean distance between the signal constellation points is explained in Section 2.3.1, while its Maximum A-Posteriori (MAP) decoder [34] is capable of achieving the minimum attainable Symbol Error Ratio (SER) is illustrated in Section 2.3.2. Subsequently, the performance of the CM schemes is analysed

[5]The transfer matrix can be derived from the appropriately selected systematic generator matrix $\boldsymbol{G}$ of an (n,k,d_{min}) linear block code [135, 136]. This linear block code should satisfied a Maximum Distance Separable (MDS) code condition for the sake of approaching the maximum minimum distance bound [141]. In our example, we use the systematic generator matrix $\boldsymbol{G}$ of the Reed Solomon (RS) codes constituting a well-known class of MDS codes is provided by the software application SAGE [142].

[6]Note that the DNC encoding and decoding will be explained in details later in Chapter 6.

Characteristics	**Chapter 3**	**Chapter 4**	**Chapter 5**	**Chapter 6**
Source Code	VLC	No	No	No
Channel Code	TTCM	TTCM	TTCM	TTCM
Scheme Type	JSCM (TTCM-VLC) Figure 3.2	perfect side-information A-DJSTTCM Figure 4.1	DJSTTCM-SPM Figure 5.2	DJSTTCM-ADNC Figure 6.1
Transmission Structure	two-way relaying Figure 3.1	direct link Figure 4.1	RN-aided SPM Figure 5.1	NC with multiple RNs Figure 6.7
Decoder Type	iterative TTCM-VLC	iterative DJSTTCM	iterative DJSTTCM	iterative DJSTTCM and NC decoder
MUD Type	ML, MMSE-IC	ML	ML, MMSE-SIC	ML
Analysing Tool	EXIT, DCMC	BER, DCMC	EXIT, DCMC	BER
Performance Metrics	BER, PSNR, subjective-image	BER, rate region, MSP	BER, rate region	BER, FER
Channel Type	uncorrelated Rayleigh fading	uncorrelated Rayleigh and Nakagami fading	uncorrelated Rayleigh fading	uncorrelated Rayleigh and quasi-static fading

Table 1.5: Summary of the system models considered in each chapter. Please see the glossary for the anonymous abbreviations.

for transmission over both Additive White Gaussian Noise (AWGN) as well as Rayleigh fading channels in Section 2.4. Later in Section 2.5, the powerful semi-analytical tool of EXIT charts is introduced, followed by an insightful example on how they can be utilised for analysing the decoding convergence behaviour.

- In **Chapter 3** we proposes and investigate an attractive Joint Source-coding, Channel-coding and Modulation (JSCM) scheme, by amalgamating TTCM and VLC as the TTCM-VLC scheme in a two-way relaying arrangement. The chapter commences by quantifying the Discrete-input Continuous-output Memoryless Channel (DCMC) capacities for each of the transmission phases in Section 3.2. Inspired by the DCMC analysis, we propose a Power Sharing (PS) technique for the two phases. In Section 3.3, the classic EXIT charts technique is used for investigating the decoding convergence of the joint source and channel decoder as well as for the overall system design. The quality of the decoded source signals is quantified using the Bit Error Ratio (BER) metric. Subsequently, we quantify the Peak Signal to Noise Ratio (PSNR) as well as the subjective image performance attained in Section 3.4.

- In **Chapter 4** the bandwidth-efficient Adaptive TTCM concept was incorporated into our DJSC design, resulting in the Adaptive Distributed Joint Turbo Trellis-Coded Modulation (A-DJSTTCM) scheme for transmission over both Rayleigh and Nakagami-m fading channels. The chapter commences by describing the system model in Section 4.2, where the A-DJSTTCM encoder and decoder structures are outlined. Next, both the BER as well as the DCMC capacities and the Slepian-Wolf Shannon limit (SW/S limit) are characterised in Section 4.3, so that our adaptive scheme may be compared against them. Similarly, the SW/S bounds derived for Nakagami-m channels using different fading parameter values are also evaluated. The BER curves as well as the rate regions are also documented as our performance metrics in Section 4.4. Additionally, the Mode Selection Probability (MSP) of selecting each of the transmission modes versus the SNR are utilised for characterising our adaptive scheme.

- In **Chapter 5** the more practical MAC scenario is considered. More explicitly, unlike in Chapter 4, where the side-information $\{b_2\}$ is assumed to be known at the receiver, in this chapter both the sources $\{b_1\}$ and $\{b_2\}$ are transmitted through a Rayleigh fading channel. The overall cooperative model is detailed in Section 5.2, where both source transmissions are supported by a SuperPosition Modulation (SPM)-based Relay Node (RN), resulting in the Distributed Joint Source TTCM (DJSTTCM)-SPM regime. Both transmission phases, namely Phase-I and Phase-II are investigated in Section 5.3 and Section 5.4, respectively. EXIT charts, BER curves and the associated rate regions are used for designing and analysing both phases. Similar to Chapter 4, the SW/S bound is determined with the aid of the DCMC capacity curves. In Section 5.6, a reduced-complexity Block Syndrome Decoding (BSD)-based DJSTTCM is introduced. Our BSD-based scheme is also incorporated for providing an accurate correlation coefficient estimate.

- In **Chapter 6** Network Coding (NC) was invoked for supporting the transmission of cor-

related sources, where the NC has the capability of improving the overall throughput, at a constant energy level. Our scheme proposed in Section 6.2 encounters a hostile channel that experienced both fast fading (small-scale uncorrelated Rayleigh fading) and slow fading (quasi-static Rayleigh fading). The chapter commences by describing the system model in Section 6.2, before illustrating briefly the NC encoder and decoder in Section 6.2.2 and Section 6.2.6, respectively. The overall system transmission rate as well as the diversity order are also analysed in Section 6.2.3 and Section 6.2.5, respectively. Finally, in Section 6.3 the performance of our proposed scheme is quantified in terms of Frame Error Ratio (FER) curves.

1.5.2 Novel Contributions of This Thesis

The contributions of this thesis focus on proposing a range of algorithms as well as transmission schemes for DJSC designed for communicating over noisy channels. Based on the following publications [44, 123, 143, 144, 145, 146, 147] the novel contributions are summarised as follows:

1. In [123], we quantified the achievable capacity of two-way relay-aided communication. The single-user JSCM schemes of [122, 148] were extended to a two-user-based two-way relay-aided system. In order to make our joint scheme suitable for wireless multimedia transmission, the number of the trellis states of our VLC was considerably reduced. The resultant low-complexity source-coding schemes were investigated in the context of image transmission over two-way relay-aided channel.

2. In [146] we proposed an energy-efficient video codec. Explicitly, our scheme is capable of exploiting the improved spectral efficiency offered by two-way relay-aided communication as well as by making use of the residual redundancy of the video coded stream. To elaborate a little, a low-complexity source encoder [123] designed, with the specific objective of considerably reducing the VLC decoding complexity, by exploiting the correlation amongst video pixels.

3. In [44], we proposed an amalgamated Distributed Joint Source-coding and TTCM (DJSTTCM) scheme for SW coding, which is capable of attaining a near-SW/S performance for a wide range of source correlation values. Our new scheme exhibits no error floor[7], despite its low complexity. Furthermore, a carefully constructed modified symbol-based MAP algorithm, as outlined in Section. 2.4.2, is conceived for exploiting the side-information available at the decoder. Additionally, we eliminated the idealized simplifying assumptions exploited in the prior literature [12, 149, 150], and considered more realistic fading channels, including uncorrelated Rayleigh fading, Nakagami-m fading and binary symmetric channels. Additionally, the adaptive A-DJSTTCM scheme was conceived for accommodating the near-instantaneously time-varying nature of the wireless channel as well as for exploiting the s

[7] As documented in Figure 4.6, no error floor is observed above a BER level of 10^{-6}, hence our scheme is suitable for wireless applications.

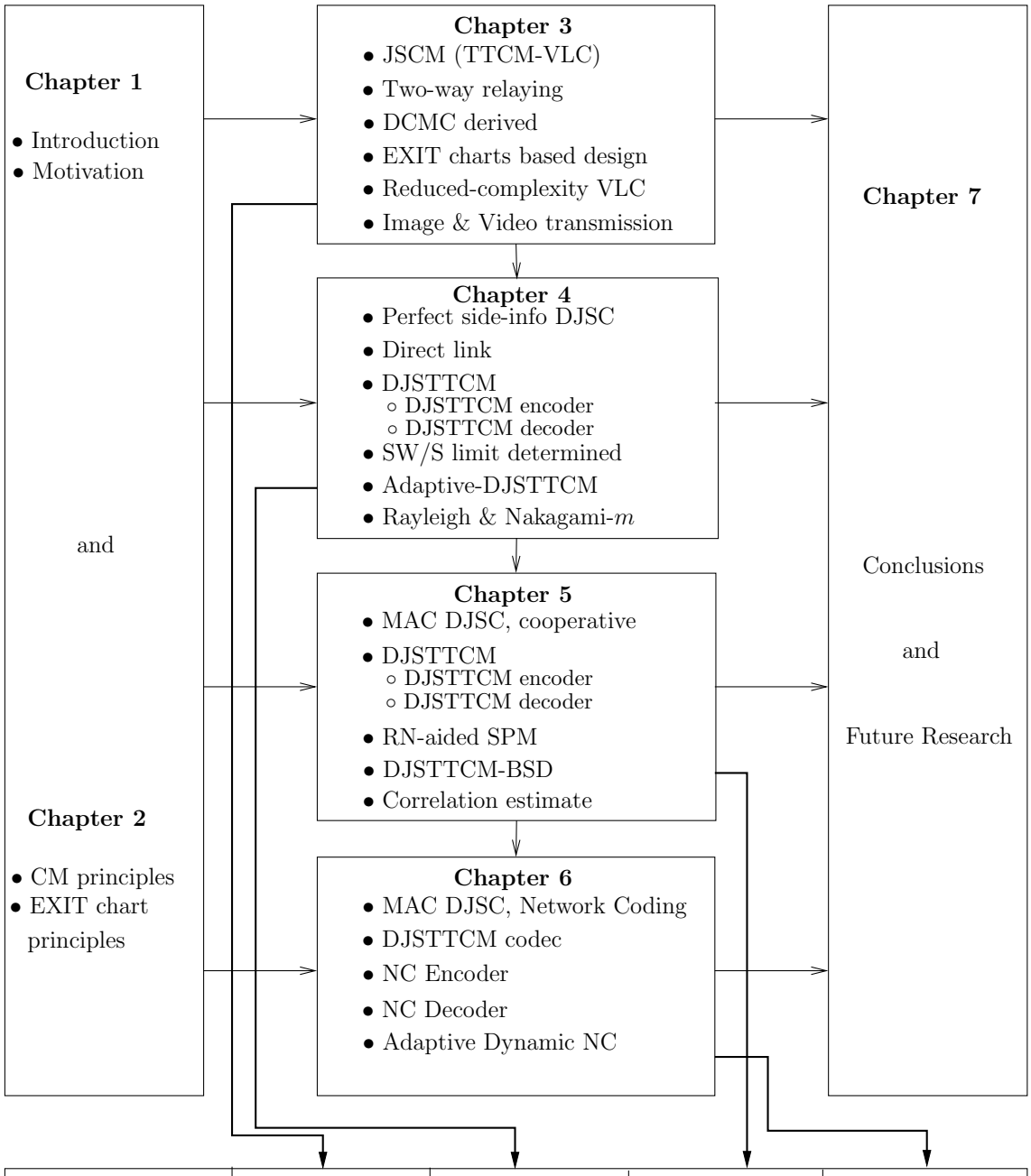

Challenges	Chapter 3	Chapter 4	Chapter 5	Chapter 6
CE			√	
RC	√		√	
RA		√		√
DJSC		√	√	√
CSC	√	√	√	
CS	√		√	√

Figure 1.15: Thesis outline showing each chapter's corresponding design challenges that are shown in Figure 1.10, namely Correlation Estimation (CE), Reduced-Complexity (RC), Rate-Adaptive (RA), Coded-Stream Compression (CSC), Distributed Joint Source-Channel coding (DJSC) and Cooperative System (CS).

correlation coefficient fluctuations amongst the sources. More explicitly, the system adapts its parameters according to both the channel quality and the correlation coefficient ρ of the sources[8], while maintaining a given target BER. Our A-DJSTTCM scheme of [44] has also been examined in [147] for a wide range of realistic Nakagami-m fading scenarios, where the DCMC capacity formula was derived for specifying the SW/S limit of all the scenarios considered.

4. In [143], we proposed a uniquely integrated DJSTTCM scheme for more realistic cooperative scenario, when both sources are communicating over a noisy MAC. Hence, we have eliminated the idealised simplifying assumption of having perfectly decoded side-information of [44]. The scheme is capable of attaining a near-SW/S performance for a wide range of correlation coefficients ρ. Additionally, when compared to similar schemes that were proposed for correlated sources transmitted over noisy MAC [8, 46, 49, 50], our scheme exhibits no error floor[9], despite its low complexity. In comparison to the systems proposed in [8,46,48,50], where BPSK modulation was used, our scheme is a more bandwidth-efficient scheme, since high-order modulation schemes were invoked. A novel SPM technique is employed at the RN that is equipped with two different operational modes, resulting in an improved power efficiency as well as more flexibility. Moreover, the semi-analytical EXIT charts tool is used for determining the most appropriate number of iterations between the constituent components of the decoder, for the sake of achieving an early decoding convergence.

5. In [145], the bandwidth-efficient DJSTTCM scheme investigated in [143] is further developed with the aid of Dynamic Network Coding (DNC). The amalgamated scheme is referred to as the DJSTTCM-DNC arrangement, which is proposed for supporting correlated source transmissions over hostile channels experiencing both small-scale and large-scale fading. Additionally, we have also conceived the novel Adaptive Dynamic Network Coding (ADNC) design of [133] for our DJSTTCM scheme, resulting in the DJSTTCM-ADNC regime, where the RNs would adaptively transmit their corresponding frames depending on weather the signal of the sources have been successfully received at the destination or not. Hence, the scheme's overall effective throughput could be enhanced. In our cooperative NC-based scheme, only two time slots are required for completing a full transmission cycle, as the transmission is carried out simultaneously using Space-Division Multiple Access (SDMA). By contrast, the Time-Division Multiple Access (TDMA)-based cooperative transmission regimes of [133, 134, 139] requires four time slots for completing a full transmission cycle, which could lead to a spectral efficiency loss. The NC-based cooperative systems proposed in [66, 64] cannot support more than two users, because the RN signals were constructed using a simple bit-wise XOR operator. By contrast, in our NC model the RN signals are composed using non-binary linear coefficients-based equations, leading to a further scalability in our design.

[8] Where ρ is expressed using a cross-over probability p_e as $\rho = 1 - 2p_e$.

[9] As shown in Figure 5.6, no error floor is observed at above BER level of 10^{-6}, hence our scheme is evidently suitable for wireless applications.

Chapter 2

Coded Modulation and Convergence Analysis

2.1 Introduction

Coded Modulation (CM) constitutes a bandwidth-efficient scheme that incorporates both coding and modulation functions without extending the bandwidth. In general, four CM-based schemes, namely Trellis-Coded Modulation (TCM) [151], Turbo TCM (TTCM) [152], Bit-Interleaved Coded Modulation (BICM) [153] and BICM with Iterative Decoding (BICM-ID) [154] have attracted the most substantial interest in both research and practical applications[1]. All the four schemes advocated were designed for improving the attainable throughput by considering the design of error correction codes and modulation, where the parity bits are absorbed without any bandwidth expansion by increasing the number of bits per modulated symbol.

By contrast, conventional channel codes, such as turbo and Low-Density Parity-Check (LDPC) codes, impose a bandwidth expansion for accommodating the parity bits. This chapter surveys the history of CM in Section 2.2, while Section 2.3 investigates the TCM principles. The TTCM encoder and decoder are explored in Section 2.4.1 and Section 2.4.2, respectively, followed by a simulation study in Section 2.4.3. Section 2.5 introduces the EXtrinsic Information Transfer (EXIT) chart tool [157], before the chapter is concluded in Section 2.6.

2.2 A Historical Review of Coded Modulation

The history of the channel codes including CM goes back to Shannon's seminal work [118] in which the foundation of the information theory was outlined. The maximum achievable channel capacity limit derived in [118] has motived researchers to design channel codes that are capable of approaching this limit, while achieving an infinitesimally low error probability. Ungerböck firstly

[1] An insightful comparative study of the four schemes was conducted in [155] and in [156, Chapter 14].

proposed the TCM design that relies on symbol-based channel interleaving and Set Partitioning (SP)-based [151, 158] signal labelling. Motivated by the near capacity performance exhibited by the turbo codes [34], Robertson and Wörz proposed TTCM in [152], which adopts the turbo-like structure of [34], where two TCM components are concatenated in parallel but separated through a symbol-based interleaver. Both TCM and TTCM invoked SP-based signal labelling for assuring the maximum Free Euclidean Distance (FED) between the least resilient bits of a coded symbol in the constellation [159]. Zehavi proposed BICM in [153] using a bit-based channel interleaver and Gray mapping-based signal labelling. Furthermore, BICM-ID was proposed in [154], where iterative decoding exchanging extrinsic information between the channel decoder and the demapper was considered. In a nutshell, Table 2.1 offers a state-of-the-art historical review on the family of CM schemes.

2.3 TCM Principles

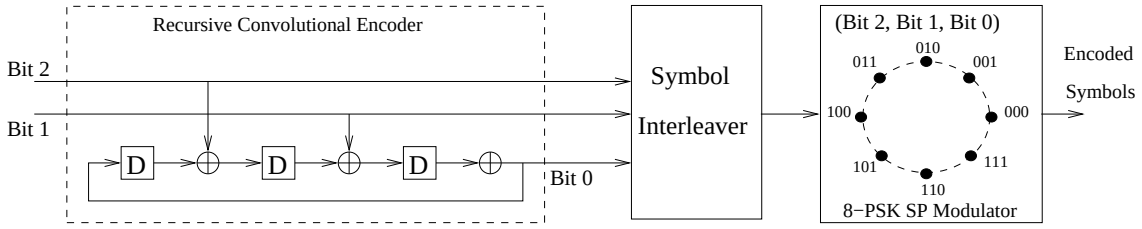

Figure 2.1: Schematic diagram of 8PSK TCM encoder using Ungerböck's RSC encoder and SP-based modulator [158] shown in Figure 2.2.

Again, TTCM code relies on a pair of parallel concatenated TCM codes. Typically, the TCM encoder comprises a serial concatenation of a Recursive Systematic Code (RSC) and a modulator [158]. Unlike conventional channel codes, here the modulator employs the SP mapping technique and the extra parity bit is absorbed by expanding the signal constellation. Figure 2.1 illustrates the schematic of an eight-state TCM encoder. The systematic RSC employed can be fully characterised using a generator polynomial of the form [156]:

$$G^j(D) = g^j_v.D^v + g^j_{v-1}.D^{v-1} + ... + g^j_1.D + g^j_0\,, \tag{2.1}$$

where D represents the shift register delay unit, while we have $g^j_v \in \{0,1\}$ according to the presence or absence of a connection between the information bits and the modulo-2 operator $\oplus$, for $j \geq 1$, explicitly, $g^j_v = 0$ implies having no connection, while $g^j_v = 1$ means that there is a connection between the j^{th} information bit and the v^{th} shift register stage [158]. On the other hand, the parity bit generator polynomial requires that the output of the last shift register is connected to the input of the first shift register, i.e. that we have $g^0_v = g^0_0 = 1$. By doing so, we can guarantee that the parity bit would have the same transition, whenever two path diverge from or merge into a common state in the trellis [156, 158]. Let us consider our TCM example of Figure 2.1, where the

Year	Author(s)	Contribution
1948	Shannon [118]	Founded the information theory and formulated the capacity.
1955	Elias [160]	Proposed convolutional codes.
1962	Gallager [35]	Proposed Low-Density Parity-Check (LDPC) codes.
1972	Bahl *et al.* [161]	Proposed the Maximum *A Posteriori* (MAP) algorithm.
1974	Bahl *et al.* [162]	Adapted the MAP algorithm for minimising the symbol error rate.
1982	Ungerböck [151]	Proposed Trellis-Coded Modulation (TCM) based on SP.
1989	Hagenauer *et al.* [163]	Introduced the use of soft information in Soft-Output Viterbi Algorithm (SOVA).
1992	Zehavi [153]	Introduced Bit-Interleaved Coded Modulation (BICM).
1993	Berrou *et al.* [34]	Proposed the novel turbo codes based on the MAP algorithm [161].
1994	Kofman *et al.* [164]	Investigated the multi level coded modulation performance.
	Le Goff *et al.* [165]	Proposed an improved BICM referred to as Turbo Coded Modulation (TuCM).
1995	Robertson *et al.* [166]	Introduced reduced-complexity Approx-Log-MAP algorithm.
1997	Li and Ritcey [154]	Proposed an improved BICM with Iterative Decoding (BICM-ID).
1998	Robertson and Wörz [152]	Proposed Turbo Trellis-Coded Modulation (TTCM) using similar structure to that of [34].
2004	Hanzo *et al.* [159]	Carried out an intensive comparative study between TCM, TTCM, BICM and BICM-ID schemes.
2006	Nana *et al.* [167]	Improved the decoding of LDPC coded modulations.
2008	Ng *et al.* [168]	Proposed near-capacity EXIT chart-aided design of TTCM design-aided.
	Maunder *et al.* [114]	Proposed a novel irregular VLC-TTCM scheme for near-capacity JSCC.
2009	Ng *et al.* [169]	Introduced distributed TTCM for cooperative communications.
2011	Islam *et al.* [170]	Analysis and design of cooperative BICM-OFDM systems.
2015	Liang *et al.* [139]	Proposed TTCM-aided adaptive dynamic network coding.

Table 2.1: Summary of major contributions on CM.

generator polynomials can be expressed as:

$$G^0(D) = 1001\,, \tag{2.2}$$

$$G^1(D) = 0010\,, \tag{2.3}$$

$$G^2(D) = 0100\,. \tag{2.4}$$

Conventionally, the overall polynomial is characterised in octal format as:

$$\mathbf{G(D)} = [G^0(D)\ \ G^1(D)\ \ G^2(D)] = [11\ \ 02\ \ 04]_8\,. \tag{2.5}$$

Then, the 3-bit codewords are interleaved using a symbol-based interleaver aiming for spreading the bursty symbol errors encountered, when communicating over fading channels [156].

2.3.1 Set-Partitioning

Although Gray mapping is widely used in wireless communication, since it has the minimum Bit Error Ratio (BER) for uncoded BPSK communicating over AWGN channels, it is not suitable for TCM [156]. More explicitly, in higher-order modulation schemes parallel transition might occur in the trellis diagram more frequently than in their lower-order counterparts [156, 158]. SP was proposed by Ungerböck [158] for assuring a high Euclidean distance among the constellation points that might exhibit parallel transitions. The minimum Euclidean distance of the signal points in the new subset should increase at each partitioning step. Figure 2.2 illustrates the SP process of an 8-PSK signal in which the constellation map is divided into multiple sets, where the minimum Euclidean distance is gradually increased during each consecutive partitioning step.

With reference to our TCM encoder of Section 2.1, the interleaved 3-bit codeword (b_2, b_1, b_0) will be mapped onto an 8-PSK constellation, where the parity bit b_0, which is used for protecting the other information bits itself unprotected. The two original information bits (b_2, b_1) are more error-resilient than b_0, while b_2 receives the highest error protection, because as seen in Figure 2.2, the 'noise-protection distance' of the points was gradually expanded from d_0 to d_2.

2.3.2 Maximum-A-Posteriori Algorithm

The binary Maximum *A Posteriori* (MAP) decoding algorithm was originally invented by Bahl, Cocke, Jelinek and Raviv [162][2]. Its capability of generating bit-by-bit soft decision-based output is however pivotal for employment in any iterative decoding scheme, such as turbo codes [34]. Later Robertson and Wörz proposed the non-binary MAP algorithm [152]. The minimum Symbol Error Ratio (SER) can indeed be attained by the MAP algorithm, but again naturally, at a higher complexity than that of the Viterbi algorithm used in non-iterative decoders.

The non-binary MAP algorithm deals with symbol probabilities. Moreover, more than two

[2]It is also referred to as the BCJR algorithm.

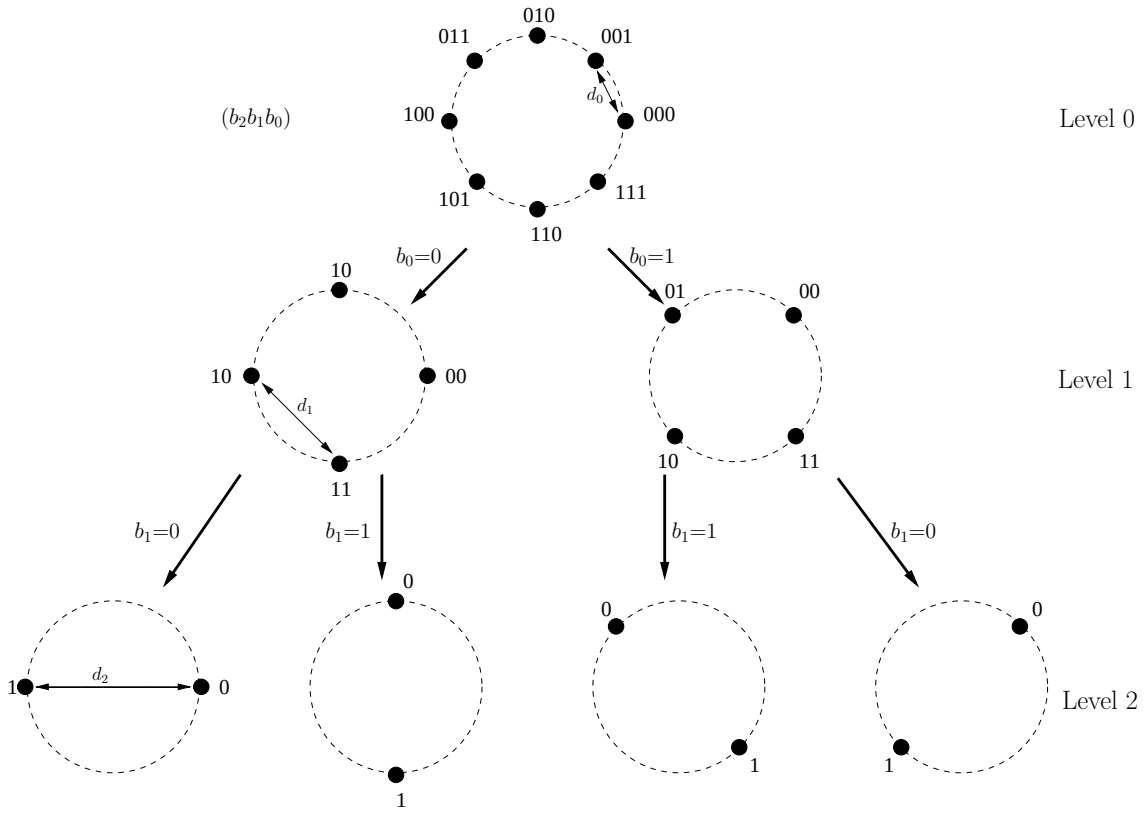

Figure 2.2: Set-Partitioning of a 8PSK signal constellation. [156].

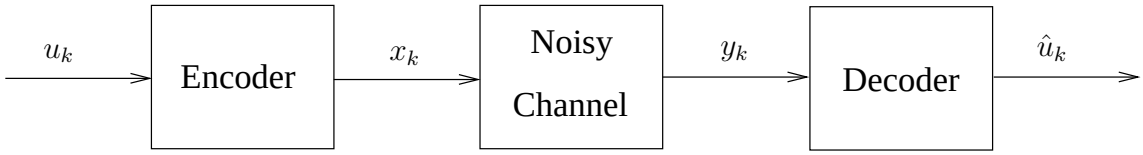

Figure 2.3: The transmission system [151, 156].

branches might emerge from each node of the non-binary MAP trellis than the pair of branches in its binary counterpart [156]. In this section we will briefly illustrate the reduced-complexity non-binary MAP algorithm employed in our CM decoder.

Let us consider the transmission schematic of Figure 2.3, where the information source symbol sequence is given by $\mathbf{u} = \{u_k\}$, for $k = 1, 2, \ldots, N$. Each source information symbol may assume $(M-1)$ possible values, i.e. we have $u_k \in \{1, 2, \ldots, M\}$. For example, in our TCM example of Figure 2.1 we have $M = 2^2 = 4$. Accordingly, each information symbol carries $\mathtt{m} = \log_2 M = \log_2(4) = 2$ information Bit Per Symbol (BPS). The encoder generates symbols $\mathbf{x} = \{x_k\}$, where $x_k \in \{\mu(1), \mu(2), \ldots, \mu(\bar{M})\}$ and $\mu(\cdot)$ is the QAM/PSK bit-to-symbol mapping function and $\bar{M} = 2^{\mathtt{m}+1}$ is the number of legitimate phasor combinations of the QAM or PSK constellation. Thus, in our 8-PSK example of Figure 2.1 we have $\bar{M} = 2^{2+1} = 8$-PSK. The received symbol sequence $\mathbf{y} = \{y_k\}$, upon transmitting $\mathbf{x}$ through an AWGN channel is formulated

as:

$$\mathbf{y} = \mathbf{x} + \mathbf{n} \,, \tag{2.6}$$

where $\mathbf{n} = \{n_k\}$ denotes the complex-valued AWGN sequence.

At the receiver, the received symbol sequence $\mathbf{y}$ is fed into a MAP algorithm-based decoder, which chooses the specific information source symbol $\mathbf{u}$ that maximises $\Pr(\mathbf{u} \mid \mathbf{y})$, i.e. $\hat{\mathbf{u}}$ is chosen according to:

$$\hat{\mathbf{u}} = \underset{u_k \in \{1,\ldots,M\}}{\operatorname{argmax}} \Pr(\mathbf{u} \mid \mathbf{y}) \,, \tag{2.7}$$

Note that, we have $\Pr(u_k) = \Pr(x_k)$ due to the one-to-one $x_k = \mu(u_k)$ QAM/PSK mapping function used. The probability $\Pr(\mathbf{u} \mid \mathbf{y})$ is referred to as the *A Posteriori* Probability (APP) for $\mathbf{u}$, where the MAP algorithm selects the information source symbol associated with the maximum APP. Thus, the MAP algorithm guarantees that the Symbol Error Ratio (SER) is minimised [156]. By contrast, the Maximum Likelihood (ML) estimation based on Viterbi algorithm chooses the particular information source symbol $\mathbf{u}$ that is most likely to have produced the received sequence $\mathbf{y}$. More specifically, the ML estimator will select the information source symbol $\mathbf{u}$ that maximises $\Pr(\mathbf{y} \mid \mathbf{u})$, i.e. $\hat{\mathbf{u}}$ is chosen according to:

$$\hat{\mathbf{u}} = \underset{u_k \in \{1,\ldots,M\}}{\operatorname{argmax}} \Pr(\mathbf{y} \mid \mathbf{u}) \,. \tag{2.8}$$

Assuming a memoryless channel, the conditional probability of receiving $\mathbf{y}$ given that $\mathbf{u}$ was transmitted can be written as:

$$\Pr(\mathbf{y} \mid \mathbf{u}) = \prod_{k=1}^{N} \Pr(y_k \mid u_k) \,. \tag{2.9}$$

The MAP algorithm relies on the code's trellis, in which there is a branch emerging from the previous trellis state $S_{k-1} = \grave{s}$ towards the current trellis state $S_k = s$ according to the input symbol $u_k = m$ encountered, given the received sequence $\mathbf{y}$. Subsequently, the APP of Equation (2.7) can be expressed as $APP_{k,m} = \Pr(u_k = m \mid \mathbf{y})$. Additionally, since the trellis structure allows us to traverse through the trellis from state to state in both a forward and backward manner, the APP can be determined using the summation of the different set of probabilities formulated as [156]:

$$APP_{k,m} = \Pr(u_k = m \mid \mathbf{y}) = \sum_{\text{all } \grave{s},s} \Pr(u_k = m \,,\, S_{k-1} = \grave{s} \,,\, S_k = s \mid \mathbf{y}) \,, \tag{2.10}$$

where the summation indicates adding all probabilities linked to all nodes $\grave{s}$ and s that are encountered, when we have $u_k = m$. According to [156], the APP can be estimated using:

$$APP_{k,m} = A_{k,m} \,. \sum_{\substack{(\grave{s},s) \Rightarrow \\ u_k = m}} \alpha_{k-1}(\grave{s}) \, \eta_k(\grave{s}, s) \, \beta_k(s) \,, \tag{2.11}$$

where $A_{k,m}$ is the *a priori* probability that is equiprobable for the first decoding iteration according

to:

$$A_{k,m} = \Pr(u_k = m) = \frac{1}{M} \, . \tag{2.12}$$

The term $\eta_k(\grave{s}, s)$ represents the transition probability from state $\grave{s}$ to s, when $u_k = m$ is encountered, which is given by [156]:

$$\eta_k(\grave{s}, s) = \exp\left(-\frac{|y_k - x_k|^2}{N_0}\right) \, , \tag{2.13}$$

where $N_0/2$ is the AWGN variance per-dimension and again $\mu(\cdot)$ is the QAM/PSK bit-to-symbol mapping function and $\bar{M} = 2^{m+1}$ is the number of possible phasor combinations in the QAM or PSK constellation. Incorporating the *a priori* probability of Equation (2.12), the channel-induced transition probability $\gamma(\grave{s}, s)$ shown in Equation (2.11) can be expressed using:

$$\gamma(\grave{s}, s) = A_{k,m} \, . \, \eta_k(\grave{s}, s) \, , \tag{2.14}$$

which will be used for recursively computing both the forward and backward recursions as [156]:

$$\alpha_k(s) = \sum_{\text{all } \grave{s}} \gamma(\grave{s}, s) \, . \, \alpha_{k-1}(\grave{s}) \, , \tag{2.15}$$

$$\beta_{k-1}(\grave{s}) = \sum_{\text{all } s} \gamma(\grave{s}, s) \, . \, \beta_k(s) \, , \tag{2.16}$$

respectively. Finally, the APP can be obtained from Equation (2.11). In a nutshell, the non-binary MAP algorithm can be summarised using Figure 2.4.

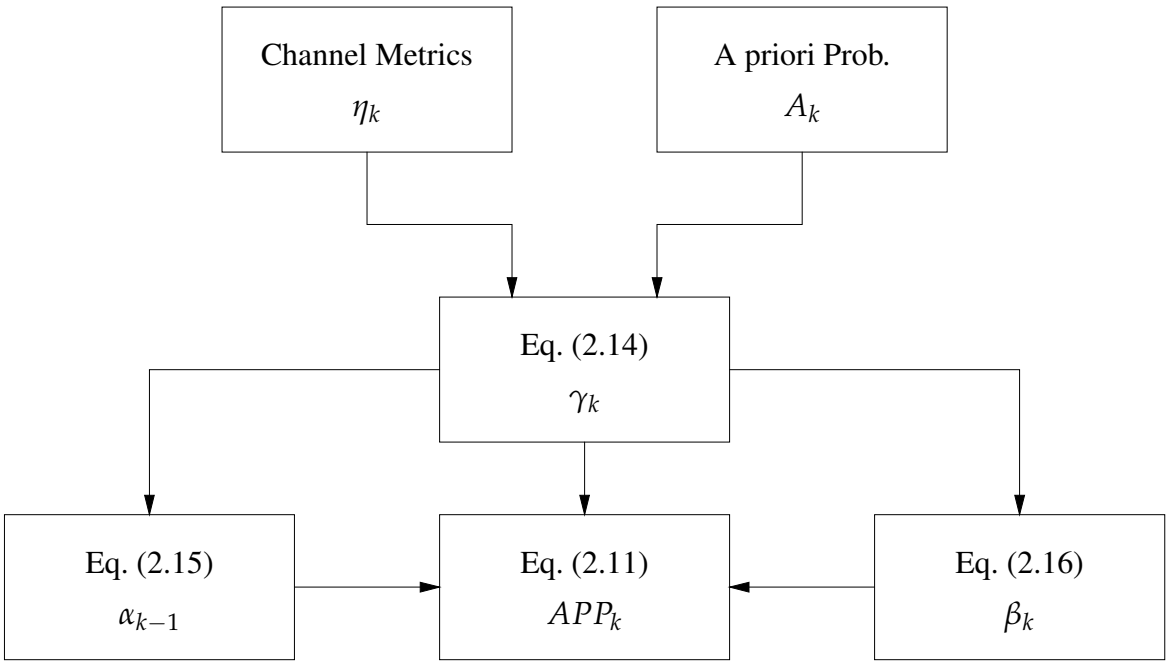

Figure 2.4: Summary of the symbol-based MAP algorithm operations [156].

As seen from the above discussion, the MAP algorithm relies on a considerable number of multiplication operations, hence imposing a high computational and hardware complexity. Furthermore, the multiplication of small probability values might also lead to numerical instability [156]. As a remedy, the logarithmic-domain MAP (Log-MAP) algorithm was introduced in [166], where a multiplication becomes addition and an addition, which based on the Jacobian logarithm formulated as [156]:

$$\begin{aligned} g(\Phi_1,\Phi_2) &= \ln(e^{\Phi_1}+e^{\Phi_2}) && (2.17)\\ &= \max\{\Phi_1,\Phi_2\}+\ln(1+e^{-|\Phi_1-\Phi_2|}) && (2.18)\\ &= \max\{\Phi_1,\Phi_2\}+f_c(|\Phi_1-\Phi_2|)\,. && (2.19) \end{aligned}$$

The correction factor f_c of Equation (2.19), can be estimated using three different methods:

- The Exact-Log-MAP algorithm [166], which is defined by computing the exact value of the correction term f_c using [156]:

$$f_c = \ln(1+e^{-|\Phi_1+\Phi_2|})\,. \quad (2.20)$$

- The Approx-Log-MAP algorithm [166] employs an approximation of the correction term f_c. A look-up table containing eight values of f_c ranging from 0 to 5 gives practically the same performance as the Exact-Log-MAP algorithm [166].

- The Max-Log-MAP [162], which simply relies on $\max\{\Phi_1,\Phi_2\}$ term only. Compared to the Approx-Log-MAP algorithm, it has a poorer performance, but imposes a reduced complexity.

Based on the above discussions, the Approx-Log-MAP algorithm is the best compromise scheme in terms of its performance and complexity. Hence it was employed for all simulations in this treatise, unless stated otherwise.

2.4 Turbo Trellis-Coded Modulation

TTCM [152] has a structure similar to that of binary turbo codes, where two identical parallel-concatenated TCM schemes-rather than convolutional codes-are employed as component codes. The classic TTCM design was outlined in [152], based on the search for the best TCM component codes using the so-called 'punctured' minimal distance criterion, in order to approach the capacity of the AWGN channel. The following two sections discuss the TTCM encoder and decoder.

2.4.1 TTCM Encoding

Figure 2.5 portrays the schematic of the TTCM encoder, which relies on a turbo-like encoder structure comprised of a pair of parallel concatenated TCM encoders linked by a symbol interleaver.

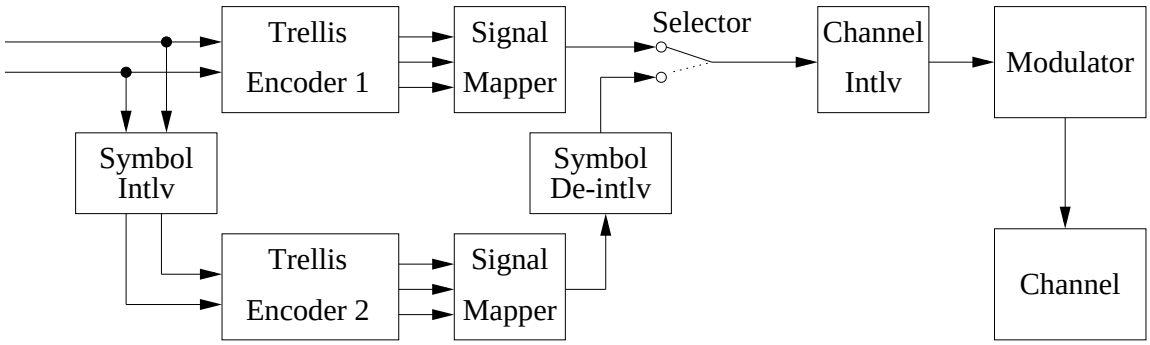

Figure 2.5: Schematic of the TTCM encoder [152].

Here, each TCM encoder consists of a trellis encoder and a SP-based bit-to-symbol mapper. The first TCM scheme encodes the original information bit sequence, while its second TCM encodes the interleaved version. Then each TCM-encoded codeword is mapped to complex phasors using the SP mapper of Section 2.3.1. The output of the second TCM encoder is de-interleaved, as seen in Figure 2.5. At this stage the two codewords of both branches have identical information bits but different parity bits. Hence, the Selector block of Figure 2.5 alternates between the lower and upper TCM components, puncturing half of the parity and transmitting the information bits only once. Next, the output of the Selector of Figure 2.5 is fed to the symbol-based channel interleaver in order to disperse the bursty symbol error when transmitting over fading channels.

2.4.2 TTCM Decoding

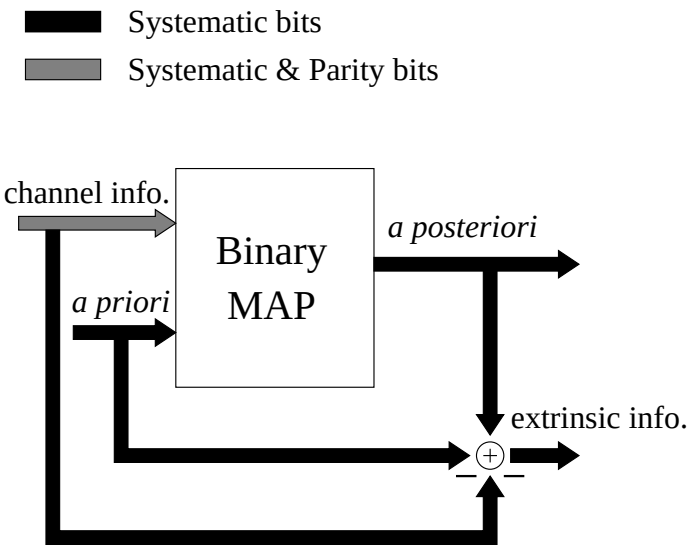

Figure 2.6: Schematic of a binary turbo component decoder [156].

Before embarking onto analysing the TTCM decoder, let us first highlight the main differences between the binary turbo decoder and the non-binary TTCM decoder. The schematic of the binary turbo decoder and of a non-binary TTCM decoder is shown in Figure 2.6 and Figure 2.7, respec-

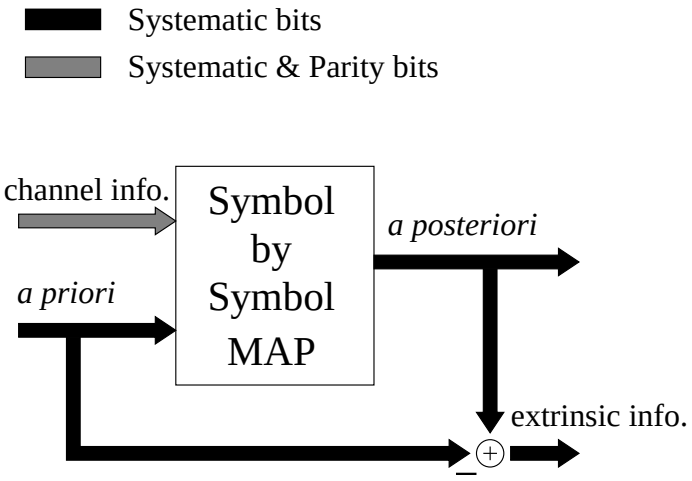

Figure 2.7: Schematic of a non-binary TTCM component decoder [156].

tively. The schemes differ in the nature of the information passed from one decoder component to the other. In a turbo-like structure each decoder alternately processes its corresponding encoder's channel-impaired output symbol and then the other encoder's channel-impaired output symbol. Before passing these extrinsic information to the other component decoder all intrinsic information contributions directly related to the processed information bit u_k has to be removed first [34]. This is important in order avoid any dependency of the constitute decoders' information on each other, because this dependency might prevent the decoder from achieving an iteration gain. In a binary turbo coding scheme the component decoder's output can be divided into three additive parts for each information bit u_k at step k, which are detailed below:

1. the systematic component $(S^{(1)}/S^{(2)})$, which is the received systematic value for bit u_k;
2. the *a priori* component $(A^{(1)}/A^{(2)})$, which corresponds to the information provided by the other component decoder for bit u_k;
3. the extrinsic information component $(E^{(1)}/E^{(2)})$, which does not depend on bit u_k itself, but on the surrounding bits.

By contrast, the non-binary TTCM codeword contains $\mathtt{m}$ number of information bits and a parity bit, which cannot be separated, since they are transmitted together in the same modulated symbol. Thus, the intrinsic information related to the original bits is inseparable from the extrinsic information, since both the systematic and party bits form part of the same symbol, encountering similar channel noise and fading. Therefore, observe with the aid of Figure 2.8 that the symbol-based TTCM decoder's output has only two components:

1. the *a priori* component of a non-binary symbol $(A^{(1)}/A^{(2)})$, which is provided by the other component decoder;

2. the inseparable extrinsic and systematic component of a non-binary symbol, which is denoted by $(E^{(1)}\&S^{(1)}/E^{(2)}\&S^{(2)})$.

Figure 2.8 illustrates the TTCM decoder in further detail, where the received symbols are fed into the "Metric" block for generating a $\bar{M} = 2^{m+1}$-element vector of probabilities using Equation (2.13). Each element of this vector represents the probability that a certain symbol of the $\bar{M}$-ary constellation was transmitted. The selector switches seen before the pair of the MAP decoders of Figure 2.8 select the current symbol's vector of probabilities, if the current symbol was not punctured according to the corresponding encoder. Alternatively, puncturing will be applied, in which the corresponding symbol's vector of probabilities will be set to zero, when using the logarithmic domain. Let the superscripts 1 and 2 denote the probabilities related to the first and (second) TCM decoder, respectively. Each TCM decoder has two inputs.

The first is the inseparable parity and systematic information $P^{(1)}\&S^{(1)}/(P^{(2)}\&S^{(2)})$ provided by the Metric block of Figure 2.7, while the second is the *a priori* information $A^{(1)}/(A^{(2)})$ provided by other component decoder. Next, the first (second) MAP decoder generates the *a posteriori* information $[E^{(1)}\&S^{(1)}] + A^{(1)}/([E^{(2)}\&S^{(2)}] + A^{(2)})$ information in which the term $A^{(1)}/(A^{(2)})$ can be subtracted yielding the extrinsic information. The resultant $[E^{(1)}\&S^{(1)}]/[E^{(2)}\&S^{(2)}])$ information is interleaved or (de-interleaved) in order to provide $(A^{(2)})/A^{(1)}$ for the other decoder component. This decoding process progresses iteratively in order to provide a reliable set of information exchanged between the decoder's constituent components. Finally, the 2^m-element vector of the probabilities of the lower decoder is subjected to a hard decision, for selecting the specific symbols that are associated with the maximum *a posteriori* probabilities, as Figure 2.8 shows.

2.4.3 TCM and TTCM Performance Results

This section examines the performance of both the TCM and TTCM schemes, when communicating over both AWGN and uncorrelated Rayleigh fading channels. Additionally, we investigate the TTCM performance, when both the frame length N_s and the number of iterations are varied. Note that, the number of iterations between the pair of the TCM constituent components of the TTCM decoder of Figure 2.8 is denoted by I.

Before proceeding with our analyses, let us first define the relationship between the Signal-to-Noise Ratio (SNR) and the SNR per bit E_b/N_0. The CM encoder generates n-bit codewords from the k-bit information symbols, hence the coding rate is given by $R_{cm} = k/n$. Next, the n-bit codeword will be modulated using an $\bar{M}$-ary constellation, where each transmitted symbol caries $\log_2(\bar{M}) = $ m Bit Per Symbol (BPS). Assume each symbol is transmitted at a rate of R_s symbol per timeslot, while L is the number of transmit antennas. Hence, the overall effective throughput of the system becomes:

$$\eta = R_{cm} \cdot \log_2(\bar{M}) \cdot R_s \cdot L \,. \tag{2.21}$$

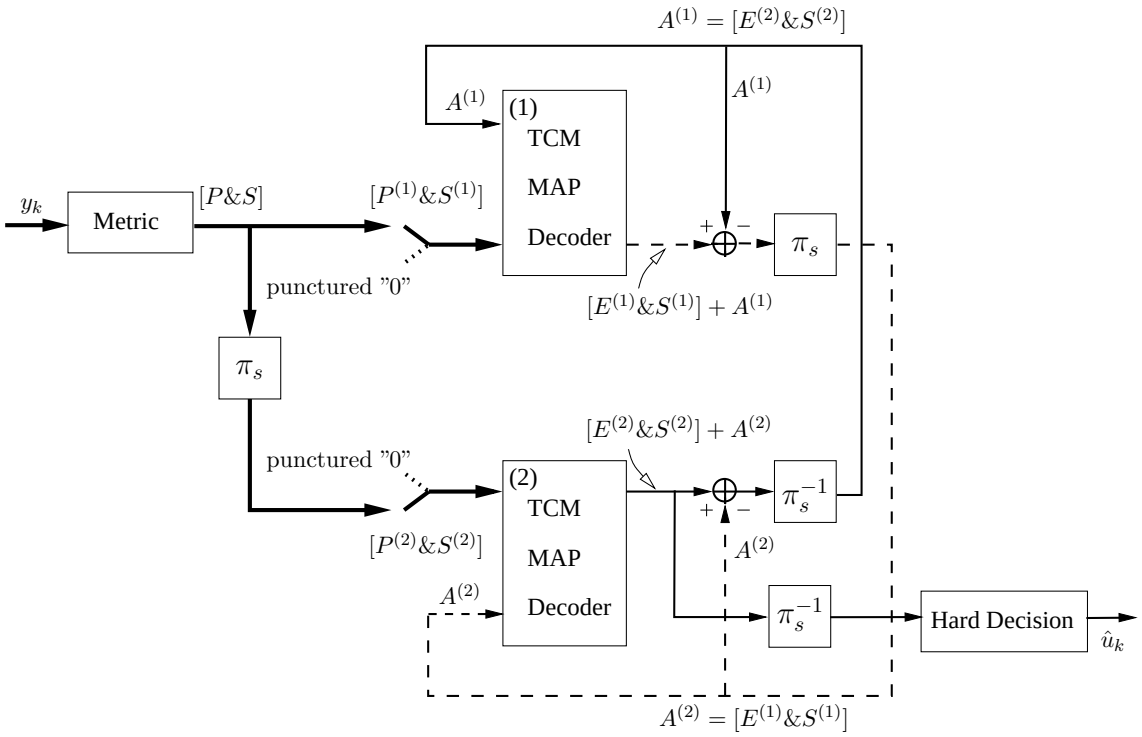

Figure 2.8: Schematic of the TTCM decoder where P, S, A and E represent parity information, systematic information, *a priori*, and extrinsic probabilities, respectively. The superscripts 1 and 2 denote the probabilities of the first and second TCM decoder, respectively, and π_s and π_s^{-1} denote the symbol interleaver and symbol de-interleaver that have similar arrangement order to their counterparts in the TTCM encoder of Figure 2.5.

Thus, the SNR is related to E_b/N_0 according to:

$$E_b/N_0 = \frac{1}{\eta}\text{SNR}\,, \tag{2.22}$$

and in dBs as:

$$E_b/N_0\ [\text{dB}] = \text{SNR}\ [\text{dB}] - 10\log_{10}(\eta)\ . \tag{2.23}$$

Figure 2.9 and Figure 2.10 present the BER performance of different TCM and TTCM coding schemes communicating over AWGN channels. Upon comparing both figures, all the TTCM schemes considered outperform the its TCM counterparts for similar encoding settings. More explicitly, for attaining an infinitesimally low BER level of 10^{-6} the "TCM-QPSK" scheme needs SNR= 5.1 dB, while the "TTCM-QPSK" scheme requires only SNR= 1.8 dB. This significant performance enhancement is an explicit benefit of the turbo-like structure of the TTCM facilitating efficient extrinsic information exchange between the TCM MAP-based decoders [155]. Note that for the sake of fair comparisons each of the TCM scheme employs a memory length of $\widetilde{\text{m}} = 6$ associated with $2^6 = 64$, states , while each TTCM scheme employs $\widetilde{\text{m}} = 3$ also corresponding to $I \times 2^3 \times 2 = 64$ states, when using four TTCM iterations. Moreover, both the E_b/N_0 and SNR required for attaining the target BER of 10^{-6} for TCM and TTCM, when communicating over

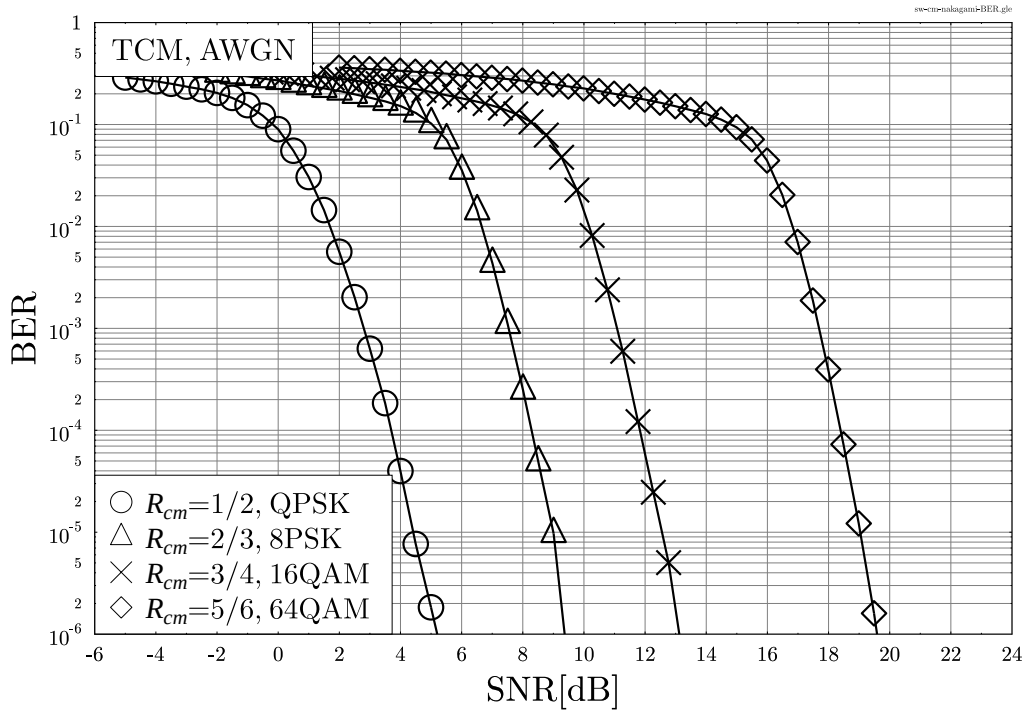

Figure 2.9: BER versus SNR performance of **TCM**-aided QPSK, 8PSK, 16QAM and 64QAM modulators when communicating over the **AWGN** channels and using code memory length of $\widetilde{\mathrm{m}} = 6$. The simulation parameters are listed in Table 2.2 and Table 2.3 while the related results are summarised in Table 2.4.

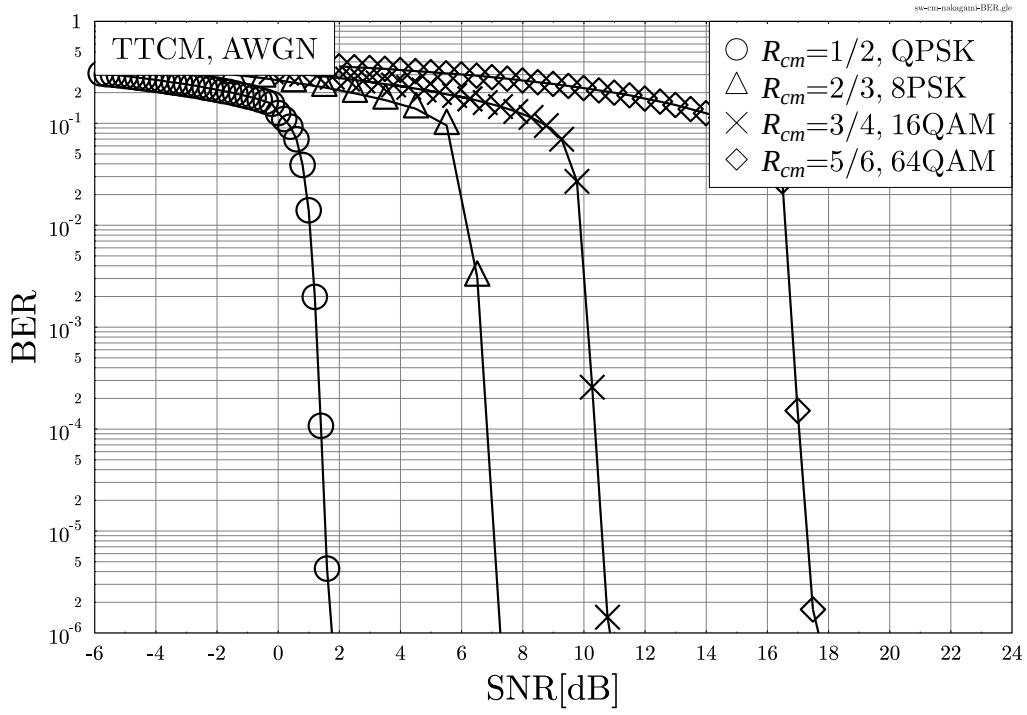

Figure 2.10: BER versus SNR performance of **TTCM**-aided QPSK, 8PSK, 16QAM and 64QAM modulators when communicating over **AWGN** channels using four TTCM iterations and code memory length of $\widetilde{\mathrm{m}} = 3$. The simulation parameters are listed in Table 2.2 and Table 2.3 while the related results are summarised in Table 2.4.

Coded Modulation	**TCM, TTCM**
Modulation Scheme	QPSK, 8PSK, 16QAM, 64QAM
Mapper type	Set-Partitioned
Number of iterations, TTCM	$I = 4$
Code Rate, R_{cm}	1/2, 2/3, 3/4, 5/6
Decoder type	Approximate Log-MAP
Demapper type	Maximum Likelihood (ML)
Symbols per frame	12 000
Number of frames	10 000
Channel	AWGN, Uncorrelated Rayleigh fading channel

Table 2.2: Simulation parameters for TCM and TTCM schemes that are used in Figures 2.9– 2.14, where the associated CM specifications are listed in Table 2.3.

CM Scheme	**Modulator Scheme**	**Code Memory,** $\widetilde{\mathrm{m}}$	**States Number**	**Generator Polynomials G(D)**
TCM	QPSK	6	64	$[117\ 26]_8$
	8PSK	6	64	$[103\ 30\ 66]_8$
	16QAM	6	64	$[101\ 16\ 64\ 0]_8$
	64QAM	6	64	$[101\ 16\ 64\ 0\ 0\ 0]_8$
TTCM	QPSK	3	8	$[13\ 06]_8$
	8PSK	3	8	$[11\ 02\ 04]_8$
	16QAM	3	8	$[11\ 02\ 04\ 10]_8$
	64QAM	3	8	$[11\ 02\ 04\ 0\ 0\ 0]_8$
		5	32	$[41\ 02\ 04\ 10\ 20\ 40]_8$

Table 2.3: Code specifications of TCM and TTCM schemes that are used in Figures 2.9–2.14, where octal format were used for representing the generator polynomials [152, 156]

AWGN channels are listed in Table 2.4.

Similarly, Figure 2.11 and Figure 2.12 show the BER versus SNR performance of the TCM and TTCM schemes in conjunction with different number of modulation levels, when communicating over uncorrelated Rayleigh fading channels. In line with the AWGN performance, TTCM schemes always outperform the TCM schemes apart from the 64QAM scenario that using a memory length of $\widetilde{\mathrm{m}} = 3$, where both TCM and TTCM exhibit similar trends. This is not unexpected, since using a memory length of $\widetilde{\mathrm{m}} = 3$ associated with the generator polynomial of $\mathbf{G(D)} = [11\ \ 02\ \ 04\ \ 0\ \ 0\ \ 0]_8$ three of the five systematic bits are not encoded, i.e. not protected. These unprotected bits impose a severe error floor in the uncorrelated Rayleigh fading transmission scenario, when a bursty of error accrue [155]. As a remedy, we can increase the memory length up to $\widetilde{\mathrm{m}} = 5$ corresponding to $\mathbf{G(D)} = [41\ \ 02\ \ 04\ \ 10\ \ 20\ \ 40]_8$, where all of the five information bits are encoded. By doing so,

CM Scheme	Modulator Scheme	Code Memory	η (BPS)	$E_b/N_0(dB)$ (**BER** = 10^{-6})	SNR(dB) (**BER** = 10^{-6})
TCM	QPSK	6	1	5.1	5.1
	8PSK	6	2	7.49	9.2
	16QAM	6	3	8.22	13.0
	64QAM	6	5	12.51	19.5
TTCM	QPSK	3	1	1.8	1.8
	8PSK	3	2	6.19	7.2
	16QAM	3	3	6.22	11.0
	64QAM	3	5	10.71	17.7

Table 2.4: E_b/N_0 and SNR thresholds at BER=10^{-6} for TCM and TTCM schemes when communicating over the **AWGN** channels. The simulation parameters are listed in Table 2.2 and Table 2.3, while the results are extracted from Figure 2.9 and Figure 2.10.

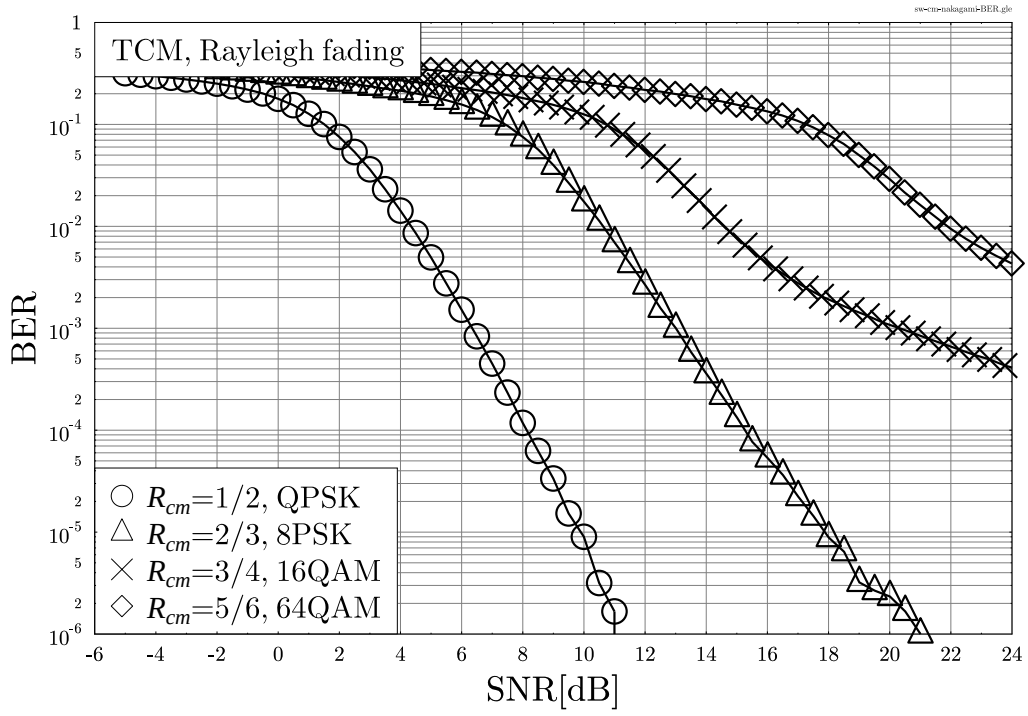

Figure 2.11: BER versus SNR performance of **TCM**-aided QPSK, 8PSK, 16QAM and 64QAM modulators when communicating over the **uncorrelated Rayleigh fading** channels and using code memory length of $\widetilde{m} = 6$. The simulation parameters are listed in Table 2.2 and Table 2.3 while the related results are summarised in Table 2.5.

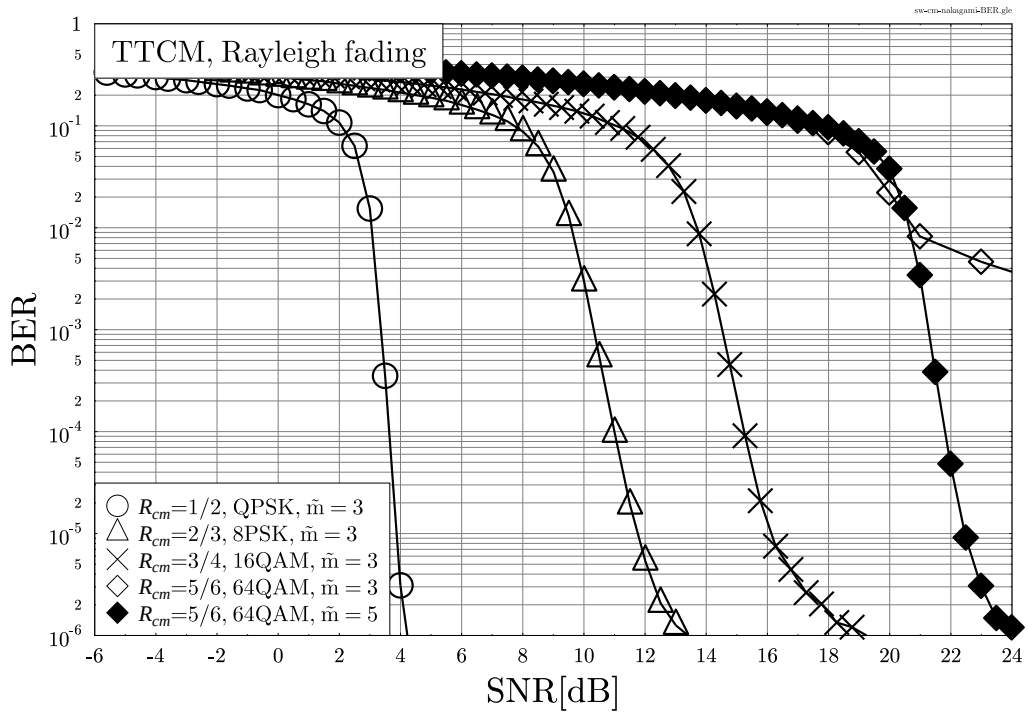

Figure 2.12: BER versus SNR performance of **TTCM**-aided QPSK, 8PSK, 16QAM and 64QAM modulators when communicating over the **uncorrelated Rayleigh fading** channels using four TTCM iterations and code memory length of $\tilde{m} = 3$, while $\tilde{m} = 5$ is used for the TTCM-64QAM scheme. The simulation parameters are listed in Table 2.2 and Table 2.3 while the related results are summarised in Table 2.5.

the severe error floor is significantly reduced as shown in Figure 2.12. Table 2.5 summarises the performance of both the TCM and TTCM schemes, when aiming for attaining BER = 10^{-6}.

The effects of varying the number of iterations between the two TCM components in the TTCM decoder of Figure 2.8 is illustrated in Figure 2.13, when TTCM-QPSK scheme was used for transmission over uncorrelated Rayleigh fading channel. As the BER curves of Figure 2.13 suggested, more than one iteration is needed in order to avoid a severe error floor. Doubling the number of iterations from $I = 2$ to $I = 4$ provides us with a significant SNR gain of approximately 2.5 dB at a BER level of 10^{-6}. However, for the same BER level a marginal SNR of 0.6 dB will be achieved upon doubling the number of iterations further to $I = 8$, which may result in excessive decoding complexity.

One of the important factors when designing channel codes especially for uncorrelated Rayleigh fading channels is the interleaver size, i.e. the number of transmitted symbols per frame, N_s. A longer interleaver would give a better performance by spreading bursty errors more evenly. Figure 2.14 shows the effect of the frame size, where transmitting $N_s = 1200$ symbols induces an error floor, but increasing it to $N_s = 12\,000$ symbols suppresses the error floor to a BER level below 10^{-6}, as documented in Figure 2.14. Further doubling this number to $N_s = 24\,000$ would provide a negligible additional BER improvement.

CM Scheme	Modulator Scheme	Code Memory	η (BPS)	$E_b/N_0(dB)$ (**BER =** 10^{-6})	SNR(dB) (**BER =** 10^{-6})
TCM	QPSK	6	1	11.0	11.0
	8PSK	6	2	19.99	23.0
	16QAM	6	3	$--$	$--$
	64QAM	6	5	$--$	$--$
TTCM	QPSK	3	1	4.2	4.2
	8PSK	3	2	10.39	13.4
	16QAM	3	3	14.23	19.0
	64QAM	3	5	$--$	$--$
		5	5	18.0	25.0

Table 2.5: E_b/N_0 and SNR thresholds at BER=10^{-6} for TCM and TTCM schemes when communicating over the **uncorrelated Rayleigh fading channel**. The simulation parameters are listed in Table 2.2, while the results are extracted from Figure 2.11 and Figure 2.12.

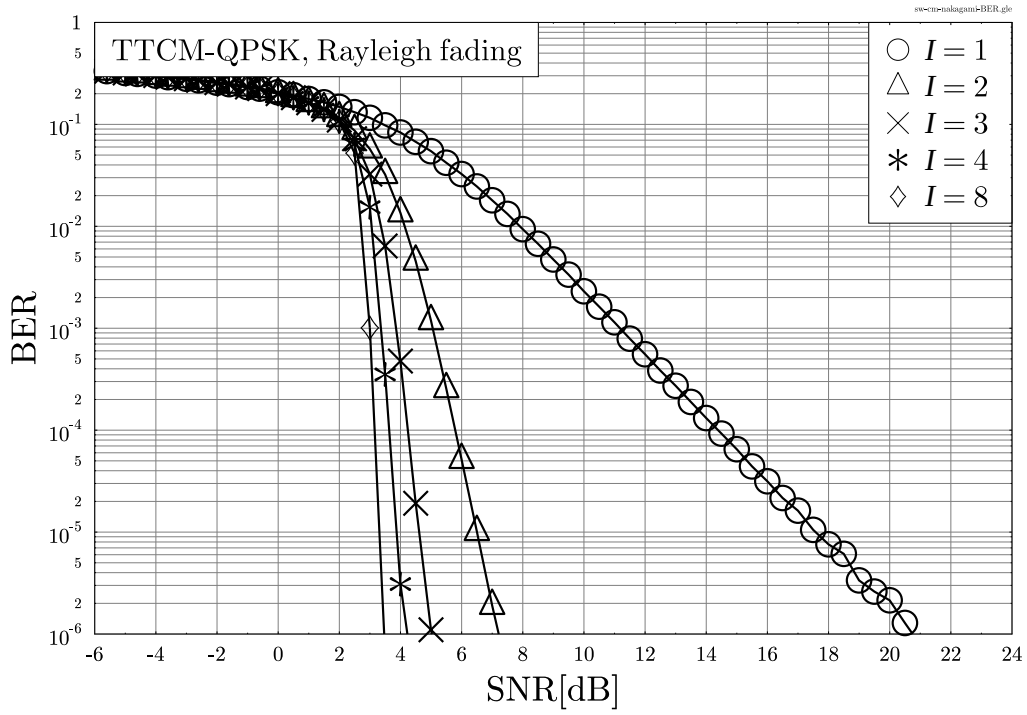

Figure 2.13: BER versus SNR performance of **TTCM-QPSK** scheme when communicating over **uncorrelated Rayleigh fading** channels using various number of TTCM iterations $I = \{1, 2, 3, 4, 8\}$. The simulation parameters are listed in Table 2.2 and Table 2.3.

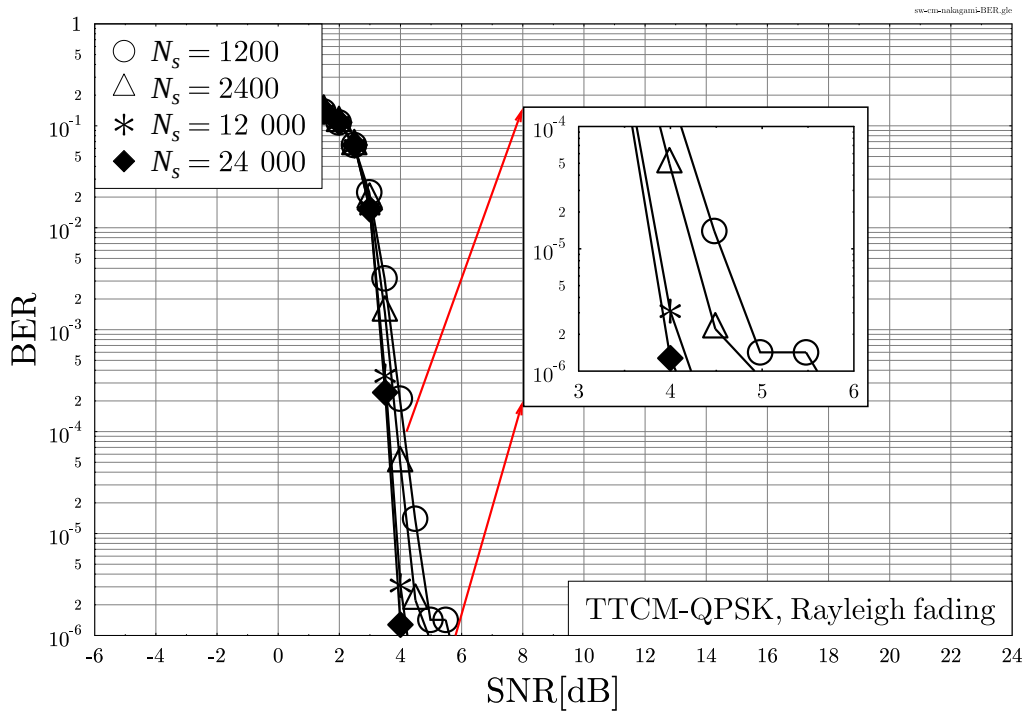

Figure 2.14: BER versus SNR performance of **TTCM-QPSK** scheme when communicating over **uncorrelated Rayleigh fading** channel for various block sizes $N_s = \{1200,\ 2400,\ 12\ 000,\ 24\ 000\}$. The simulation parameters are listed in Table 2.2 and Table 2.3.

2.5 EXtrinsic Information Transfer Charts

EXIT charts [157] constitute a powerful semi-analytical tool devised for analysing the convergence behaviour of iterative decoding schemes. Explicitly, they characterise the quality of the information exchanged between the constituent components of a concatenated decoder[3]. Thus, they were used for designing serial concatenated JSCC schemes in [113, 114, 119, 122, 123] as well as parallel concatenated schemes of both binary [157] and non-binary coding schemes [112, 172]. A novel non-binary EXIT chart aided method was proposed in [112] to aid the design of symbol-based CM schemes. Moreover, the area between the EXIT curves of the constituent decoders can be used for characterising the decoder's ability to approach its capacity limit. The problem of approaching the channel capacity can be considered as simple curve fitting exercise [171]. The non-binary EXIT chart technique of [112] has been invoked for designing a near-capacity TTCM schemes in [172]. This subsection will briefly introduce the concept of symbol-based EXIT charts based on [172,173].

2.5.1 EXIT Chart Basics

Following the EXIT chart-based design of [173] and [156, Chapter 14], let us now highlight the main principles of symbol-based EXIT charts. Consider Figure 2.15, which illustrates a serial

[3]Readers can refer to the insightful survey and tutorial paper of [171].

concatenated coding scheme constituted by three stages, where the N_u-length information symbols frame as well as the N_x-length coded symbol sequences of the i^{th} encoder are denoted as $\mathbf{u}_i = \{u_{i,1}, u_{i,2}, \ldots u_{i,N_u}\}$ and $\mathbf{x}_i = \{x_{i,1}, x_{i,2}, \ldots x_{i,N_x}\}$, respectively. The received sequence is denoted as $\mathbf{y}$, while $\hat{\mathbf{u}}$ represents the estimated sequence of $\mathbf{u}$. Moreover, similar to the notations used in Section 2.4.2, we have $A(\mathbf{x})_i = \{A(x)_{i,1}, A(x)_{i,2}, \ldots A(x)_{i,N_x}\}$ and $E(\mathbf{x})_i = \{E(x)_{i,1}, E(x)_{i,2}, \ldots E(x)_{i,N_x}\}$, denoting both the *a priori* and extrinsic probability sequences of the coded symbols associated with the i^{th} decoder. Both $A(\mathbf{u})_i$ and $E(\mathbf{u})_i$ can be defined in a similar manner. The intermediate decoder, namely the "2nd Decoder" of Figure 2.15, is modelled

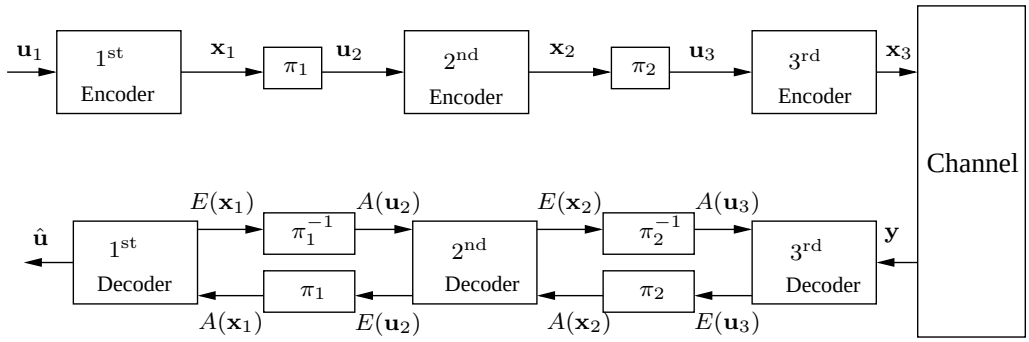

Figure 2.15: Schematic of a three-stage serially concatenated coding scheme [173], where π and π^{-1} represents the interleaver and deinterleaver, respectively.

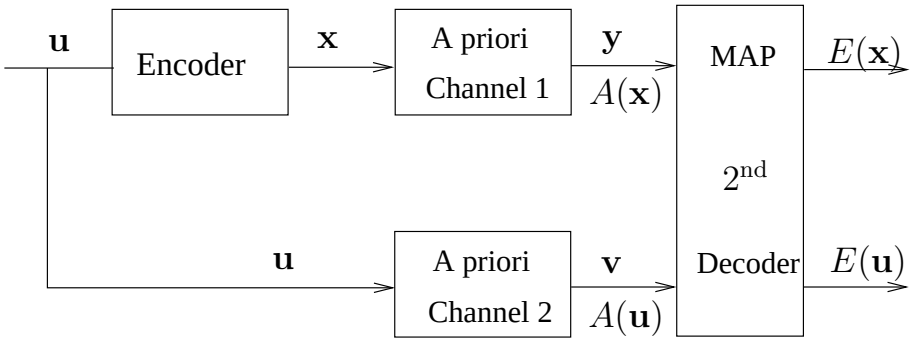

Figure 2.16: Modelling the encoding and decoding of the intermediate encoder of Figure 2.15 [173].

in Figure 2.16, where the "*A priori* Channel 1" is used for modelling the inner decoder having transition probabilities of $\Pr(y_k \mid x_k)$, where we have $k \in \{1, 2, \ldots N_x\}$. Accordingly, the lower "*A priori* Channel 2" of Figure 2.16 is invoked to model an outer decoder associated with the transition probability of $\Pr(v_k \mid u_k)$ representing the generation of the codeword v_k, given the input u_k, where $k \in \{1, 2, \ldots N_u\}$. Consequently, the EXIT chart technique in our scenario is used to visualise the input and the output of the MAP decoder of Figure 2.16 based on the average Mutual Information (MI) transfer according to the following equations:

- average MI between $\mathbf{u}$ and $A(\mathbf{u})$:

$$I_A(u) = \frac{1}{N_u} \sum_{k=1}^{N_u} I[u_k; A(u_k)] \; ; \tag{2.24}$$

- average MI between $\mathbf{x}$ and $A(\mathbf{x})$:

$$I_A(x) = \frac{1}{N_x} \sum_{k=1}^{N_x} I[x_k; A(x_k)] \; ; \tag{2.25}$$

- average MI between $\mathbf{u}$ and $E(\mathbf{u})$:

$$I_E(u) = \frac{1}{N_u} \sum_{k=1}^{N_u} I[u_k; E(u_k)] \; ; \tag{2.26}$$

- average MI between $\mathbf{x}$ and $E(\mathbf{x})$:

$$I_E(x) = \frac{1}{N_x} \sum_{k=1}^{N_x} I[x_k; E(x_k)] \; ; \tag{2.27}$$

where again, the length of the symbol sequences $\mathbf{u}$ and $\mathbf{x}$ is given by N_u and N_x, respectively. Given very long interleavers, the EXIT chart analysis assumes that [157, 171]:

1. the *a priori* information inputs may be assumed to be fairly uncorrelated;
2. the Probability Density Function (PDF) of the a *a priori* information inputs can be modelled using the Gaussian distribution.

Accordingly, the average extrinsic MI of $\mathbf{u}$, namely $I_E(u)$ of Equation (2.26), can be computed as [112, 171, 173]:

$$I_E(u) = \log_2(M) - \frac{1}{N_u} \sum_{k=1}^{N_u} \sum_{m=1}^{M} E\left(u_k^{(m)}\right) \log_2\left(E\left(u_k^{(m)}\right)\right) \; , \tag{2.28}$$

where, $E\left(u_k^{(m)}\right) = \Pr\left({u_k}^{(m)} \mid \mathbf{y}, \mathbf{v}_{[k]}\right)$ represents the extrinsic probabilities generated by the MAP decoder when the information symbol ${u_k}^{(m)}$ for $m \in \{1, \ldots, M\}$ is '*virtually*' transmitted over the "*A priori* Channel 2" of Figure 2.15. Based on the discussions of Section 2.3.2, for example for 2/3 TCM or TTCM we have $M = 2^2 = 4$ possible symbols. Similarly, average extrinsic MI of $\mathbf{x}$, namely $I_E(x)$ of Equation (2.27), can be characterised using [112, 171, 173]:

$$I_E(x) = \log_2(\bar{M}) - \frac{1}{N_x} \sum_{k=1}^{N_x} \sum_{m=1}^{\bar{M}} E\left(x_k^{(m)}\right) \log_2\left(E\left(x_k^{(m)}\right)\right) \; , \tag{2.29}$$

where $E\left(x_k^{(m)}\right) = \Pr\left(x_k^{(m)} \mid \mathbf{y}_{[k]}, \mathbf{v}\right)$ is the extrinsic probability of the transmitted symbol $x_k^{(m)}$, which may assume $m \in \{1, \ldots, \bar{M}\}$, where $\bar{M} = 2^{m+1}$.

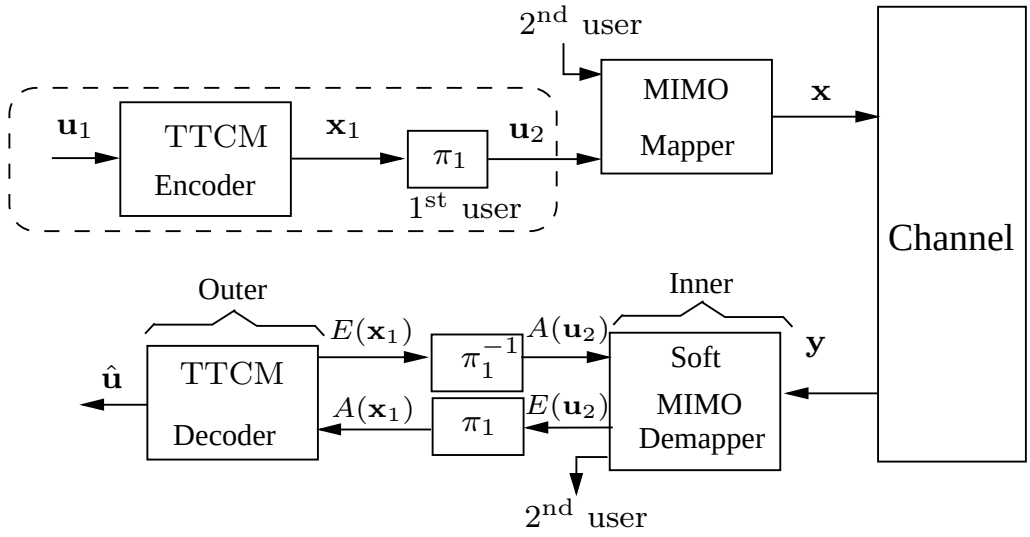

Figure 2.17: Schematic of a two-stage serially concatenated coding scheme supporting two users when communicating over uncorrelated Rayleigh fading (2×2) MIMO channel. Note that the second user's encoder and decoder are similar to the first user's counterparts.

To motivate the employment of EXIT charts, let us consider the transmission scenario of Figure 2.17, where the interleaved codeword sequence $\mathbf{u}_2$ of the first user is mapped before transmitting it through a (2×2) Multiple-Input Multiple-Output (MIMO) channel. The receiver can be partitioned into two decoders, namely the "Inner Decoder", which in our in case is the ML-based Multi-User Detector (MUD) and the "Outer Decoder", which is the TTCM decoder. As seen in Figure 2.17, the inner and outer decoders exchange their information through the so-called Outer Iterations, which is denoted as I_{out} in our simulation results.

Coded Modulation	**TTCM**
Modulation Scheme	QPSK
Mapper type	Set-Partitioned
Number of iterations,I	4
Code Rate, R_{cm}	1/2
Code Memory	3
Decoder type	Approximate Log-MAP
Demapper type	Maximum Likelihood (ML)
Symbols per frame	12 000
Number of frames	10 000
Channel	(2×2) Uncorrelated Rayleigh fading channel

Table 2.6: Simulation parameters for the two-stage serially concatenated coding scheme of Figure 2.17 that are employed in Figures 2.18.

Figure 2.18 shows the stylised relationship between the BER and EXIT charts. As shown in Figure 2.18(b), an SNR of 2.5 dB is required for facilitating an open EXIT chart tunnel, where

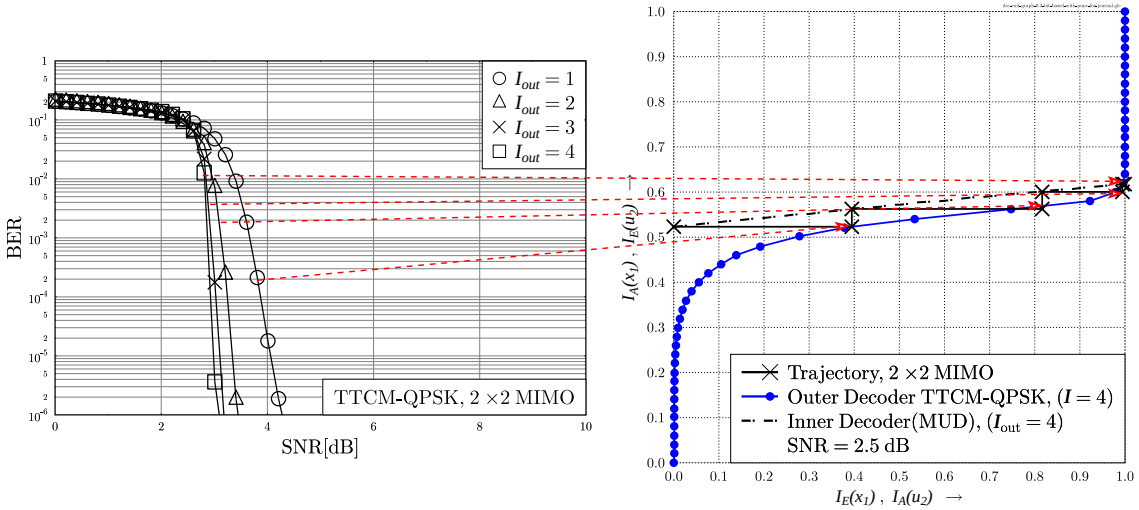

Figure 2.18: The relationship between the EXIT chart curves and the BER performance for **TTCM-QPSK** scheme when communicating over 2×2 MIMO **uncorrelated Rayleigh fading** channels. The overall transmission schematic is shown in Figure 2.17 while the corresponding simulation parameters are listed in Table 2.6.

the arrows illustrate the relationship between the BER and the MI visualized by the EXIT charts. More specifically, as seen in Figure 2.18(a), the BER curve is gradually shifted to the left, while the decoding trajectory Figure 2.18(b) is approaching the top-right corner of the EXIT chart associated with a vanishingly low BER. Explicitly, using four outer iterations, $I_{\text{out}} = 4$, between the ML-based demapper and the TTCM decoder is sufficient for the trajectory to travel through the tunnel and to approach the right hand side of Figure 2.18. Additionally, as shown in [171] for a given SNR value, the area under the inner decoder's EXIT-curve indicates the effective throughput limit of the scheme.

2.6 Chapter Conclusions

In this chapter, we introduced and discussed various CM schemes and the EXIT chart technique. A brief historical review was provided in Section 2.2, where the main principles of CM schemes, namely the SP and the symbol-based MAP algorithm were illustrated in Section 2.3. The classic TCM schematic was given in Figure 2.1, where a RSC is serially concatenated with SP-assisted signal labelling. The SP labelling technique, which was proposed for attaining a higher FED between the unprotected bits of the constellation, was reviewed in Section 2.3.1. Section 2.4.1 portrayed the TTCM encoder of Figure 2.5 comprised of two parallel concatenated TCM encoders connected through a symbol-based interleaver. Subsequently, the TTCM decoder of Figure 2.8 was detailed in Section 2.4.2, where the inseparable nature of the information passed from one decoder to the other was described.

The performance of QPSK, 8PSK, 16QAM and 64QAM-aided TCM and TTCM over both

AWGN and uncorrelated Rayleigh fading channels was evaluated in Section 2.4.3. The superiority of TTCM transmission was demonstrated in both channels through BER performance curves. To elaborate, it was found in Figure 2.9 and Figure 2.10 that TTCM-QPSK requires SNR= 1.8 dB for achieving a BER level of 10^{-6}, while an SNR= 5.1 dB was needed by the TCM scheme for communicating over AWGN channels. Similarly, when an uncorrelated Rayleigh fading channel is considered, the TTCM-QPSK outperformed the TCM-QPSK by a significant 11.8 dB at a BER level of 10^{-6}. Both the TCM and TTCM schemes' performance was summarised over both AWGN as well as uncorrelated Rayleigh fading channels in Table 2.4 and Table 2.5, respectively. Additionally, the number of iterations, I, required between the parallel TCM decoders was quantified using the BER curves of Figure 2.13, which advised us that four iterations exhibited a good trade-off between the performance and the decoding complexity. As many as $N_s = 12\,000$ symbol-per-frame were required for the TTCM scheme for avoiding an error-floor above the BER level of 10^{-6}, as documented in Figure 2.14.

The powerful semi-analytical EXIT chart technique is capable of visualising the convergence behaviour of iterative decoding schemes through exploiting the relationships between the MI of the input and output of each constituent decoder, as it was discussed in Section 2.5. Finally, an insightful example on how the EXIT charts can be utilised to optimise the two-stage coding scheme of Figure 2.17 was discussed in Section 2.5.1. The EXIT charts were used to design and optimise our scheme as follows:

- Figure 2.18 determined the minimum transmit SNR required for facilitating an open EXIT tunnel needed in order to attain a vanishingly low BER.
- The number of iterations between the inner and outer decoders required was evaluated in the stair-case-shaped trajectory of Figure 2.18. Our EXIT chart predictions were confirmed by our Monte-Carlo simulation-based BER curves.

Chapter 3

Joint Source Coding, Channel Coding and Modulation Design for Two-Way Relaying

3.1 Introduction

As outlined in Section 1.3, we are motivated by the practical benefits offered by Joint Source-coding and Channel-coding (JSCC) schemes. Additionally, we are inspired by the bandwidth-efficiency of the family of Coded Modulation (CM) schemes, as discussed in Section 2.4. In this chapter, we will investigate an intriguing application of CM-based JSCC. More specifically, we propose a Joint Source-coding, Channel-coding and Modulation (JSCM) scheme [122, 174, 175] by amalgamating Turbo Trellis-Coded Modulation (TTCM) and Variable Length Code (VLC) as the TTCM-VLC scheme in a two-way relaying arrangement. Two-way or bi-directional relay systems have drawn increasing research attention, since they overcome the potential spectral efficiency loss of one-way relaying schemes [176, 177, 178]. The two-way relaying systems support two-or-more user-terminals acting as Source Node (SN)s, which want to exchange their information with the aid of one-or-more Relay Nodes (RN)s, as shown in Figure 3.1. In the conventional one-way relaying schemes, four time slots are required for accomplishing a full-duplex information exchange. By contrast, two-way relaying requires only two time slots for achieving a duplex information exchange between two SNs. The two-way relay channel's capacity achieved for Gaussian-input signals and for a quasi-static fading profile has been investigated in [179, 180] and in the references therein. Recently, TTCM [152]-aided two-way relaying based on a beneficial SN and RN power-sharing technique was investigated in [181], where a significant Bit Error Ratio (BER) improvement was achieved. However, the capacity of the power-sharing-based two-way relay channel has not been quantified.

As stated in Section 1.3, JSCC schemes constitute a family of serial concatenation codes, that

are capable of attaining substantial coding gains, while maintaining a realistic decoding complexity. More explicitly, JSCC techniques have been designed for limited-delay, limited-complexity image/video systems communicating over wireless channels, because in this practical scenario Shannon's source and channel coding separation theorem [118] has a limited validity. An attractive JSCC scheme based on the bit-based trellis structure of [105] was proposed in [108], while a range of near-capacity JSCM schemes were investigated in [122, 182]. Recently, the JSCM schemes of [182] was extended to a one-way cooperative communication system in [148], where a significant amount of coding and relaying gain was attained at the cost of halving the throughput due to the employment of a half-duplex relay node.

Furthermore, as discussed in Section 2.5, EXIT charts [156, 157] have been used for investigating the convergence behaviour of the iterative decoding of JSCC schemes. For example, the joint decoding schemes of [148, 183, 184] were designed using EXIT charts to attain a near-capacity performance. In this chapter, we employ EXIT charts for the following three reasons. Firstly, they are used for investigating the minimum required Signal-to-Noise Ratio (SNR) in both the Phase-I and Phase-II links of our relay-aided system in order to derive the optimum power allocation. Secondly, EXIT charts have been invoked for finding the most appropriate number of iterations between the TTCM and VLC decoders by striking a trade-off in terms the performance attained versus the complexity imposed. This can be achieved by creating an open EXIT chart tunnel [114, 185] for the sake of achieving decoding convergence to an infinitesimal low BER at a channel SNR close to the channel's capacity bound. Thirdly, EXIT charts are used for investigating the decoding convergence by exchanging extrinsic information between the joint TTCM-VLC decoder and the Multi-User Detector (MUD). In a nutshell, the EXIT chart technique allows us to entirely move away from the classic design principles relaying on finding codes with a large minimum distance. Instead, a large design-space may be readily explored by simply finding the components, which allow the system to reach the $(1, 1)$ point in the EXIT chart of perfect convergence to a vanishingly low BER.

Against the above background, this chapter aims for designing an energy-efficient JSCM scheme that can simultaneously exploit the capacity of the two-way relay channel and the residual redundancy of the source signals. More specifically, the proposed JSCM scheme is designed with the aid of EXIT charts for attaining a high transmission energy-efficiency with the aid of iterative decoding. Further transmission energy savings may be attained with the aid of our proposed power-allocation technique. Then, low-complexity source coding schemes are invoked for attaining processing energy-efficiency by exploiting the source signals' residual redundancy and by using VLCs. Iterative detection exchanging extrinsic information between the MUD detectors, TTCM decoder and VLC decoder invoked which is jointly optimized using EXIT charts for achieving both transmission and processing energy-efficiencies. In other words, the capacity of the two-way relay channel and the redundancy of the source signals can be jointly exploited via extrinsic mutual information exchange between the MUD detectors and the JSCM (TTCM-VLC) decoder.

The chapter is organized as follows. Our system model is described in Section 3.2. The design of our scheme will be detailed in Section 3.3, while the achievable performance of the JSCM in

two-way relaying arrangement is investigated in Section 3.4. Then, our final analysis is offered in Section 3.5.

3.2 System Model

In this section, we will illustrate the transmission model used in this chapter. Both the Source to Relay Transmission SR (Phase-I) as well as the Relay to Destination Transmission RD (Phase-II) links will be detailed in Section 3.2.1, while the corresponding capacities of both phases will be analysed in Section 3.2.2.

3.2.1 Two-Way Relay Channel

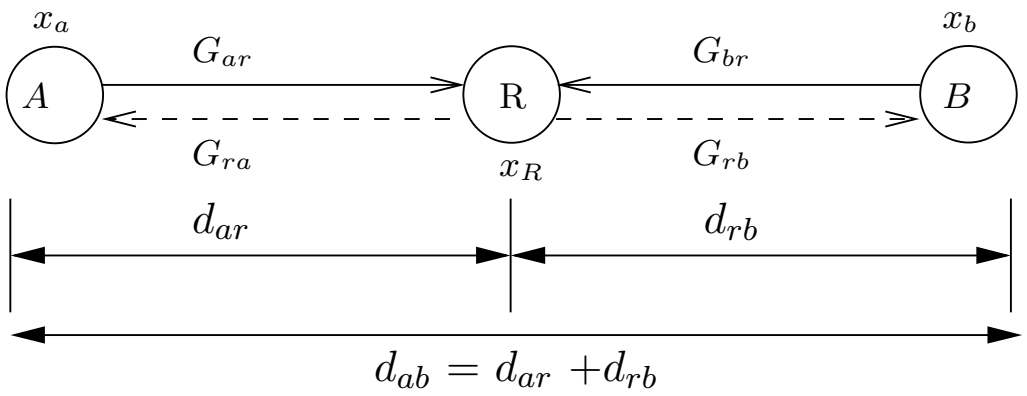

Figure 3.1: Schematic of a two-way relay-aided system, where d_{ab} is the geographical distance between node a and node b.

The schematic of our proposed two-way relaying scheme is shown in Figure 3.1, where both users A and B have a single antenna each. They exchange their information with the aid of a RN equipped with two antennas. The two users may also be treated as a single two-transmitter distributed *virtual* SN. The communication paths shown in Figure 3.1 are subjected to both path-loss and uncorrelated Rayleigh fading. Assuming a path-loss exponent of three for an outdoor environment [186], the corresponding reduced-pathloss-induced geometrical gain experienced by the SR and RD link with respect to the Source to Destination transmission (SD) link may be calculated, respectively, as [185, 187]:

$$G_{ar} = \left(\frac{d_{ab}}{d_{ar}}\right)^3 \; ; \; G_{rb} = \left(\frac{d_{ab}}{d_{rb}}\right)^3 , \tag{3.1}$$

where d_{ab} denotes the distance between node a and node b. Without loss of generality, we assume that the twin-antenna-assisted RN is located midway between the two SNs. Hence, we have $G_{ar} = G_{rb} = 8$, which corresponds to 9 dBs. If $P_{t,a}$ is the power transmitted from node a, the average

receive SNR per-user per-receive antenna at node b is given by [181]:

$$\begin{aligned} \mathrm{SNR}_r &= \frac{P_{t,a}\mathrm{E}\left[G_{ab}\right]}{N_0}.\frac{\sum_{b_i=1}^{N_b}\sum_{a_j=1}^{N_a}\mathrm{E}\left[|h_{b_i a_j}|^2\right]\mathrm{E}\left[|x_{a_j}|^2\right]}{N_b N_a} \\ &= \frac{P_{t,a}G_{ab}}{N_0}\,, \end{aligned} \tag{3.2}$$

where the number of antennas at node a and b is represented by N_a and N_b, respectively. Moreover, x_{a_j} is the symbol transmitted from the j^{th} antenna of node a, $h_{b_i a_j}$ represents the channel coefficients for the link between the j^{th} antenna of node a and the i^{th} antenna of node b, while the expected values are given by $\mathrm{E}\left[|h_{b_i a_j}|^2\right] = 1$ and $\mathrm{E}\left[|x_{a_j}|^2\right] = 1$. It is convenient for our discussions to define the term referred to as transmit SNR[1] as the ratio of the power transmitted from node a to the noise power experienced at the receiver of node b as $\gamma_T = P_{t,a}/N_0$. Thus, we have $\gamma_R = \gamma_T G_{ab}$, which can be expressed in decibel as:

$$\Gamma_R \;=\; \Gamma_T + 10\log_{10}(G_{ab})\;[\mathrm{dB}]\,, \tag{3.3}$$

where we have $\Gamma_R = 10\log_{10}(\gamma_R)$ and $\Gamma_T = 10\log_{10}(\gamma_T)$. Hence the receive SNR is larger than the transmit SNR when the geometrical gain, which is normalized with respect to the SD link, is higher than unity.

The Phase-I transmission from the $L = 2$ SNs to the $P = 2$ antenna-based RN may be viewed as a Space-Division Multiple Access (SDMA) [61] based scheme, where MUD techniques can be employed at the RN. The channel between the two users and the RN can be represented by an $(P \times L)$-dimensional channel matrix $\mathbf{H}$ and the received signal at the RN may be written as:

$$\mathbf{y} = \mathbf{H}\mathbf{x} + \mathbf{n}\,, \tag{3.4}$$

where the transmitted symbol $\mathbf{x} = [x_0, x_1, \cdots, x_{L-1}]^T$ is an $(L \times 1)$-dimensional vector, while the received signal $\mathbf{y} = [y_0, y_1, \cdots, y_{P-1}]^T$ is an $(P \times 1)$-dimensional vector and $\mathbf{n} = [n_0, n_1, \cdots, n_{P-1}]^T$ represents the complex-valued $(P \times 1)$-dimensional AWGN vector having a variance of $N_0/2$ per dimension. We incorporated the reduced-pathloss-induced geometrical gain [169, 187] and the transmitted power factor in $\mathbf{H}$ of Equation (3.4). Therefore the channel of the Phase-I link can be expressed as:

$$\mathbf{H} = \begin{bmatrix} \sqrt{G_{ar_1}}\sqrt{P_{t,a}}h_{ar_1} & \sqrt{G_{br_1}}\sqrt{P_{t,b}}h_{br_1} \\ \sqrt{G_{ar_2}}\sqrt{P_{t,a}}h_{ar_2} & \sqrt{G_{br_2}}\sqrt{P_{t,b}}h_{br_2} \end{bmatrix}\,, \tag{3.5}$$

where the i^{th} receive antenna of the RN is denoted by the subscript r_i, while $P_{t,a}$ represents the power transmitted from user A and h_{ar_i} signifies the Channel State Information (CSI) coefficient between user A and antenna r_i. The reduced-pathloss-induced geometrical gains between user A (user B) and antenna r_i is denoted by G_{ar_i} (G_{br_i}). The RN invokes three types of SDMA-based

[1] However, the concept of transmit SNR [187] is unconventional, as it relates quantities to each other at two physically different locations, namely the transmit power to the noise power at the receiver.

MUDs, namely the optimum but relatively complex Maximum Likelihood (ML), Minimum Mean-Square Error-assisted Interference Cancellation (MMSE-IC) and the sub-optimum Zero Forcing (ZF) MUDs.

Phase-II transmission is shown in the lower part of Figure 3.2. The RN concatenates the two decoded N-bit sequences into a $2N$-bit sequence, yielding $\widehat{u}_3 = [\widehat{u}_1 \ \widehat{u}_2]$. Then, the combined VLC-encoded sequence $\widehat{b}_3$ is encoded by a TTCM encoder before it is broadcast from the RN back to the two users. The Phase-II transmission channel may be viewed as in an SDMA system using two transmit antennas and one receive antenna. Each user then detects and decodes the signal in a similar manner to that used at the RN. In our simulations we only consider the ML MUD in the challenging rank-deficient Phase-II link, since the number of receiver antennas should be at least equal to the number of transmit antennas when using MMSE and ZF schemes [188]. In order to further improve the attainable performance of the MMSE MUD, interference cancellation MMSE-IC [181] has been invoked for iteratively eliminating the inter-user interference. Further details on SDMA detection can be found from [181, 188].

The proposed scheme can be extended to support an arbitrary number of users having in mind the following limitations:

- Higher hardware complexity at the RN:
  If the number of receive antennas at the RN is equal to or higher than the number of users, then low complexity MMSE and ZF MUDs can be implemented at the RN. During the Phase-II transmission, each RN's transmit antenna can be used for carrying independent user signals by forming an SDMA system. However, this leads to a significant increase in the RN's hardware complexity.

- Higher detection complexity and lower bandwidth efficiency:
  If the number of receive antennas at the RN is less than the number of users, then a high complexity ML MUD has to be employed at the RN, which leads to a higher detection complexity at the RN. Furthermore, SDMA cannot be used during the Phase-II transmission. Hence, more timeslots (TDMA) or frequency bands (CDMA/FDMA) are required, which leads to a lower bandwidth efficiency during the Phase-II transmission.

Before quantifying the achievable channel capacity, let us first describe our source encoder in order to specify the overall throughput of our scheme.

3.2.1.1 Throughput Analysis

The block diagram of the TTCM-VLC-aided SDMA-based two-way relaying (TTCM-VLC-2Way) scheme is shown in Figure 3.2, where each user employs a serial-concatenated trellis-based Reversible Variable Length Code (RVLC)[2] and a TTCM scheme. Note that a bit-based interleaver is

[2]Our design is applicable to any VLCs. However, the reversible VLCs are particularly suitable for iterative detection, because they have a minimum free distance of 2, as detailed in [114, 119]. This allows the iterative detector to approach a vanishingly low BER at low SNR. Additionally, RVLC trellis construction is briefly illustrated in Appendix A.

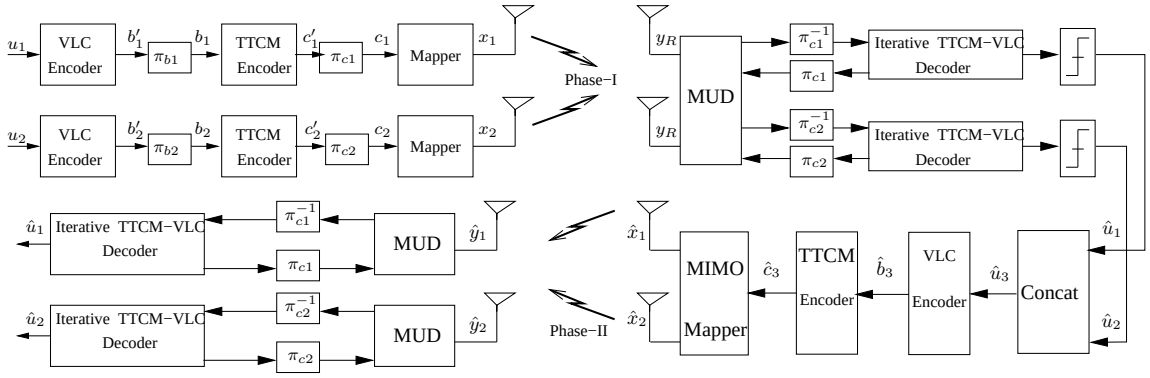

Figure 3.2: Schematic of the joint TTCM-VLC-aided SDMA-assisted two-way relay TTCM-VLC-2Way system.

used between each pair of the VLC and TTCM encoders. We employed the same source as that used in [122, 148, 182] so that all results are comparable. More specifically, we invoked the RVLC of [189], where the source symbols are $u = \{0, 1, 2, 3, 4\}$ and the corresponding probabilities of occurrence are given by $P(u) = \{0.33, 0.30, 0.18, 0.10, 0.09\}$. The legitimate VLC codewords are $C = \{00, 11, 010, 101, 0110\}$ and the associated entropy is $L_s = 2.1391$ bits/symbol, while the calculated average codeword length is $L_{vlc} = 2.46$ bits/VLC symbol. Hence, the source coding efficiency is given by $R_{vlc} = L_s/L_{vlc} = 0.87$.

The interleaved VLC-encoded bits, b_1 and b_2 are encoded with the aid of an 8PSK-based rate-$2/3$ TTCM encoder. Memory-three TCM constituent codes having an octally represented generator polynomial of $[11\ \ 02\ \ 04]_8$ are employed. The two TTCM-VLC codewords c_1 and c_2 are then fed into a virtual MIMO mapper after being interleaved by the symbol interleaver π_{c1} (or π_{c2}), as shown in Figure 3.2. The estimated information sequences $\widehat{u}_1$ and $\widehat{u}_2$ are detected by exchanging extrinsic information between the MUD and the iterative joint TTCM-VLC decoders, as shown in the upper part of Figure 3.2.

The overall throughput of the two-way relaying scheme may be formulated as:

$$\eta \quad = \quad \frac{LN_i}{N_s + N_r}\,, \tag{3.6}$$

where N_i is the number of information bits transmitted within a duration of $(N_s + N_r)$ symbol periods and L denotes the number of users. Furthermore, N_s is the number of modulated symbols per frame transmitted from the SNs during the first time slot and N_r is the number of modulated symbols per frame transmitted from the RN during the second time slot. We have $N_s = N_r$ and we do not apply trellis termination for the TTCM encoder. Therefore, we have $N_i = m \cdot R_{vlc} \cdot N_s = 1.74N_s$, since we have $m = 2$ information bits per 8PSK symbol after using $2/3$-TTCM encoder. Hence, the overall effective throughput of our system is $\eta = 1.74$ Bits Per Symbol (BPS). Again, as stated in Section 2.4.3 the SNR relates to E_b/N_0 according to:

$$E_b/N_0\ [\text{dB}] = \text{SNR}\ [\text{dB}] - 10\log_{10}(\eta)\ . \tag{3.7}$$

3.2.2 Two-Way Relay Channel Capacity

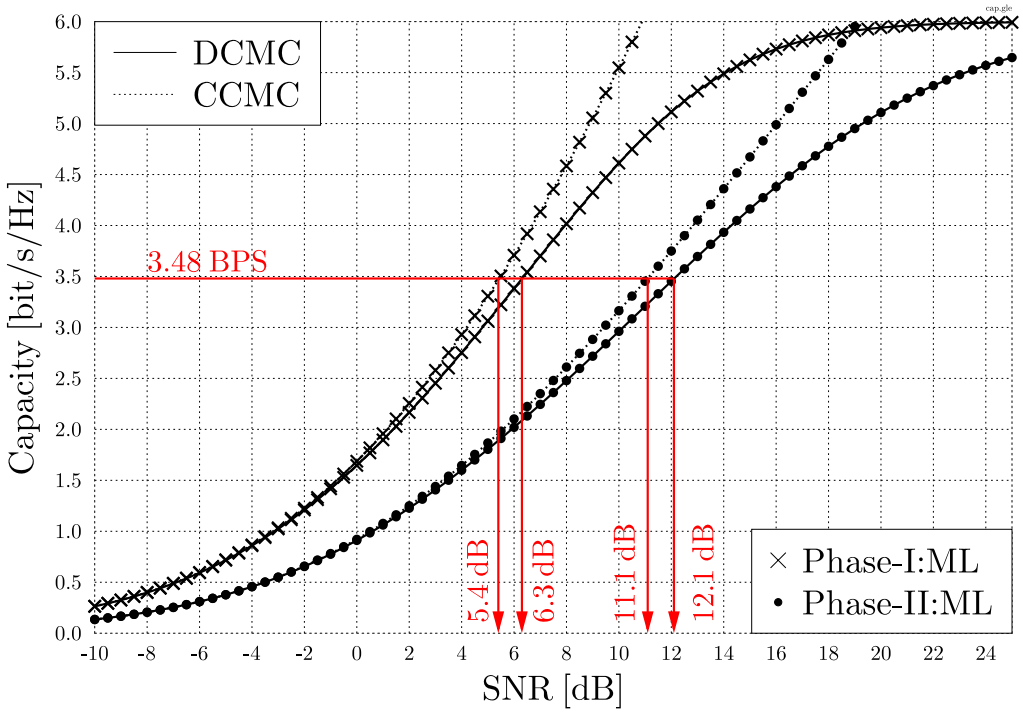

Figure 3.3: DCMC and CCMC capacity curves of the 8PSK-based non-relaying transmission for both phases, namely (2×2) Phase-I and (2×1) Phase-II links, where the curves were computed based on [190, 191].

The Continuous-input Continuous-output Memoryless Channel (CCMC) and the Discrete-input Continuous-output Memoryless Channel (DCMC) [190, 191] capacities of the (2×2) Phase-I link and the (2×1) Phase-II links are shown in Figure 3.3. Although the overall throughput per timeslot is given by 1.74 BPS, the throughput during each timeslot is 3.48 BPS. Based on the DCMC (CCMC) capacity curves of Figure 3.3, the corresponding SNR limits Γ_{lim} for Phase-I and Phase-II at a throughput of $\eta = 3.48$ BPS are 6.3 dB (5.4 dB) and 12.1 dB (11.1 dB), respectively.

According to the max-flow min-cut theorem [192], the information flow from the source to the destination is limited by the specific link having the minimum capacity. Since the capacity of the (2×2) Phase-I link is higher than that of the (2×1) Phase-II link, the capacity of the two-way relay channel is limited by the Phase-II link if the power- and time-allocation is not optimized. More specifically, the capacity of the two-way relay channel may be formulated as:

$$C_{\text{2way}}(\overline{\Gamma}_R) = \max_{\text{Power \& Time}} \min\left[\lambda_I C_I(\Gamma_{R,s}), \lambda_{II} C_{II}(\Gamma_{R,r})\right] , \tag{3.8}$$

which is maximized by appropriate dynamic transmission power- and/or time-allocation, where λ_I and λ_{II} are the fraction of transmission duration for Phase-I and Phase-II, respectively. From Equation (3.8), when λ_I (λ_{II}) is low, the transmission duration of the SN (RN) is short. Thus, the coding rate of a fixed modulation scheme and/or the modulation levels used in an adaptive coding and modulation scheme has to be increased in order to achieve an increased throughput. Naturally,

the receiver has to be aware of the detection time, coding rate and/or modulation mode.

Furthermore, $C_I(\Gamma_{R,s})$ is the Phase-I link capacity at a receive SNR of $\Gamma_{R,s} = 10\log_{10}(\gamma_{R,s})$ and $C_{II}(\Gamma_{R,r})$ is the Phase-II link capacity, when the receive SNR of that link is given by $\Gamma_{R,r} = 10\log_{10}(\gamma_{R,r})$. The average receive SNR, $\overline{\Gamma}_R = 10\log_{10}(\overline{\gamma}_R)$, of the two-way relay scheme is given by:

$$\overline{\Gamma}_R = 10\log_{10}\left(\frac{10^{\frac{\Gamma_{R,s}}{10}} + 10^{\frac{\Gamma_{R,r}}{10}}}{2}\right). \tag{3.9}$$

In our system, we have $\lambda_I = \lambda_{II} = 0.5$[3], because the transmission periods for both phases are identical, i.e. $N_s = N_r$. It may be seen from Equation (3.8) that $C_{2\text{way}}(\overline{\Gamma}_R)$ is maximized for a given $\overline{\Gamma}_R$, when $C_I(\Gamma_{R,s}) = C_{II}(\Gamma_{R,r})$ if $\lambda_I = \lambda_{II}$. Hence, the two-way relay channel capacity may be expressed as:

$$C_{2\text{way}}(\overline{\Gamma}_R) = 0.5\, C_I(\Gamma_{R,s}) = 0.5\, C_{II}(\Gamma_{R,r})\,, \tag{3.10}$$

when $\lambda_I = \lambda_{II}$.

3.2.2.1 Quasi-Static Rayleigh Fading Channel

For quasi-static fading channels, the CCMC-based two-way relay channel capacity is achieved, when the CCMC capacity of Phase-I, $C_I^*(\Gamma_{R,s})$, equals that of Phase-II, $C_{II}^*(\Gamma_{R,r})$, as follows:

$$C_I^*(\Gamma_{R,s}) = C_{II}^*(\Gamma_{R,r}) \tag{3.11}$$

$$\log_2\left(\prod_{k=1}^{2}(1+\gamma_{R,k})\right) = \log_2(1+\gamma_{R,0})\,, \tag{3.12}$$

where $\gamma_{R,k} = \gamma_{T,s}\lambda_k/N_t$ is the receive SNR in the k^{th} sub-channel of the (2×2) MIMO channel, $\sqrt{\lambda_k}$ is the k^{th} singular value of the (2×2) MIMO channel in Equation (3.5) and $\gamma_{T,s}$ is the transmit SNR of each user in the virtual SN equipped with $N_t = 2$ antennas. Similarly, $\gamma_{R,0} = \gamma_{T,r}\lambda_0/N_t$ is the receive SNR in the first (and only) sub-channel of the (2×1) channel, which has a singular value of $\sqrt{\lambda_0}$, while $\gamma_{T,r}$ is the transmit SNR of the RN, which has $N_t = 2$ antennas. At a given transmit SNR of $\gamma_{T,s}$ at the SN, we can derive the optimal transmit SNR $\gamma_{T,r}$ at the RN based on Equation (3.12) as:

$$\gamma_{T,r} = \frac{(1+\lambda_1\gamma_{T,s}/2)\,(1+\lambda_2\gamma_{T,s}/2)-1}{\lambda_0/2}\,. \tag{3.13}$$

[3]It is not necessary for the two phases to have an equal duration for achieving an improved capacity, hence the time-resource-allocation techniques of [193] can also be invoked. In contrast to the time-resource-allocation techniques, the proposed PS method does not require any overhead or side-information for informing the receiver of the transmission power used. However, the time-resource-allocation technique relies on side-information for conveying the coding rate used and the modulation scheme employed to the receiver.

The corresponding optimal average transmit SNR may be formulated as:

$$\overline{\gamma}_T = \frac{\gamma_{T,s} + \gamma_{T,r}}{2} \tag{3.14}$$

$$= \frac{1}{\lambda_0}\left(\lambda_1\lambda_2\left(\frac{\gamma_{T,s}}{2}\right)^2 + (\lambda_0+\lambda_1+\lambda_2)\frac{\gamma_{T,s}}{2}\right) . \tag{3.15}$$

Hence, we can determine the optimal transmit SNR of the two-way relaying scheme for quasi-static fading channel, once the singular value of the Phase-I and Phase-II channels are determined.

3.2.2.2 Power Sharing Technique

However, the optimal transmit SNR of the two-way relaying system cannot be determined based on Equation (3.15), when communicating over uncorrelated Rayleigh fading channels. More specifically, we can express the ergodic CCMC capacities of the Phase-I and Phase-II transmissions, as functions of their corresponding receive SNRs as:

$$C'_I = F_I(\Gamma_{R,s}) \; ; \; C'_{II} = F_{II}(\Gamma_{R,r}) \, , \tag{3.16}$$

which represent the CCMC capacity curves shown in Figure 3.3. The corresponding receive SNR required for achieving a given target throughput can then be inferred from the capacity curves. Explicitly, the receive SNR required for achieving a throughput of 3.48 BPS may be expressed as:

$$\Gamma_{R,s} = F_I^{-1}\left(C'_I = 3.48\right) = 5.4 \text{ dB} \, , \tag{3.17}$$

$$\Gamma_{R,r} = F_{II}^{-1}\left(C'_{II} = 3.48\right) = 11.1 \text{ dB} \, . \tag{3.18}$$

When the RN is located midway between the two SNs ($G_{rb} = G_{ar}$), the difference in terms of transmit SNR can be expressed as:

$$\begin{aligned} \Gamma_{R,\Delta} &= \Gamma_{R,r} - \Gamma_{R,s} \\ &= (\Gamma_T + 10\log_{10}(G_{rb})) - (\Gamma_T + 10\log_{10}(G_{ar})) \\ &= \Gamma_{T,r} - \Gamma_{T,s} \text{ [dB]} = \Gamma_{T,\Delta} \, , \end{aligned} \tag{3.19}$$

where $\Gamma_{R,\Delta} = 10\log_{10}(\gamma_{R,\Delta})$, $\Gamma_{T,\Delta} = 10\log_{10}(\gamma_{T,\Delta})$ and we have $\Gamma_{T,\Delta} = \Gamma_{R,\Delta} = 11.1 - 5.4 = 5.7$ dB in our CCMC case. Hence, the transmit SNR difference in the non-logarithmic domain is given by:

$$\gamma_{T,\Delta} = \frac{\gamma_{T,r}}{\gamma_{T,s}} \, . \tag{3.20}$$

When using Equation (3.14) and Equation (3.20), the new transmit SNR of the SN may be formulated as:

$$\gamma_{T,s} = \frac{2\overline{\gamma}_T}{1+\gamma_{T,\Delta}} \, . \tag{3.21}$$

Similarly, the transmit SNR of the RN is given by:

$$\gamma_{T,r} = \frac{2\overline{\gamma}_T \gamma_{T,\Delta}}{1+\gamma_{T,\Delta}} . \tag{3.22}$$

Hence, at a given average transmit SNR budget of $\overline{\gamma}_T$, we can allocate the appropriate transmit SNR for the SN and for the RN based on Equation (3.21) and Equation (3.22), respectively, once the transmit SNR difference $\gamma_{T,\Delta}$ was computed from the CCMC capacity curves. We refer to this transmit SNR computation as the Power Sharing (PS) technique. The same procedure may be repeated for computing the corresponding transmit SNRs in the DCMC scenario.

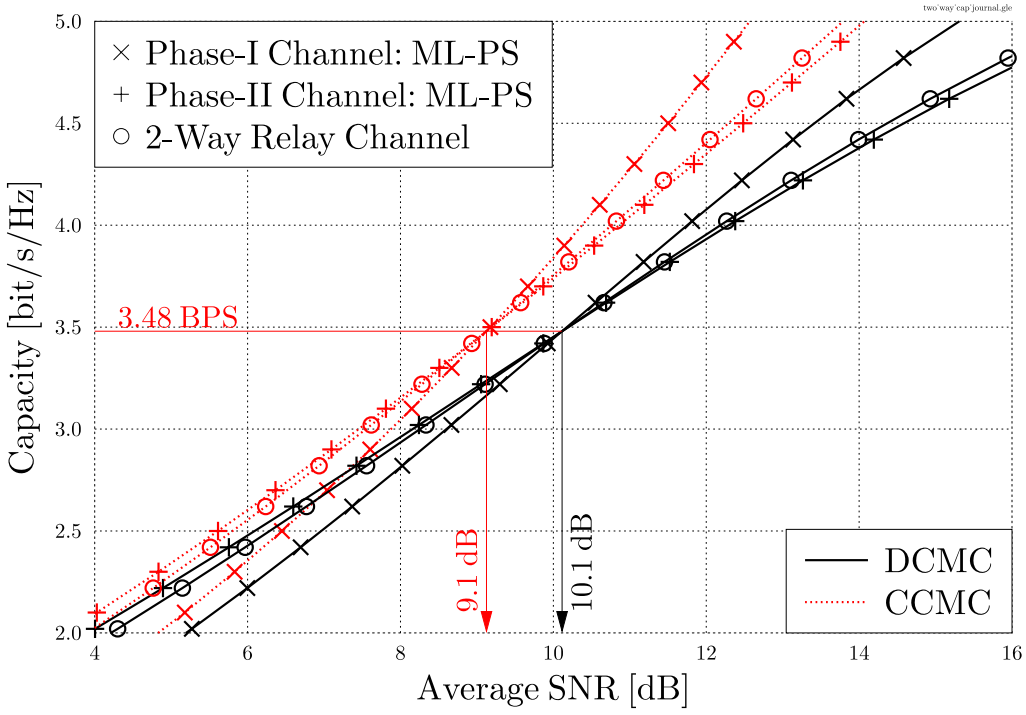

Figure 3.4: Capacity versus average receive SNR curves of the (2×2) Phase-I and (2×1) Phase-II channels as well as that of the two-way relay channel after invoking the PS technique.

Figure 3.4 shows the capacity curves of the Phase-I and Phase-II channels, when aiming for achieving a target throughput of 3.48 BPS. It may be seen from Figure 3.4 that the CCMC (or DCMC) capacity curves of both Phase-I and Phase-II overlap at a throughput of 3.48 BPS, when the average receive SNR is 9.1 dB (or 10.1 dB). By computing the SNR differences for different throughput values based on the capacity curves of Figure 3.3, we arrive at the CCMC (and the DCMC) capacity curves of the two-way relay channel, as shown in Figure 3.4 according to:

$$C'_{2\text{way}}(\overline{\Gamma}_R) = 0.5\, F_I \left(10\log_{10}\left(\frac{2\overline{\gamma}_T}{1+\gamma_{T,\Delta}} \right) \right) , \tag{3.23}$$

$$= 0.5\, F_{II} \left(10\log_{10}\left(\frac{2\overline{\gamma}_T \gamma_{T,\Delta}}{1+\gamma_{T,\Delta}} \right) \right) . \tag{3.24}$$

Note that we did not consider the factor 0.5, when plotting the two-way relay channel's capacity

curves in Figure 3.4 for the sake of clearly illustrating the point, where they intersect with the corresponding Phase-I and Phase-II capacity curves at a throughput of 3.48 BPS.

3.3 Design and Analysis

Having analysed our system's maximum achievable rate as well as illustrating the need for the PS technique of Section 3.2.1. Let us now characterise the attainable decoding convergence of our joint decoder in Section 3.3.1, before proposing a low-complexity source-coding scheme in Section 3.3.2. It is worth emphasising that the outer Iterations I_{out} represent the number of iterations between the (TTCM-VLC) decoder of Figure 3.2 and the MUD. By contrast, the inner Iterations I_{in} refer to the number of iterations between the VLC and TTCM decoders. Additionally, the number of iterations between the parallel TCM decoders of the TTCM decoder of Figure 2.8 is denoted by I. Our simulation parameters are summarised in Table 3.1.

3.3.1 EXIT Chart Based Design

Based on the PS technique of Section 3.2.2.2, the achievable rate of the TTCM-VLC-2Way scheme may be computed based on its Phase-I and Phase-II performances. Note that user B is the Destination Node (DN) of user A and vice versa. Firstly, we have to find the minimum required receive SNRs at the RN and DN, which ensure that both links are capable of achieving the required target reliability. These SNRs may be found either from the semi-analytical EXIT chart [148, 183, 184], outlined in Section 2.5 by observing the SNR where an open EXIT-tunnel emerges, or from the simulation-based BER curves of Figure 3.6. The non-binary EXIT chart technique of [112] is used for visualising the input/output mutual information transfer characteristics of the TTCM-VLC and MUD decoders. The EXIT chart of our TTCM-VLC-aided SDMA decoder recorded for the SR (Phase-I) and RD (Phase-II) links is displayed in Figure 3.5. It can be seen from Figure 3.5 that the "$I_{\text{in}} = 4$" inner iterations within the outer block constituted by the TTCM and VLC can facilitate an open EXIT chart channel, while relaying on a lower number of iterations would lead to a closed tunnel, which results in a residual BER. However, increasing the number of inner TTCM-VLC iterations to "$I_{\text{in}} = 8$ " would only provide a marginal gain at the cost of doubling the decoding complexity. As seen from Figure 3.5, an open EXIT tunnel leading to the right-hand axis becomes available for the Phase-I transmission at SNR$=$ 8.6 dB, which indicates that a decoding convergence to a vanishingly low BER is possible. Similarly, it is possible to attain an infinitesimally low BER at SNR$=$ 15.8 dB for the Phase-II transmission. These EXIT chart predictions are confirmed by our simulation results shown in Figure 3.6, where we have BER $\leq 10^{-6}$ at these SNR values. Note that since the open area of the EXIT chart tunnels is relatively wide, the Phase-I and Phase-II links operate at a considerable distance away from the corresponding DCMC capacities[4],

[4]It is possible to further minimize the gap with regard to capacity by using irregular code designs [114, 185] at the cost of a higher decoding complexity, and a high interleaver length, i.e. latency, precluding inter-active lip-synchronised video communication.

TTCM-VLC Parameters	
VLC Parameters	
VLC Type	RVLC
Source Symbols	$u = \{0,1,2,3,4\}$
Probabilities of Occurrence	$P(u) = \{0.33, 0.30, 0.18, 0.10, 0.09\}$.
VLC Codewords	$C = \{00, 11, 010, 101, 0110\}$
Source Entropy	$L_s = 2.1391$ BPS
Codeword Length	$L_{vlc} = 2.46$ BPS
Coding Rate	$R_{vlc} = 0.87$ BPS
TTCM Parameters	
CM Type	TTCM
CM Code Rate	$R_{cm} = 2/3$
Mapper Type	Set-Partitioned
Number of TTCM Iterations	$I = 4$
Decoder Algorithm	Approximate Log-MAP
Modulation Level	8PSK
Generator Polynomials	$\mathbf{G(D)} = [11\ \ 02\ \ 04]_8$
Source to Relay transmission:Phase-I	
Channel	Rayleigh Fading (2×2) MIMO
MUD Type	ML,MMSE-IC and ZF
Effective Throughput	$\eta = 3.48$
G_{ar}	8 (9.03 dB)
Relay to Destination transmission:Phase-II	
Channel	Rayleigh Fading (2×1) MISO
MUD Type	ML
Effective Throughput	$\eta = 3.48$
G_{rb}	8 (9.03 dB)

Table 3.1: System parameters corresponding to Phase-I and Phase-II transmission of Figure 3.2.

as illustrated in Figure 3.6. Observe in Figure 3.6 that at a BER of 10^{-6} a marked improvement is exhibited for the ML-based scheme, when the number of inner iterations is increased. A slight improvement can be seen in Figure 3.6 for the MMSE-based scheme, when the number of outer iterations is increased from one to four. The PS method is used for determining the optimum transmission power levels at each node required for exactly matching the capacity limit, as detailed in Section 3.2.2.2. However, when practical coding and modulation schemes are employed, we have to find a more practical power allocation scheme based on the EXIT charts and simulation curves. More explicitly, the corresponding EXIT chart-based and simulation-based SNR difference is given by $\Gamma_{T,\Delta} = \Gamma_{R,\Delta} = 15.8 - 8.6 = 7.2$ dB, as opposed to the DCMC-based SNR difference of $12.1 - 6.3 = 5.8$ dB. We employ the PS technique based on Equation (3.21) and Equation (3.22) using the SNR difference of 7.2 dB for our TTCM-VLC-2Way system. We will

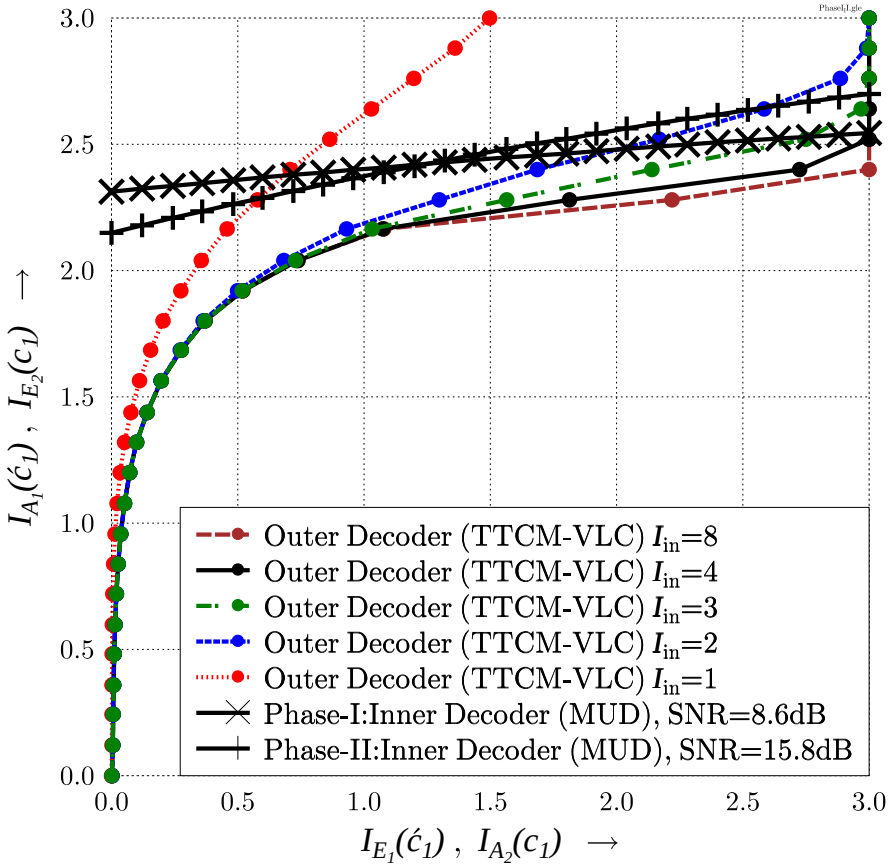

Figure 3.5: EXIT curves of the **TTCM-VLC**-aided SDMA scheme for **Phase-I** and **Phase-II** transmissions which are shown in Figure 3.2, with different number of inner iterations I_{in}. Note that **ML** MUDs are employed during both Phase-I and Phase-II, while the simulation parameters corresponding to both phases are listed in Table 3.1.

Transmission	**Scheme**	Γ_{lim}	$\Gamma_{10^{-6}}$	**Gap**[dB]
Phase-I	TTCM-VLC-ML	6.3	8.6	2.3
	TTCM-VLC-MMSE-IC	6.3	11.4	5.1
	TTCM-VLC-ZF	6.3	13.0	6.7
Phase-II	TTCM-VLC-ML	12.1	15.8	3.7
	TTCM-VLC-MMSE-IC	12.1	16.2	4.1
	TTCM-VLC-ZF	12.1	17.0	4.9

Table 3.2: System performance of the **TTCM-VLC**-aided SDMA scheme for **Phase-I** and **Phase-II** transmissions of Figure 3.2, where the simulation parameters of Table 3.1 are used. The results are extracted from Figure 3.6 for the cases of $I_{\text{in}} = I_{\text{out}} = 4$, where $\Gamma_{10^{-6}}$ denotes the SNR values associated with BER level 10^{-6}. Γ_{lim} denotes the SNR limit corresponding the DCMC capacity curve of Figure 3.3.

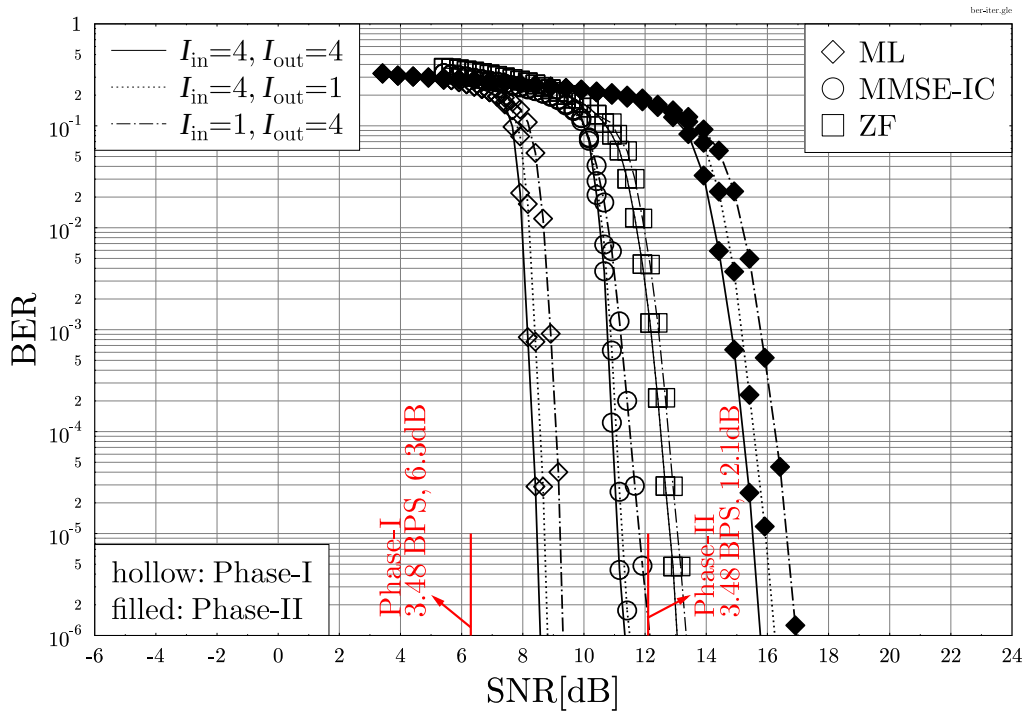

Figure 3.6: BER versus SNR performance of **TTCM-VLC**-aided SDMA scheme where **ML, MMSE-IC and ZF** MUDs are employed at the RN during Phase-I transmission while **ML** MUD is employed in Phase-II link. The SNR limits linked with the DCMC capacity bounds that are obtained from Figure 3.3. The simulation parameters corresponding to both phases are listed in Table 3.1, while the related results are summarised in Table 3.2.

use the non-cooperative Phase-II transmission using TTCM-VLC-ML scheme, which was simulated in Figure 3.6 as our benchmark. Our TTCM-VLC-2Way schemes have the same throughput and also enjoy a geometrical gain of 9 dB, due to employing a RN. Hence, the corresponding transmit SNR at the two-way relay-based DCMC capacity is given by $\text{SNR}_t = \text{SNR} - 9 = 1.1$ dB, where the SNR$=$ 10.1 dB limit is illustrated in Figure 3.4. The BER versus SNR_t performance of our proposed 8PSK-based TTCM-VLC-2Way schemes, when communicating over uncorrelated Rayleigh fading channels, are depicted in Figure 3.7. Again, the three different MUD techniques, namely the above-mentioned ML, MMSE-IC and ZF were invoked in the RN during the first time slot, while only the ML was used at the DN during the second time period. It can be seen from Figure 3.7 that without using the PS technique, the ML-based TTCM-VLC-2Way (denoted by a square marker with a dotted line) scheme outperformed the TTCM-VLC-ML benchmark scheme, by 9.0 dB at a BER of 10^{-6}. By contrast, a further 2.4 dB SNR gain can be attained by the ML-based TTCM-VLC-2Way scheme, when the PS technique is invoked. The performance of the "MMSE-IC-PS" and the "ZF-PS" based TTCM-VLC-2Way schemes was 0.65 dB and 1.24 dB poorer than that of the "ML-PS" based TTCM-VLC-2Way scheme at a BER of 10^{-6}. At a BER of 10^{-6} the proposed ML-PS based TTCM-VLC-2Way scheme is approximately $4.3 - 1.1 = 3.2$ dB away from the DCMC capacity bound. The achievable gains of our proposed scheme when when compared to the non-cooperative benchmark are summarised in Table 3.3.

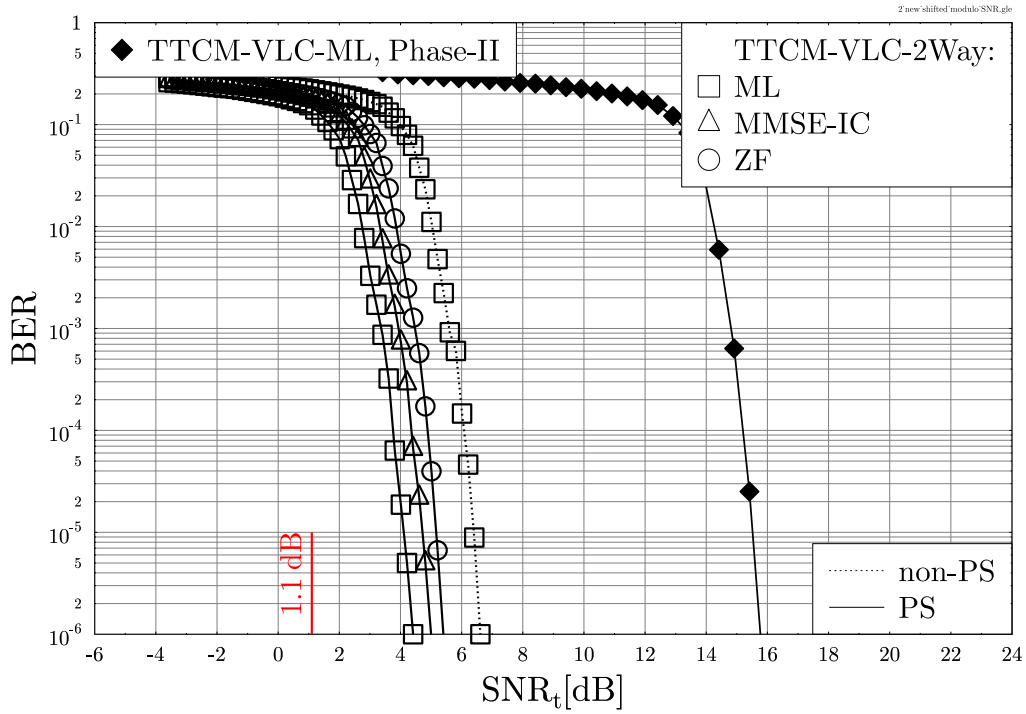

Figure 3.7: BER versus SNR$_t$ performance of 8PSK based **TTCM-VLC-2Way** scheme of Figure 3.2, where **ML, MMSE-IC and ZF** MUDs are employed at the RN during Phase-I transmission while **ML** MUD is employed in Phase-II link. The SNR limits linked with the DCMC capacity bounds are obtained from Figure 3.4. The simulation parameters corresponding to both phases are listed in Table 3.1, while the related results are summarised in Table 3.3.

Transmission	**Scheme**	$\Gamma_{\text{benchmark}}$	$\Gamma_{10^{-6}}$	**Gain** [dB]
TTCM-VLC-2Way	ML-PS	15.6	4.2	11.4
	MMSE-IC-PS	15.6	5	10.6
	ZF-PS	15.6	5.5	10.1
	ML-non-PS	15.6	6.6	9.0

Table 3.3: System performance of the **TTCM-VLC-2Way** scheme of Figure 3.2 when compared to non-cooperative Phase-II transmission benchmark, where the SNRs Γ are recorded at BER level of 10^{-6}. The simulation parameters of Table 3.1 are used, while the results are extracted from Figure 3.7.

In conclusion, our proposed mobile multimedia system provides a beneficial source compression with the aid of an RVLC, an improved error resilience by TTCM, as well as attaining both relaying and iterative gains. Let us now embark to our reduced-complexity source code before investigating the performance of the proposed TTCM-VLC-2Way schemes based on image and video transmissions in Section 3.4.

3.3.2 Reduced-Complexity Source Code

We propose a pair of low-complexity methods for image and video compression, which rely on representing the pixels with the aid of a reduced number of codewords. This would lead to a significant reduction in the complexity of the VLC decoder by decreasing the number of trellis-states. For example, in our image-based simulations, when encode the (256×256)-pixel "*Lena*" image. The most straightforward source encoding would rely on mapping each pixel to a VLC source symbol, where the alphabet size is $2^8 = 256$, since each pixel is represented by 8 bits. However, this would incur a complex VLC trellis, which consists of 965 states, according to the bit-based trellis structure of [105]. The VLC decoding complexity would therefore become excessive. Hence, as a remedy, in the following we will apply two different low-complexity methods.

In our first proposed method (M1), each 8 Bits Per Pixel (BPP) symbol of the image is split into two 4 BPP symbols. This would reduce the number of possible symbols from $2^8 = 256$ to $2^4 = 16$, while the total number of source symbols is increased from $256 \times 256 = 65\,536$ to $65\,536 \times 2 = 131\,072$. The number of VLC trellis states will be dramatically reduced from 965 to 25, as shown in Figure 3.8. The trellis diagram between the bit indices n and $n+1$ is shown in Figure 3.8, where there is a single root state corresponding to the root node R of the code tree[5] and a number of further states, that are labelled by the internal nodes $\mathrm{I}_1 \ldots \mathrm{I}_{24}$ of the code tree. All terminal nodes lead again to the root state $R = T$. This is a time-invariant bit-based trellis structure designed according to [105]. Our second method (M2) aims for further reducing the VLC decoding complexity by encoding the differences of the pixel values, rather than the actual pixel values. Let us assume for a moment that the encoder is processing the video pixel $\mathbf{u}^i_{x,y}$, which is represented by the shaded small box in Frame i of Figure 3.10, where the subscripts x and y represent the index of the height and width of each frame, respectively. Then, the current pixel $\mathbf{u}^i_{x,y}$ will be predicted by averaging the adjacent left and the adjacent top pixels as well as the pixel in the previous frame in the same position with reference to the current pixel as:

$$\mathbf{u}^P_1 = \frac{1}{3}\left[\mathbf{u}^{i-1}_{x,y} + \mathbf{u}^i_{x-1,y} + \mathbf{u}^i_{x,y-1}\right] . \tag{3.25}$$

As shown in Figure 3.10, the difference $\mathcal{D}$ between the current and the predicted pixels will then be fed into a lossless quantizer Q_L for generating the 'pixel-difference' symbols $\mathbf{u}_1$, as illustrated in **Algorithm 1**.

[5]The code tree can be constructed in similar way that outlined in [119, Chapter 3]. Additionally, Figure A.1 of Appendix A presents an example of trellis construction.

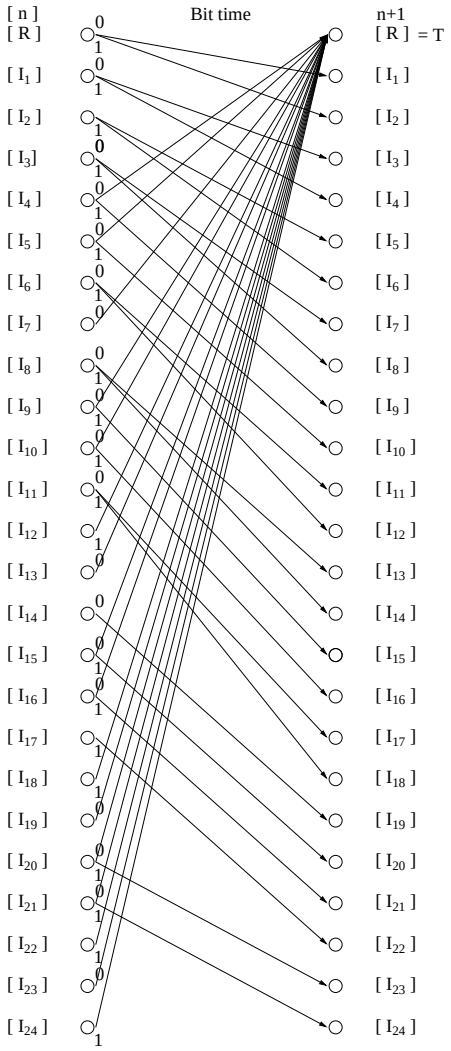

Figure 3.8: Trellis diagram for M1 scheme.

Algorithm 1 Flow-chart of the loss less quantizer "Q_L" block shown in Figure 3.10.

if $|\mathcal{D}| \geq \frac{(V-1)}{2}$; **then**
  if $\mathcal{D} \geq 0$; **then**
    $\mathbf{u}_i \leftarrow (1)$
    $\mathcal{D} = \mathcal{D} + (V - 2)$;
  else
    $\mathbf{u}_i \leftarrow (V)$
    $\mathcal{D} = \mathcal{D} - (V + 2)$;
  end if
else
  $\mathbf{u}_i \leftarrow \left(\mathcal{D} + \frac{(V+1)}{2}\right)$.
end if

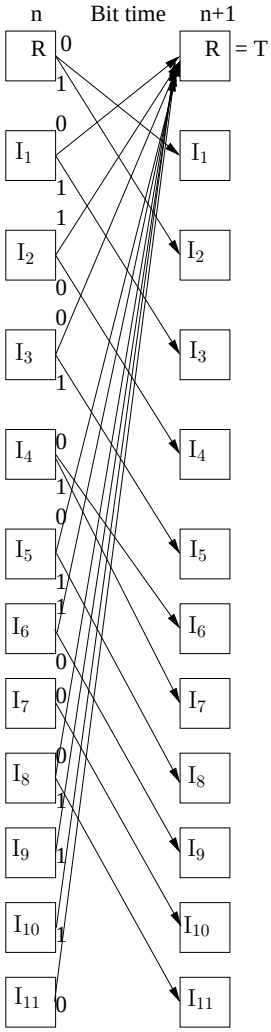

Figure 3.9: Trellis diagram for M2 scheme.

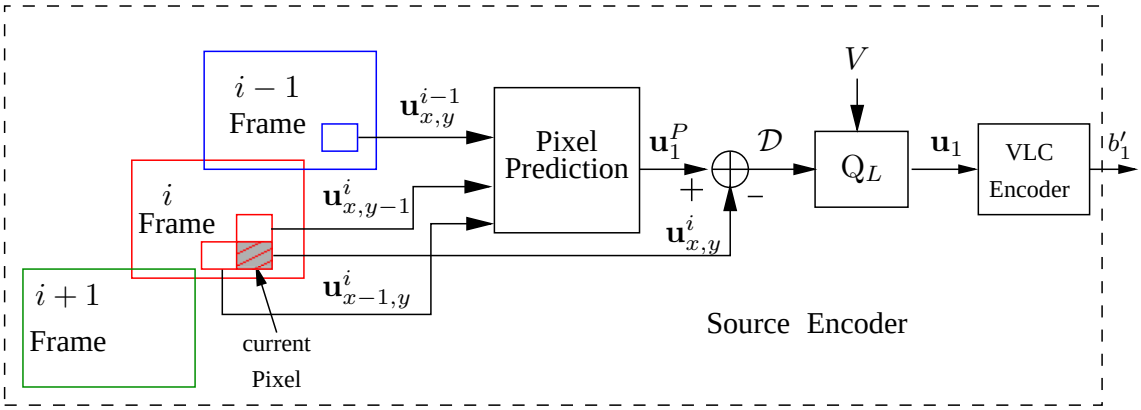

Figure 3.10: Schematic of the low complexity source encoder using the second method **M2**, where "Q_L" is a loss less quantizer illustrated in **Algorithm 1**.

The pixel-difference symbols $\mathbf{u}_1$ are encoded row-by-row from the top-left corner to the bottom-right corner. The complexity of the scheme and the number of codewords is controlled by the variable V. Note that in our simulations we have chosen $V = 9$ since it strikes a good trade-off between the bit rate and the VLC decoding complexity. The number of states in the corresponding bit-based trellis is further reduced to 12, as illustrated in Figure 3.9. Table 3.4 summarises the parameters of M1 and M2, when using the above-mentioned "*Lena*" image, where M1 has a smaller number of source symbols compared to M2, but it exhibits reduced source-symbol correlations, when the 8 BPP symbols are converted to 4 BPP symbols. As a result, the coding efficiency of M1 becomes lower and the total number of VLC bits required is $\lceil N_{ss} \times L_{vlc} \rceil = 604\,164$, where N_{ss} denotes the Number of Source Symbols. By contrast, M2 has a higher number of source symbols, but it efficiently reduces the average VLC codeword length by exploiting the inherent source correlations. As a result, the total number of VLC encoded bits in M2 is about 22% lower than that of M1. The transmit SNR per information bit, $[E_b/N_0]_t$, for M1 and M2 can calculated using Equation (3.7), where we have $\eta = 1.7$ BPS and $\eta = 1.78$ BPS for M1 and M2 schemes, respectively, which have a difference of 0.08 BPS. The Peak Signal-to-Noise Ratio (PSNR) for an $(m \times n)$-pixel monochrome image is given by [194]:

$$PSNR = 10\log_{10}\left(\frac{I_{\max}^2}{\frac{1}{mn}\sum_{i=1}^{m}\sum_{j=1}^{n}\left|I_{i,j}-\hat{I}_{i,j}\right|^2}\right), \tag{3.26}$$

where we have $m = n = 256$ in our case, while $I_{i,j}$ is the original image pixel, $\hat{I}_{i,j}$ is the estimated image pixel and $I_{\max}^2$ is the maximum possible pixel value of the image. Following VLC and pixel-recovery, we have $I_{\max}^2 = 2^8 - 1 = 255$ for both M1 and M2. Since VLCs constitute lossless codes, when there is no error in the reconstructed pixels, we have $PSNR = \infty$. In order to avoid this, we normalize the PSNR values such that the maximum PSNR is given by $PSNR_{\max} = 10\log_{10}(I_{\max}^2) = 48.13$ dB, where $1 \leq |I_{i,j} - \hat{I}_{i,j}| \leq 255$.

Method	**M1**	**M2**
Number of Source Symbols, N_{ss}	131072	153060
Number of VLC codewords	16	9
Minimum codeword length	3	2
Maximum codeword length	7	6
Number of VLC trellis states	25	12
Average codeword length, L_{vlc}	4.6094	3.0932
VLC entropy, L_s	3.9189	2.7855
Coding efficiency, R_{vlc}	0.8502	0.8918
Total number of VLC bits	604,164	473,446

Table 3.4: Comparison of parameters between **M1** and **M2** when employing (256×256)-pixel "*Lena*" image as source input.

3.4 Performance Results

In this section we evaluate the proposed scheme based on the transmission of image and video across the two-way relay channel, where both phases suffer from uncorrelated Rayleigh fading. The simulation parameters are shown in Table. 3.5.

TTCM-VLC Parameters	
VLC type	RVLC
CM type	TTCM
Modulation level	8PSK
CM Code Rate	$R_{cm} = 2/3$
Mapper Type	Set-Partitioned
Decoder Algorithm	Approximate Log-MAP
Generator Polynomials	**G(D)** $= [11\ \ 02\ \ 04]_8$
Number of TTCM Iterations	$I = 4$
Number of Inner Iterations	$I_{\text{in}} = 4$
Image Used	(256 $\times$ 256)-pixel "*Lena*"
Video Used	(176 $\times$ 144)-pixel QCIF "*Akiyo*"
Source to Relay transmission:Phase-I	
Channel	Uncorrelated Rayleigh fading 2 $\times$ 2 MIMO
MUD Type	ML,MMSE-IC and ZF
Effective Throughput	**M1**, $\eta = 3.40$ BPS
	M2, $\eta = 3.56$ BPS
G_{ar}	4 (6.02dB)
Relay to Destination transmission:Phase-II	
Channel	Uncorrelated Rayleigh fading 2 $\times$ 1 MISO
MUD Type	ML
Effective Throughput	**M1**, $\eta = 3.40$ BPS
	M2, $\eta = 3.56$ BPS
G_{rb}	4 (6.02dB)

Table 3.5: Simulation parameters for image/video performance analysis.

3.4.1 Image Performance Results

The subjective image quality of the TTCM-VLC-2Way scheme employing M1 and M2 is depicted in Figure 3.11 and Figure 3.12, respectively, while the corresponding PSNR versus transmitted $[E_b/N_0]_t$ performance are shown in Figure 3.13. As seen from Figure 3.13, both the M1 and M2 based schemes are capable of achieving the asymptotic (error-free) PSNR at $[E_b/N_0]_t = 3.5$ dB

(a) $I_{\text{out}} = 1$ (b) $I_{\text{out}} = 2$ (c) $I_{\text{out}} = 4$

Figure 3.11: Subjective image quality when transmitting "*Lena*" image with $[E_b/N_0]_t =$ 3.5 dB using the 8PSK-based **TTCM-VLC-2Way** scheme of Figure 3.2. Note, **ML** MUDs are invoked during both phases transmission and **M1**-based source coding method is used. The corresponding simulation parameters are listed in Table 3.4 and Table 3.5, and the number of outer iterations, I_{out}, between the TTCM-VLC decoder of Figure 3.2 and the MUD detector are (from left) one, two and four, respectively.

(a) $I_{\text{out}} = 1$ (b) $I_{\text{out}} = 2$ (c) $I_{\text{out}} = 4$

Figure 3.12: Subjective image quality when transmitting "*Lena*" image with $[E_b/N_0]_t =$ 3.5 dB using the 8PSK-based **TTCM-VLC-2Way** scheme of Figure 3.2. Note, **ML** MUDs are invoked during both phases transmission and **M2**-based source coding method of Figure 3.10 is used. The corresponding simulation parameters are listed in Table 3.4 and Table 3.5, and the number of outer iterations, I_{out}, between the TTCM-VLC decoder of Figure 3.2 and the MUD detector are (from left) one, two and four, respectively.

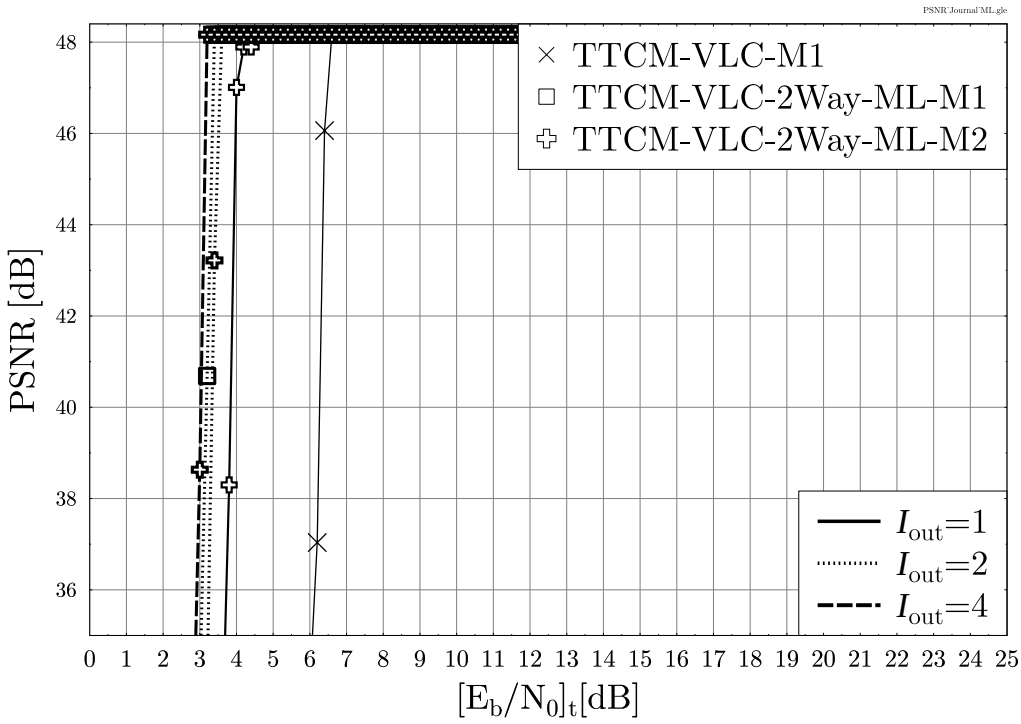

Figure 3.13: PSNR versus $[E_b/N_0]_t$ performance when transmitting "*Lena*" using the 8PSK-based **TTCM-VLC-2Way** scheme of Figure 3.2, where the **ML** MUDs are implemented during both phases. The corresponding simulation parameters are listed in Table 3.4 and Table 3.5.

after the fourth iteration. Hence, the reconstructed images shown in Figure 3.11(c) and Figure 3.12(c) after the fourth iteration are perfect. However, the images shown in Figure 3.11(b) and Figure 3.12(b) at the second iteration are distorted in different ways. The M1-based image exhibits a few horizontal artefacts, while the M2-based image exhibits segments moved to a different location. When aiming for a perfect transmission, the M2-based scheme only requires approximately 0.2 dB higher $[E_b/N_0]_t$ value than that of the M1-based scheme. Furthermore, M2 benefits from a lower complexity due to a lower number of VLC trellis states and a lower VLC bit rate, as summarised in Table 3.4. Hence, the M2-based scheme offers a better trade-off in terms of complexity and transmission bit rate. Additionally, all of our proposed TTCM-VLC-2Way schemes outperform the non-cooperative TTCM-VLC benchmark scheme, as shown in Figure 3.13. Note that, the single user performance of a non-cooperative scheme is considered as our benchmarker, which is termed as the "TTCM-VLC-M2" scheme in Figure 3.13, where a single user transmits to a single receiver that employs ML MUD.

3.4.2 Video Performance Results

Having characterised our cooperative scheme for still-imaged-based source, let us now consider a video-based sequence transmission. Here, we use the grey-scale QCIF "*Akiyo*" video test as our source input sequence. Similar to the analysis used in Section 3.3.1, we opted for employing the

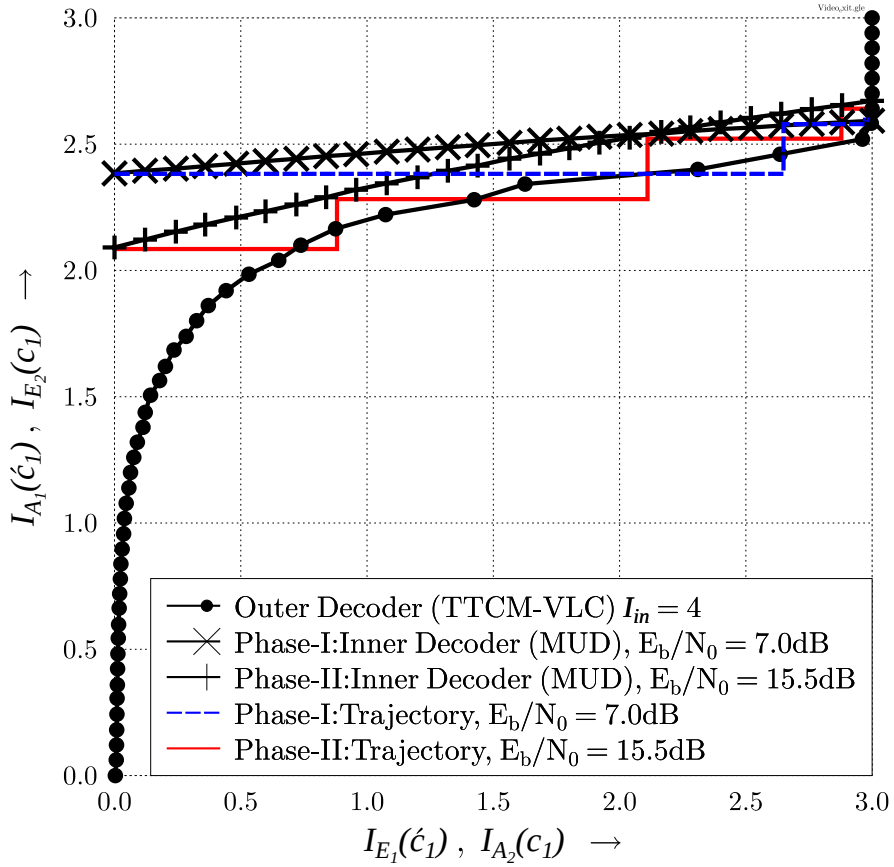

Figure 3.14: EXIT curves of the **TTCM-VLC**-aided SDMA scheme for **Phase-I** and **Phase-II** transmissions which are shown in Figure 3.2 when transmitting "*Akiyo*" video sequence. Note, **ML** MUDs are invoked during both phases and **M2**-based source coding method is used, while the simulation parameters corresponding to both phases are listed in Table 3.5.

non-binary EXIT chart technique for characterising the convergence behaviour of our non-binary TTCM-VLC and MUD decoders. As shown in Figure 3.14, an open EXIT tunnel leading to the right-hand axis is achieved for the Phase-I transmission at $E_b/N_0 = 7.0$ dB, hence indicating decoding convergence at the RN. Observe in Figure 3.14 that, three decoding iterations are needed between the TTCM-VLC decoder and the MUD during Phase-I transmission for achieving convergence, as illustrated by the stair-case-shaped decoding trajectory of the same figure. However, Phase-II link requires $E_b/N_0 = 15.5$ dB and four decoding iterations in order to attain a an infinitesimally low BER, as shown in Figure 3.14. It can be readily seen from the EXIT chart that there is a significant difference of $E_b/N_0 = 15.5 - 7.0 = 8.5$ dB, when aiming for attaining a low BER between the Phase-I and Phase-II transmissions. Thus, the power sharing regime that was outlined in Section 3.2.2.2 has to be implemented here as well.

Furthermore, the PSNR versus $[E_b/N_0]_t$ performance curves are portrayed in Figure 3.15. Again similar to the discussion in Section 3.3.2, the maximum value of the PSNR is set to $PSNR_{\max} = 10\log_{10}\left((2^8)-1\right)^2 = 48.13$ dB. Without this normalization, we would have $PSNR_{\max} = \infty$

when there are no errors in the reconstructed pixels, since the VLCs employed constitute lossless codes.

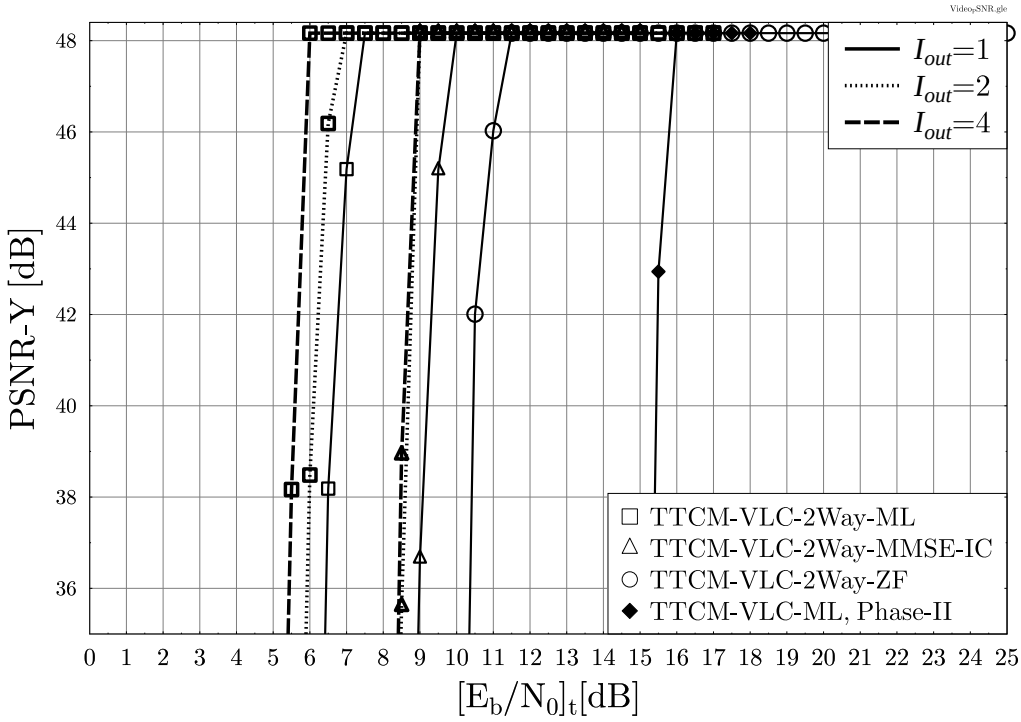

Figure 3.15: PSNR-Y versus $[E_b/N_0]_t$ performance when transmitting "*Akiyo*" video sequence using the 8PSK-based **TTCM-VLC-2Way** scheme of Figure 3.2. Note that, **M2**-based source coding method of Figure 3.10 is used, while the corresponding simulation parameters are listed in Table 3.5.

In line with the BER results of Figure 3.7, significant PSNR gains can be observed for all two-way relaying schemes compared to the non-relaying benchmarker. More explicitly, the proposed systems based on the ML, MMSE-IC and ZF MUDs require $[E_b/N_0]_t$ of 4.5 dB, 6.5 dB and 10 dB, respectively, to achieve the maximum, attainable PSNR associated with an infinitesimally low BER, as seen in the corresponding subjective video quality results of Figure 3.16.

Additionally, the effects of the number of outer iterations for ML-based scheme is shown in Figure 3.17, where the reconstructed frame is totally corrupted after the first iteration, as shown in Figure 3.17(a). By contrast, using four iterations will lead to a perfect video recovery, as seen in Figure 3.17(c).

3.5 Chapter Conclusions

In this chapter we have investigated the design of a jointly optimized end-to-end source-coding, channel-coding and modulation scheme, which was assisted by a two-way relaying scheme. This arrangement enables an exchange of two information frames between two users using only two, rather than four, time slots. The EXIT chart technique outlined in Section 2.5 was employed for

(a) **ML** : $[E_b/N_0]_t$ = 6.5dB (b) **MMSE-IC** : $[E_b/N_0]_t = 9.0$dB (c) **ZF** : $[E_b/N_0]_t$ = 11.5dB

Figure 3.16: Subjective video quality when transmitting the 10th frame of "*Akiyo*" video sequence using the 8PSK-based **TTCM-VLC-2Way** scheme of Figure 3.2, when the **ML**, $\mathbf{MMSE-IC}$ and **ZF** MUDs are employed at the RN. Note, **M2**-based source coding method of Figure 3.10 is used, while the corresponding simulation parameters are listed in Table 3.5.

(a) $I_{\text{out}} = 1$ (b) $I_{\text{out}} = 2$ (c) $I_{\text{out}} = 4$

Figure 3.17: Subjective video quality when transmitting the 10th frame of "*Akiyo*" video sequence with $[E_b/N_0]_t = 6.5$ dB using the 8PSK-based **TTCM-VLC-2Way** scheme of Figure 3.2. Note, **ML** MUDs are invoked during both phases transmission and **M2**-based source coding method of Figure 3.10 is used. The corresponding simulation parameters are listed in Table 3.4 and the number of outer iterations, I_{out} are (from left) one, two and four, respectively.

investigating the decoding convergence behaviour of the proposed scheme and for optimizing the overall system. The transmission regime was modelled in Section 3.2, where the Phase-I link can be interpreted as a (2×2) MIMO channel, while the Phase-II links can be represented as a (2×1) MISO channel. In Section 3.2.2, the two-way relay channel's capacity was derived, which motivated the power sharing technique of Section 3.2.2.2. Consequently, it was shown in Figure 3.7 that the proposed scheme outperformed the benchmark scheme dispensing with relaying by as much as 11.4 dB, when the appropriate power allocation strategy was invoked. Additionally, we have also proposed a pair of low-complexity source coding in Section 3.3.2 schemes for transmission over our two-way relaying system, that exhibited a substantial complexity reduction, since the number of VLC trellis states has been reduced from 965 states to just 25 and 12 states, for M1 and M2 of Table 3.4, respectively. Substantial BER, PSNR and subjective image and video quality improvements were attained, as outlined in Section 3.4. The PSNR values needed for achieving the asymptotic (error-free) PSNR of 48.13 for our proposed schemes are summarises in Table 3.6. In

this chapter we were able to attain a beneficial source compression using the powerful trellis-based VLC of [119]. In the next chapter, however, we will investigate whether it is possible to design a DJSC that is capable of achieving source compression, whilst dispensing with the VLCs.

Scheme		**TTCM-VLC-2Way**	
Schematic		Figure 3.2	
Simulation Parameters		Table 3.5	
Source	Figure	$[E_b/N_0]_t$ [dB] at PSNR= 48.13	
Lena image	3.13	ML-M2, $I_{\text{out}} = 1$	4.5
		ML-M1, $I_{\text{out}} = 2$	3.4
		ML-M2, $I_{\text{out}} = 2$	3.6
		ML-M2, $I_{\text{out}} = 4$	3.2
Akiyo video	3.15	ZF-M2, $I_{\text{out}} = 1$	11.5
		MMSE-M2, $I_{\text{out}} = 1$	10.0
		MMSE-M2, $I_{\text{out}} = 2$	9.0
		MMSE-M2, $I_{\text{out}} = 4$	9.0
		ML-M2, $I_{\text{out}} = 1$	7.5
		ML-M2, $I_{\text{out}} = 2$	7.0
		ML-M2, $I_{\text{out}} = 4$	6.0

Table 3.6: $[E_b/N_0]_t$ threshold values of various TTCM-VLC-2Way schemes for transmitting image and video sources when targeting the asymptotic (error-free) PSNR of 48.13. The results are extracted from Figures 3.13, Figures 3.15.

Chapter 4

TTCM-Aided Rate-Adaptive Distributed Joint Source-Channel Coding

4.1 Introduction

Motivated by the example introduced in Section 1.1, Distributed Source Coding (DSC) is capable of offering a practical answer to the question raised in the previous chapter's conclusion. However, Distributed Joint Source-Channel coding (DJSC) offers further benefits when the correlated sources' signals are transmitted over noisy channels [10, 8, 9]. Additionally, as summarised in Section 1.2, the theoretical foundations of DSC were established by Slepian and Wolf [4] in 1973. Later, the idea of using channel coding techniques was suggested by Wyner in [195][1] allowed practical solutions to be developed. This chapter will consider the relying on perfect side-information scenario which is also referred to as source coding with side-information [3, 10, 12, 196], where a pair of correlated sources are transmitted to a destination node. More explicitly, the first source sequence is encoded and compressed, before it is transmitted through a noisy channel, while the second source signal is assumed to be perfectly decoded and hence can be used at the destination for exploitation as side-information for improving the attainable decoding performance of the first source. As further new development, the next chapter will consider the more practical scenario, where the correlated sources are transmitted through a noisy Multiple Access Channel (MAC).

Practical Slepian-Wolf coding schemes using Turbo Codes (TC) were proposed for example in [9, 196, 197], whereas Low-Density Parity-Check (LDPC) codes were considered in [36, 38, 39]. However, finding the best code for approaching the Slepian-Wolf Shannon (SW/S) limit was not considered in [9, 196, 197]. Later, a so-called "super" turbo code was proposed in [11], aiming for

[1] As stated in Section 1.2.2, since the correlation between the sources may be interpreted as the ameliorating effect of a "virtual" channel, a good channel code having for example a maximum minimum Hamming distance will be a good SW code [10].

approaching the SW/S limit, when communicating over Additive White Gaussian Noise (AWGN) channels. However, the scheme proposed in [11] for an AWGN channel suffers from an error floor, when communicating over Rayleigh fading channels which makes the system less suitable for wireless applications. A modified LDPC code was proposed in [37] for mitigating the error floor, but nonetheless, a high error floor persists, when the correlation between the sources is low. A joint-turbo equaliser and decoder scheme was proposed for relying on perfect side-information DJSC in [43], while an iterative joint-turbo equaliser and decoder scheme was conceived for transmission over a multi-path Rayleigh fading multiple access channel in [50]. Both schemes have achieved a near-SW/S performance, albeit at a high joint decoding complexity. More specifically, 35 iterations were invoked between the decoder components in [43], while as many as 350 iterations were required in [50] for attaining a near-SW/S performance. By contrast we only invoke 8 turbo iterations in our TTCM decoder, where both constituent decoders have a comparable complexity [156].

Furthermore, in practice the short-term correlation amongst the sources might be time-variant, hence adaptive-rate schemes have to be considered, where the code-rate is controlled via a feedback channel. More specifically, if the Bit Error Ratio (BER) evaluated after decoding exceeds a given threshold, more syndromes (or parity bits if parity puncturing is used) will be requested from the transmitter. A pair of innovative adaptive-rate LDPC schemes were proposed in [12], while adaptive-rate turbo codes were designed in [149]. In [12], the encoder stored the syndromes and incrementally transmitted them to the receiver, when the decoder failed to find the legitimate codeword. Both papers considered relying on perfect side-information DSC structure based on the puncturing of the syndrome generated by the channel encoders, while stipulating the idealised simplifying assumption of modelling the channel as the parallel combination of a perfect channel and a Binary Symmetric Channel (BSC). More advanced adaptive-rate schemes considered the employment of a polar code [58], or efficient particle-based belief propagation-aided decoding [55] and density evolution based decoding techniques [12]. Against this background, this chapter will adopt the family of bandwidth-efficient TTCM schemes, which combine the functions of coding and modulation for conceiving a new DJSC system, which we term as the Distributed Joint Source TTCM (DJSTTCM) scheme. Inspired by our discussions in Section 2.4, the TTCM code advocated was designed for improving the attainable throughput by considering the joint design of error correction codes and modulation, where the parity bits are absorbed without any bandwidth expansion by increasing the number of bits per modulated symbol. Additionally, near-instantaneously adaptive-rate mechanisms will be designed for increasing the system's effective throughput, while ensuring an infinitesimally low BER. The resultant near-instantaneously adaptive scheme is referred to as the A-DJSTTCM arrangement.

The rest of the chapter is organised as follows. The distributed system model is described in Section 4.2. The achievable rate region will be analysed in Section 4.3, while the performance of the DJSTTCM scheme is investigated in Section 4.4. Finally, our conclusions are offered in Section 4.5.

4.2 System Model

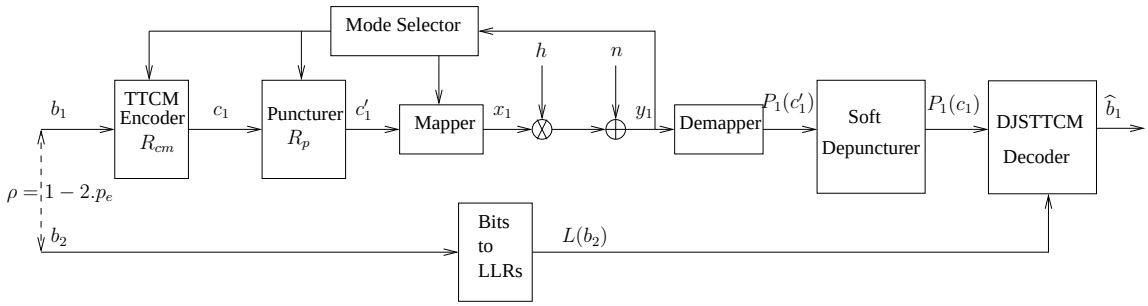

Figure 4.1: Block diagram of the A-DJSTTCM system communicating over fading channels. The sources $\{b_1\}$ and $\{b_2\}$ are assumed to be correlated, i.e. we have $H(b_1 \mid b_2) \neq H(b_1)$, and $L(\cdot)$ denotes the Logarithmic-Likelihood Ratios (LLR). The DJSTTCM decoder is further illustrate in Figure 4.2.

The relying on perfect side-information DJSC scenario of Figure 4.1 was considered here, where a sequence $\{b_2\}$ is transmitted at the rate of $R_2 = H(b_2)$, which is typically referred to as 'side-information' in most contributions [10,9,196] albeit again, it can also be interpreted as another desired source signal, which was perfectly recovered. The sequence $\{b_2\}$ can also be transmitted through an independent noisy channel in which case a encoder structure similar to that of the first source $\{b_1\}$ has to be implemented. The correlated sequence $\{b_1\}$ is then compressed to a rate of $R_1 = H(b_1|b_2)$ for the sake of approaching the Slepian-Wolf bound, namely point A of Figure 1.6, in order to achieve the overall rate of $H(b_1, b_2)$. Typically the BSC-based abstraction is used for modelling the correlation between the two source sequences $\{b_1\} = \{b_1^1, b_1^2, \cdots, b_1^i, \cdots, b_1^N\}$ and $\{b_2\} = \{b_2^1, b_2^2, \cdots, b_2^i, \cdots, b_2^N\}$, where N is the length of each source block.

For example, when $\{b_1\}$ and $\{b_2\}$ have a correlation coefficient of $\rho = 0.9$ given the perfect knowledge of $\{b_2\}$, $\{b_1\}$ may be interpreted as the BSC's output signal which was contaminated by the bit-flipping error events occurring with a probability of p_e. The source sequence $\{b_1\}$ is generated by an equiprobable binary symmetric i.i.d. source, while $\{b_2\}$ can be defined as: $b_1^i = b_2^i \oplus e_i$, where $\oplus$ is the modulo-2 addition operation and e_i is an independent binary random variable assuming the logical value 1 with a cross-over probability of p_e and 0 with a probability of $(1 - p_e)$. Both the random variables of b_1^i and b_2^i in the pair of bit streams $\{b_1\}$ and $\{b_2\}$ may be assumed to be i.i.d. for the bit index i, hence both sources emit equiprobable [50] bits. Consequently, the entropy of each source is unity, which yields a conditional entropy of:

$$H(p_e) = H(b_1|b_2) = \lim_{i\to\infty} \frac{1}{i} H\left[\left((b_1^1, \cdots, b_i^1, \cdots b_N^1)|(b_1^2, \cdots, b_i^2, \cdots b_N^2)\right)\right], \quad (4.1)$$

where $H(p_e) = p_e \log_2\left(\frac{1}{p_e}\right) + (1 - p_e)\log_2\left(\frac{1}{1-p_e}\right)$ is the entropy of the binary random variable and e_i is used for parametrising the side-information. Therefore, the achievable SW rate region is

given by the following three inequalities [50]

$$R_1 \geq H(p_e),\ R_2 \geq H(p_e),$$
$$R_1 + R_2 \geq 1 + H(p_e)\ . \tag{4.2}$$

Let us now embark on the detailed design of the encoder and the decoder of our distributed scheme for the sake of minimising the SNR required for approaching the SW/S bound, while maintaining reliable communications.

4.2.1 Adaptive-Distributed Joint Source-TTCM Encoder

The block diagram of the proposed A-DJSTTCM scheme considered for transmitting correlated sources is illustrated in Figure 4.1, where $L()$ denotes the Logarithmic-Likelihood Ratios (LLR) of the bits. As shown in Figure 4.1, the input sequence $\{b_1\}$ is fed into a TTCM encoder, which has a coding rate of $R_{cm} = \frac{m}{m+1}$ and invokes a $M = 2^{m+1}$-level modulation scheme. The TTCM encoded bits are then punctured at a rate of R_p. The resultant bit sequence $\{c_1'\}$ is then mapped to the corresponding modulated symbols $\{x_1\}$, before their transmission over uncorrelated Rayleigh or Nakagami-m fading channels. Note that each specific symbol of the modulated symbol sequence, $\{x_1\}$, is mapped using $\mu(\cdot)$-QAM/PSK mapping function. The second bit sequence $\{b_2\}$ will be converted to the LLRs $L(b_2) = L_e$, which will be exploited as side-information. This conversion is necessary because the joint decoder is a soft-decision-based one. These LLRs are characterised by the above-mentioned cross-over probability p_e and can be estimated as:

$$\begin{aligned} L(b_1|b_2) &= \ln\left(\frac{\Pr(b_2=+1|b_1)}{\Pr(b_2=-1|b_1)}\right) \\ &= \ln\left(\frac{(1-p_e)\Pr(b_2=+1)+p_e\Pr(b_2=-1)}{(1-p_e)\Pr(b_2=-1)+p_e\Pr(b_2=+1)}\right)\ . \end{aligned} \tag{4.3}$$

We assume that these LLRs are available at the destination and to be exploited by the joint decoder, while p_e can be estimated at the decoder using Equation (4.17).

As an example, we use a rate $R_{cm} = 1/2$ TTCM encoder relying on a puncturer of rate $R_p = 2/1$, which punctures one bit out of two encoded bits. We assume that all the systematic bits are punctured, while all the parity bits are transmitted to the decoder. Hence, the overall code rate is $R_1 = R_{cm} \cdot R_p = 1$. However, the parity bit sequence may also be further punctured in order to achieve an increased compression ratio. The resultant bits are then mapped to BPSK symbols, i.e. the modulation mode has been changed from QPSK to BPSK (QPSK/BPSK). Thus, the corresponding effective throughput is given by $\eta = R_1 \cdot \log_2(2) = 1$ Bit Per Symbol (BPS). Note that the SNR can be calculated in dB as $\mathrm{SNR(dB)} = E_b/N_0\mathrm{(dB)} + 10\log_{10}(\eta)$. Then the modulated symbol sequence $\{x_1\}$ is transmitted over an uncorrelated Rayleigh fading channel and

the received symbol y_1 is given by:

$$y_1 = hx_1 + n\,, \tag{4.4}$$

where h is the channel's fading coefficient and n is the AWGN having a variance of $N_0/2$ per dimension. Therefore, the channel information probability of receiving y_1 given x_1^i was transmitted, gleaned from the soft demapper can be expressed as [156]:

$$\Pr(y_1 \mid x_1^{(m)}) = \frac{1}{(\pi N_0)} \exp\left(-\frac{\left|y_1 - hx_1^{(m)}\right|^2}{N_0}\right)\,, \tag{4.5}$$

where $m \in \{0, \cdots, M-1\}$. Additionally, the short-term average received SNR is given by:

$$\mathrm{SNR}_r = \frac{\mathrm{E}\left[|h|^2\right]\mathrm{E}\left[|x_1|^2\right]}{N_0}\,, \tag{4.6}$$

where x_1 represents the modulated symbols of source $\{b_1\}$ after puncturing. Furthermore, we have $\mathrm{E}\left[|x_1|^2\right] = 1$ and the SNR of $\gamma_r = 10\log_{10}\left(|h|^2/N_0\right)$ [dB] is estimated for each received block. Note that $\{b_2\}$ is related to $\{b_1\}$ according to $b_2^i = b_1^i \oplus e_i$.

4.2.2 Adaptive Mode Selection

Adaptive coded modulation systems form an attractive design that are capable of attaining robust and spectrally efficient communications over fading channels, in particular in multi-path fading scenarios exhibiting substantial quality fluctuations [159, 198, 199]. Thus, in order to counteract this problem, the near-instantaneously adaptive coded modulation scheme of [159, 198, 200] will be invoked in our system for adapting the affordable transmission rate according to the specific channel characteristics. Naturally, a higher-rate code and/or a higher-order modulation mode will be activated, when the instantaneous estimated channel quality is high, in order to increase the number of Bits Per Symbol (BPS) transmitted. By contrast, when the instantaneous channel quality is low, more robust lower-rate codes and/or a lower-order modulation modes will be activated with the goal of maintaining the target Bit Error Ratio (BER). As depicted in Figure 4.1, the transmitter selects the appropriate code rate and/or the modulation order 'just' capable of achieving the target-integrity and signal it back to the receiver. Diverse effective throughputs may be derived by carefully varying R_{cm} and R_p. In our A-DJSTTCM scheme the following modes are chosen at the encoder for ensuring that the BER $< 10^{-5}$:

- No transmission,
- DJSTTCM-QPSK/BPSK ,
- DJSTTCM-8PSK/QPSK ,
- DJSTTCM-16QAM/8PSK ,

- DJSTTCM-32QAM/16QAM .

4.2.3 Distributed Joint Source-TTCM Decoder

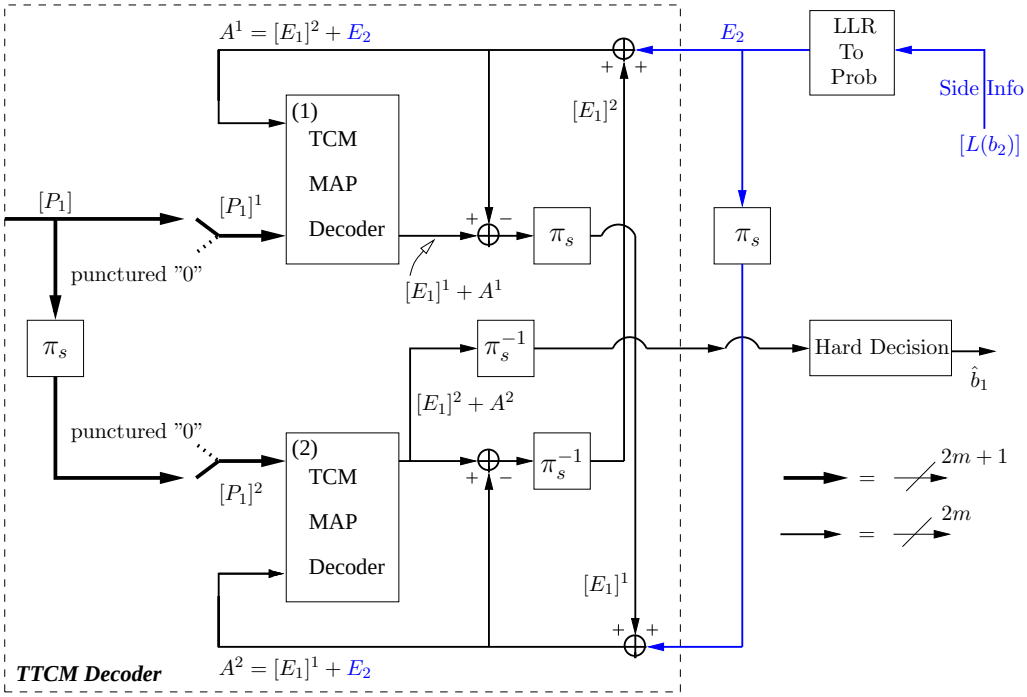

Figure 4.2: Block diagram of the DJSTTCM decoder of the A-DJSTTCM scheme of Figure 4.1, the notations π_s and π_s^{-1} represent the symbol interleaver and deinterleaver, respectively, while the side-information $L(b_2)$ is converted using the relevant LLR-to-symbol probability conversion, which is explained in Appendix B.

Our joint decoder is depicted in Figure 4.2, where both TCM decoders invoke the symbol-based MAP algorithm of [156, 159] operating in the logarithmic-domain. As detailed in Section 2.4.2, the TCM decoders are labelled with the round-bracketed indices, while the notation P, A and E represent the logarithmic probabilities of the parity, as well as *a priori* and of the *extrinsic* information, respectively, where we have $L_{b_2} = L(b_2|b_1)$. The $2^{(m+1)}$-ary P_1 probabilities, given in Equation (4.5), associated with a specific $(m+1)$-bit TTCM-coded symbol $\{c_1'\}$ are fed into the TTCM MAP decoder. A pair of signal components are generated by the constituent TCM decoders [156, 159] specifically, the *extrinsic* probability E is generated by each of the TCM decoders, while the *a priori* probability A is gleaned by each TCM decoder from the other one. Furthermore, as seen in Figure 4.2 the additional *extrinsic* probability, E_2, extracted from the side-information $\{b_2\}$ is also added to the *a priori* probability A, yielding $A^{(1,2)} = [E_1]^{(2,1)} + E_2$. Each of the constituent TCM blocks of Figure 4.2 calculates the A Posteriori Probabilities (APP) using the forward and backward recursion method[2]. Upon recalling the analysis of Section 2.4.2

[2]Detailed descriptions can be found in [156, Section 14.3]. Note that we illustrate the MAP process in the logarithmic domain in order to render it compatible with Figure 4.2.

and from Equation (4.4), we are now in the position to formulate the channel's transition metric as:

$$\eta_i(\grave{s}, s) = \ln\left(\exp\left(-\left|y_i - h_i x_i\right|^2 / N_0\right)\right) . \tag{4.7}$$

Then, both the backward and forward recursion of [156] are invoked for calculating $\beta_{i-1}(\grave{s})$ and $\alpha_i(s)$ as follows:

$$\alpha_i(s) = \max_{\text{all } \grave{s}}{}^{*}(\alpha_{i-1}(\grave{s}) + \eta_i(\grave{s}, s) + A^{(1,2)}) , \tag{4.8}$$

$$\beta_{i-1}(\grave{s}) = \max_{\text{all } s}{}^{*}(\beta_i(s) + \eta_i(\grave{s}, s) + A^{(1,2)}) , \tag{4.9}$$

where $\max^{*}$ represents the Jacobian logarithm [156] evaluating all variables in the logarithmic domain, with $(\grave{s}, s)$ denoting the transitions emerging from the previous state $\grave{s}$ to the present state s.

4.2.4 Decoding with Side-Information

Coded Modulation	TTCM
Modulation Scheme	QPSK, 8PSK, 16QAM
Code Rate	$R_{cm} = 1/2, 2/3, 3/4$
Puncturing Rate	$R_p = 1$
Effective Throughput	$\eta = 1, 2, 3$ BPS
Decoding Algorithm	Approximated Log-MAP
Mapper Type	Set-Partitioned
Decoding Iteration	$I = 8$
Number of Symbol	$N_s = 12\,000$ symbols per frame
Number of Frames	1000
Channel	Uncorrelated Rayleigh fading
Channel State Information (CSI)	Known
MUD Type	ML

Table 4.1: Simulation parameters for the DJSTTCM scheme of Figure 4.1 employed for quantifying the results of Figure 4.3, Figure 4.4 and Figure 4.5.

As expected, the DJSTTCM scheme proposed benefits from the side-information gleaned from the second source, as documented by the BER curves of Figures 4.3, 4.4 and 4.5, when the coded sequences $\{c_1\}$ are mapped to QPSK, 8PSK and 16QAM signals, respectively, for transmission over uncorrelated Rayleigh fading channels. In this section the coded sequence $\{c_1\}$ shown in Figure 4.1 will exhibit no puncturing, since we first aim for investigating our scheme's as a function of the side-information. Observe in the three figures, that the BER performance improves upon

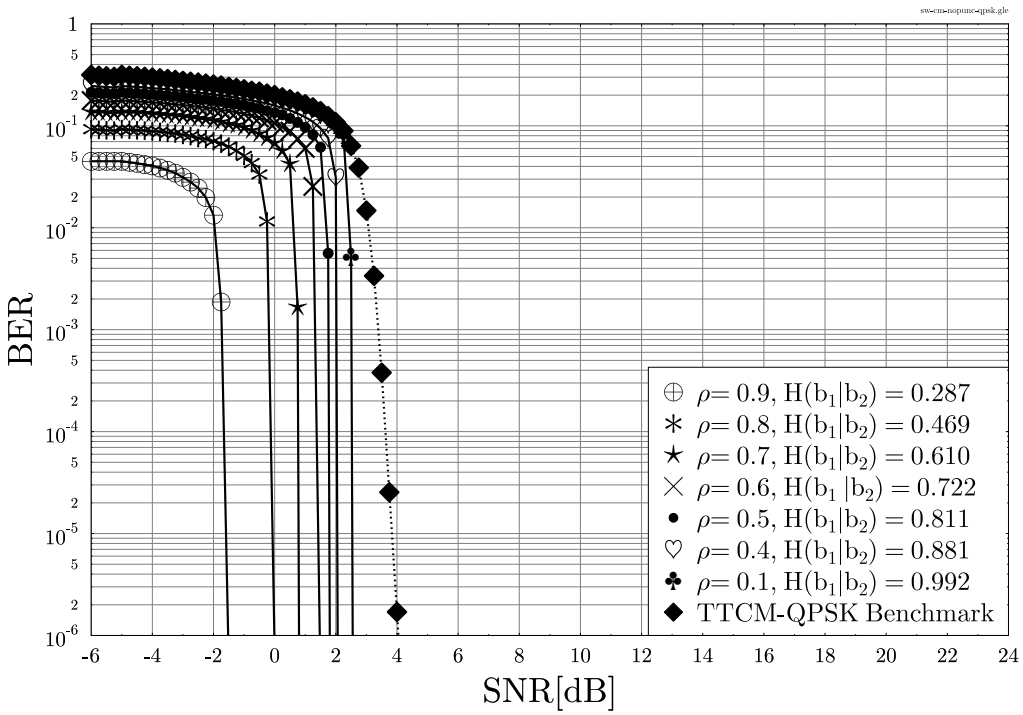

Figure 4.3: BER versus SNR performance of the proposed **DJSTTCM-QPSK** scheme of Figure 4.1 for correlation coefficients of $\rho = \{0.9, 0.8, 0.7, 0.6, 0.5, 0.4, 0.1\}$ when transmitting over **uncorrelated Rayleigh fading channels**. The number of decoding iterations between the pair of TCM MAP Decoders of Figure 4.2 is $I = 8$, while the simulation parameters are shown in Table 4.1 and the related results are summarised in Table 4.2.

increasing the correlation coefficient ρ[3], where the corresponding simulation parameters are listed in Table 4.1.

More explicitly, our proposed QPSK based DJSTTCM scheme has a significant gain of 5.6 dB over its counterpart -relying on separate-rather than joint processing at a BER level of 10^{-5} at correlation coefficient of value $\rho = 0.9$ associated with the BSC cross-over probability of $pe = 0.05$. However, for a low correlation of $\rho = 0.1$ only a marginal gain of 1.3 dB can be attained over the above-mentioned benchmark at a similar BER level of 10^{-5}. This is not unexpected, since the sources $\{b_1\}$ and $\{b_2\}$ are only loosely correlated. Similar trends can be observed for the BER curves corresponding to the DJSTTCM-8PSK and DJSTTCM-16QAM based schemes of Figure 4.4 and Figure 4.5, respectively. Thus, our proposed joint processing-aided scheme exhibits a beneficial correlation exploitation capability, where the achievable gains are summarised in Table 4.2 with SNR(10^{-5}) representing the SNR required for approaching a BER level of 10^{-5}.

4.3 Rate Region Design and Analysis

Having characterised our joint processing-aided scheme, let us now discuss the achievable rate of the proposed system. The following two sections will examine our scheme against the SW/S bound

[3]The higher the cross-over probability p_e, the lower the correlation between the two sources as $\rho = 1 - 2p_e$.

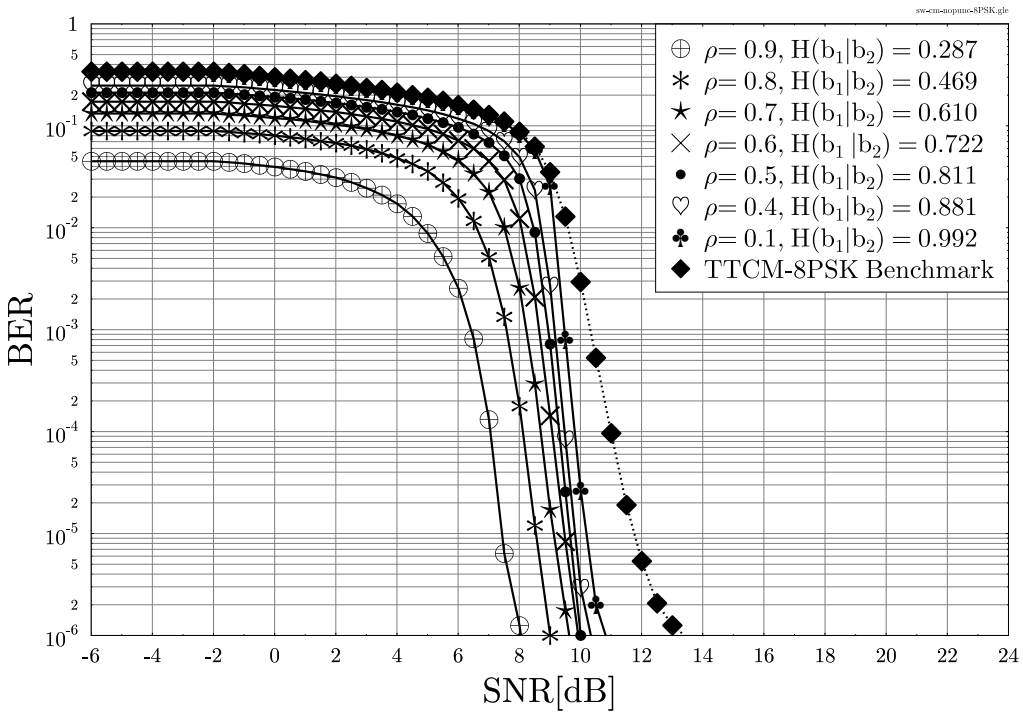

Figure 4.4: BER versus SNR performance of the proposed **DJSTTCM-8PSK** scheme of Figure 4.1 for correlation coefficients of $\rho = \{0.9, 0.8, 0.7, 0.6, 0.5, 0.4, 0.1\}$ when transmitting over **uncorrelated Rayleigh fading channels**. The number of decoding iterations between the pair of TCM MAP decoders of Figure 4.2 is $I = 8$, while the simulation parameters are shown in Table 4.1 and the related results are summarised in Table 4.2.

as well as the achievable compression rate, when transmitting over both Rayleigh and Nakagami fading channels.

4.3.1 Slepian-Wolf/Shannon Bound for Rayleigh Fading Channels

In a noisy environment, the rate region bound defined in Equation (4.2) can be rewritten as [8, 37, 50, 11]:

$$\begin{aligned} H(b_1, b_2) &\leq \frac{C_1}{R_1} + \frac{C_2}{R_2} \\ &\leq \frac{1}{R_1}\mathrm{E}\left[\log_2(1+\gamma_1)\right] + \frac{1}{R_2}\mathrm{E}\left[\log_2(1+\gamma_2)\right] \ , \end{aligned} \tag{4.10}$$

where $C_1 = \mathrm{E}\left[\log_2(1+\gamma_1)\right]$ and $C_2 = \mathrm{E}\left[\log_2(1+\gamma_2)\right]$ denote the ergodic channel capacities between each of the sources and the destination, while γ_1 and γ_2 denote the corresponding received SNRs. In our system relying on perfect side-information we assume that $\{b_2\}$ is transmitted at $R_2 = H(b_2) = 1$, while we aim for compressing $\{b_1\}$ to its minimum rate, namely to $R_1 = H(b_1|b_2)$. Then, based on Equation (4.10), the effective throughput of our scheme for the $\{b_1\}$ link can be expressed as $\eta_{SW} = R_1 \cdot H(b_1|b_2)$, while the SW/S bound is calculated as [43]:

$$R_1 \cdot H(b_1|b_2) \leq C_1 \ , \tag{4.11}$$

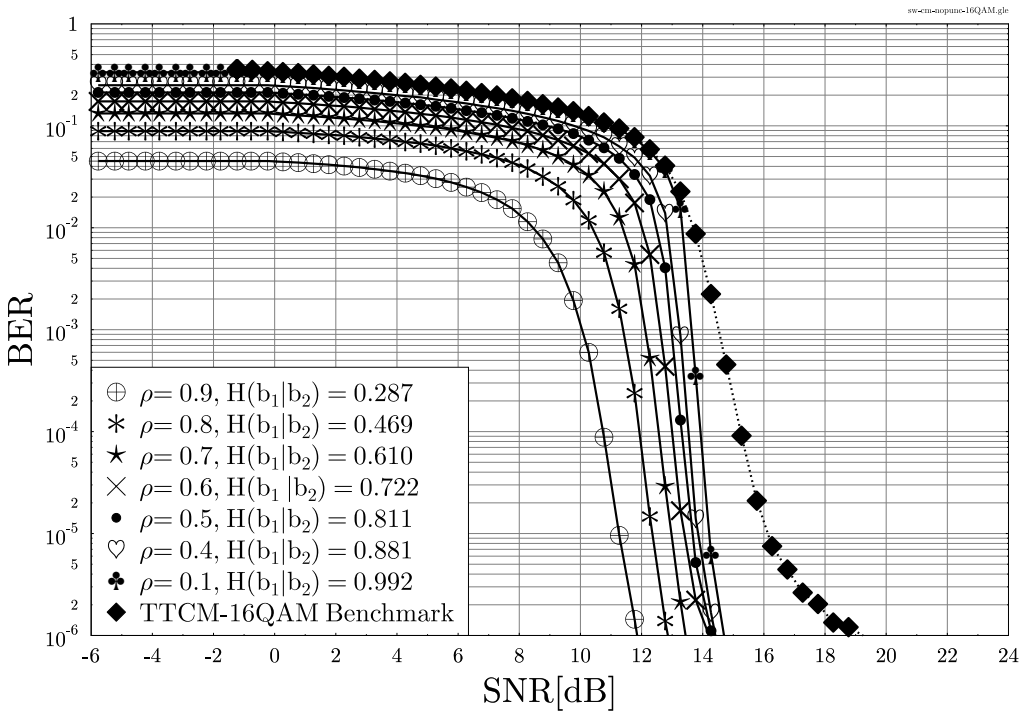

Figure 4.5: BER versus SNR performance of the proposed **DJSTTCM-16QAM** scheme of Figure 4.1 for correlation coefficients of $\rho = \{0.9, 0.8, 0.7, 0.6, 0.5, 0.4, 0.1\}$ when transmitting over **uncorrelated Rayleigh fading channels**. The number of decoding iterations between the pair of TCM MAP decoders of Figure 4.2 is $I = 8$, while the simulation parameters are shown in Table 4.1 and the related results are summarised in Table 4.2.

where C_1 represents the ergodic capacity of the uncorrelated Rayleigh fading channel.

First we characterise the BER performance of our DJSTTCM-QPSK/BPSK scheme employing a range of correlation coefficients $\rho = \{0.93, 0.9, 0.8, 0.7, 0.6\}$. We opted for using 1/2-rate TTCM for encoding a block of $N_S = 12\,000$ symbols, resulting in $N_b = 24\,000$ bits before we remove all of the systematic bits from the TTCM coded sequence with the aid of puncturing. The BER versus SNR performance of the proposed system is illustrated in Figure 4.6. Identically to the example of Section 4.2.1, the effective throughput in the QPSK/BPSK scenario is $\eta = 1$, hence we have SNR $= E_b/N_0$.

The minimum SNR, Γ_{lim}, required for approaching the SW/S bound can be inferred from Figure 4.8, which shows both the Continuous-input Continuous-output Memoryless Channels (CCMC) capacity and the corresponding BPSK based Discrete-input Continuous-output Memoryless Channel's (DCMC) capacity curves. For example, when aiming for a target throughput of $\eta_{SW} = 0.469$ BPS for our DJSTTCM-QPSK/BPSK scheme, the DCMC curve indicates requiring an minimum SNR of $\Gamma_{\text{lim}} = -1.75$ dB, as illustrated in Figure 4.8. Note that Γ_{lim} is represented with the aid of vertical lines in Figure 4.6, while again $\eta_{SW} = R_1 \cdot H(b_1|b_2)$.

As expected, the proposed scheme benefits from the availability of perfect side-information constituted by $\{b_2\}$, while compressing the source sequence $\{b_1\}$. Note in Figure 4.6 that all distributed schemes outperform the conventional TTCM-QPSK benchmark scheme dispensing with

Scheme	p_e	ρ	SNR(10^{-5})	**Gain** (dB)
DJSTTCM-QPSK	0.05	0.90	-1.8	5.6
	0.10	0.80	-0.1	3.9
	0.15	0.70	0.75	3.05
	0.20	0.60	1.5	2.3
	0.25	0.50	1.75	2.05
	0.30	0.40	2.0	1.8
	0.45	0.10	2.5	1.3
DJSTTCM-8PSK	0.05	0.90	7.4	4.4
	0.10	0.80	8.5	3.3
	0.15	0.70	9.1	2.7
	0.20	0.60	9.5	2.3
	0.25	0.50	9.6	2.2
	0.30	0.40	9.7	2.1
	0.45	0.10	10.1	1.7
DJSTTCM-16QAM	0.05	0.90	11.3	4.8
	0.10	0.80	12.3	3.8
	0.15	0.70	13.0	3.1
	0.20	0.60	13.4	2.7
	0.25	0.50	13.6	2.5
	0.30	0.40	13.9	2.2
	0.45	0.10	14.3	1.8

Table 4.2: System performance of the DJSTTCM scheme of Figure 4.1, when the simulation parameters of Table 4.1 are used. The results are extracted from Figure 4.3, Figure 4.4 and Figure 4.5 and contrasted to the corresponding separate processing-based benchmark at BER$= 10^{-5}$, respectively.

joint decoding, which is labelled by the diamond markers, regardless of the correlation coefficient ρ, except for the very low correlation scenarios of $\rho = \{0.7, 0.6\}$. More explicitly, at a BER $= 10^{-5}$ the proposed DJSTTCM has an SNR gain of 7.1 dB, 5.75 dB and 2.75 dB for $\rho = 0.93$, $\rho = 0.9$ and $\rho = 0.8$, respectively. However, as expected, with low correlation values the proposed scheme has an SNR loss of 1.7 dB and 3.6 dB, namely when we have $\rho = 0.7$ and $\rho = 0.6$, respectively. Again, this is not unexpected, because for lower correlation cases the sources may be deemed to be uncorrelated and hence they in fact provide, mis-information, misleading the joint decoder. It may be readily observed from Figure 4.6 that at BER$= 10^{-5}$ the scheme having $\rho = 0.93$ has the minimum distance with respect to the SW/S limit, i.e. we have $\Gamma_{10^{-5}} - \Gamma_{\text{lim}} = (-3.5) - (-6.5) =$ 2.0 dB, while the scheme associated with $\rho = 0.6$ has a 4.25 dB distance from the limit.

The effect of the number of iterations I between the TCM decoders of Figure 4.2, on the overall DJSTTCM-QPSK/BPSK scheme's performance is illustrated by Figure 4.7. It can be observed that doubling the number of iterations from $I = 2$ to $I = 4$ will improve the scheme's performance by 1.5 dB, while doubling the complexity further will only enhance the system's performance by 0.5 dB. Furthermore, doubling the complexity beyond $I = 8$ would not provide any further gain, despite further increasing the decoding complexity. Hence we invoke $I = 8$ iterations in our decoder.

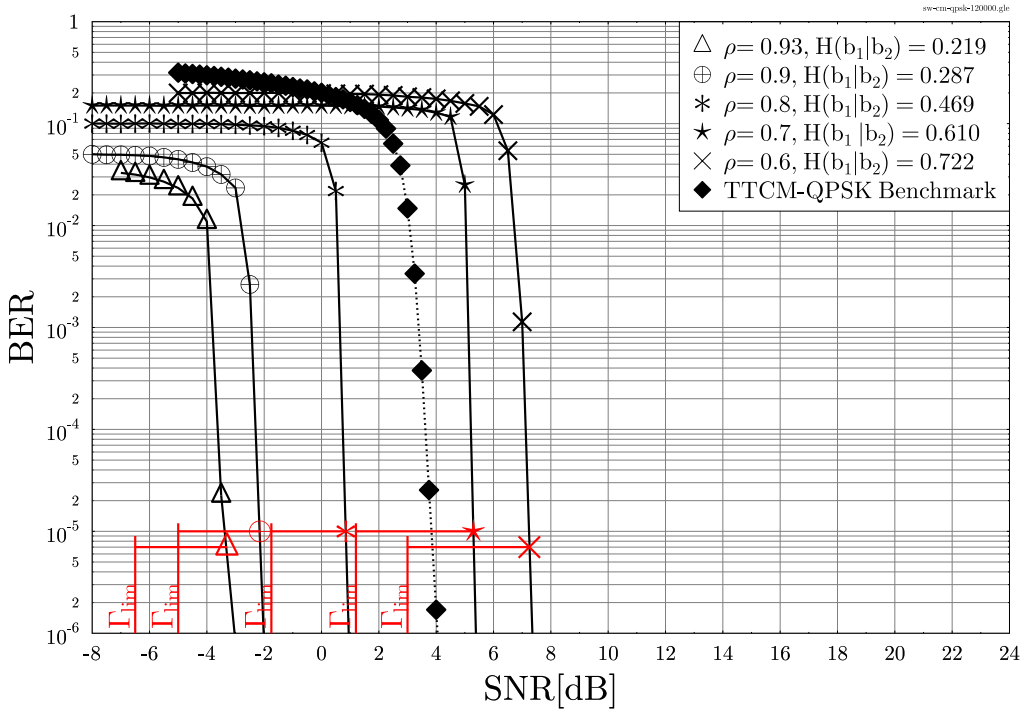

Figure 4.6: BER versus SNR performance of the proposed **DJSTTCM-QPSK/BPSK** scheme of Figure 4.1 for correlation coefficients of $\rho = \{0.93, 0.9, 0.8, 0.7, 0.6\}$ when transmitting over **uncorrelated Rayleigh fading channels**. Note that, we apply puncturing rate of $R_p = 2/1$, while the other simulation parameters are listed in Table 4.1 and the related results are summarised in Table 4.3.

p_e	ρ	η_{SW}	$\eta_{10^{-5}}$	**SW-Gap** (bits)	Γ_{lim}	$\Gamma_{10^{-5}}$	**Gap** (dB)
0.035	0.93	0.219	0.35	0.13	-6.5	-3.5	2.0
0.05	0.90	0.287	0.41	0.12	-5.0	-2.15	2.65
0.1	0.80	0.469	0.60	0.14	-1.75	0.85	2.6
0.15	0.70	0.610	0.80	0.19	1.2	5.3	4.1
0.2	0.60	0.722	0.85	0.13	3.0	7.25	4.25

Table 4.3: System performance of the proposed DJSTTCM-QPSK/BPSK scheme of Figure 4.1 when the puncturing rate is $R_p = 2/1$ and simulation parameters of Table 4.1 are used. The results are extracted from Figure 4.6 and Figure 4.9 when aiming for BER level of $= 10^{-5}$.

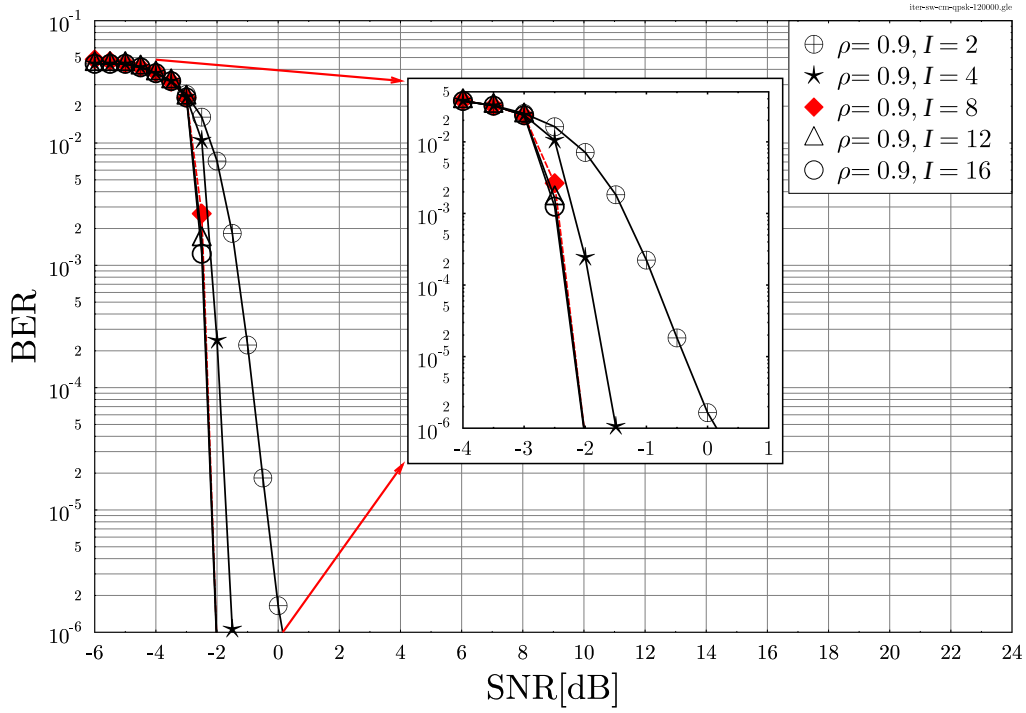

Figure 4.7: BER versus SNR performance of the proposed **DJSTTCM-QPSK/BPSK** scheme of Figure 4.1 for correlation coefficient of $\rho = \{0.9\}$ when transmitting over **uncorrelated Rayleigh fading channels**. The number of decoding **iterations** between the pair of TCM MAP decoders of Figure 4.2 are $I = \{2,\ 4,\ 8,\ 12,\ 16\}$, and we apply puncturing rate of $R_p = 2/1$, while the other simulation parameters are shown in Table 4.1.

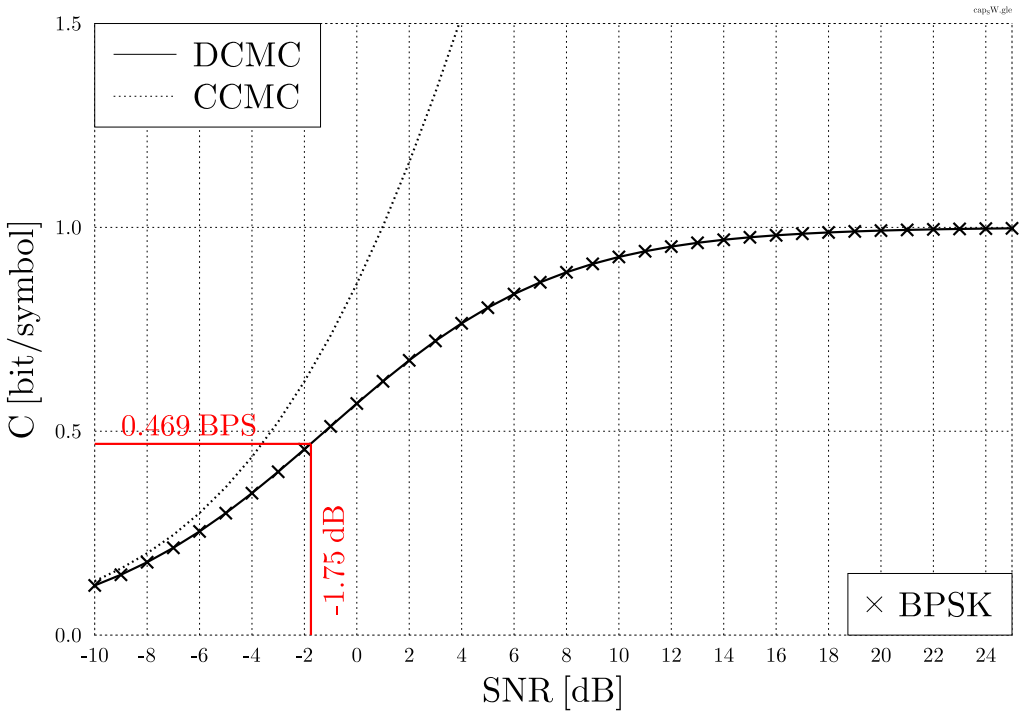

Figure 4.8: DCMC and CCMC capacity curves when transmitting BPSK symbols over **uncorrelated Rayleigh fading channels**, here the curves were computed based on [191].

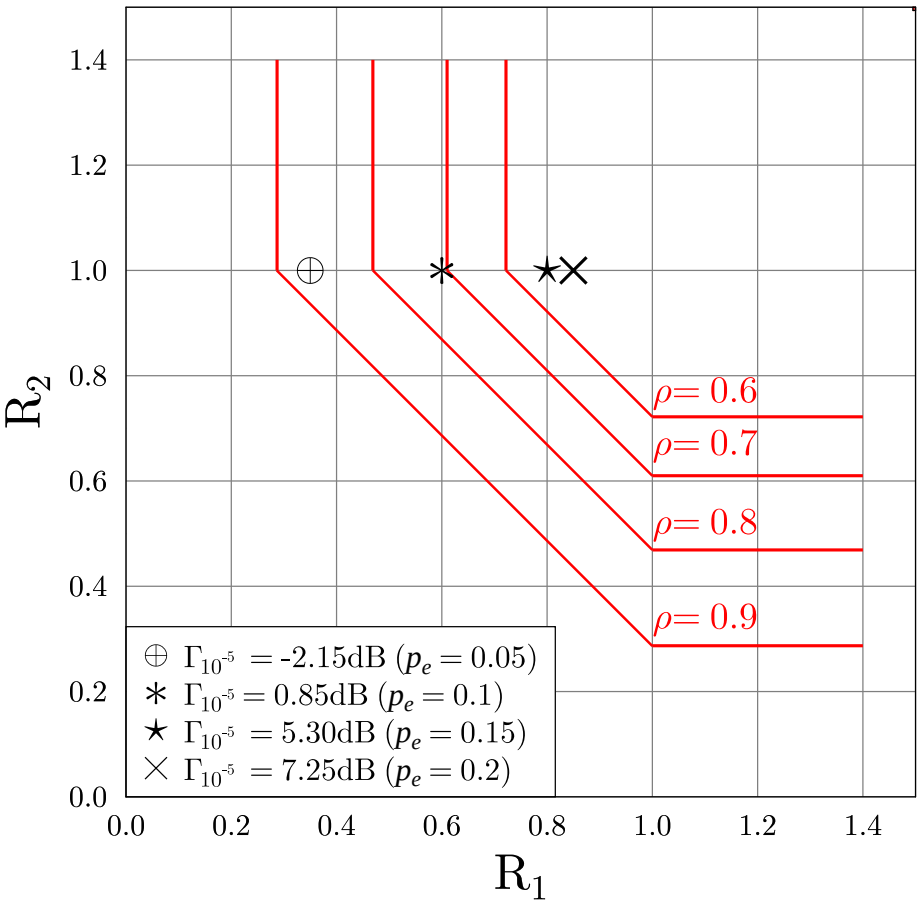

Figure 4.9: Theoretical SW bound as well the rates (R_1, R_2) achieved by the proposed **DJSTTCM-QPSK/BPSK** scheme of Figure 4.1 for different p_e values, where $\Gamma_{10^{-5}}$ denotes the SNR required for achieving a BER = 10^{-5}.

The SW theoretical bound and the achievable rates obtained for the proposed DJTTCM-QPSK/BPSK schemes are shown, respectively, in Figure 4.9. The rates achieved correspond to a BER of 10^{-5} and on average the system's throughput is only 0.14 bits away from the compression bound seen in Figure 4.6. Table 4.3 summarized the performance of the proposed scheme.

4.3.2 Slepian-Wolf/Shannon Bound for Nakagami Fading Channels

In this section we will investigate our scheme for transmission over Nakagami-m fading channels, since they are capable of characterising a wide range propagation scenarios, including both Rayleigh and Rician fading transmissions [201, 202]. Similarly, the received signal y_1 can be obtained using Equation (4.4), while the channel's fading coefficient $h = r\exp(j\theta)$ is complex-based and i.i.d, where the phase θ is uniformly distributed and independent of the envelope r. The envelope r follows a wide range of realistic Nakagami-m distributions obeying the Probability Density

Coded Modulation	**TTCM**
Modulation Scheme	BPSK
Code Rate	$R_{cm} = 1/2$
Puncturing Rate	$R_p = 2/1$
Effective Throughput	$\eta = 1$ BPS
Decoding Algorithm	Approximated Log-MAP
Mapper Type	Set-Partitioned
Decoding Iteration	$I = 8$
Number of Symbol	$N_s = 12\,000$ symbols per frame
Number of Frames	1000
Channel	Nakagami-m fading channel
Fading parameter	$m = \{1.0, 2.0, 4.0, 6.0\}$
Channel State Information (CSI)	Known
MUD Type	ML

Table 4.4: Simulation parameters for the DJSTTCM-QPSK/BPSK scheme of the schematic of Figure 4.1 when considering Nakagami-m fading channels in the Figure 4.11 and Figure 4.12.

Function (PDF) of [203]:

$$p(r) = \frac{2}{\Gamma(m)} \left(\frac{m}{\Omega_r}\right) \gamma_r^{2m-1} \exp\left(\frac{-mr^2}{\Omega_r}\right) , \tag{4.12}$$

where $\Gamma(\cdot)$ denotes the Gamma function, while $\Omega_r \triangleq \mathrm{E}\left[r^2\right]$ is the average received power and m represents the fading parameter defined as $m \triangleq \mathrm{E}\left[\left(r^2 - \Omega_r\right)^2\right]$, where $m \geqslant 0.5$.

The parameter m characterising the fading depth, which is reduced upon increasing m [201, 203]. For example, when m is equal to its minimum value of $m = 0.5$, Equation (4.12) will represent a single-sided Gaussian distribution. By contrast, the Nakagami PDF approaches a Rayleigh fading distribution for $m = 1$, and when we have $m \to \infty$, the channel becomes an AWGN channel. Hence, the Nakagami-m distribution may be considered to be a generalised distribution that characterises diverse propagation scenarios [203, 204]. Furthermore, the Nakagami-m distribution can be conveniently analysed using both numerical and analytical approaches [203, 204].

Following the rate region analysis of Section 4.3.1, we first have to quantify the DCMC capacity for our Nakagami-m channel. More explicitly, the CCMC capacity of Nakagami-m fading channel is given by:

$$C_{\mathrm{CCMC}}^{\mathrm{Nak}} = \mathrm{E}\left[\log_2(1 + r\gamma_1)\right] , \tag{4.13}$$

where the received SNR γ_1 of the Gaussian channel is weighted by the Nakgami-m channel's

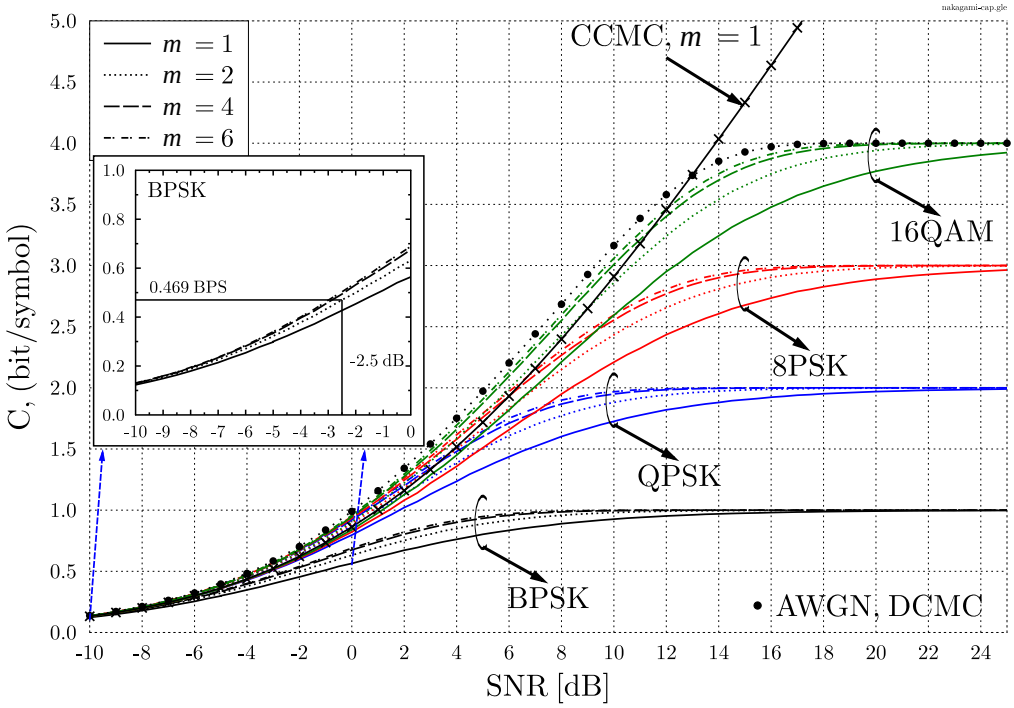

Figure 4.10: DCMC capacity curves of **Nakagami-m fading channels** for BPSK, QPSK, 8PSK and 16QAM having $m = \{1.0, 2.0, 4.0, 6.0\}$. Note that CCMC capacity when $m = 1$ as well as AWGN DCMC capacity for 16QAM were included for the sake of comparison, where the curves were computed following the procedure of [191].

envelope r, which obeys the PDF of Equation (4.12). The resultant capacity has to be averaged by either summation or integration over the specific range of SNRs encountered. The CCMC capacity, as the terminology suggested, assumes a continuous-amplitude optimally-distributed signal input, where the capacity is only limited by the transmit energy and by the bandwidth [191,202]. However, the DCMC capacity considers both the effects of having discrete inputs as well as the specifics realistic non-Gaussian distributed transmit signals of practical modulation scheme [191]. Thus, it is more appropriate for our joint design, where the DCMC capacity of a single link capacity can be expressed as follows [205,206]:

$$C_{\text{DCMC}}^{\text{Nak}} = \max_{p(\mathbf{x}_1 \cdots \mathbf{x}_M)} \sum_{j=1}^{M} \int_{-\infty}^{\infty} \cdots \int_{-\infty}^{\infty} p(\mathbf{y} \mid \mathbf{x}_j) p(\mathbf{x}_j) \cdot \log_2 \left[\frac{p(\mathbf{y} \mid \mathbf{x}_j)}{p(\mathbf{y})} \right] d\mathbf{y} \quad \text{[bit/sym]}\,, \tag{4.14}$$

where again, the channel's input $\mathbf{x}_m = \{x_j^1, x_j^2, \cdots, x_j^N\}$ is constituted by M-ary symbols with N-dimensional size where $x_j \in \{1, 2, \ldots, M\}$ and $\mathbf{y} = \{y^1, y^2, \cdots, y^N\}$ is the received signal with N-dimensional size. The conditional probability $p(\mathbf{y} \mid \mathbf{x}_j)$ can be determined using the PDF of the Nakagmi-m channel in Equation (4.12). Furthermore, Equation (4.14) can be be simplified

to [191, 202]:

$$C_{\text{DCMC}}^{\text{Nak}} = \log_2(M) - \frac{1}{M}\sum_{j=1}^{M} \text{E}\left[\log_2 \sum_{i=1}^{M} \exp(\Psi_i^j)\right] \quad \text{[bit/sym]}\,, \tag{4.15}$$

where we have:

$$\Psi_i^j = \frac{-\left|\mathbf{y} - \mathbf{h}\cdot\mathbf{x}_m + \mathbf{n}\right|^2 + \left|\mathbf{n}\right|^2}{N_0}\,. \tag{4.16}$$

The DCMC capacity curves of our four different modulation modes namely of, BPSK, QPSK, 8PSK and 16QAM, associated with different Nakagami-m fading parameters are depicted in Figure 4.10. As m increases, the achievable capacity of the Nakagami-m channel increase. For example, when we consider the case of 16QAM in Figure 4.10, as the fading parameter increases from $m = 1$ to $m = 4$, the capacity approaches that of the AWGN channel. It is also shown in Figure 4.10 that increasing the fading parameter from $m = 1$ to $m = 2$ significantly improves the achievable capacity. However, the improvements will become more marginal for $m > 3$.

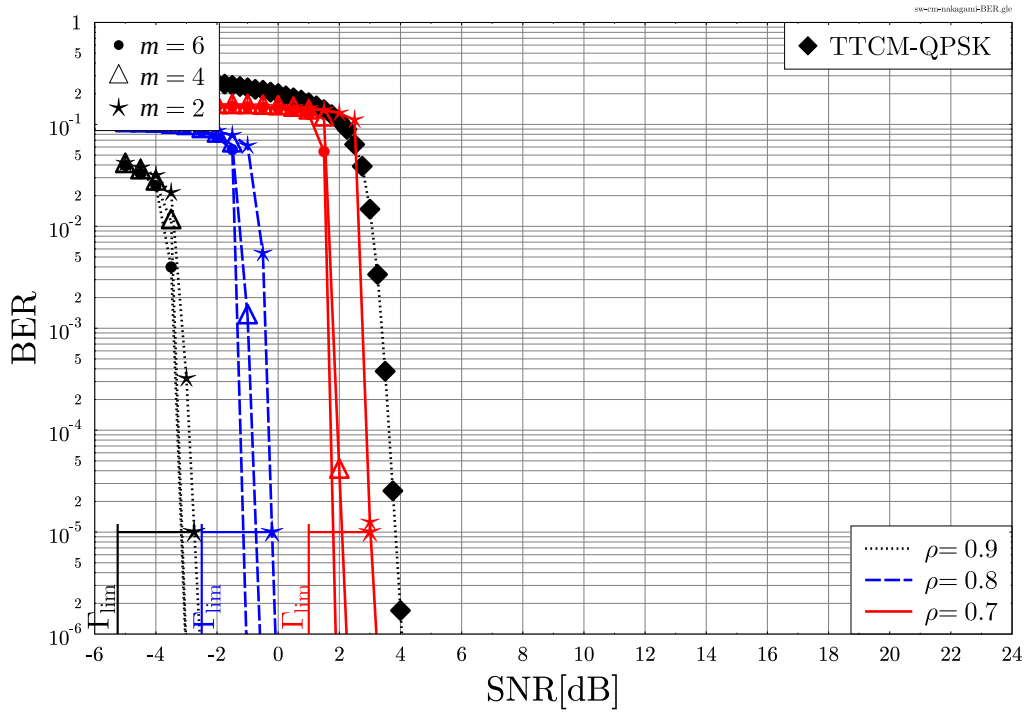

Figure 4.11: BER versus SNR performance comparison of **DJSTTCM-QPSK/BPSK** scheme when transmitting over **Nakagami-m fading channels** with different $m = \{2.0, 4.0, 6.0\}$ where the correlation coefficients are $\rho = \{0.9, 0.8, 0.7\}$. The simulation parameters are listed in Table 4.4, while the associated results are summarised in Table 4.5.

Similar to the analysis adopted in Section 4.3.1, we commence by characterising the BER performance of the lowest-throughput DJSTTCM scheme, where the QPSK/BPSK mode is employed. Figure 4.11 illustrates the BER performance of our scheme for a range of correlations

$\rho = \{0.9, 0.8, 0.7\}$ and for the fading parameters of $m = \{2.0, 4.0, 6.0\}$, respectively. Here we employ a half-rate TTCM code associated with $N_S = 12\,000$ symbols in each of the encoding blocks in conjunction with $I = 8$ decoding iterations. As shown in Figure 4.11, all the proposed DJSTTCM schemes outperform the classical TTCM-aided QPSK benchmark scheme, which is labelled by the filled diamonds, while dispensing with side-information availability. To elaborate further, at a BER of 10^{-5} and $\rho = 0.8$, our distributed scheme is capable of attaining coding gains of 3.8 dB, 4.35 dB and 4.65 dB for $m = 2$, $m = 4$ and $m = 6$, respectively. Additionally, the proposed system associated with $\rho = 0.9$ and $\rho = 0.7$ exhibits a similar trend, as shown in Figure 4.11. The impact of different m values on the attainable BER performance can be also seen in Figure 4.11, where as expected from the DCMC curves of Figure 4.10, when m decreases, the BER performance will be degraded, since the fading becomes more severe.

m	p_e	ρ	η_{SW}	$\eta_{10^{-5}}$	**SW gap**[bits]	Γ_{lim}	$\Gamma_{10^{-5}}$	**SW/S gap**[dB]
2	0.05	0.90	0.287	0.45	0.16	-5.25	-2.75	2.5
	0.10	0.80	0.469	0.61	0.14	-2.5	-0.20	2.3
	0.15	0.70	0.610	0.80	0.19	0.0	3.0	3.0
4	0.05	0.90	0.287	0.42	0.13	-5.6	-3.25	2.35
	0.10	0.80	0.469	0.60	0.13	-2.7	-0.75	1.95
	0.15	0.70	0.610	0.80	0.19	-0.5	2.1	2.6
6	0.05	0.90	0.287	0.42	0.13	-5.75	-3.25	2.5
	0.10	0.80	0.469	0.57	0.10	-2.8	-1.05	1.75
	0.15	0.70	0.610	0.75	0.14	-0.4	1.75	2.15

Table 4.5: System performance of the DJSTTCM-QPSK/BPSK scheme of Figure 4.1 when communicating over Nakagami-m fading channel, where the simulation parameters of Table 4.4 are used. The results are extracted from Figure 4.11 and Figure 4.12 for targeted-integrity of BER level of $= 10^{-5}$.

The minimum required SNR Γ_{lim} can be inferred from Figure 4.10. For example, when aiming for a target throughput of $\eta_{SW} = 0.469$ BPS for the DJSTTCM-QPSK/BPSK scheme associated with $m = 2$ and $\rho = 0.8$, the DCMC curve of Figure 4.10 indicates a minimum SNR of $\Gamma_{\text{lim}} = -2.5$ dB. Note that Γ_{lim} recorded for the fading parameter of $m = 2$ is shown with the aid of the vertical lines seen in Figure 4.11. Furthermore, both the SW theoretical bound and the achievable rates obtained for the DJSTTCM-QPSK/BPSK schemes considered are presented in Figure 4.12. These rates correspond to a BER level of 10^{-5} and on average the system's throughput is only 0.145 bits away from the SW bound. Note that the effective SW throughput namely $\eta_{10^{-5}}$ is obtained by reversing the procedure of estimating Γ_{lim}, i.e. by substituting back the $\Gamma_{10^{-5}}$ value into the DCMC curves of Figure 4.10[4]. The DJSTTCM-QPSK/BPSK performance against

[4]For example, an SNR of $\Gamma_{10^{-5}} = -0.2$ dB is needed by our scheme as shown in BER curve associated with $m = 2$ and $\rho = 0.8$, which is labelled with blue star, of Figure 4.11. The value $\Gamma_{10^{-5}} = -0.2$ dB will be inferred back into the corresponding DCMC curve of Figure 4.10, resulting into $\eta_{10^{-5}} = 0.61$ BPS.

the SW(bits) bound as well as against the SW/S(dB) limit are tabulated in Table. 4.5 for different Nakagami-m fading values.

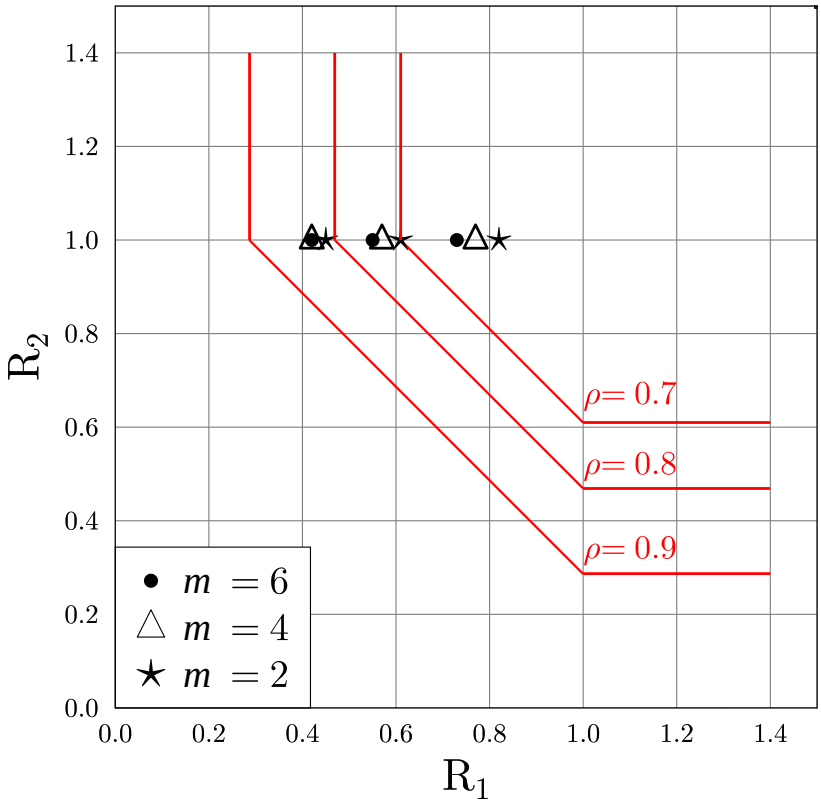

Figure 4.12: Theoretical SW bound as well the rates (R_1, R_2) achieved by the proposed **DJSTTCM-QPSK/BPSK** scheme of Figure 4.1 when communicating over Nakagami-m fading channel for different p_e and m values, where each point was recorded corresponding to the SNR required for achieving a BER = 10^{-5}.

4.4 Performance Results

In Sections 4.3.1 and 4.3.2 we have contrasted our joint scheme against the SW/S bound, when using the lowest modulation order of QPSK/BPSK for transmission over Rayleigh and Nakagami-m fading channels, respectively. In, the following sections, we will investigate the performance of our scheme when invoking higher-order modulation schemes, followed by out near-instantaneously adaptive system.

4.4.1 Rate-Adaptive Scheme for Rayleigh Fading Channel

As stated in Section 4.2.2, adaptive coded modulation schemes are required for counteracting both the near-instantaneous time-varying nature of the wireless channel as well as the time-variant corre-

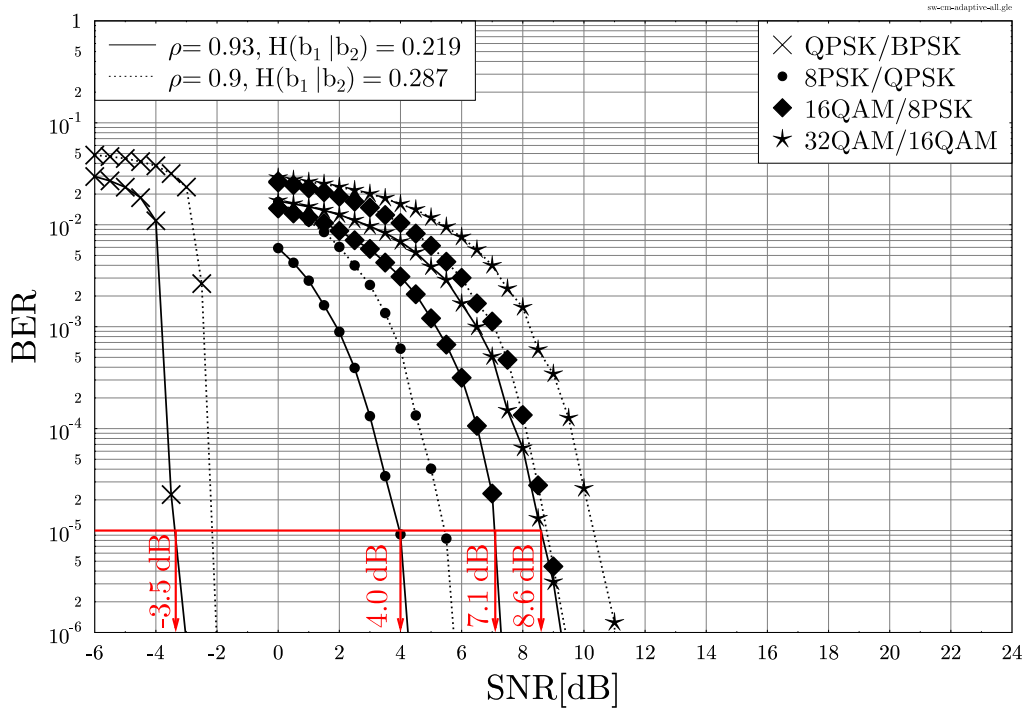

Figure 4.13: BER versus SNR performance of the proposed **DJSTTCM** scheme of Figure 4.1 using different modes, for $\rho = 0.93$ and $\rho = 0.9$ for transmission over **uncorrelated Rayleigh fading channels**.

lations between the two sources [200]. Thus, our proposed design has also been extended to higher-order modulation modes in order to conceive an adaptive scheme. Figure 4.13 shows the BER performance of the different DJSTTCM modes for $\rho = 0.93$ and $\rho = 0.9$ associated with cross-over probabilities of $p_e = 0.035$ and $p_e = 0.05$, respectively, while using a block length of $N_S = 12\,000$ symbols for all the modulation modes. A total of 1000 blocks have been used in our simulations. The performance of the higher-order modulation schemes seen in Figure 4.13 suggests that the A-DJSTTCM is readily applicable to our DJSC problem. In each mode we puncture the least significant bit of each coded symbol, which results in puncturing rates of $R_p = \{2/1,\ 3/2,\ 4/3,\ 5/4\}$ for QPSK/BPSK, 8PSK/QPSK, 16QAM/8PSK and 32QAM/16QAM, respectively. Observe by comparing Figure 4.6 and Figure 4.13 that as expected, the "QPSK/BPSK" scheme outperforms its counterparts in terms of its BER performance, since it has a lower throughput. The flow-chart of Figure 4.14 illustrates the adaptation process, where the current frame, namely F_i, will be transmitted first using the highest-order 32QAM/16QAM modulation mode. Furthermore, the cross-over probability p_e which controls the correlation coefficient of $\rho = 1 - 2p_e$ is assumed to be perfectly known at the receiver[5], although it can be estimated using [11]:

$$\hat{p}_e = \frac{1}{N}\sum_{k=1}^{N} \Pr(b_1 = +1)\Pr(b_2 = -1) + \Pr(b_1 = -1)\Pr(b_2 = +1)\,. \tag{4.17}$$

[5]Section 5.6 proposes a novel way for estimating the cross-over probability p_e, at the receiver.

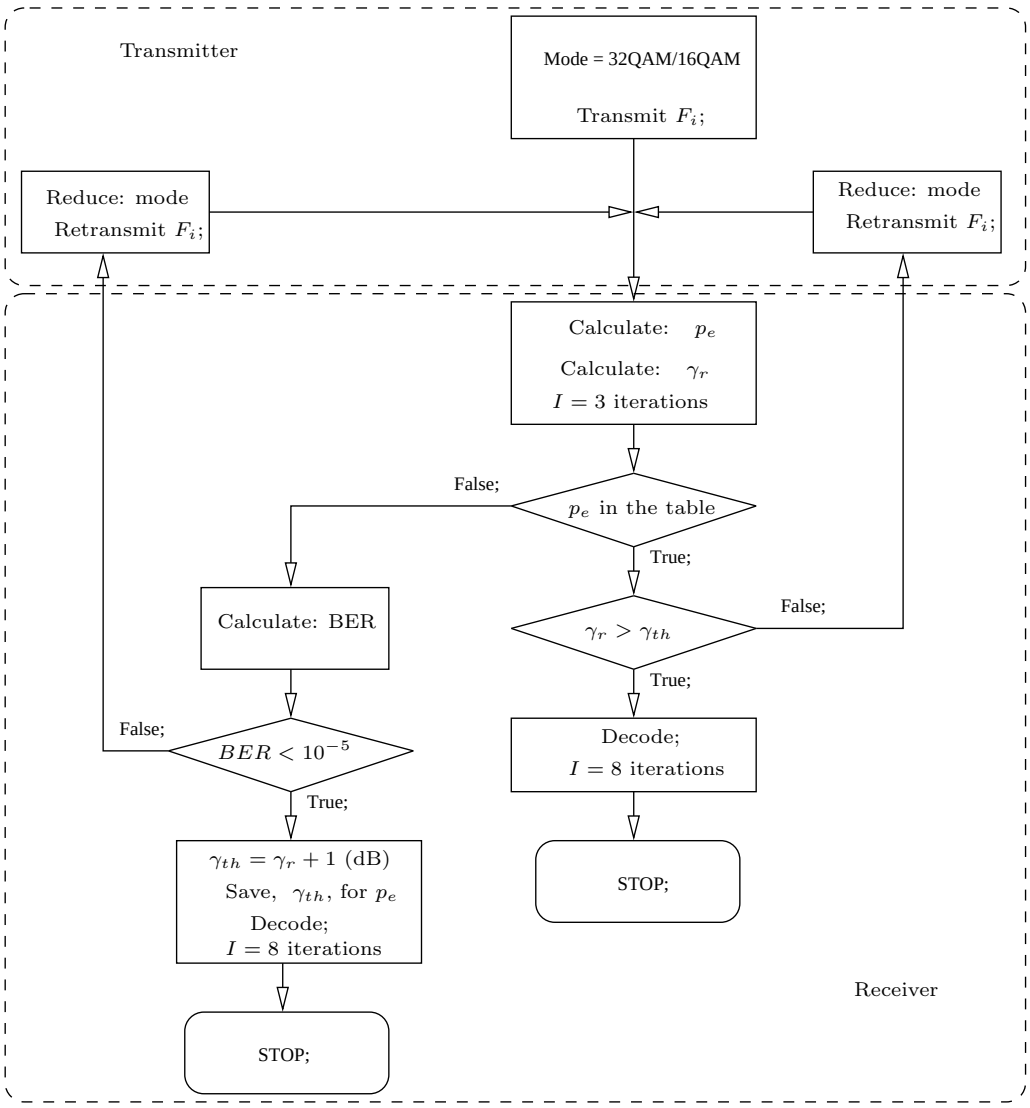

Figure 4.14: The flow-chart of the Adaptive mechanism invoked in the DJSTTCM scheme of Figure 4.1.

Next, the near-instantaneous received SNR γ_r is calculated using the following equation:

$$\gamma_r = 10\log_{10}\left(|h|^2/N_0\right)\,[\text{dB}]\,. \tag{4.18}$$

Then the decoder will compare the probability p_e to the pre-stored look-up table. The aim of this table is to reduce the overall complexity of the adaptation process. As shown in the flow-chart, if p_e is not found in the table, the decoder will estimate the BER of the received block, where the BER is estimated after decoding by comparing the source sequence bits $\{b_1\}$ with the decoded bits $\{\hat{b}_1\}$. Provided that the estimated BER is below 10^{-5}, the corresponding received SNR, γ_r, which are indicated by the vertical arrows of Figure 4.13 will be saved in the look-up table as the threshold of $\gamma_{th} = \gamma_r + 1$ (dB). Note that, the additional one dB as well as the 3 iterations used will reassure that the performance of the adaptive scheme will remain below a BER of 10^{-5}. However, when we have BER $< 10^{-5}$ or $\gamma_r < \gamma_{th}$, a feedback acknowledgement will be transmitted to the transmitter

which triggers a reduction of the transmission mode index/throughput. Thus our adaptive mode selection regime relies on using a set of switching SNR threshold values, $[\{\gamma_1, \gamma_2, \gamma_3, \gamma_4\}]$, that are obtained based on target BER level [200]. To elaborate further, with the aid of Figure 4.14 our adaptive selection method can be outlined as:

- No transmission (No TX): 0 BPS, if $\gamma_r \leqslant \gamma_1$,
- DJSTTCM-QPSK/BPSK: 1 BPS, if $\gamma_1 < \gamma_r \leqslant \gamma_2$,
- DJSTTCM-8PSK/QPSK: 2 BPS, if $\gamma_2 < \gamma_r \leqslant \gamma_3$,
- DJSTTCM-16QAM/8PSK: 3 BPS, if $\gamma_3 < \gamma_r \leqslant \gamma_4$,
- DJSTTCM-32QAM/16QAM: 4 BPS, if $\gamma_4 < \gamma_r \leqslant \gamma_5$.

We opt to start with a higher-rate mode in order to reduce the number of feedback requests[6]. Hence, the overall complexity and time required for performing this adaptive rate-adjustment process has been reduced. Furthermore, the Mode of Selection Probability (MSP) of each DJSTTCM mode versus the average SNR is shown in Figure 4.15 along with the related BPS curves recorded for different correlation of $\rho = \{0.9, 0.8, 0.7, 0.6\}$, respectively. Naturally, the choice of the specific DJSTTCM modes is governed by the particular near-instantaneous SNR experienced by the individual transmission frames at any specific average SNR value of Figure 4.15. The adaptive scheme maintains BER target of $< 10^{-5}$. It can be seen from Figure 4.15 that as the SNR increases, the higher-order DJSTTCM modes are activated more often than the lower-rate ones. Consequently, the effective BPS throughput increases smoothly upon increasing the SNR. It may also be observed from the figure that in the presence of a high correlation between the two sources, such as $\rho = 0.9$, the no transmission "No Tx" mode has effectively "disappeared". By contrast, for low correlations the scheme requires a higher SNR for achieving a non-zero effective throughput.

4.4.2 Rate-Adaptive Scheme for Nakagami Fading Channel

In line with Section 4.4.1, we shall first examine the BER performance of the higher-order modulation modes, before conceiving our near-instantaneously adaptive scheme for transmission over Nakagami-m fading channels. The performance of DJSTTCM schemes employing the 8PSK/QPSK, 16QAM/8PSK and 32QAM/16QAM modes, for $\rho = \{0.9, 0.8, 0.7\}$ is shown in Figure 4.16, when communicating over Nakagami-m fading channels associated with $m = 4$. Again, a block length of $N_S = 12\,000$ symbols is used for all the modulation modes invoked for a total of 1000 blocks, while the number of decoding iterations is $I = 8$. The performance of the higher-order modulation schemes simulated in Figure 4.16 exhibits no error floor hence suggesting that the A-DJSTTCM is readily applicable to SW coding in wireless applications. Similarly, the least significant bit of each TTCM coded symbol will be punctured, hence resulting in puncturing rates of

[6] An incremental mode-based adaptive scheme can also be implemented subject to additional considerations.

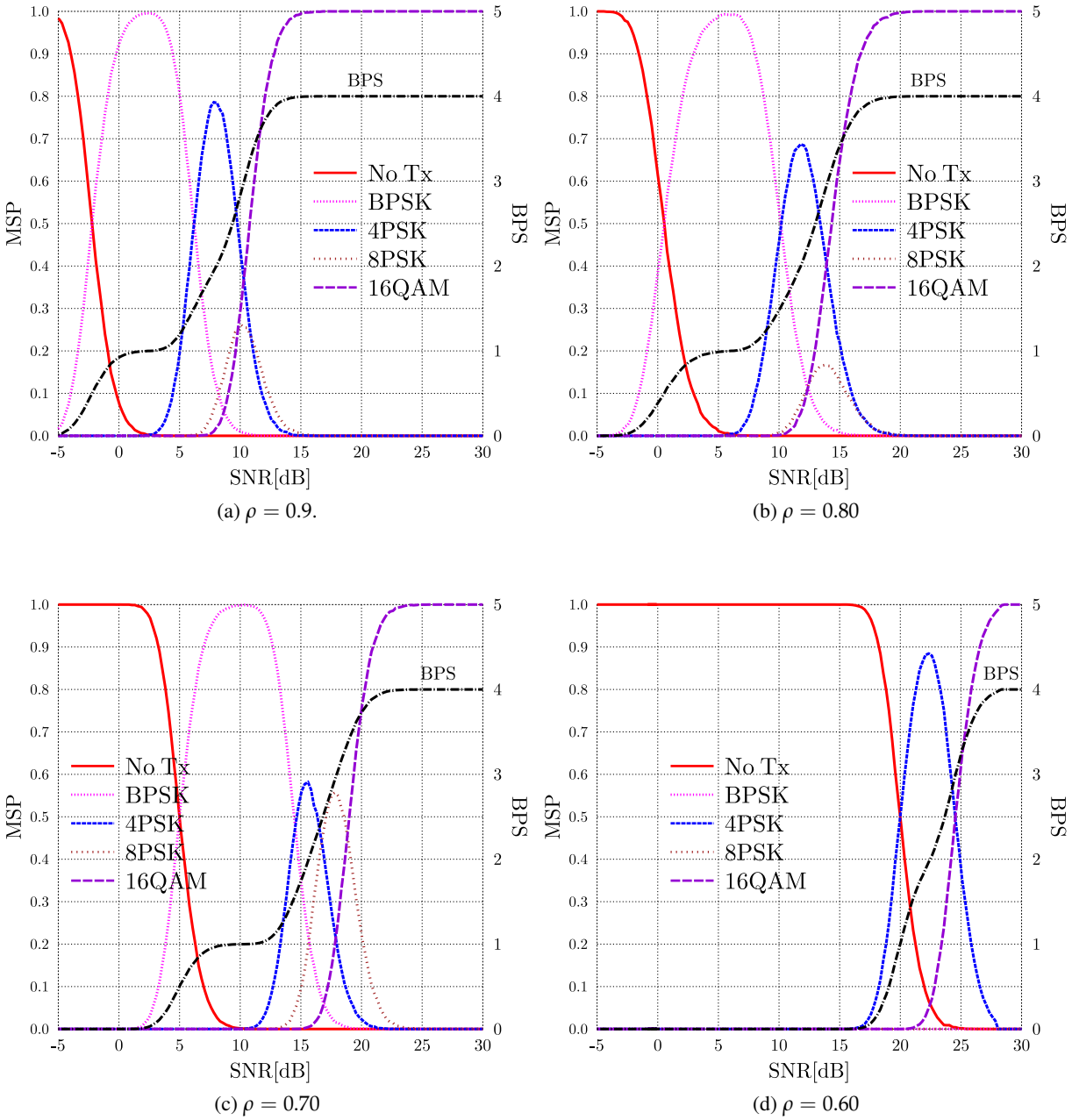

(a) $\rho = 0.9$. (b) $\rho = 0.80$

(c) $\rho = 0.70$ (d) $\rho = 0.60$

Figure 4.15: MSP of all **DJSTTCM** modes (left hand vertical axis) versus the SNR values and the corresponding BPS (right hand vertical axis) for $\rho = \{0.9, 0.8, 0.7, 0.6\}$, when communicating over a **uncorrelated Rayleigh fading channels**. The adaptive mechanism can be illustrated in the flow-chart of Figure 4.14.

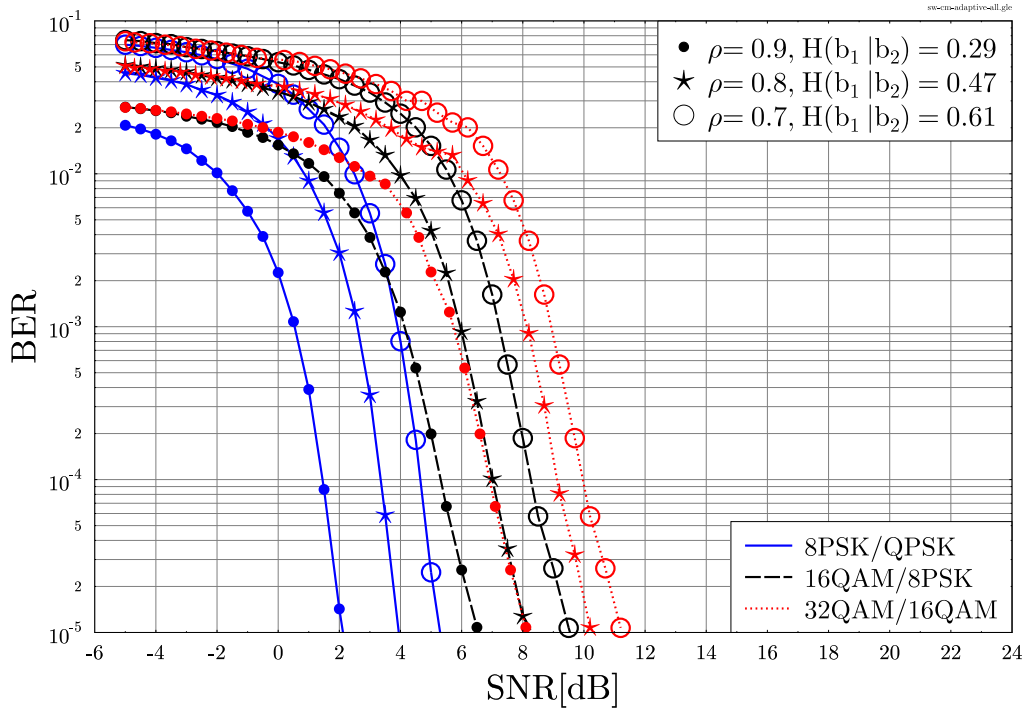

Figure 4.16: BER versus SNR performance of the proposed **DJSTTCM** scheme of Figure 4.1 using different modes, for correlation coefficients of $\rho = \{0.9, 0.8, 0.7\}$ when transmitting over **Nakagami-m fading channels** with $m = 4$.

$R_p = \{3/2,\ 4/3,\ 5/4\}$ for "8PSK/QPSK", "16QAM/8PSK" and "32QAM/16QAM", respectively. It can be observed in Figure 4.16 that the "8PSK/QPSK" scheme outperforms its counterparts using higher order modulation schemes. More explicitly, at a BER level of 10^{-5} and $\rho = 0.9$, the "8PSK/QPSK" scheme has an SNR gain of 4.2 dB and of 6 dB in comparison to the "16QAM/8PSK" and "32QAM/16QAM" schemes, respectively. However, the "32QAM/16QAM" scheme associated with $\rho = 0.9$ outperforms the "16QAM/8PSK" associated with the lower correlation coefficient of $\rho = 0.7$. Thus the effect of correlation becomes more dominant in higher-order modulation modes.

Figure 4.17 portrays the MSP along with the corresponding BPS throughput of all of the DJSTTCM modes against the received SNR for different cross-over probabilities of $p_e = \{0.05, 0.10, 0.15, 0.20\}$, respectively. For each received block both the cross-over probability as well as the near-instantaneous SNR, γ_r, are estimated and compared to a look-up table. Then, as illustrated in Figure 4.14, if γ_r is higher than the threshold γ_{th}, then the decoding will proceed. Otherwise, the BER of the received block will be estimated if BER $> 10^{-5}$, and a feedback acknowledgement flag will be transmitted to the transmitter, requesting a reduction of the transmission throughput. Figure 4.17 reveals that, as the SNR increases, the higher-order DJSTTCM modes are most likely to be activated, than the lower-order ones. Thus, the aggregate BPS throughput increases smoothly along with the SNR. Similar to the Rayleigh fading case, it may be observed from the figure that in the presence of a high correlation between the two sources, such as $\rho = 0.9$, the no transmission, "No Tx" mode has effectively 'disappeared'. However, for low correlations the scheme requires a

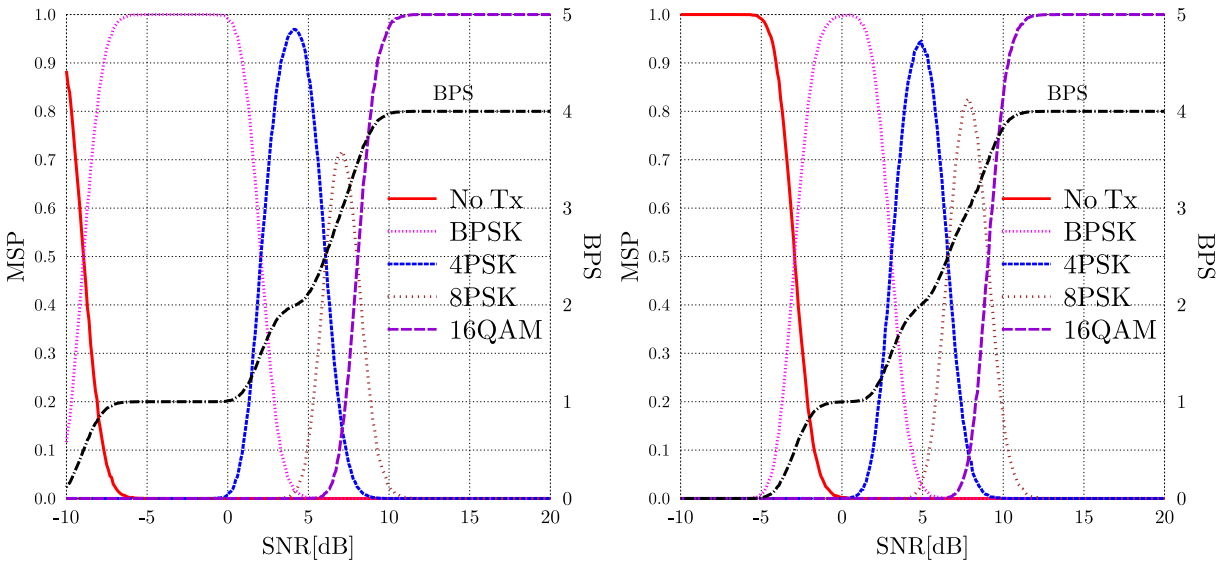

(a) $\rho = 0.90$. (b) $\rho = 0.80$

(c) $\rho = 0.70$ (d) $\rho = 0.60$

Figure 4.17: MSP of all **DJSTTCM** modes (left hand vertical axis) versus the SNR values and the corresponding BPS (right hand vertical axis) for for $\rho = \{0.9, 0.8, 0.7, 0.6\}$, when communicating over **Nakagami-m fading channels** with $m = 4$. The adaptive mechanism can be illustrated in the flow-chart of Figure 4.14.

higher SNR for achieving a non-zero throughput.

4.5 Chapter Conclusions

In this chapter, we have proposed the near-instantaneously adaptive DJSTTCM scheme of Figure 4.1 for relying on perfect side-information DJSC arrangement. A modified symbol-based MAP algorithm was proposed in Section 4.2.3 relying on the idealised simplifying assumption of having perfect side-information at the receiver. The proposed system outperformed the benchmark scheme dispensing with joint decoding, almost regardless of cross-over probabilities. Explicitly, the benefits of having perfect side-information were demonstrated in Section 4.2.4. For example, for $\rho = 0.90$ and at a BER of 10^{-5} our DJSTTCM-16QAM scheme had a performance gain of 4.8 dB when compared to the non-joint benchmark, as seen in Figure 4.5. The theoretical SW/S bounds, when communicating over uncorrelated Rayleigh fading channels were evaluated in Section 4.3.1 where our proposed DJSTTCM-QPSK/BPSK scheme was shown to operate within 2 dB from it, for $\rho = 0.93$ at a BER of 10^{-5} as documented in Figure 4.6. Our proposed scheme shows a beneficial compression capability, since it operates within 0.13 bits from the maximum achievable compression rate of the above-mentioned scenario, as seen in the rate-region graph of Figure 4.9.

Section 4.3.2 investigated the performance of the DJSTTCM scheme of Figure 4.1, when communicating over a variety of realistic Nakagami-m fading channels. The DCMC capacity of the Nakgami-m channel was investigated in Section 4.3.2 in order to contrast the scheme against the SW/S bound. Moreover, our proposed scheme exhibited a robust performance for a wide range of source correlations. For example, for a BER level of 10^{-5} associated with $p_e = 0.1$ and $m = 2$, the proposed scheme operates within 2.3 dB from the theoretical SW/S bound. Furthermore, it is capable of operating within 0.14 bits of the maximum achievable SW compression bound, as suggested by Figure 4.11 and Figure 4.12, respectively. Furthermore, a practical bandwidth-efficient adaptive scheme was proposed based on a range of adaptive modem modes for transmitting correlated signals, when communicating over both uncorrelated Rayleigh fading and Nakagami-m fading channels in Section 4.4.1 and Section 4.4.2, respectively. The transmitter adapts its coding and modulation modes according to both the short-term channel conditions for ensuring that the BER remains below 10^{-5}. It is worth noting that our the SNR threshold values at the target BER of 10^{-5} recorded for the various DJSTTCM schemes are summarized in Table 4.6.

The DJSC design relying on perfect side-information of this chapter will now be extended to a more realistic cooperative architecture in the next chapter.

Scheme		**DJSTTCM**				
Schematic		Figure 4.1				
Decoder		TTCM MAP of Figure 4.2				
Channel		Rayleigh fading		Nakagami-m fading, $m = 4$		
BER result		Figure 4.13		Figure 4.11 and Figure 4.16		
Mode	BPS	SNR [dB] at BER$= 10^{-5}$ for ρ				
		$\rho = 0.93$	$\rho = 0.9$	$\rho = 0.9$	$\rho = 0.8$	$\rho = 0.7$
QPSK/BPSK	1	-3.5	-1.9	-3.25	-0.75	2.1
8PSK/QPSK	2	4.0	5.6	1.4	3.3	4.8
16QAM/8PSK	3	7.1	9.0	5.5	7.0	8.2
32QAM/16QAM	4	8.6	10.2	7.0	9.2	10.0

Table 4.6: SNR threshold values of various DJSTTCM schemes when transmitting over uncorrelated Rayleigh fading and Nakagami-m fading channels. The results are extracted from Figures 4.13, Figures 4.11 and Figures 4.16.

Chapter 5

TTCM-Aided Distributed Joint Source-Channel Coding-Based Superposition Modulated Relaying

5.1 Introduction

Chapter 4 has discussed and analysed a sophisticated Distributed Joint Source-Channel coding (DJSC) architecture relying on perfect side-information, in which the second source sequence, relied upon as the side-information $\{b_2\}$ is assumed to be perfectly known at the receiver. However, this idealised simplifying assumption is impractical, since in real-based applications the availability of error-free side-information cannot be assured. In this chapter, we will relinquish this idealised assumption. Explicitly, both sources are TTCM encoded and then compressed before transmission through a Rayleigh fading Multiple Access Channel (MAC). Additionally, both sources are supported by a Relay Node (RN) in the context of a cooperative communications regime. Explicitly, the RN transmits both users' signals with the aid of a powerful SuperPosition Modulation (SPM) technique, which judiciously allocates the transmit power between the pair of correlated signals. Both the RN and Destination Node (DN) invoke a powerful turbo-style DJSTTCM-based decoder explicitly designed for exploiting the correlation amongst the source signals. Similar to Section 4.3, we commence our system analysis by deriving the achievable Slepian-Wolf/Shannon (SW/S) bound. Additionally, in line with our analysis adopted in Chapter 3, EXIT charts will be used for investigating the decoding convergence of the joint source and channel decoder for supporting the overall system design. The resultant cooperative scheme will be referred to as the DJSTTCM-SPM arrangement.

Similar to the discussions in Section 4.1, applying DSC techniques, such as Slepian-Wolf (SW) coding [4] or Wyner-Ziv (WZ) coding, has facilitated efficient and low-cost signal processing in sensor networks, where the complexity has been moved from the battery-limited Source Node

(SN)s to the central base station [7, 8] or to the RN. More explicitly, using DSC techniques in wireless sensor networks has led to a new processing paradigm, where the potential computational complexity has been moved from the battery-limited SNs to the central decoder connected to the mains supply. As a consequence, the critical power constraint, which directly predetermines the life-span of the wireless SN is fulfilled [7].

As stated in Chapter 4, the idea of using channel coding techniques has enabled practical solutions to be developed, where the correlation between the sources is modelled by invoking the philosophy of a Binary Symmetric Channel (BSC). Numerous solutions have been proposed based on novel channel codes. More specifically, turbo codes were proposed for example in [9, 196, 197], whereas Low-Density Parity-Check (LDPC) codes were considered in [36, 38, 39]. However, these contributions relied on the idealised simplifying assumption of having noiseless auxiliary genie channel between the source nodes and the base station. Whilst, the separate design of source and channel coding was shown to be optimal by Shannon [8, 46] where perfect entropy-coding and capacity-achieving Forward Error Correction (FEC) codes are used, provided that both a potentially infinite delay and an infinite complexity are acceptable, in practical multi-user fading channels they have limited applicability. Indeed, they would lead to catastrophic error propagation in realistic MAC scenarios, as illustrated in [8, 16]. Several solutions were proposed for similar scenarios relying on the design of DJSC arrangement for MAC transmissions. More explicitly, the turbo code based design proposed in [11] for communicating over a benign AWGN channel would suffers from an error floor, when communicating over hostile Rayleigh fading channels. This makes the system less suitable for wireless applications.

Later, a modified LDPC code was proposed in [37] for mitigating the above-mentioned error floor, but nonetheless, a substantial error floor persisted, when the correlation between the sources was low. Recently, an iterative joint-turbo equaliser and decoder scheme was conceived for transmission over a multi-path Rayleigh fading multiple access channel in [43, 50]. Both schemes have achieved a near-SW/S performance, albeit this was attained at a high joint decoding complexity. More specifically, as many as $I = 35$ iterations were invoked between the decoder components in [43], while a potentially excessive number of $I = 350$ iterations were required in [50] for attaining a near-SW/S performance. By contrast, we will demonstrate that only invoking as few as $I = 8$ turbo iterations is sufficient with the advent of our TTCM decoder in the context of scheme proposed in this chapter. We consider a DF-aided cooperative relaying scheme relying on a stationary relay. TTCM-aided Symbol-based SPM is employed at the RN for generating the RN's transmitted signal. Both source signals will be superimposed and appropriately rotated for transmission at the RN. As a benefit, the communications between the RN and the DN would only require a single timeslot, which doubles the spectral efficiency [207, 208].

In Chapter 4, we have assumed that the correlation coefficient, ρ, is perfectly known to the decoder, which also constitutes an idealised impractical assumption. In order to relinquish this assumption, later in Section 5.6 we will design a novel reduced-complexity Block Syndrome Decoding (BSD)-based TTCM scheme for our DJSTTCM, which is capable of blindly estimating the

correlation coefficient. Accurate estimation of the correlation coefficient at the decoder is one of the cornerstones when designing practical DJSC systems, since its inaccurate estimation would mislead the joint decoder hence potentially inflicting catastrophic error propagation during the decoding process [54]. Thus, the blind online estimation of the correlation coefficient[1] ρ at the receiver still remains a persistent challenge in the practical design of DJSC schemes, since the correlation coefficient ρ tends to vary over both space and time [53]. Several solutions were proposed for addressing this issue. For example, in [52] the (Log Likelihood Ratios) LLRs of the LDPC decoder corresponding to the syndrome bits were used for estimating ρ. However, the scheme proposed in [52] only works for highly correlated sources having $\rho \geq 0.95$. On the other hand, an Expectation Maximization (EM) based decoder was proposed in [209] where a Maximum-Likelihood (ML) based search was used for finding an accurate initial estimate. Furthermore, an Expectation Propagation (EP) based estimator was introduced in [54]. The schemes of [54, 209] were invoked for handling both weak and strong correlation scenarios. However, all of the above-mentioned three schemes [209, 52, 54] considered relying on perfect side-information DSC, while in this treatise we consider more practical DJSC scenarios.

Against this background, this chapter we conceive an SPM-aided cooperative relaying scheme for our DJSC paradigm. Again, unlike the scheme proposed in Figure 4.1, where we have assumed that the second source's signal is flawlessly received at the destination as side-information for correlation exploitation, here we consider a more practical scenario, in which both source signals are transmitted over hostile uncorrelated Rayleigh fading channels. To be consistent with Chapter 4, both correlated sequences will be encoded using a bandwidth-efficient TTCM scheme [152] which combines the functions of coding and modulation. This leads to the conception of our DJSTTCM scheme[2].

The rest of the chapter is organised as follows. The proposed cooperative system model is described in Section 5.2, while the Phase-I encoder and decoder as well as our rate-region analysis are discussed in Section 5.3. Then a brief discussion concerning the SPM design will be presented in Section 5.4, followed by the corresponding analysis of our results in Section 5.5. Our BSD decoder will be evaluated in Section 5.6, while the Section 5.7 concludes the chapter.

5.2 System Model

Let us now first take a quick look into the cooperative communications scheme, which constitutes an effective technique of supporting users either with objective of combating the channel fading or enhancing the overall transmission throughput [60, 61, 62]. Consider the cooperative scheme portrayed in Figure 5.1, where the pair of Source Nodes (SNs) transmit their information to the RN during the first time slot (Phase-I). Then, the RN retransmits the information during the second time slot (Phase-II). Over the years a large variety of protocols have been designed for processing

[1] ρ signifies the correlation between the sources and can be estimated as: $\rho = 1 - 2p_e$, where p_e is the cross-over probability when using the BSC model.

[2] Readers are referred back to Section 2.4 for more TTCM-related details.

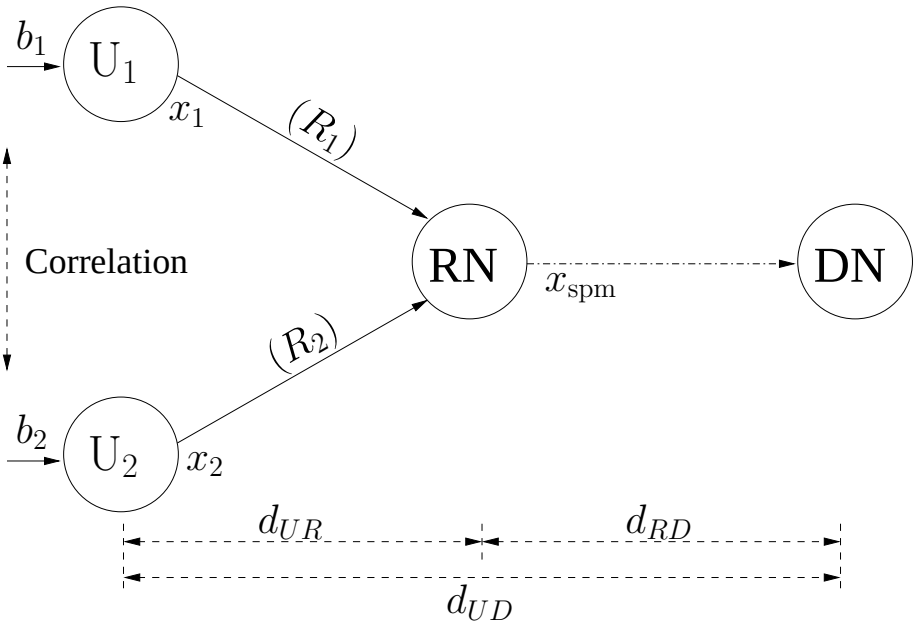

Figure 5.1: Schematic diagram of the DJSC-aided RN-assisted SPM of Figure 5.11, where d_{UD} is the geographical distance between the nodes $U_{1,2}$ and DN.

the SNs' transmitted signals [60, 61, 62, 210]. In general, these protocols can be classified into fixed relaying and adaptive relaying [62]. In the former family, the available communication resources, of time, frequency, space, transmitted power[3] etc., are divided between the SNs and RNs in a time-invariant fashion. By contrast, in the latter schemes, as suggested by the terminology, these resources will be shared adaptively in sophisticated ways [62,210]. Then, according to how the RN would deal with its received signals, each relaying scheme might be further categorised into four main classes, namely the Amplify-and-Forward (AF) [211], Decode-and-Forward (DF) [176,212], Compress-and-Forward (CF) [213] and Coded Cooperation [214] protocols.

Let us again, consider the schematic of Figure 5.1, where $\{b_1\}$ and $\{b_2\}$ are pair of correlated binary information sequences at the SNs, where one/both of them has/have to be compressed before their transmission to the RN. More explicitly, the encoders of both the source nodes U_1 and U_2 have to encode and then compress $\{b_1\}$ and $\{b_2\}$ independently of each other. In other words, neither the source's observations from the other source nor the correlation coefficient are known by one of the SNs concerning the other. However, the RN is capable of reconstructing both sequences through exploiting the correlation between $\{b_2\}$ and $\{b_1\}$ [8].

The schematic of our proposed single-relay-aided cooperative model is shown in Figure 5.1, where both SNs, namely U_1 and U_2 have a single antenna each. They transmit their correlated information signals to the Destination Node (DN) with the aid of a twin-antenna-aided RN. The communication paths shown in Figure 5.1 are subject to both path-loss as well as to uncorrelated Rayleigh fading. Assuming a free-space path-loss exponent of $\alpha = 2$, the corresponding reduced-pathloss-induced geometrical gain experienced by the Sources-to-Relay (SR) link and Relay-to

[3]The power sharing technique that were proposed in Section 3.2.2.2 could be considered as an adaptive relaying protocol in this sense.

Destination (RD) link with respect to the Source-to-Destination (SD) link may be calculated, respectively, as [185, 187]:

$$G_{UR} = \left(\frac{d_{UD}}{d_{UR}}\right)^2 \;;\; G_{RD} = \left(\frac{d_{UD}}{d_{RD}}\right)^2 , \tag{5.1}$$

where d_{UD} denotes the distance between the source nodes U_1, U_2 and the DN. In our model the RN is situated exactly at the mid-point between the SNs and DN. Thus, we have $d_{UR} = d_{RD} = d_{UD}/2$, hence $G_{UR} = G_{RD} \approx 6.02$ dB. Similar to Section 3.2.1 discussion, it is convenient for our discussions to define the term referred to as transmit SNR[4] as the ratio of the power transmitted from node a to the noise power experienced at the receiver of node b as:

$$\text{SNR}_t = \frac{\text{E}\left[|x_a|^2\right]}{N_0} = \frac{1}{N_0} . \tag{5.2}$$

Thus, we arrive at:

$$\begin{aligned} \text{SNR}_r &= \text{SNR}_t \; G_{ab} \\ \Gamma_R &= \Gamma_T + 10\log_{10}(G_{ab}) \; [\text{dB}] , \end{aligned} \tag{5.3}$$

where we have $\Gamma_R = 10\log_{10}(\text{SNR}_r)$ and $\Gamma_T = 10\log_{10}(\text{SNR}_t)$.

Similar to the source correlation model adopted in Chapter 4, the BSC philosophy is used for modelling the correlation between the source sequences $\{b_1\} = \{b_1^1, b_1^2, \cdots, b_1^i, \cdots, b_1^N\}$ and $\{b_2\} = \{b_2^1, b_2^2, \cdots, b_2^i, \cdots, b_2^N\}$, where N is the length of each source block. More explicitly, the source sequence $\{b_1\}$ is generated by an equiprobable binary symmetric i.i.d. source, while $\{b_2\}$ can be formulated as $b_1^i = b_2^i \oplus e_i$, where $\oplus$ is the modulo-2 addition operation and e_i is an independent binary random variable assuming the logical value 1 with a cross-over probability of p_e and 0 with a probability of $(1 - p_e)$. Both the random variables of b_1^i and b_2^i in the pair of bit streams $\{b_1\}$ and $\{b_2\}$ may be assumed to be i.i.d. for the bit index i, hence both sources emit equiprobable bits [50]. Therefore, the entropy of each source can be safely assumed to be unity, which yields a conditional entropy of:

$$\begin{aligned} &H(p_e) = H(b_1|b_2) = \\ &\lim_{N\to\infty} \frac{1}{i} H\left[\left((b_1^1, \cdots, b_i^1, \cdots b_N^1)|(b_1^2, \cdots, b_i^2, \cdots b_N^2)\right)\right] , \end{aligned} \tag{5.4}$$

where $H(p_e) = p_e \log_2\left(\frac{1}{p_e}\right) + (1 - p_e)\log_2\left(\frac{1}{1-p_e}\right)$ is the entropy of the binary random variable and e_i is used for parametrising the side-information. Therefore, the achievable SW rate region is

[4] However, the concept of transmit SNR [187] is unconventional, as it relates quantities to each other at two physically different locations, namely the transmit power to the noise power at the receiver.

given by the following three inequalities [50]:

$$\begin{aligned} R_1 &\geq H(p_e)\,, \\ R_2 &\geq H(p_e)\,, \\ R_1 + R_2 &\geq 1 + H(p_e)\,, \\ &\geq H(b_1, b_2)\,. \end{aligned} \tag{5.5}$$

Let us now embark on the design of a joint source-channel encoding/decoding scheme for the RN and DN.

5.3 First Time Slot (Phase-I)

The following two subsections will introduce our distributed joint encoder and decoder, respectively.

5.3.1 Distributed Joint Source-TTCM Encoder

The basic block diagram of the DJSTTCM-SPM scheme is shown in Figure 5.2, which relies on the Phase-I and Phase-II transitions during the first and second timeslots, respectively. Our system can be viewed as a two-stage serially concatenated structure. Explicitly, in the first timeslot, the pair of correlated sequences, $\{b_1\}$ and $\{b_2\}$, are encoded by the powerful TTCM encoders, or "outer encoders", where each has a coding rate of $R_{cm} = \frac{m}{m+1}$ and invokes a 2^{m+1}-level modulation scheme. Note that the second user stream $\{b_2\}$ is separated by a user-specific bit-interleaver π_b from $\{b_1\}$ in order to exploit the user correlations via the inner iteration (I_{in}) that is between the two TTCM decoders at the RN and DN, as illustrated in Figure 5.3. Then both TTCM-encoded sequences, namely $\{c_1\}$ and $\{c_2\}$ will be interleaved aiming for facilitating iterative information exchange between the TTCM decoder and the Multi-User Detector (MUD), which we refer to as the outer iteration (I_{out}). Here, the symbol-based interleavers, namely π_1 and π_2, are invoked for introducing time-diversity by scrambling the codeword sequences. As a consequence, this would provide much-needed independent *a priori* information at the output of the outer decoder, when aiming for combating the deleterious effect of channel fading [156, 171]. Next, the TTCM-interleaved coded bit sequences $\{c'_1\}$ and $\{c'_2\}$ are punctured at a rate of R_p, before they are mapped to the corresponding modulated symbols $\{x_1\}$ and $\{x_2\}$ using the mappers of Figure 5.2, for transmission over an uncorrelated Rayleigh fading MAC. Each specific symbol of both modulated symbol sequences is mapped using QAM/PSK mapping function.

Similar to the two-way relay channel discussed in Section 3.2.1, Phase-I transmission from the $L = 2$ SNs (U_1 and U_2) to the $P = 2$-antenna based RN, might be interpreted as a Space-Division Multiple Access (SDMA) [156] scenario. Hence, when each user invokes M'-ary PSK-or-QAM,

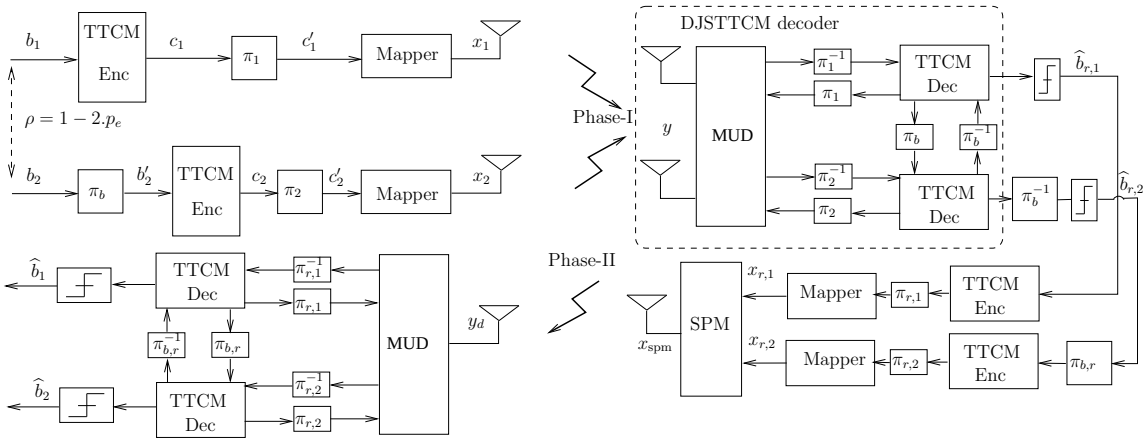

Figure 5.2: Block diagram of the DJSTTCM-SPM (Phase-I and Phase-II), when communicating over Rayleigh fading channels. The DJSTTCM decoder is further illustrated in Figure 5.3.

the signal received at the RN can be written as:

$$\mathbf{y = Hx + n}\,, \tag{5.6}$$

where $\mathbf{y} = [y_0, y_1, \cdots, y_{P-1}]^T$ and $\mathbf{n} = [n_0, n_1, \cdots, n_{P-1}]^T$ are $(P \times 1)$-dimensional vectors that represent the Phase-I received signals and noise vectors, respectively. Note that each element in $\mathbf{n}$ represents the complex-value of AWGN having a variance of $N_0/2$ per dimension. Additionally, the channel is represented by the $(P \times L)$-element matrix $\mathbf{H}$, while the transmitted signal $\mathbf{x} = [x_0, x_1, \cdots, x_{L-1}]^T$ is an $(L \times 1)$-element vector. Assuming perfectly synchronised transmission between U_1 and U_2, there are $M = M'^L$ possible phasor combinations for the transmitted signal vector $\mathbf{x}$.

5.3.2 Distributed Joint Source-TTCM Decoder

As the decoder schematic of Figure 5.3 shows, during I_{in}, the decoding process of $\{b_1\}$ at the output of "TTCM Dec_1", would utilise the LLR estimate corresponding to $\{b_2\}$, namely $L_e(b_2)$ extracted from "TTCM Dec_2", which is also referred to as the side-information. Likewise, the decoding of $\{b_2\}$ requires the LLR of $\{b_1\}$, namely $L_e(b_1)$. Note that, each TTCM decoder employs a symbol-based MAP algorithm, where the side-information LLRs will be converted to symbol probabilities[5] and then incorporated in the channel's transition metric as well as in the backward and forward recursion of the MAP algorithm, similar to Equations (4.7), (4.8) and (4.9), respectively. Accordingly, the *a posteriori* probabilities of the uncoded information gleaned from both of the TTCM decoders, will be converted to LLRs $L_o(b_1)$ and $L_o(b_2)$ during the I_{in}.

Thus, the employment of turbo-like parallel architectures would be appropriate in this context for approaching the theoretical performance limits [156], which efficiently exploits the source-

[5]The probability-to-LLRs as well as LLRs-to-probability conversions are illustrated in Appendix B.

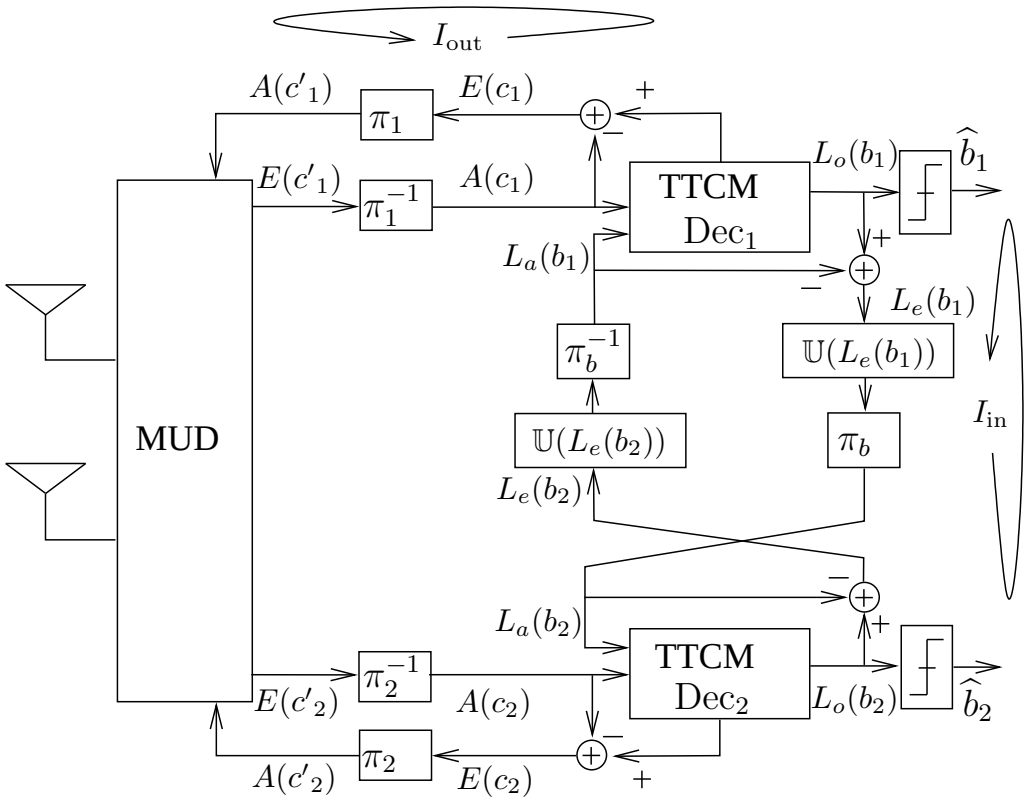

Figure 5.3: Schematic of the DJSTTCM decoder employed at the RN and DN of the DJSTTCM-SPM scheme of Figure 5.1, the notation $L(\cdot)$ denotes the LLR sequences, and the superscript *a*, *e* and *o* denote *a priori*, *extrinsic* and *a posteriori* nature of the LLR, respectively. $A(\cdot)$ and $E(\cdot)$ represent the *a priori* and *extrinsic* probabilities, and the notations π_i and π_i^{-1} represent the symbol-based interleaver and deinterleaver for i^{th} user, respectively while π_b and π_b^{-1} denotes the bit-based interleaver and deinterleaver.

correlation, as documented in [8, 50, 11]. Hence, at the RN the estimated information sequences, $\widehat{b}_{r,1}$ and $\widehat{b}_{r,2}$ are determined by exchanging extrinsic information in a parallel manner between the constituent decoders and the MUD.

First, the MUD detects the received signal using the robust, but potentially complex ML detector that aims for choosing the specific received symbol $\mathbf{x}$ that maximise the received signal probability. Note that in Section 5.6, we will propose a reduced-complexity MMSE-SIC detector that has exhibited a comparable Bit Error Ratio (BER) performance to that of its ML-based counterpart. The probability of the receiving vector $\mathbf{y}$ conditioned on the transmission of $\mathbf{x}^{(r)}$, where each symbol in $\mathbf{x}$ might assume $r \in \{1, \cdots, M\}$ possibilities is characterised by [156]:

$$\Pr(\mathbf{y} \mid \mathbf{x}^{(r)}) = \frac{1}{(\pi N_0)^P} \exp\left(-\frac{\left\| \mathbf{y} - \mathbf{H}\mathbf{x}^{(r)} \right\|^2}{N_0} \right), \tag{5.7}$$

where $\|(.)\|$ denotes the Frobenius norm of the vector $(.)$.

In our Phase-I transmission each user employs QPSK scheme, hence we have $M = 4^2 = 16$

$\mathbf{x}^{(r)}$	$\{x_2, x_1\}$	$\{x_2^i, x_1^i\}$
$\mathbf{x}^{(1)}$	$\{00, 00\}$	$\{x_2^1, x_1^1\}$
$\mathbf{x}^{(2)}$	$\{00, 01\}$	$\{x_2^1, x_1^2\}$
$\mathbf{x}^{(3)}$	$\{00, 10\}$	$\{x_2^1, x_1^3\}$
$\mathbf{x}^{(4)}$	$\{00, 11\}$	$\{x_2^1, x_1^4\}$
$\mathbf{x}^{(5)}$	$\{01, 00\}$	$\{x_2^2, x_1^1\}$
$\mathbf{x}^{(6)}$	$\{01, 01\}$	$\{x_2^2, x_1^2\}$
$\mathbf{x}^{(7)}$	$\{01, 10\}$	$\{x_2^2, x_1^3\}$
$\mathbf{x}^{(8)}$	$\{01, 11\}$	$\{x_2^2, x_1^4\}$
$\mathbf{x}^{(9)}$	$\{10, 00\}$	$\{x_2^3, x_1^1\}$
$\mathbf{x}^{(10)}$	$\{10, 01\}$	$\{x_2^3, x_1^2\}$
$\mathbf{x}^{(11)}$	$\{10, 10\}$	$\{x_2^3, x_1^3\}$
$\mathbf{x}^{(12)}$	$\{10, 11\}$	$\{x_2^3, x_1^4\}$
$\mathbf{x}^{(13)}$	$\{11, 00\}$	$\{x_2^4, x_1^1\}$
$\mathbf{x}^{(14)}$	$\{11, 01\}$	$\{x_2^4, x_1^2\}$
$\mathbf{x}^{(15)}$	$\{11, 10\}$	$\{x_2^4, x_1^3\}$
$\mathbf{x}^{(16)}$	$\{11, 11\}$	$\{x_2^4, x_1^4\}$

Table 5.1: Table of all possible combinations, where both x_1 and x_2 uses QPSK-based Set-Partition labelled mapping.

possible transmitted phasor combinations that are defined explicitly in Table 5.1. Thus, given the combinations shown in Table 5.1, the channel information probabilities of receiving $\mathbf{y}$ given that x_1 and x_2 were transmitted can be extracted from the $M = 16$-ary set of probabilities of Equation (5.22), respectively, as:

$$\Pr(\mathbf{y} \mid x_1 = x_1^{(i)}) = \sum_{j=1}^{M'} \Pr\left(\mathbf{y} \mid \mathbf{x}^{(i+(M'\times(j-1)))} = x_1^{(i)}\right) , \tag{5.8}$$

$$\Pr(\mathbf{y} \mid x_2 = x_2^{(i)}) = \sum_{j=1}^{M'} \Pr\left(\mathbf{y} \mid \mathbf{x}^{(j+(M'\times(i-1)))} = x_2^{(i)}\right) , \tag{5.9}$$

where $M' = 4$ and $i \in \{1, \cdots, M'\}$. Based on Equation (5.8) and Equation (5.9), the channel probabilities feed into the pair of TTCM decoders at the RN can be expressed using:

$$\Pr(x_1^{(i)} \mid \mathbf{y}) = \Pr(\mathbf{y} \mid x_1 = x_1^{(i)}) \times \Pr(x_1^{(i)}) , \tag{5.10}$$

$$\Pr(x_2^{(i)} \mid \mathbf{y}) = \Pr(\mathbf{y} \mid x_2 = x_2^{(i)}) \times \Pr(x_2^{(i)}) , \tag{5.11}$$

where $\Pr(x_1^{(i)}) = \Pr(x_2^{(i)})$ are all equiprobable probabilities of $1/M'$ during the first outer itera-

tion. Additionally, for the case when there is no outer iteration, we have $\Pr(x_{1,2}^{(i)}) = \Pr(c_{1,2}^{(i)})$ due to the one-to-one mapping $\mu(\cdot)$ function used. However, for further outer iterations, i.e. when $I_{\text{out}} > 1$, the $\Pr(c_{1,2}^{(i)})$ signify the *a priori* probabilities of the codewords $A(c'_{1,2})$ which are the feedbacks gleaned from the pair of the TTCM decoders to the MUD, as Figure 5.3 illustrated. Therefore, the *a priori* probabilities $\Pr(c_{1,2}^{(i)})$ will no longer be equiprobable, which results in decoding performance enhancement. Next,the MUD estimates the *extrinsic* probabilities $E(c'_{1,2})$ that are forwarded, after applying the appropriate de-interleavers, to the TTCM decoders for completing the outer iteration I_{out}, as illustrated in Figure 5.3.

Both TTCM decoders invoke a symbol-based MAP algorithm as detailed in Section 2.4. Each decoder will first estimate the *a posteriori* probabilities related to the uncoded information bits. These probabilities will be converted into LLRs, namely $L_o(b_1)$ and $L_o(b_2)$, which are then updated and appropriately de/interleaved to generate the *a priori* LLRs, $L_a(b_1)$ and $L_a(b_2)$, as shown in Figure 5.3. These LLRs are then exchanged between the two TTCM decoders through the I_{in} in order to exploit the correlation knowledge between the two users U_1 and U_2. However, during the I_{in} process the LLRs have to be updated in order to avoid the error propagation using the BSC cross-over probability p_e, as follows [37, 48]:

$$\mathbb{U}(L_e(b_{1,2})) = \ln \frac{(1-p_e)\exp[L_e(b_{1,2})] + p_e}{(1-p_e) + p_e \exp[L_e(b_{1,2})]}\,, \tag{5.12}$$

where $\mathbb{U}$ is the updating function shown in Figure 5.3. Moreover, the BSC's cross-over probability p_e can be estimated by comparing the reliable *extrinsic* LLR gleaned from each decoder, namely $L_e(b_1)$ and $L_e(b_2)$ as [37]:

$$\widehat{p}_e = \frac{1}{N} \sum_{i=1}^{N} \frac{\exp[L_e(b_{1,i})] + \exp[L_e(b_{2,i})]}{(1+\exp[L_e(b_{1,i})])\,(1+\exp[L_e(b_{2,i})])}\,. \tag{5.13}$$

5.3.3 Decoding with Side-Information

In this section, we will evaluate the performance of our joint decoder using the estimated side-information during the Phase-I transmission of Figure 5.2. Here we opted for employing the powerful semi-analytical EXIT charts technique for analysing the convergence behaviour of the joint decoder. The EXIT curves of the outer DJSTTCM decoder recorded for various correlation values of $\rho = \{0.9, 0.8, 0.6, 0.4, 0.2, 0.1\}$ are shown in Figure 5.4, where the related simulation parameters are tabulated in Table 5.2. Note that here we do not perform any puncturing in any of the coded bit sequences.

These EXIT curves characterise the relationship between the *a priori* input, $A(c_1)$ and the *extrinsic* output, $E(c_1)$, of the TTCM-Dec$_1$ shown in Figure 5.3, while the number of inner iterations is fixed to ($I_{\text{in}} = 4$). Thus, the EXIT characteristics of the outer decoder are independent of SNR[6].

[6]Readers are referred to the discussion in Section 2.5 for more details.

Coded Modulation	**TTCM**
Modulation Scheme	QPSK
Code Rate	R_{cm} =1/2
Puncturing Rate	R_p =1
Decoding Algorithm	Approximated Log-MAP
Mapper Type	Set-Partitioned
TTCM Iteration	$I = 4$
Number of Symbol	$N_s = 12\,000$ symbols per frame
Number of Frames	4000
Channel	2×2 Uncorrelated Rayleigh fading MAC
Effective Throughput	$R' = 2$ BPS
Channel State Information (CSI)	Known
MUD Type	ML

Table 5.2: Simulation parameters for the Phase-I transmission of the schematic of Figure 5.2.

As expected, the higher the correlation, the faster the convergence upon increasing $I_A(c_1)$ where the area above the outer decoder's EXIT curve is higher for larger values of correlation coefficients ρ. This rapid converge will facilitate having an open EXIT tunnel for lower SNR values, hence saving a significant amount of transmit energy, as it will be illustrated in Section 5.3.4.

5.3.4 Rate Region Design and Analysis

As stated in Section 5.1, the source/channel separation is not optimal for our Phase-I transmission scenario. Nonetheless, the theoretical limit that we will consider in our work assumes source/channel separation. Giving this assumption, the limit of reliable communication for correlated sources may be defined using Equation (5.5). By contrast, the CCMC capacity of each phase of the scheme shown in Figure 5.2 for transmission over fading channels, when invoking the SDMA scheme can be defined as [215]:

$$C = \mathrm{E}\left[\log_2 \det\left(I_N + \frac{\mathbf{H}Q_x\mathbf{H}^H}{N_0}\right)\right] , \tag{5.14}$$

where E denotes the expectation operation and Q_x is the covariance matrix of the transmitted vectors, while $\mathbf{H}^H$ is the Hermitian transpose of the channel matrix. Note that effective transmission rate of Phase-I is given by:

$$R' = R_p \cdot R_{cm} \cdot \log_2(M) \cdot L , \tag{5.15}$$

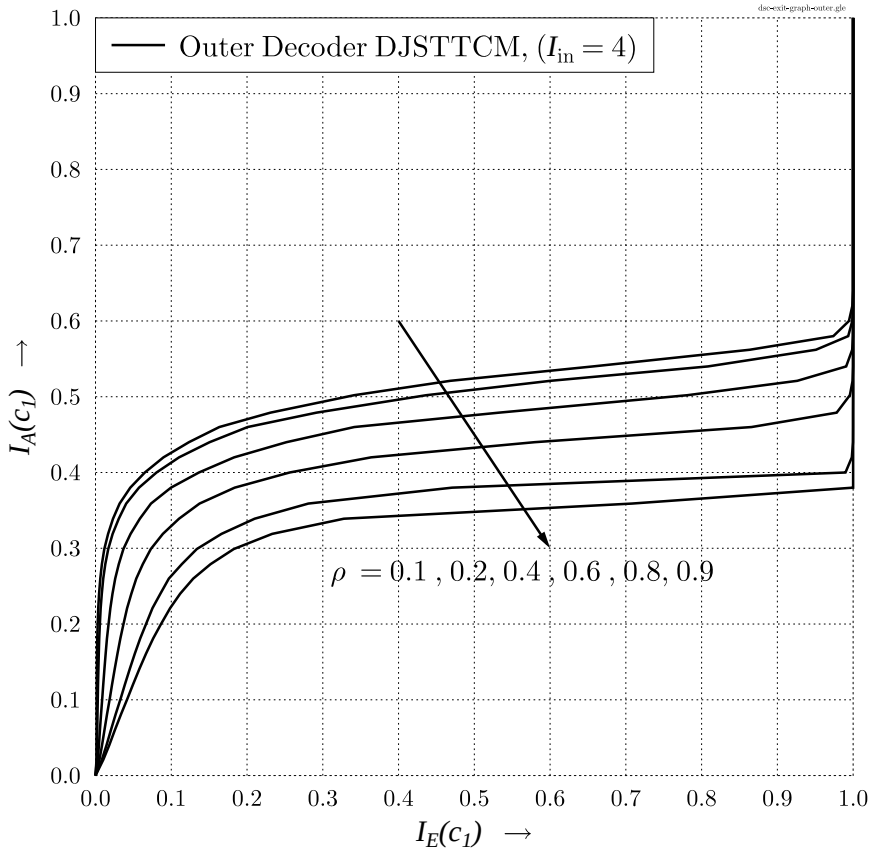

Figure 5.4: EXIT curves of the outer decoder of the **DJSTTCM** scheme seen in Figure 5.3 for the correlation coefficients of $\rho = \{0.9, 0.8, 0.6, 0.4, 0.2, 0.1\}$, where we have $I_{\textbf{in}} = 4$. All parameters are listed in Table 5.2.

where SNR(dB)$= E_b/N_0(dB) + 10\log_{10}(R')$ and L denotes the number of transmit antennas. Thus, the overall Phase-I transmission capacity can be expressed from Equation (5.5) and Equation (5.14) as:

$$H(b_1, b_2) \leq \frac{1}{R'} \mathrm{E}\left[\log_2 \det\left(I_N + \frac{\mathbf{H} Q_x \mathbf{H}^H}{N_0}\right)\right], \tag{5.16}$$

assuming an equal power allocation, where U_1 and U_2 transmit at the same power. The corresponding effective throughput of a single source is given by $\eta_{SW} = 1/2 \cdot R' \cdot H(b_1, b_2)$. The above CCMC capacity assumes having an optimally-distributed/continuous-amplitude input signal, in which the capacity is only bounded by the power transmitted as well as by the bandwidth allocated [215]. Hence, the employment of the DCMC capacity is more accurate in our DJSTTCM scheme design, since the bound considers both the effects of having discrete inputs as well as specifics of practical non-Gaussian distributed transmit signal of realistic digital modulation

schemes. The DCMC capacity can be expressed From [191] as:

$$C_{\text{DCMC}} = \max_{p(\mathrm{x}_1 \cdots \mathrm{x}_M)} \sum_{m=1}^{M} \int_{-\infty}^{\infty} \cdots \int_{-\infty}^{\infty} p(\mathbf{y} \mid \mathbf{x}^m) p(\mathbf{x}^m) \cdot \log_2 \left[\frac{p(\mathbf{y} \mid \mathbf{x}^m)}{p(\mathbf{y})} \right] d\mathbf{y} \quad \text{[bit/sym]} \,, \tag{5.17}$$

where symbol definitions of Equation (5.6) and Equation (5.7) are still valid. Furthermore, Equation (5.17) can be be simplified for M-ary phasor combinations as follows [191]:

$$C_{\text{DCMC}} = \log_2(M) - \frac{1}{M} \sum_{m=1}^{M} \mathrm{E} \left[\log_2 \sum_{i=1}^{M} \exp(\Psi_i^m) \right] \quad \text{[bit/sym]} \,, \tag{5.18}$$

where we have:

$$\Psi_i^m = \sum_{i=1}^{P} \frac{-|\mathbf{y}_i - \mathbf{h}_i \mathbf{x}_m + \mathbf{n}_i|^2 + |\mathbf{n}_i|^2}{N_0} \,, \tag{5.19}$$

where again, P is the number of receive antennas at the RN. The EXIT chart of Figure 5.5 charac-

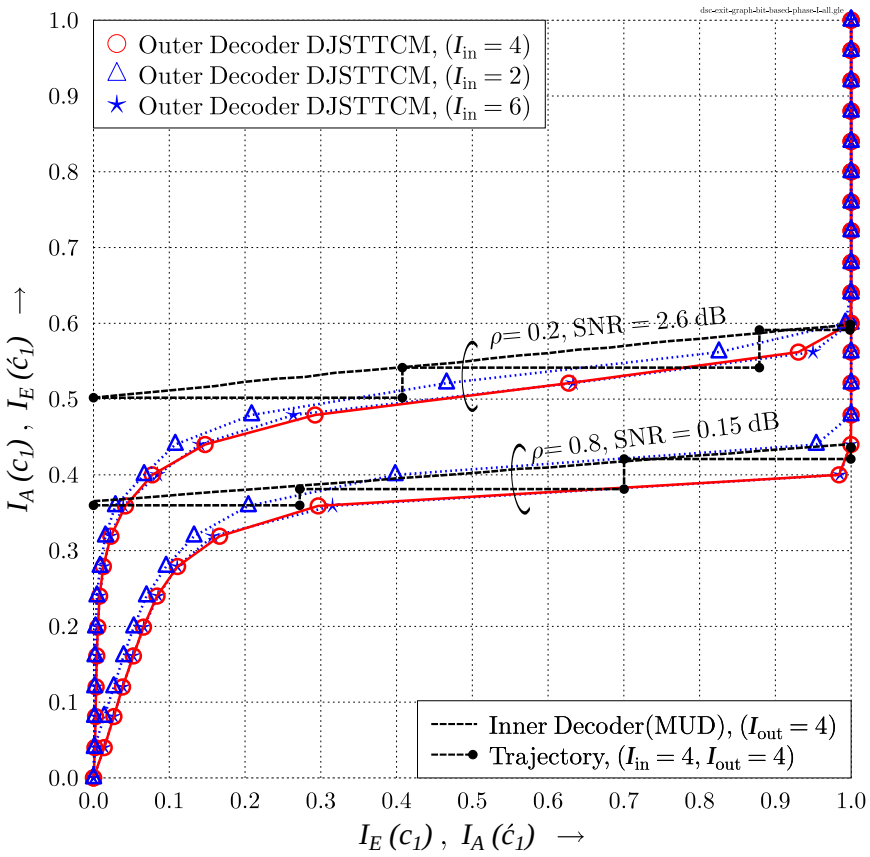

Figure 5.5: EXIT curves that characterise **DJSTTCM-QPSK** scheme for correlation coefficients of $\rho = \{0.8, 0.2\}$ when transmitting over **uncorrelated Rayleigh fading MAC** for **Phase-I** transmission. Table 5.2 summarises the main simulation parameters.

terises our iterative joint decoder, when the transmit SNR of 0.15 dB and 2.6 dB are invoked along

with the source correlations of $\rho = 0.8$ and $\rho = 0.2$, respectively. All the other simulation parameters are listed in Table 5.2. Specifically, Figure 5.5 suggests that four inner iterations "$I_{\text{in}} = 4$" between the outer decoder constituted by the pair of TTCM decoders of Figure 5.3 will facilitate an open EXIT tunnel for both correlation values of $\rho = \{0.8, 0.2\}$. Hence, as infinitesimally low BER can be achieved at the same level of the transmit SNR. Nevertheless, reducing the number inner iterations to "$I_{\text{in}} = 2$" would result in a closed EXIT tunnel hence leading to a residual BER. More explicitly, as seen in Figure 5.5, increasing the number inner iterations to "$I_{\text{in}} = 6$" would not results in any noticeable performance gain, despite increasing the decoding complexity. For the case of achieving an open EXIT tunnel and for the trajectories to reach the right-hand axis, a transmit SNR of 0.15 dB and 2.6 dB is needed for $\rho = 0.8$ and $\rho = 0.2$, respectively, as shown in Figure 5.5. Additionally, four outer iterations "$I_{\text{out}} = 4$" between the MUD the pair of TTCM decoders is required as illustrated, in the trajectories of the same figure. The Bit Error Ratio (BER) results depicted in Figure 5.6 support the prediction documented by the EXIT charts of Figure 5.5.

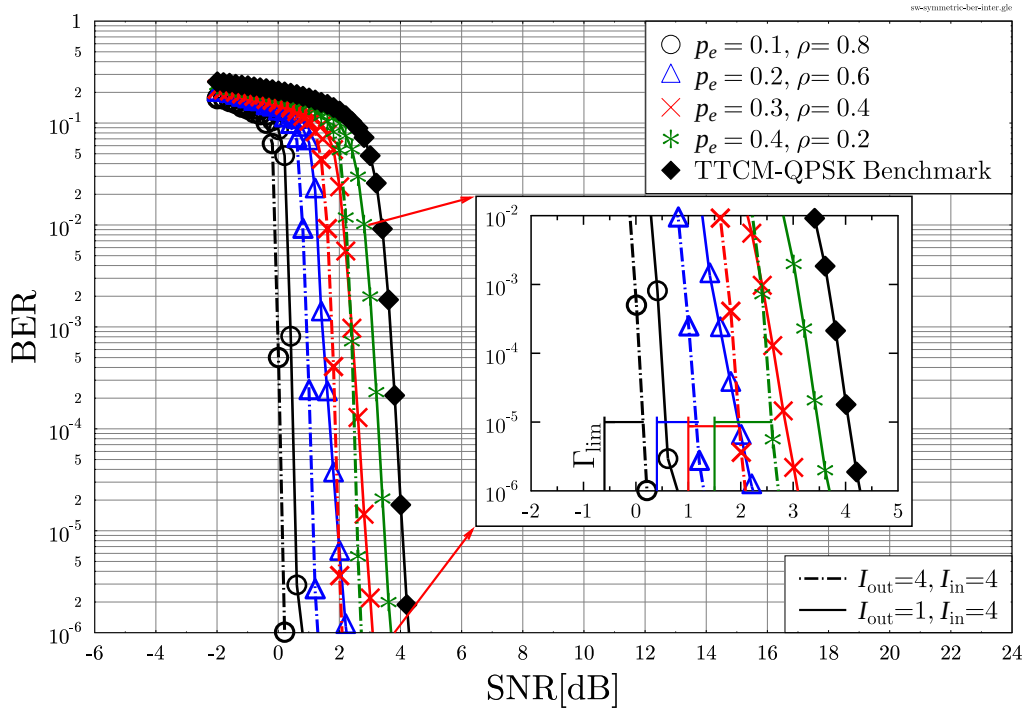

Figure 5.6: BER versus SNR performance of the proposed **DJSTTCM-QPSK** scheme of Figure 5.2 for correlation coefficients of $\rho = \{0.8, 0.6, 0.4, 0.2\}$, when transmitting over **uncorrelated Rayleigh fading MAC** during the **Phase-I** transmission. Table 5.2 summarises the main simulation parameters. The related results are summarised in Table 5.3, while the SNR limits values Γ_{lim} are extracted from the DCMC capacity curves of Figure 5.7.

We first characterise the BER performance of DJSTTCM when QPSK modulation is employed for $\rho = \{0.8, 0.6, 0.4, 0.2\}$. Here, we opted for invoking 1/2-rate TTCM as a channel coding scheme for a block of 12 000 symbols for both users and transmitted a total of 4000 blocks. Table 5.2 summarised the rest of the parameters. The attainable BER versus SNR performance is

depicted in Figure 5.6, where the SNR is given by SNR(dB) $= E_b/N_0(dB) + 10\log_{10}(R')$, where the effective throughput in this case $R' = R_{cm} \cdot R_p \cdot \log_2(M) \cdot L = 1/2 \cdot 1 \cdot 2 \cdot 2 = 2$ BPS. As portrayed in Figure 5.6, our proposed scheme outperformed the conventional TTCM-QPSK benchmark dispensing with joint decoding, when communicating over the 2×2 MAC considered. Note that our benchmark scheme is represented by the filled diamonds. As expected, our distributed scheme benefits from the correlation among the two sources. To elaborate further, at a BER level of 10^{-5} the proposed scheme associated with "$I_{\text{in}} = 4$" and "$I_{\text{out}} = 4$" has an SNR gain of 3.8 dB, 2.8 dB, 2.05 dB and 1.4 dB for $\rho = \{0.8, 0.6, 0.4, 0.2\}$, respectively.

In order to evaluate our system's performance, we have to estimate the minimum SNR, Γ_{lim}, required for approaching the SW/S bound. More explicitly, the Γ_{lim} values are obtained from the DCMC capacity shown in Figure 5.7. The CCMC capacity curve is also shown in Figure 5.7 for comparison. More specifically, we invoke DJSTTCM associated with $\rho = 0.8$, where the maximum overall achievable throughput is $\eta_{SW} = 1/2 \cdot R' \cdot H(b_1, b_2) = 1.469$ BPS. The DCMC capacity curve suggests that the minimum required SNR corresponding to $\eta_{SW} = 1.469$ BPS is $\Gamma_{\text{lim}} = -0.7$ dB, as shown in Figure 5.7. Similarly, the Γ_{lim} values of the related schemes associated with different correlation coefficients are inferred from the DCMC curves, explicitly, they are indicated with the aid of vertical lines in Figure 5.6. At BER $= 10^{-5}$ the scheme having the highest correlation of $\rho = 0.8$ has the minimum distance from the SW/S limit, as readily seen from Figure 5.6. More explicitly, we have $\Gamma - \Gamma_{\text{lim}} = (0.15) - (-0.7) = 0.55$ dB, while the scheme associated with the lowest correlation of $\rho = 0.2$ operates within 1.1 dB of the bound.

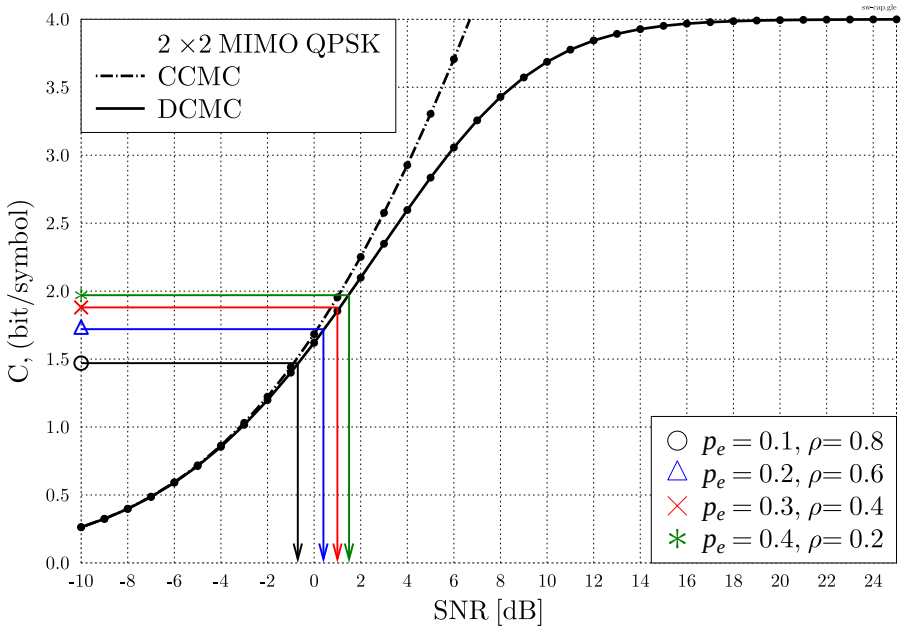

Figure 5.7: DCMC and CCMC capacity curves of 2×2 MAC for uncorrelated Rayleigh fading, where the curves were computed based on [191]. The vertical lines correspond to the SNR limits Γ_{lim} that are plotted in Figure 5.6.

Moreover, the effect of increasing the number of outer iterations between the joint TTCM de-

coders and the MUD, denoted as I_{out} in Figure 5.3, is outlined in Figure 5.6. Increasing the number of iterations from "$I_{\text{out}} = 1$" to "$I_{\text{out}} = 4$" will enhance the system's performance by about 0.75 dB. It is also worth mentioning that, more than one inner iterations, in Figure 5.3 are required, in order

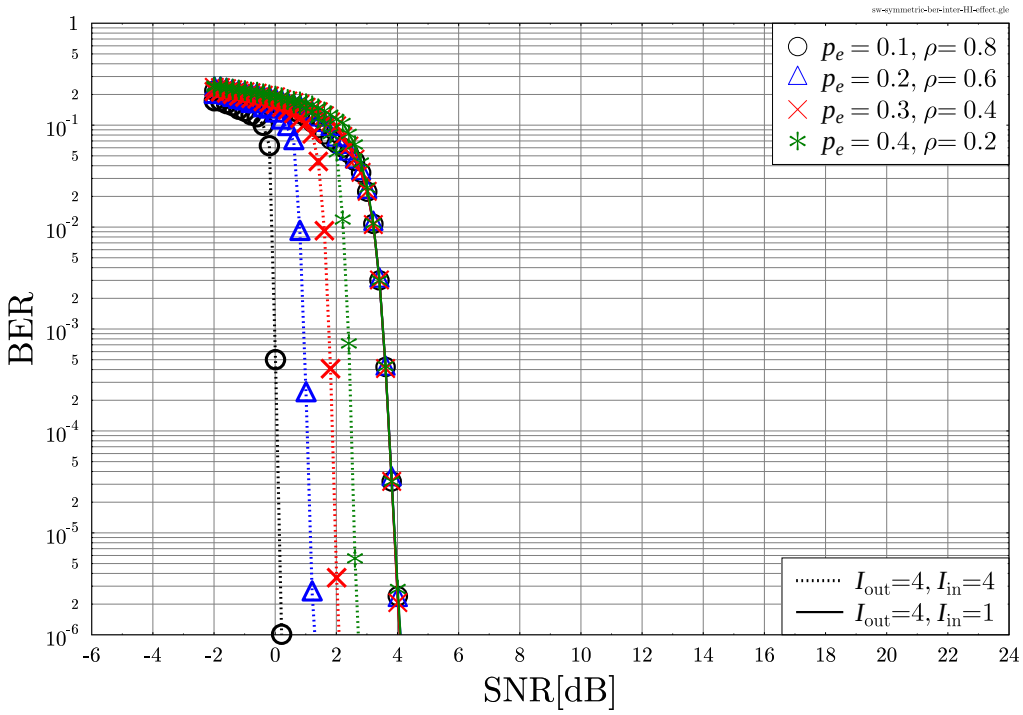

Figure 5.8: BER versus SNR performance of the proposed **DJSTTCM-QPSK** scheme of Figure 5.2 for correlation coefficients of $\rho = \{0.8, 0.6, 0.4, 0.2\}$ when communicating over **uncorrelated Rayleigh fading MAC** for **Phase-I** transmission. Table 5.2 summarises the main simulation parameters.

to efficiently exploit the joint decoding design, as illustrated in Figure 5.8. Employing a single I_{in}, will fail to exploit the signal correlation, hence the BER curves recorded for all correlation coefficients using $I_{\text{in}} = 1$ in Figure 5.8 would overlap. This is not unexpected, because the *extrinsic* LLRs $L_e(b_{1,2})$ are set to zero for the first iteration. Thus, we opted for "$I_{\text{in}} = 4$" and "$I_{\text{out}} = 4$" in our simulations. The rate region based on the SW theoretical bound as well as the achievable rates are presented in Figure 5.9. Similar to the SW/S limit, Γ_{lim}, the minimum achievable rates $\eta_{10^{-5}}$ of our scheme can be evaluated as follows:

- First, the SNR values capable of achieving a BER level of 10^{-5} or better will be recorded.
- Next these SNRs will be linked back to the effective throughput, $\eta_{10^{-5}}$, using the DCMC capacity curves of Figure 5.7.

Recall that, we assume that both U_1 and U_2 have a similar coding and transmission rate, hence they have similar maximum achievable rates. Our proposed scheme is capable of operating within 0.11 bits from the SW rate region for $\rho = \{0.8, 0.6, 0.4, 0.2\}$, as depicted in Figure 5.9. Specifically, the Phase-I transmission performance is summarised at a glance in Table. 5.3. For further

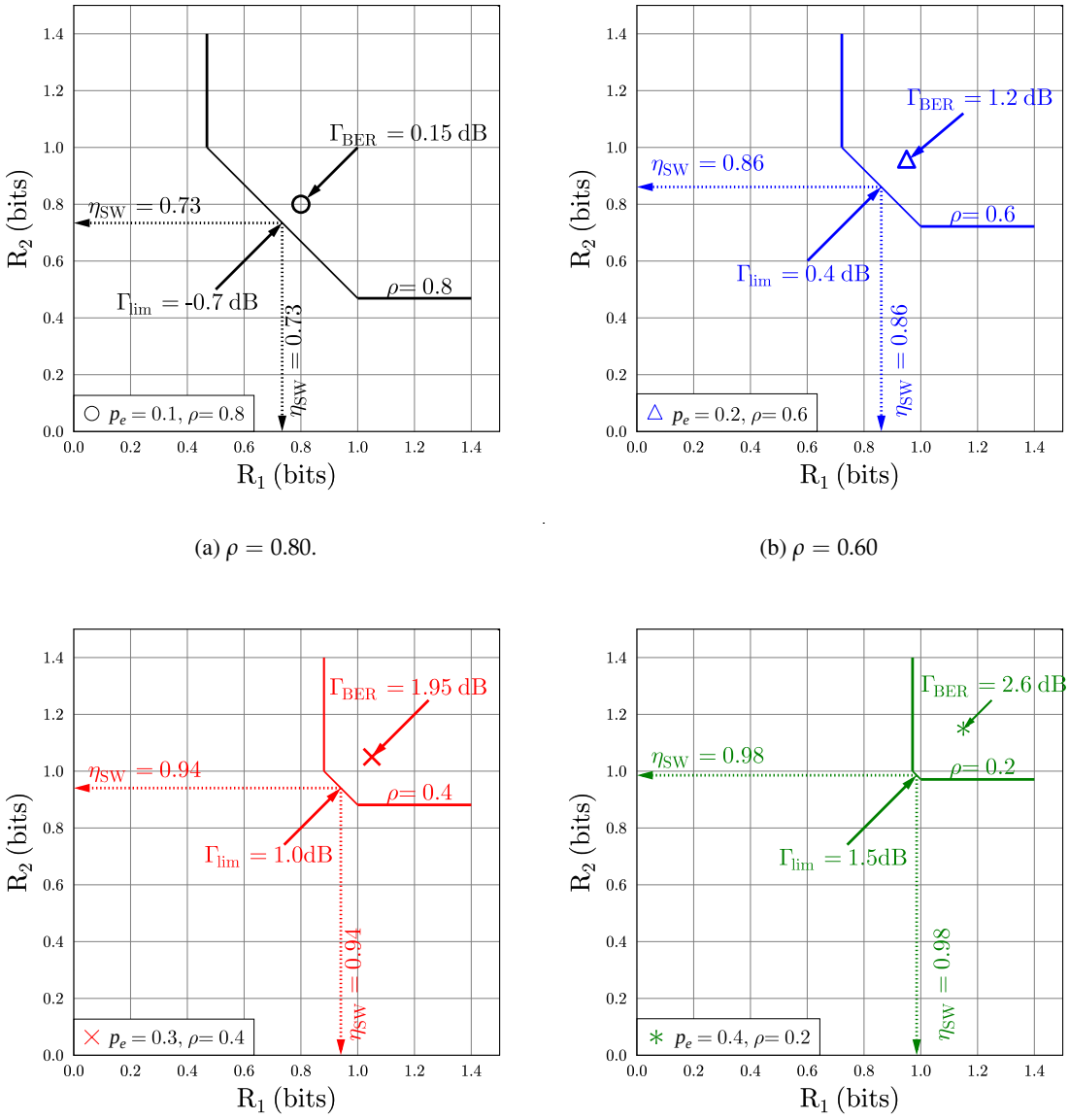

(a) $\rho = 0.80$.

(b) $\rho = 0.60$

(c) $\rho = 0.40$

(d) $\rho = 0.20$

Figure 5.9: Theoretical SW bound for each user rate (R_1, R_2) attained using the **DJSTTCM-QPSK** scheme of Figure 5.2 for **Phase-I** transmission for different correlation coefficient values. The main simulation parameters are listed in Table 5.2, while the related results are summarised in Table 5.3.

visualization, Figure 5.10 illustrates both the rate region as well as the achievable compression rates of our proposed scheme in a 3D diagram.

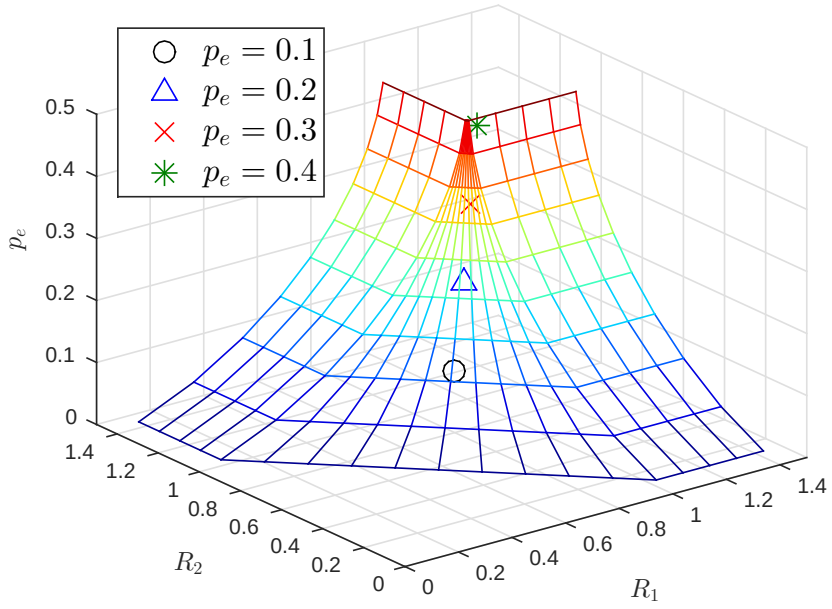

Figure 5.10: Theoretical SW bound having the achievable rates R_1 and R_2 of $BER = 10^{-5}$ for $\rho = \{0.8, 0.6, 0.4, 0.2\}$ corresponding to p_e. The parameters of Table 5.2 are used.

p_e	ρ	$H(b_1, b_2)$	Γ_{lim} (dB)	Γ (dB)	**Gap** (dB)	η_{SW}/user (bits)	$\eta_{10^{-5}}$/user (bits)	**SW-Gap** (bits)
0.1	0.8	1.47	-0.7	0.15	0.55	0.73	0.80	0.07
0.2	0.6	1.72	0.4	1.2	0.8	0.86	0.95	0.09
0.3	0.4	1.88	1.0	1.95	0.95	0.94	1.05	0.11
0.4	0.2	1.97	1.5	2.6	1.1	0.98	1.15	0.17

Table 5.3: Phase-I system performance of the DJSTTCM-QPSK of Figure 5.2, where Γ and η_{SW} are documented at BER $= 10^{-5}$. Both Γ_{lim} and Γ are in dBs. The parameters of Table 5.2 are used.

5.4 Second Time Slot (Phase-II)

In Section 5.3 we have evaluated our DJSTTCM scheme's Phase-I performance for a MAC scenario, but without employing a real puncturing in any of the coded sequences, namely in c'_1 and c'_2 of Figure 5.2, i.e. we had $R_p = 1$. However, later in Section 5.5, one of those coded sequences will experience real puncturing, leaving its modulated signal more susceptible to the effects of noise. Hence, as a remedy SPM has been invoked at the RN. Explicitly as the terminology implies, we combine multiple independent bit/symbol streams of the users for forming a combined constella-

tion, where the available protection resources might not equally distributed among the streams or users [216]. As a benefit, the total achievable rate of the entire scheme might be enhanced, while keeping the complexity manageable. The resultant combined constellation will eliminate the need for extra extra transmit antennas or time slot or bandwidth and still accommodates the transmission of an extra stream or user [207,208]. Albeit naturally of the cost of reducing the Euclidean distance amongst the constellation points, hence requiring an increased SNR. Both SPM and Hierarchical Modulation (HM) can be considered as a member of the layered modulation family, where the former combines the symbols of different users, while the latter combines bits from the same bit streams[7]. The next section will discuss the SPM that we invoke at our RN.

5.4.1 Relay-aided Low Order Superposition Modulation

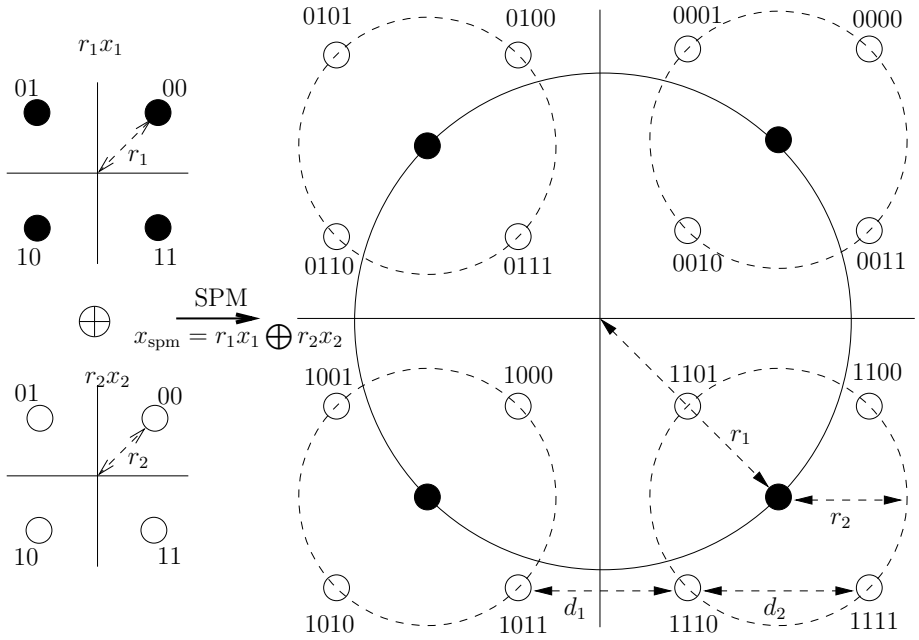

Figure 5.11: 16QAM superimposed symbol constellation generated from a pair of QPSK-based modulated signals, where we assume that $r_1 > r_2$.

The concept of cooperative transmission-aided SPM mapping was introduced in [207] and then it was further investigated in [218, 219]. In Phase-II, the RN will re-encode both $\hat{b}_{r,1}$ and $\hat{b}_{r,2}$ using a pair of 1/2-rate TTCM encoders corresponding to both users, respectively. As illustrated in the lower part of Figure 5.2, the resultant QPSK modulated signals $\hat{x}_{r,1}$ and $\hat{x}_{r,2}$ will be linearly combined to generate a 16QAM constellation x_{spm} using the SPM technique as:

$$x_{\text{spm}} = r_1\hat{x}_{r,1} + r_2\hat{x}_{r,2}\,, \tag{5.20}$$

where the transmitted signal energy is normalized to unity, i.e. we have $\mathrm{E}\left[\left|\hat{x}^2_{r,1}\right|\right] = \mathrm{E}\left[\left|\hat{x}^2_{r,2}\right|\right] = 1$, while both SPM scaling factors have to satisfy $r_1^2 + r_2^2 = 1$. To elaborate further, the 16QAM

[7]HM has the ability to transmit multiple simultaneous data streams treating them as different layers with different protection levels according to their priorities, where each of the different layers may be demodulated separately [217].

scheme obeying Equation (5.20) is shown in Figure 5.11, where the weighting factors r_1 and r_2 determine which of the QPSK signals will be given a higher protection. Explicitly, when we have $r_1 > r_2$, then $x_{r,1}$ has a higher protection, while $x_{r,2}$ will become the less well protected auxiliary signal. The minimum Euclidean distance d between the 16QAM-SPM constellation points can be either d_1 or d_2, as shown in Figure 5.11, which may be fully characterised using r_1 as [220]:

$$d = \begin{cases} \min\left(2\sqrt{1-r_1^2}, 2(r_1 - \sqrt{1-r_1^2})\right) & \text{when } (r_1 \geq r_2) \\ \min\left(2r_1, 2(\sqrt{1-r_1^2} - r_1)\right) & \text{when } (r_1 < r_2) \ . \end{cases} \tag{5.21}$$

In [220], the SPM weighting factors, r_1 and r_2, that maximise the minimum distance d were derived and the attainable performance was examined, where the optimum pair was found to be $(r_1, r_2) = (0.894, 0.447)$. Finally, the DN detects and estimates the received signal in a similar manner to that at the RN ,which was detailed in Section 5.3.2. However, the MUD will recover probability of receiving y_d given that 16QAM-SPM signal of Equation (5.20) was transmitted using [220]:

$$\Pr(y_d \mid x_{r,1}, x_{r,2}) = \frac{1}{(\pi N_0)} \exp\left(-\frac{|y_d - h(r_1 x_{r,1} + r_2 x_{r,2})|^2}{N_0}\right) , \tag{5.22}$$

specifically, and with the aid of Figure 5.11, the probabilities of receiving y_d given that $x_{r,1}$ and $x_{r,2}$ were transmitted can be extracted from Equation (5.22), respectively, as:

$$\Pr(y_d \mid x_{\text{spm}} = x_{r,1}^{(i)}) = \sum_{j=1}^{M'} \Pr\left(y_d \mid x_{\text{spm}}^{(i+(M'\times(j-1)))} = x_{r,1}^{(i)}\right) , \tag{5.23}$$

$$\Pr(y_d \mid x_{\text{spm}} = x_{r,2}^{(i)}) = \sum_{j=1}^{M'} \Pr\left(y_d \mid x_{\text{spm}}^{(j+(M'\times(i-1)))} = x_{r,2}^{(i)}\right) , \tag{5.24}$$

where we have $M' = \log_2(M) = \log_2(16) = 4$, since we use 16QAM-SPM modulation scheme and $i \in \{1, \cdots M'\}$. Thus, as shown in Figure 5.11, our SPM considers the two least significant bits for characterising $x_{r,1}$, while the two most significant bits are mapped to $x_{r,2}$. Based on Equation (5.23) and Equation (5.24) the probabilities that are provided to each of the TTCM decoders at the DN can be expressed as:

$$\Pr(x_{r,1}^{(i)} \mid y_d) = \Pr(y_d \mid x_{\text{spm}} = x_{r,1}^{(i)}) \times \Pr(x_{r,1}^{(i)}) , \tag{5.25}$$

$$\Pr(x_{r,2}^{(i)} \mid y_d) = \Pr(y_d \mid x_{\text{spm}} = x_{r,2}^{(i)}) \times \Pr(x_{r,2}^{(i)}) , \tag{5.26}$$

where the $\Pr(x_{r,1}^{(i)}) = \Pr(x_{r,2}^{(i)})$ are all equiprobable probabilities for the first iteration. The DN employs a DJSTTCM decoder which was discussed in Section 5.3.2.

Similar to the analysis used in Phase-I, we opted for using the EXIT charts to visualise the

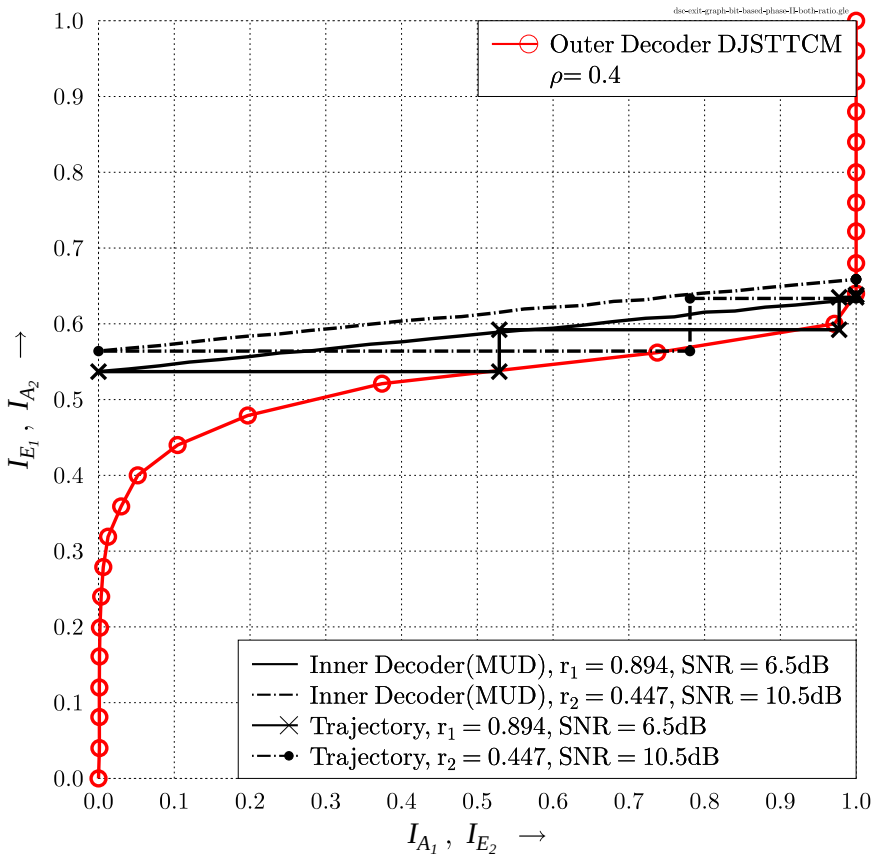

Figure 5.12: EXIT curves of the **DJSTTCM-aided 16QAM based SPM** scheme of Figure 5.11 based on the correlation coefficient of $\rho = 0.4$ for **Phase-II** transmission over **uncorrelated Rayleigh fading** channels. The simulation parameters are summarised in Table 5.4.

Coded Modulation	**TTCM**
Modulation Scheme	16QAM
Code Rate/User	$R_{cm_1} = 1/2$, $R_{cm_2} = 1/2$
Decoding Algorithm	Approximated Log-MAP
Mapper Type	16QAM-SPM
Constellation Ratios	$r_1 = 0.89$, $r_2 = 0.447$
Inner Iteration	$I_{\text{in}} = 4$
Outer Iteration	$I_{\text{out}} = 4$
Number of Symbol	$N_s = 12\,000$ symbols per frame
Number of Frames	4000
Channel	1×1 Uncorrelated Rayleigh fading MAC
Channel State Information (CSI)	Known
MUD Type	ML

Table 5.4: Simulation parameters for Phase-II transmission shown in the schematic of Figure 5.2.

information exchange between the DN's constituent decoders. The simulation parameters are tabulated in Table 5.4 and Figure 5.12 shows that the layer that invokes the lower ratio of $r_2 = 0.447$ will need a higher SNR of 10.5 dB in order to attain an open EXIT tunnel and vice versa. In other words, the QPSK signal $\hat{x}_{r,1}$ will need nearly 4.0 dB less power to achieve a low BER, when it is scaled with the aid of $r_1 = 0.894$ compared to $x_{r,2}$ weighted by $r_2 = 0.447$. Hence, using SPM of Figure 5.11 in Phase-II would equip our scheme with unequal error protection capability that will be further investigated in Section 5.5. In harmony with the Phase-I BER performance of Figure 5.6

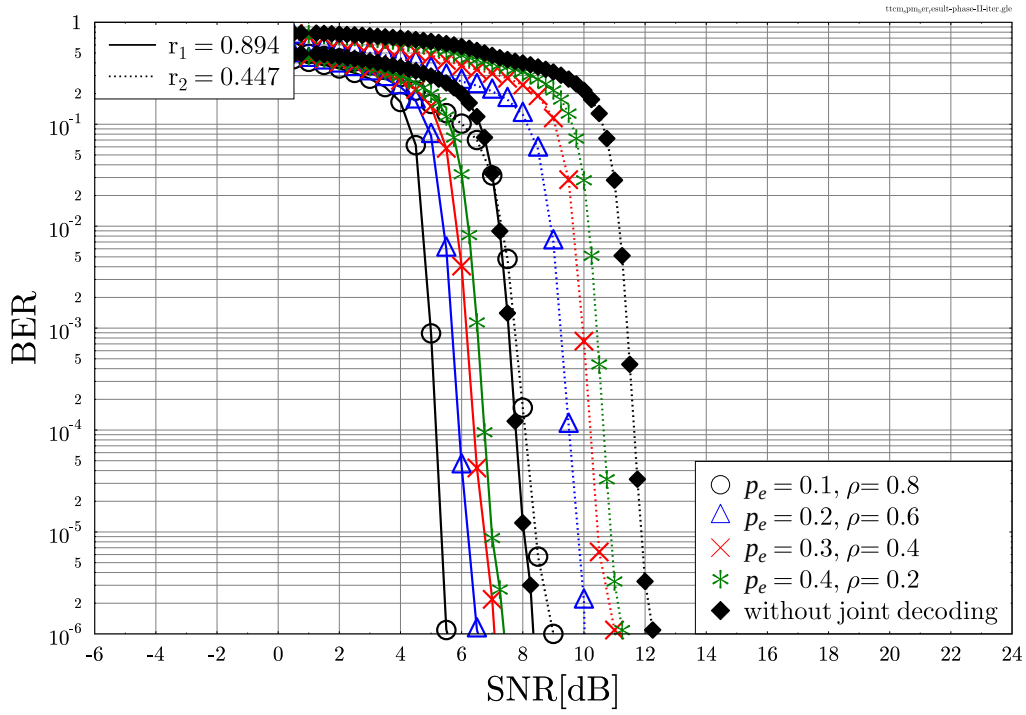

Figure 5.13: BER versus SNR performance of the **DJSTTCM-aided 16QAM based SPM** scheme of Figure 5.11 scheme for correlation coefficients of $\rho = \{0.8, 0.6, 0.4, 0.2\}$ for **Phase-II transmission**, where the simulation parameters are tabulated in Table 5.4.

discussed in Section 5.3.4, the DJSTTCM-aided 16QAM based SPM scheme has explicitly benefited from the sources' correlation after Phase-I decoding. Our joint iterative scheme outperformed the system dispensing with joint decoding, as shown in Figure 5.13, which was represented by the filled diamond. For example, at a BER level of 10^{-5} and at $\rho = 0.8$ the proposed schemes associated with $r_1 = 0.894$ and $r_2 = 0.447$ outperform the benchmarker by as much as 2.8 dB and 3.4 dB, respectively, as seen in Figure 5.13. Furthermore, as expected this gain is reduced, as the correlation diminishes, as detailed in Table 5.5.

5.5 Overall System Performance Results

In order to investigate our system in a more challenging scenarios similar to Chapter 4, we apply puncturing to one of the source user's coded sequence. During the Phase-I transmission, similar to our previous design in Chapter 4, both users will invoke the 1/2-rate TTCM code. However, the

Ratio	P_e	ρ	Γ-benchmark	$\Gamma_{10^{-5}}$	Gain[dB]
$r_1 = 0.894$	0.10	0.80	8.0	5.2	2.8
	0.20	0.60	8.0	6.1	1.9
	0.30	0.40	8.0	6.8	1.2
	0.40	0.20	8.0	7.0	1.0
$r_2 = 0.447$	0.10	0.80	11.9	8.5	3.4
	0.20	0.60	11.9	9.75	2.15
	0.30	0.40	11.9	10.4	1.5
	0.40	0.20	11.9	10.8	1.1

Table 5.5: Phase-II system performance of the DJSTTCM-16QAM based SPM scheme of Figure 5.11 when compared to the TTCM-16QAM benchmark, where Γ-benchmark $\Gamma_{10^{-5}}$ denotes the SNRs that correspond to a BER level of $= 10^{-5}$.

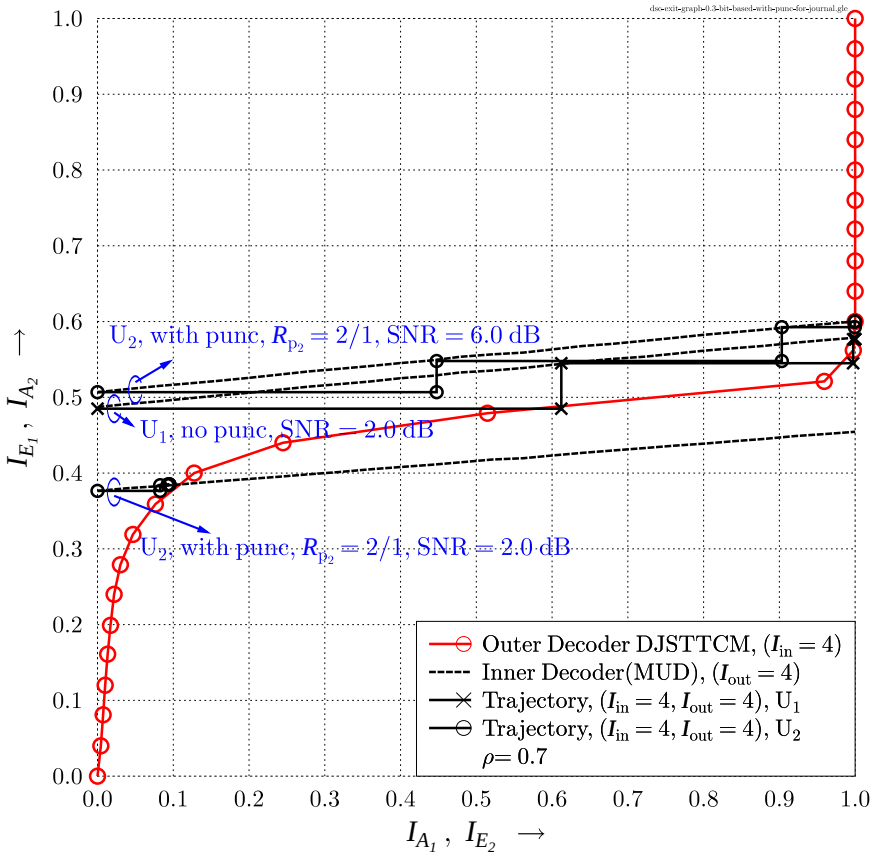

Figure 5.14: EXIT curves that characterise each user's **Phase-I** transmission schemes of Figure 5.2 with for $\rho = \{0.7\}$ when communicating over an **uncorrelated Rayleigh fading MAC**, where the U_2 sequence is **punctured** using $R_p = 2/1$. The simulation parameters are summarised in Table 5.2.

second user, U_2 will apply puncturing to its coded sequence. Explicitly, one of its pair of encoded bits is punctured, i.e. the puncturing rate is $R_{p_2} = 2/1$. As a result, all systematic bits of U_2 are punctured, retaining only the parity bits for transmission. However, the unequal protection nature of the SPM would allow us to beneficially prioritise the protection of the sources. Two different cases that might link to two practical scenarios were investigated which are as follows:

- **C**ase **O**ne: the punctured source U_2 will be assigned the high SPM ratio of $r_2 = 0.884$, which can be beneficial, when the battery charge of U_2 is limited.
- **C**ase **T**wo: the punctured source U_2 will be assigned the low SPM ratio of $r_2 = 0.447$. This case is applicable in the scenario, when the source U_1 has more valuable information, while U_2 can be considered to provide less important side-information.

In our cooperative system simulations, the RN is located at the mid-point between the SNs U_1/U_2 and the DN. Thus, from Equation (5.1), we have $G_{UR} = G_{RD} \approx 6.02$ dB, and accordingly, the received becomes SNR$_r$ =SNR$_t$ $+10\log_{10}(G_{UR}/G_{UR})$. Additionally, similar to Section 5.3.1, both the RN and DN decoders invoke "$I_{\text{out}} = 4$, $I_{\text{in}} = 4$" iterations.

The EXIT curve of Figure 5.14 illustrates that source U_2 requires a higher transmit power, in order for the tunnel to come open, than source U_1 for the same SNR of 2.0 dB. Hence, the near-error-free transmission of U_2 cannot be guaranteed for all identical transmit power and correlation. The difference in the required transmit SNR can be readily seen in Figure 5.14, where U_2 requires about 4.0 dB more power for creating an open EXIT tunnel leading to an infinitesimally low BER. Although only the parity bits of the source U_2 are transmitted, our powerful scheme was able to successfully detect the systematic bits even for a relatively low correlation of $\rho = 0.7$ i.e. when the correlation related gain is limited. Thus, this difference was almost perfectly compensated, when applying an SPM scaling factor of $r_2 = 0.894$ for the punctured source U_2 during Phase-II transmission. Explicitly, the overall performance of the non-punctured source U_1 was found to be similar to its punctured counterpart, namely within approximately one dB. Figure 5.15 shows the performance of our cooperative DJSTTCM-SPM scheme for both **C**ase **O**ne and **C**ase **T**wo, when the side-information source U_2 is assigned $r_2 = 0.894$ and $r_2 = 0.447$, respectively. As seen in Figure 5.15, there is a considerable performance difference between the two sources for **C**ase **T**wo, where the U_1 source requires 6.0 dB less power than the U_2 source on order to achieve a BER of 10^{-5}, while this distance has been reduced to about one dB for **C**ase **O**ne.

5.6 Distributed Joint Source-TTCM-Aided Block Syndrome Decoding

In this chapter as well as in Chapter 4, the correlation coefficient ρ that is controlled indirectly with the aid of the cross-over probability p_e has been assumed to be flawlessly known at the decoder. However, this idealised simplifying assumption is impractical, because the BSC's cross-over

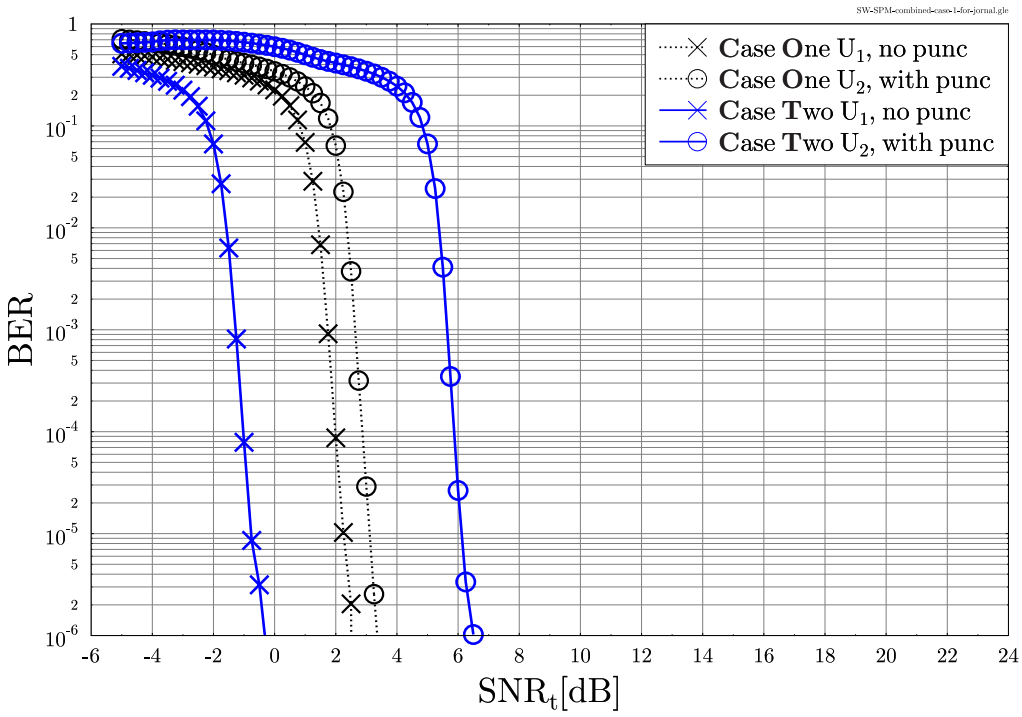

Figure 5.15: BER versus SNR_t performance of the **cooperative DJSTTCM-SPM** scheme of Figure 5.2 for a correlation of $\rho = 0.7$, for **C**ase **O**ne and **C**ase **T**wo, when all systematic bits of U_2 are punctured. The simulation parameters are summarised in Table 5.2 and Table 5.4.

probability p_e has to be estimated at the decoder [53]. Recall from Figure 5.3 that the information exchanged between both decoders, namely "TTCM-DEC_1" and "TTCM-DEC_2", corresponding to each user has to be updated through the $\mathbb{U}$ function of Section 5.3.2. This function has to be provided with an accurate BSC cross-over probability p_e, as given in Equation (5.41), because inaccurate estimation leads to mis-information, that would mislead the joint decoder of Figure 5.3 [54].

The trellis used for syndrome decoding is constructed using the syndrome former matrix $\mathbb{H}^T$, while the trellis of the classical conventional code uses the generator matrix $\mathbf{G}$ [221,222]. Moreover, the error trellis-based syndrome decoding has a specific significance, since the state probabilities of its trellis directly depend on the channel errors, rather than on the coded sequence [223, 222]. Consequently, for high SNRs or for highly correlated sources, the syndrome decoder would be more likely to experience a zero-state because of the predominantly near-error-free transmissions. This fundamental property has been exploited for designing the BSD of convolutional codes in [221,222] and of the TTCM scheme in [223]. More specifically, the BSD divides the received sequence into erroneous and error-free blocks according to their syndrome, and only the erroneous blocks are decoded by the BSD decoder, while a straightforward symbol-to-bit hard-demapper would be applied to the error-free blocks. Thus, the decoding complexity is substantially reduced for the predominantly near-error-free transmission scenarios. Our proposed estimator further exploits this beneficial feature, since the reliable LLRs associated with the error-free blocks will be used for estimating the cross-over probability of Equation (5.13), hence resulting in a performance improvement over

its to the conventional codeword-trellis based counterpart.

As further development, a turbo decoder-aided BSD technique was proposed in [223, 224], where a pre-correction sequence was evaluated at each iteration in order to update the errors in the trellis. Explicitly, the error-trellis gradually encounters more error free blocks as the iterations are continued, leading to further complexity reduction not only for high SNRs but also for higher-index iterations. In this section, we will re-design the reduced-complexity BSD-based TTCM (BSD-TTCM) scheme of [223] for estimating the cross-over probability at the base station. Additionally, the BSD-TTCM scheme will be further improved for exploiting the correlation between both sources, when communicating over a Rayleigh fading MAC, hence establishing a novel scheme that can be referred to as the DJSTTCM-BSD arrangement. For the sake of achieving a further complexity reduction, the base station opted out of using the optimum but relatively complex ML-based MUD. Instead, it employed Minimum Mean-Square Error-assisted Successive Interference Cancellation (MMSE-SIC) MUD, which is capable of iteratively eliminating the inter-user interference.

5.6.1 Trellis-based Syndrome Decoding

To elaborate further, the BSD-TTCM decoder shown in Figure 5.20 invokes trellis-based syndrome decoding, which operates over a syndrome-based error trellis [223, 221, 222]. More explicitly, each path of an error trellis corresponds to a unique channel error for a given received syndrome. Specifically, the resultant trellis will be a legitimate codeword-trellis when the syndrome zero, hence the family of conventional decoding algorithms such as the Viterbi or MAP decoders can be invoked for estimating the most likely channel error for a given syndrome. Let us now have a look at the construction procedure of the syndrome-based error trellis for the specific case of convolutional codes.

As stated in the previous section, the conventional code trellis of convolutional codes can be fully characterised using the generator matrix $\mathbf{G}$, while the error trellis can be constructed using the parity check matrix $\mathbb{H}^{\mathrm{T}}$, which is also known as the syndrome former. Following the example presented in [225], we consider the $2/3$-rate conventional code of Figure 5.16(a), where the generator matrix $\mathbf{G}$ is given by:

$$\mathbf{G} = \begin{pmatrix} 1+D & D & 1+D \\ D & 1 & 1 \end{pmatrix} . \tag{5.27}$$

The corresponding syndrome former is as follows[8]:

$$\mathbb{H}^{\mathrm{T}} = \begin{pmatrix} 1 \\ 1+D^2 \\ 1+D+D^2 \end{pmatrix} . \tag{5.28}$$

[8]The way of extracting the syndrome former from the generator matrix of Equation (5.27) can be found in Appendix C

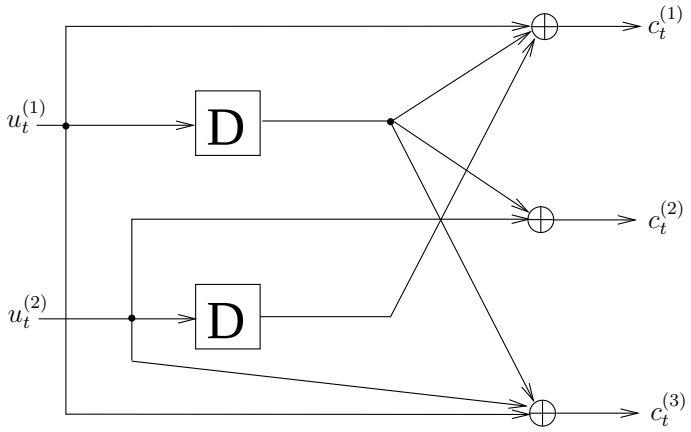

(a) Encoder based on **G** of Equation (5.27).

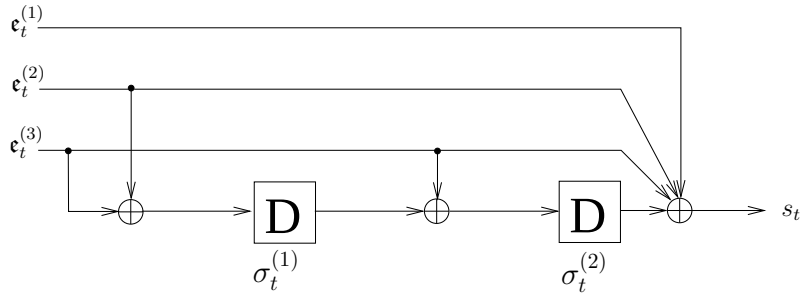

(b) Syndrome former based on $\mathbb{H}^{\mathrm{T}}$ of Equation (5.28).

Figure 5.16: Schematic diagram of a convolutional code encoder based on the syndrome matrix of Equation (5.27) and the syndrome former is given in Equation (5.28) [225].

Figure 5.16(a) illustrates the realisation of a classical (n,k) convolutional code. Then, at a particular time instant the input information sequence $\{u_t\} = \left\{u_t^{(1)}, \ldots, u_t^{(k)}\right\}$ will be encoded into $\{c_t\} = \left\{c_t^{(1)}, \ldots, c_t^{(n)}\right\}$. Let $\{y_t\} = \left\{y_t^{(1)}, \ldots, y_t^{(n)}\right\}$ denote the received sequence, which is therefore given by:

$$y_t^i = c_t^i \oplus \mathfrak{e}_t^i \,, \tag{5.29}$$

where $\{\mathfrak{e}_t\} = \left\{\mathfrak{e}_t^1, \ldots, \mathfrak{e}_t^n\right\}$ is the channel error sequence encountered during transmission, while $\oplus$ represents the modulo-two operation. Similarly, the resultant syndrome sequence, s, can be evaluated using the syndrome former $\mathbb{H}^{\mathrm{T}}$ as [223, 225]:

$$s = y\mathbb{H}^{\mathrm{T}} = (c + \mathfrak{e})\mathbb{H}^{\mathrm{T}} = \mathfrak{e}\mathbb{H}^{\mathrm{T}} \,. \tag{5.30}$$

More explicitly, Figure 5.16(b) portrays the realization of the syndrome former. The error sequence $\{\mathfrak{e}_t\}$ is then fed into the syndrome former for the case of estimating the corresponding syndrome s_t. Note that $\mathbb{H}^{\mathrm{T}}$ in our example is given by the syndrome former of Equation (5.28). Additionally, as the estimated syndrome may assume both $s_t = 0$ and $s_t = 1$, the resultant trellis can be divided into a pair of sub-trellis, as depicted in Figure 5.17. Here, each sub-trellis has four different states corresponding to 2^d, where $d = 2$ is the number of shift register stages. Hence, the state at instant t is $\sigma_t = (\sigma_t^{(1)}, \sigma_t^{(2)})$ where each branch evolves from σ_{t-1} to σ_t and is labelled by the error sequence $e_t = (e_t^{(1)}, e_t^{(2)}, e_t^{(3)})$, as seen Figure 5.17.

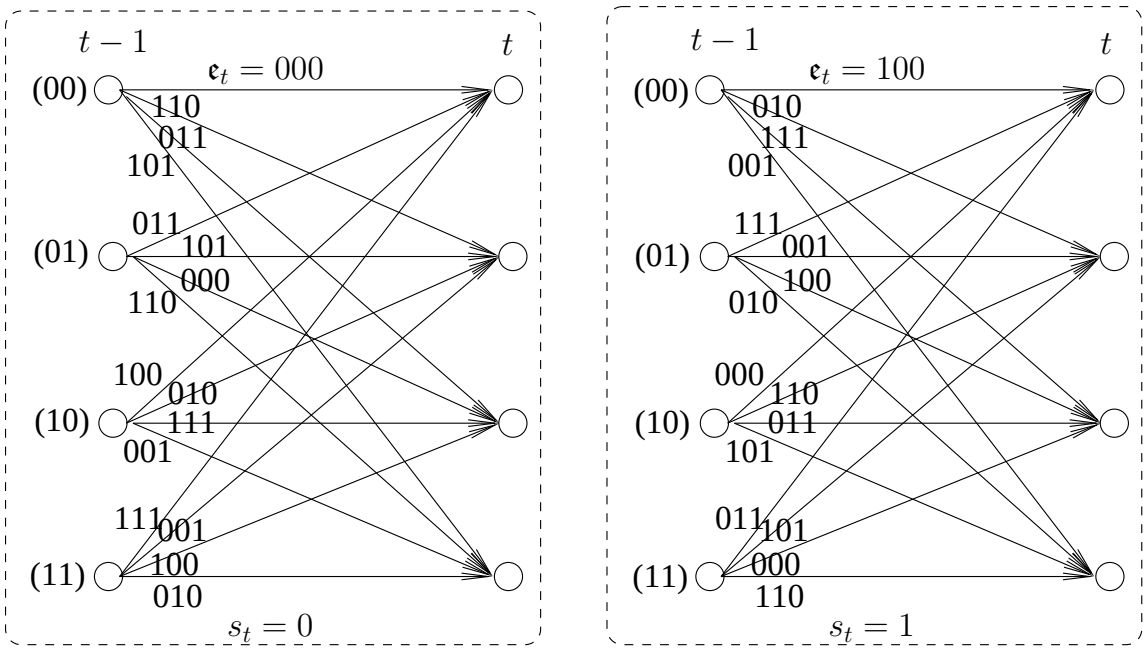

Figure 5.17: The sub-trellis of the syndrome-based error $\mathbb{H}^{\mathrm{T}}$ corresponding to both $s_t = 0$ and $s_t = 1$.

Let us assume that we have received $\{y\}_{t=1}^{3} = \{011\ 011\ 111\}$, where the received sequence and the realistic channel error sequence $\{\mathfrak{e}_t\}$ encountered yield the same syndrome according to Equation (5.30). Hence, entering the received sequence into the syndrome former circuit of Figure 5.16(b), we get $\{s\}_{t=1}^{3} = \{0,\ 1,\ 0\}$ associated with the states of $\sigma_1 = \{10\}$, $\sigma_2 = \{10\}$ and $\sigma_3 = \{10\}$, respectively. The overall trellis can be assembled by starting from the initial state $\sigma_0 = \{00\}$ and concatenating the sub-trellis of Figure 5.17 according to the estimated syndrome s_t. To elaborate a like further, we opted for serially concatenating the sub-trellis of $s_t = 0$ with $s_t = 1$ and $s_t = 0$, resulting in the overall error-based trellis of Figure 5.18.

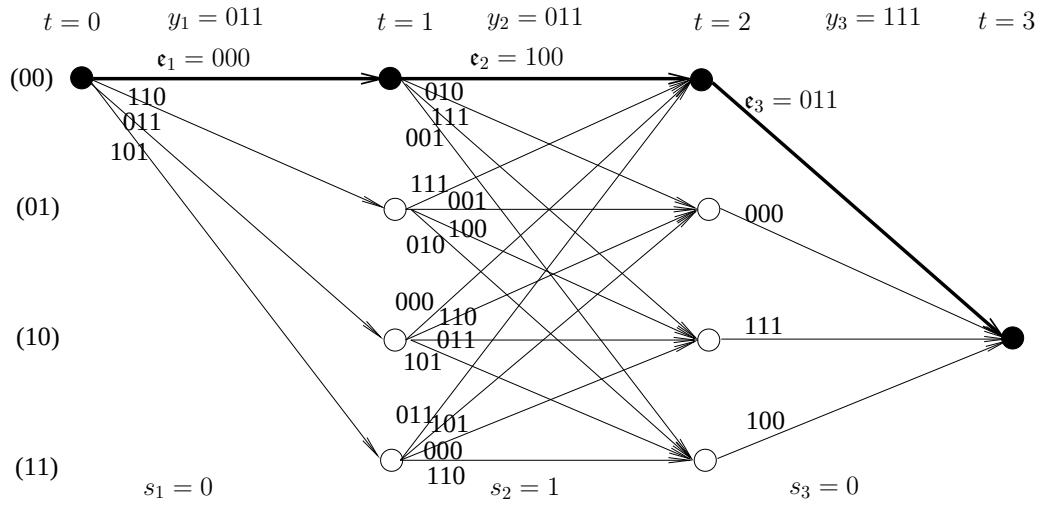

Figure 5.18: Syndrome-based error trellis using $\mathbb{H}^{\mathrm{T}}$ associated with the received sequence of $\{y\}_{t=1}^{3} = \{011\ 011\ 111\}$.

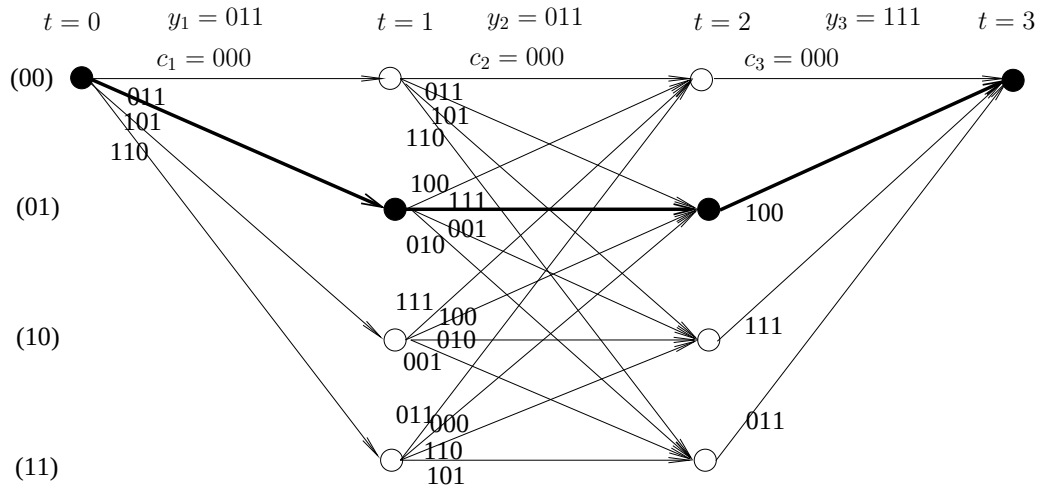

Figure 5.19: Codeword-based trellis of a convolutional code using **G** associated with the received sequence of $\{y\}_{t=1}^{3} = \{011\ 011\ 111\}$. Here each path can be mapped from Figure 5.18 using Equation (5.31).

The error trellis depicted in Figure 5.18 is reciprocal counterpart of the conventional code trellis of Figure 5.19, which is constructed using the generator **G** of Equation (5.27). Here the state at t instant is $(u_t^{(1)}, u_t^{(2)})$ while each branch is labelled with the codeword bits $c_t = (c_t^{(1)}, c_t^{(2)}, c_t^{(3)})$ as Figure 5.17 shows[9]. To elaborate further, let us consider the arbitrary error path of $\{\hat{\mathfrak{e}}\}_{t=1}^{3} = \{000\ 100\ 011\}$, which is marked by the bold line of Figure 5.18. Given the received sequence $\{y\}_{t=1}^{3} = \{011\ 011\ 111\}$, the estimated codeword sequence $\{\hat{c}\}$ can be estimated as:

$$\hat{c}_t^i = \hat{\mathfrak{e}}_t^i \oplus y_t^i\,, \tag{5.31}$$

where we have $\{\hat{c}\}_{t=1}^{3} = \{011\ 111\ 100\}$, which is shown by the thicker lines of the trellis of Figure 5.19. Thus, we have a one-to-one mapping relationship between a pair of paths of both figures [223, 225]. Every path of the error trellis corresponds to a unique path in the conventional code trellis. Therefore, typical decoding algorithms, such as Viterbi and the MAP decoders, can be invoked for estimating the most likely error of the received sequence.

5.6.2 System Model

Our system model in section can also be viewed as the Phase-I transmission of Figure 5.2, where similar to the analysis of Section 5.3, the binary sources $\{b_{1,i}\}_{i=1}^{N}$ and $\{b_{2,i}\}_{i=1}^{N}$ differ by the noise process $\{e_i\}_{i=1}^{N}$, where N is the length of each source block. The noise process is constituted by a BSC realization of a Bernoulli distributed random variable $\mathbb{E}$ associated with the parameter $p_e \in [0, 0.5]$ ($\mathbb{E} \sim \mathfrak{B}(p_e)$), s.t. $b_{2,i} = b_{1,i} \oplus e_i$ with a probability of $\Pr(b_1) \neq \Pr(b_2) = p_e$. Each user will encode its information sequence using TTCM at a coding rate of $R_{cm} = \frac{m}{m+1}$ and an $2^{m+1} = M'$-level PSK/QAM modulation scheme. Both TTCM-coded sequences, namely $\{c_{1,i}\}_{i=1}^{K}$

[9] Also, the trellis emerges and terminated at all-zero state, where termination bits are assumed to be employed.

and $\{c_{2,i}\}_{i=1}^{K}$ associated with $K = N \cdot (1/R_{cm})$, will be mapped onto the corresponding modulated symbols $\{x_1\}$ and $\{x_2\}$, respectively, before transmission over an uncorrelated Rayleigh fading MAC.

Note that $\{x_1\}$ and $\{x_2\}$ are complex-valued phasors that represent the $(m+1)$-bit transmitted codewords $\{c_1\}$ and $\{c_2\}$, which can be obtained using the $\mu(\cdot)$-QAM/PSK mapping function. Again, similar to Section 5.3, our transmission scenario might be interpreted as an SDMA [156] system that support L users, each of whom is equipped with a single antenna, while the base station has P receive antennas. Thus, the signal $\mathbf{y}$ received at the base station is a $(P \times 1)$-element vector, which can be written as:

$$\mathbf{y = Hx + n}\,, \tag{5.32}$$

where $\mathbf{H}$ is an $(P \times L)$-element channel matrix, while $\mathbf{x}$ is a $(L \times 1)$-element transmitted signal vector and $\mathbf{n}$ is an $(P \times 1)$-element noise vector with a zero mean and a variance of $N_0/2$ per dimension. In order to avoid the computational complexity associated with ML-based MUD, we opted for the low-complexity linear MMSE-based MUD [215][10]. The MMSE-detected signal can written as:

$$\begin{aligned}\mathbf{z}_{\text{mmse}} &= W_{\text{mmse}}^{H}\mathbf{y} \\ &= \left(\mathbf{H}^{H}\mathbf{H} + N_0 I_P\right)^{-1}\mathbf{H}^{H}\mathbf{Hx} \\ &+ \left(\mathbf{H}^{H}\mathbf{H} + N_0 I_P\right)^{-1}\mathbf{H}^{H}\mathbf{n}\,,\end{aligned} \tag{5.33}$$

where $\mathbf{H}^H$ is the Hermitian transpose of the channel matrix, while I_P is an $(P \times P)$-element identity matrix. The performance of a specific user can be further improved by successively cancelling the off-diagonal $\left(\mathbf{H}^{H}\mathbf{H} + N_0 I_P\right)^{-1}\mathbf{H}^{H}\mathbf{H}$ element in the left part of Equation (5.33) corresponding to the other user. Thus, we implemented the low-complexity MMSE-aided SIC MUD of [215, Section 8.3].

5.6.3 Distributed Joint Source-TTCM-BSD Decoder

Our proposed DJSTTCM-BSD decoder is shown in Figure 5.20. Here, the iterative detection follows a similar structure to that used in Section 5.3.2, where two different iterations have been used, as shown in Figure 5.20:

- Inner Iteration (I_{in}): is the iteration between the two BSD-TTCM decoders, in which the correlation is exploited by exchanging the *extrinsic* LLRs.
- Outer Iteration (I_{out}): is the iteration between the MUD and BSD-TTCM decoders, which aims for combating the deleterious effects of channel fading by exchanging the *extrinsic*

[10] All possible M^L combinations of the transmitted symbols have to be considered when using the ML detector. By contrast, only M combinations are invoked for the MMSE MUD, where M is the number of the constellation points.

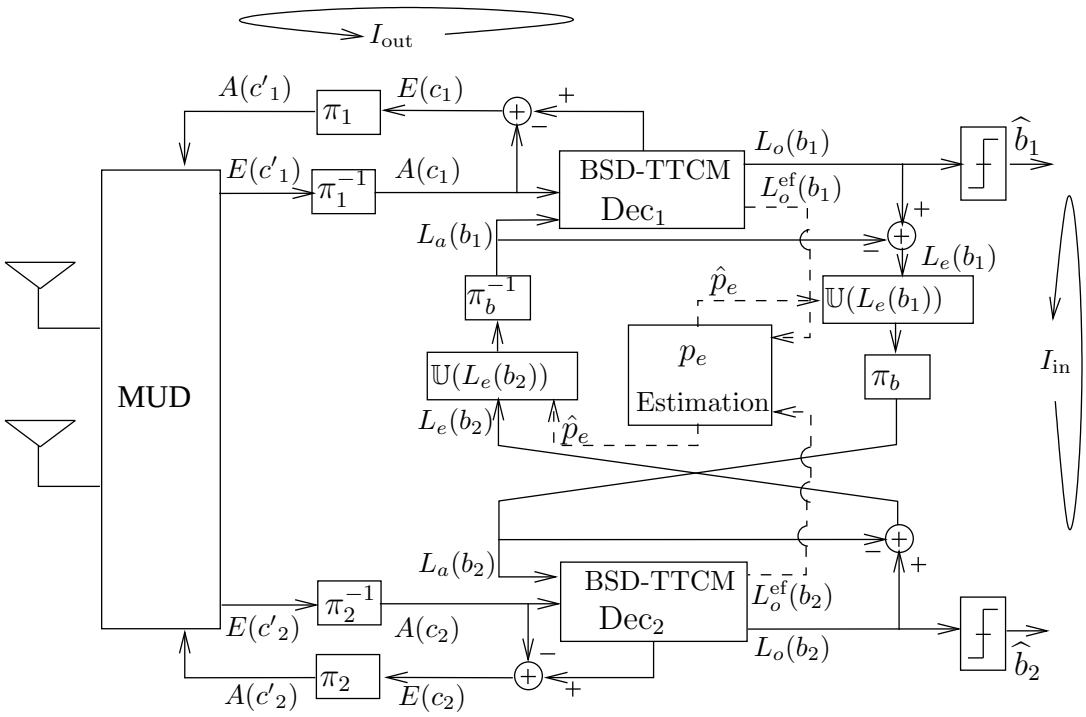

Figure 5.20: Schematic diagram of the DJSTTCM-BSD receiver communicating over a Rayleigh fading MAC. Here, the transmission might be viewed as the Phase-I link of Figure 5.2. The notation $L(\cdot)$ represents the LLR, while the subscripts *a*, *e* and *o* represent the *a priori*, *extrinsic* and *a posteriori* nature of the LLRs, respectively. $A(\cdot)$, $E(\cdot)$ and $P(\cdot)$ represent the *a priori*, *extrinsic* and *a posteriori* probabilities. The BSD-TTCM decoder is illustrated further in Figure 5.21. The block $\mathbb{U}(L_e(b_{1,2}))$ represents the update function of Equation (5.40), while the "p_e Estimation" block represents cross-over probability estimation of Equation (5.41).

probabilities [156, 171].

The channel information probabilities, $\Pr(\mathbf{y} \mid x_1)$ and $\Pr(\mathbf{y} \mid x_2)$, gleaned from the MUD's output can be estimated similar to Equation (5.8) and Equation (5.9) and that were discussed in Section 5.3.2.

Similar to the TTCM decoder of Figure 2.8, each of our BSD-TTCM decoders consists of two parallel concatenated syndrome-based TCM MAP decoders. Figure 5.21 shows the schematic of one of the two constituent decoders of the BSD-TTCM decoder block portrayed in Figure 5.20[11]. First, the k^{th} received symbol associated with our BSD-TTCM decoder is hard-demapped onto the nearest point of the corresponding transmitted symbol x_k, yielding the hard-demapped symbol $\hat{y}_k$. Recall from our discussion in Section 2.4.2 that in the TTCM the odd and even symbols are punctured for the upper and lower TCM encoders, respectively. Accordingly, the parity bits associated with the punctured hard-demapped symbols are set to zero. Next, a pre-correction sequence $\hat{\mathbf{e}}_k$ is needed for updating any predicted errors in the hard-demapped sequence, where this sequence is set to zero during the first iteration. Then, the syndrome s is computed for estimating the corrected

[11]For the sake of clearly illustration we opted to draw only one of the parallel decoders.

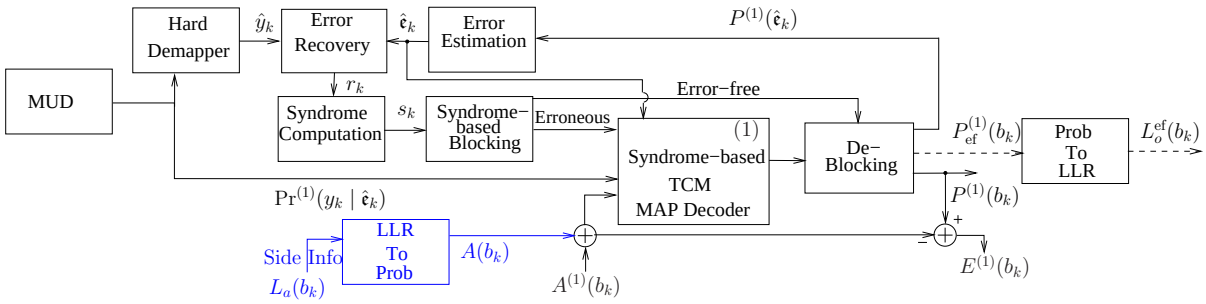

Figure 5.21: Schematic of the proposed BSD-TTCM decoder. Here only one constituent decoder is shown, where $A^{(1)}$, $E^{(1)}$ and $P^{(1)}$ represent the *a priori*, *extrinsic* and *a posteriori* probabilities related to the corresponding syndrome-based TCM MAP decoder, while $\hat{\mathfrak{e}}_k$ denotes the channel error on the transmitted k^{th} symbol. $L_a(b_k)$ denotes the *a priori* side-information LLR gleaned form the other "BSD-TTCM Dec" decoder during I_{in} of Figure 5.20.

symbol stream r via the syndrome former matrix $\mathbb{H}^T$ as [223][12]:

$$s = r\mathbb{H}^T \,, \tag{5.34}$$

where each bit of the corrected symbol stream r_k is related to both $\hat{y}_k$ and $\hat{\mathfrak{e}}_k$ as [223]:

$$r_k = \hat{y}_k \oplus \hat{\mathfrak{e}}_k \,, \tag{5.35}$$

where r_k, $\hat{y}_k$ and $\hat{\mathfrak{e}}_k$ are represented by $(m+1)$-bit.

The syndrome sequence is then analysed in order to split the received sequence into error-free and erroneous sub-blocks. Hard-decisions are applied to the error-free sub-blocks without feeding the erroneous sub-blocks into the MAP decoder. As it will be detailed later in Section 5.6.3.2, the *a posteriori* probabilities corresponding to the error-free sub-blocks will be employed for estimating the cross-over probability $\hat{p}_e$, as illustrated in Figure 5.21.

5.6.3.1 Syndrome-based Joint MAP Decoder

Again, as in the conventional TTCM decoder, which was illustrated in Section 2.4.2, both constituent decoders have a similar parallel structure in which iterative decoding is employed for exchanging extrinsic information. Here, the syndrome-based MAP decoder of [223,222] is employed in our BSD-TTCM decoder. As stated in Section 5.6.1, the syndrome-based MAP decoder relies upon the error trellis, which is constructed using the syndrome former $\mathbb{H}^{\text{T}}$. In the conventional code-based trellis, each trellis path represents a possible legitimate codeword. By contrast, each path in the error-based trellis represents a hypothetical error sequence, where as shown in our example of Section 5.6.1 every path along the error trellis corresponds to a unique path in its conventional code trellis counterpart. Furthermore, it was demonstrated in [225] that both trellises have

[12]The syndrome former matrix $\mathbb{H}^T$ associated with our scheme is constructed in Appendix C.

the same complexity. Thus, the syndrome-based MAP decoder computes the *a posteriori* probabilities for the channel errors experienced by the information symbol. More explicitly, the probability $\Pr(y_k \mid x_k)$ of receiving y_k given x_k was transmitted will be modified to $\Pr(y_k \mid \mathfrak{e}_k)$ of receiving y_k, given that the error $\mathfrak{e}_k$ is encountered, which can be expressed as:

$$\Pr(y_k \mid \mathfrak{e}_k) = \frac{1}{\pi N_0} \exp\left(-\frac{|y_k - h_k x_k|^2}{N_0}\right) . \tag{5.36}$$

The syndrome-based TCM MAP decoder shown in Figure 5.21 would calculate the *a posteriori* probabilities corresponding to the error-free sub-blocks. More explicitly, upon recalling the analysis of Section 2.3.2, the channel's transition metric is formulated as [223]:

$$\gamma_k(\grave{s}, s) = \Pr(b_k) \cdot \Pr(y_k \mid \mathfrak{e}_k) , \tag{5.37}$$

where $\Pr(b_k)$ is the *a priori* probability of the information part of $\mathfrak{e}_k$, which is initialised to be equiprobable for the first iteration, while $(\grave{s}, s)$ denotes the transition emerging from state $\grave{s}$ to state s. However, the forward and backward recursions coefficients, namely α_k and β_k have to consider the side-information provided by the other decoder which is formulated additionally as:

$$\alpha_k(s) = \sum_{\text{all } \grave{s}} \alpha_{k-1}(\grave{s}) \cdot \gamma_k(\grave{s}, s) \cdot A(b_k) , \tag{5.38}$$

$$\beta_{k-1}(\grave{s}) = \sum_{\text{all } s} \beta_k(s) \cdot \gamma_k(\grave{s}, s) \cdot A(b_k) , \tag{5.39}$$

where as shown in Figure 5.21, $A(b_k)$ is the *a priori* probability provided by the other BSD-TTCM decoder of Figure 5.20 corresponding to the LLR $L_a(b_k)$, which is the interleaved and updated version of $L_e(b_k)$.

5.6.3.2 Cross-over Probability Estimation

During the I_{in} of Figure 5.20 the exchanged LLRs have to be updated using an accurate estimate of the cross-over probability $\hat{p}_e$ by invoking the following update function:

$$\mathbb{U}(L_e(b_{1,2})) = \ln \frac{(1-\hat{p}_e)\exp[L_e(b_{1,2})] + \hat{p}_e}{(1-\hat{p}_e) + \hat{p}_e \exp[L_e(b_{1,2})]} , \tag{5.40}$$

which is shown in Figure 5.20. As stated previously, an inaccurate BSC cross-over estimate $\hat{p}_e$ could lead to an error propagation during the joint iterative decoding process of Figure 5.20. Our proposed joint decoder would provide an accurate estimate of $\hat{p}_e$ based on the reliable error-free LLRs gleaned from the two BSD-TTCM decoders' output from Figure 5.21, namely, $L_o^{\text{ef}}(b_{1,2})$ that are linked to the error-free sub-blocks as follows:

$$\hat{p}_e = \frac{1}{N_{\text{ef}}} \sum_{i=1}^{N_{\text{ef}}} \frac{\exp[L_o^{\text{ef}}(b_1^i)] + \exp[L_o^{\text{ef}}(b_2^i)]}{(1+\exp[L_o^{\text{ef}}(b_1^i)])(1+\exp[L_o^{\text{ef}}(b_2^i)])} , \tag{5.41}$$

Coded Modulation	**TTCM**
Modulation Scheme	8PSK
Code Rate	R_{cm} =2/3
Puncturing Rate	R_p =1
Decoding Algorithm	Syndrome-based MAP
TTCM Iteration	$I = 8$
Inner Iteration	$I_{\text{in}} = 2$
Outer Iteration	$I_{\text{out}} = 2$
Mapper Type	Set-Partitioned
Number of Symbol	$N_s = 12\,000$ symbols per frame
Number of Frames	4000
Channel	2×2 Uncorrelated Rayleigh fading MAC
Channel State Information (CSI)	Known
MUD Type	ML and MMSE-SIC

Table 5.6: Simulation parameters for the DJSTTCM-BSD scheme transmission of the schematic of Figure 5.20.

where N_{ef} is the error-free LLR sub-block size. Similarly, the conventional codeword-trellis based TTCM method employs the same formula of Equation (5.41) when evaluating $\hat{p}_e$. However using the entire LLR block as the conventional TTCM decoder is unable to separate the received sequence into erroneous and error-free sub-blocks. Figure 5.22 demonstrates the accuracy of our probability estimator based on the DJSTTCM-BSD of Figure 5.21 in comparison to the conventional DJSTTCM based method that its performance is shown in Figure 5.23, where p_e is artificially varied sinusoidally between 0.025 and 0.42. The simulation parameters are listed in Table 5.6. Note that in order to make the figure legible, we portray the exact p_e based cosine curve at two values, namely at $E_b/N_0 = 6$ dB and $E_b/N_0 = 9$ dB, which are represented by filled circles. We opted for using $2/3$-rate TTCM-8PSK transmission over a uncorrelated Rayleigh fading MAC using a block length of 12 000 8PSK symbols . Additionally, the decoder invokes "$I_{\text{in}} = 2$ " and "$I_{\text{out}} = 2$", while the iteration between the two TCM components of the TTCM decoder $I = 8$ iterations were used inside the TTCM and BSD-TTCM decoders of Figure 5.3 and Figure 5.20, respectively. As Figure 5.22 demonstrates, our proposed estimator was capable of achieving an accurate $\hat{p}_e$ estimation of the sinusoidally varied p_e values. More explicitly, observes in Figure 5.22 that our proposed estimator is capable of attaining an accurate BSC cross-over probability prediction at $E_b/N_0 = 6$ dB. By contrast, the conventional DJSTTCM estimator characterised in Figure 5.23 only achieved a similar estimation accuracy at the 3 dB higher value of $E_b/N_0 = 9$ dB. More explicitly, Figure 5.24(a) and Figure 5.24(b) show the slices of our 3D illustration seen in Figure 5.22 and Figure 5.23, both recorded at $E_b/N_0 = 6$ dB, respectively. Upon comparing Figure 5.22 and Figure 5.23, our proposed-BSD algorithm cis seen to generate a good estimate of a fluctuating correlation. This observation was also confirmed by our BER simulation results seen in Figure 5.25.

In order to ensure an accurate $\hat{p}_e$ estimation, we first have to determine the optimum size of the error-free sub-block LLR $L^o_{\text{ef}}(b^{1,2})$. This is achieved by heuristically finding the minimum size of $L^o_{\text{ef}}(b^{1,2})_{\text{min}}$, which was found to be $L^o_{\text{ef}}(b^{1,2})_{\text{min}} \geq 2400$.

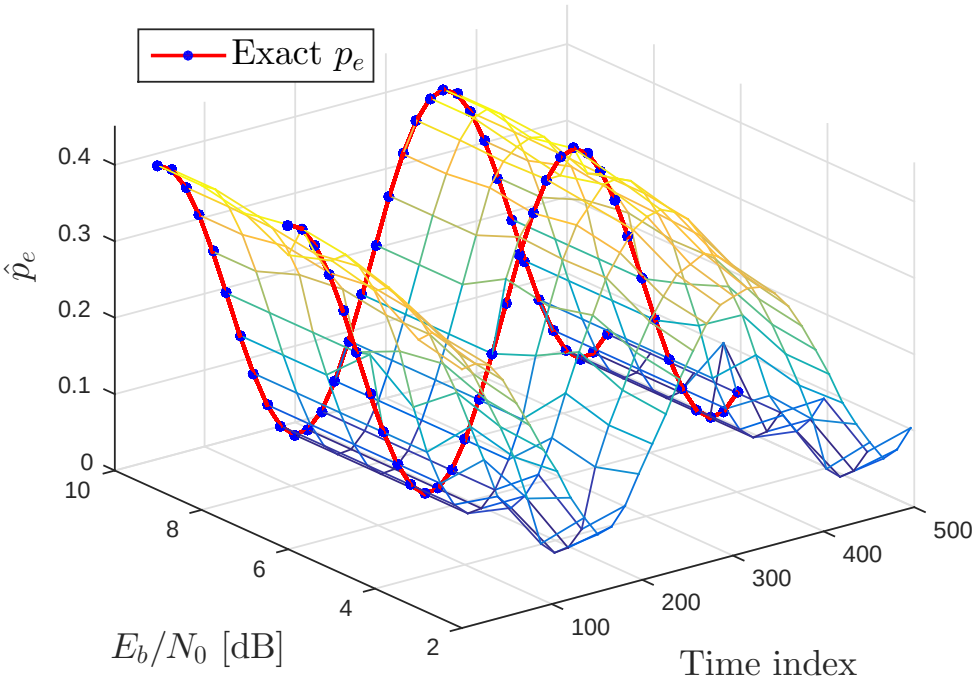

Figure 5.22: Estimated $\hat{p}_e$ versus both E_b/N_0 and varying time when using the **DJSTTCM-BSD** scheme of Figure 5.20 for sinusoidal variation of the cross-over probability, where the **MMSE-SIC** has been invoked as our MUD. Table 5.6 summarises the simulation parameters.

5.6.4 Complexity Reduction Results

The BER versus E_b/N_0 performance of our proposed scheme seen in Figure 5.20 is shown in Figure 5.25, where the two user signals are transmitted over a Rayleigh fading MAC. Again, both users employ 2/3-rate TTCM-8PSK where "$I_{\text{in}} = 2$" and "$I_{\text{out}} = 2$" are used by the decoder, where the simulation parameters are listed in Table 5.6. The correlation coefficient is $\rho = 0.4$ which corresponds to $p_e = 0.3$. Additionally, for all simulation scenarios the base station employs the MMSE-SIC as the MUD, while a single ML base MUD detection is invoked by the schematic of Figure 5.20 that is labelled by the triangle markers in Figure 5.25. It may be readily observed from Figure 5.25 that for the MMSE-SIC arrangement, the conventional decoder based distributed scheme of Figure 5.3 referred to as "DJSTTCM-Conventional MMSE-SIC" outperforms our proposed scheme for the idealised scenario when p_e is perfectly known at the base station side by about 1 dB at a BER of 10^{-6}. This is not unexpected, because the BSD scheme of Figure 5.21 has been proposed mainly as low-complexity design [223, 225]. However, for the realistic scenario, when the correlation coefficient unknown at the decoder, our proposed "DJSTTCM-BSD-MMSE-SIC" scheme has a valuable 1.5 dB gain over the conventional DJSTTCM based scheme of Figure 5.3

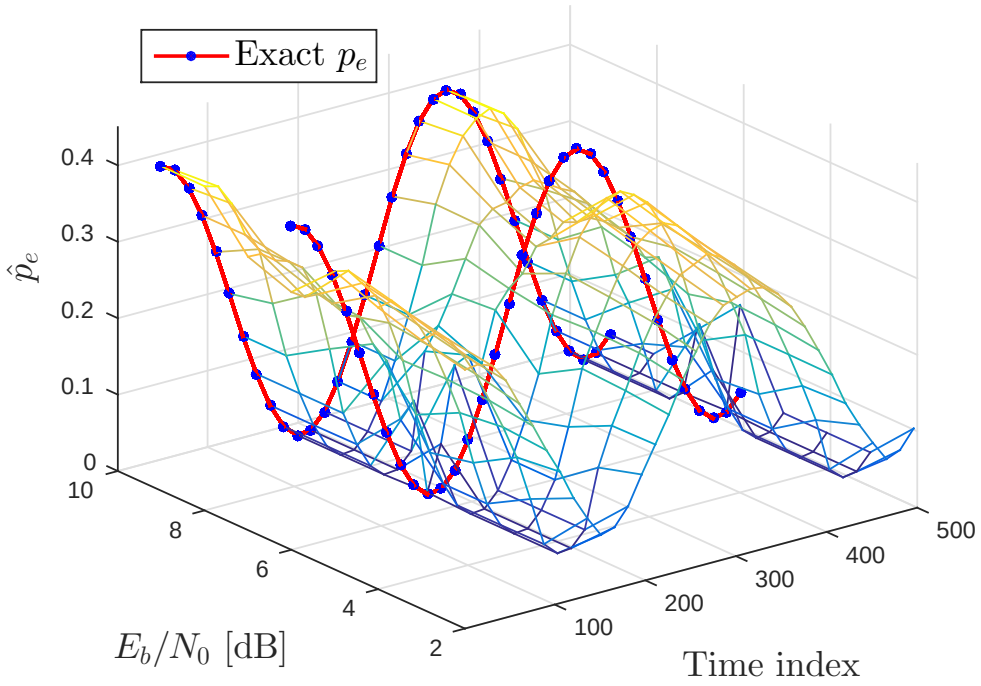

Figure 5.23: Estimated $\hat{p}_e$ versus both E_b/N_0 and varying time when using the conventional **DJSTTCM** scheme of Phase-I transmission of Figure 5.2 for sinusoidal variation of the cross-over probability, where the **MMSE-SIC** has been invoked as our MUD. Table 5.6 summarises the simulation parameters. Here we invoked Approximated Log-MAP based decoder of Figure 5.3.

as seen in Figure 5.25. Moreover, as expected, when invoking the complex ML-based MUD in the DJSTTCM-BSD scheme of Figure 5.20 the "DJSTTCM-BSD-ML" scheme outperforms the MMSE-SIC-based scheme "DJSTTCM-BSD-MMSE-SIC", by an E_b/N_0 gain of 2.5 dB as seen in Figure 5.25. In order to investigate the achievable decoding complexity reduction, we have analysed the complexity of the "DJSTTCM-BSD-MMSE-SIC" scheme of Figure 5.20 for the E_b/N_0 values spanning from 5.2 dB to 6.2 dB, as shown in Figure 5.25. Here the complexity reduction is quantified by determining the number of error-free symbols that would avoid entering the error-trellis based MAP-BSD decoder of Figure 5.21 at each iteration as a percentage of the total frame length. Note that here we consider only the first user's decoder BSD-TTCM-Dec$_1$ of Figure 5.21. As Figure 5.25 suggested, upon increasing the E_b/N_0 value the complexity was considerably reduced. Quantitatively, at $E_b/N_0 = 5.6$ dB only 40% of the transmitted sequence will be fed to the MAP-BSD block of Figure 5.21. Note that conventional turbo-like decoders would consider all symbols into the codeword for decoding, i.e. 100% of the transmitted sequence. Moreover, the effect of "I_{in}" on the overall scheme's performance is also investigated in Figure 5.25. It can be readily observed that doubling the number of iterations between the BSD-TTCM decoders from "$I_{\text{in}} = 1$" to "$I_{\text{in}} = 2$" here the turbo-cliff region of the E_b/N_0 scale would lead to a significant increase in the percentage of the error-free symbols. For example, when $E_b/N_0 = 5.6$ dB, a 40% boost in the error-free symbols will attained by adding one additional inner iteration.

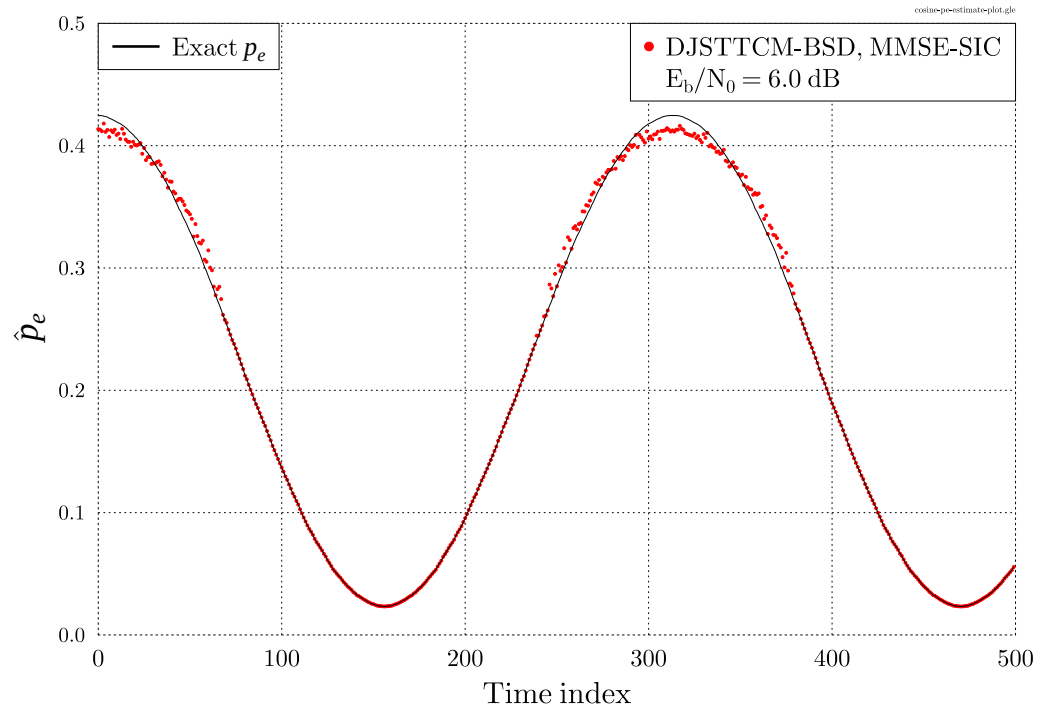

(a) DJSTTCM-BSD.

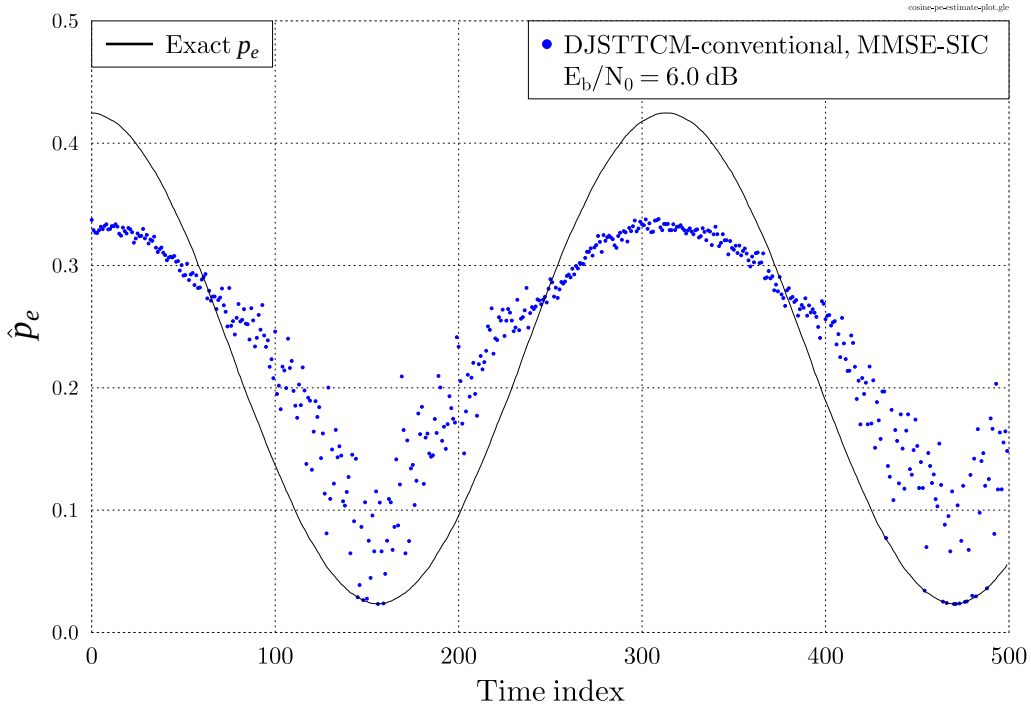

(b) DJSTTCM.

Figure 5.24: Estimated $\hat{p}_e$ versus E_b/N_0 comparison between the **DJSTTCM-BSD** and the Conventional **DJSTTCM** for sinusoidal variation, where the **MMSE-SIC** has been invoked as our MUD at the base station.

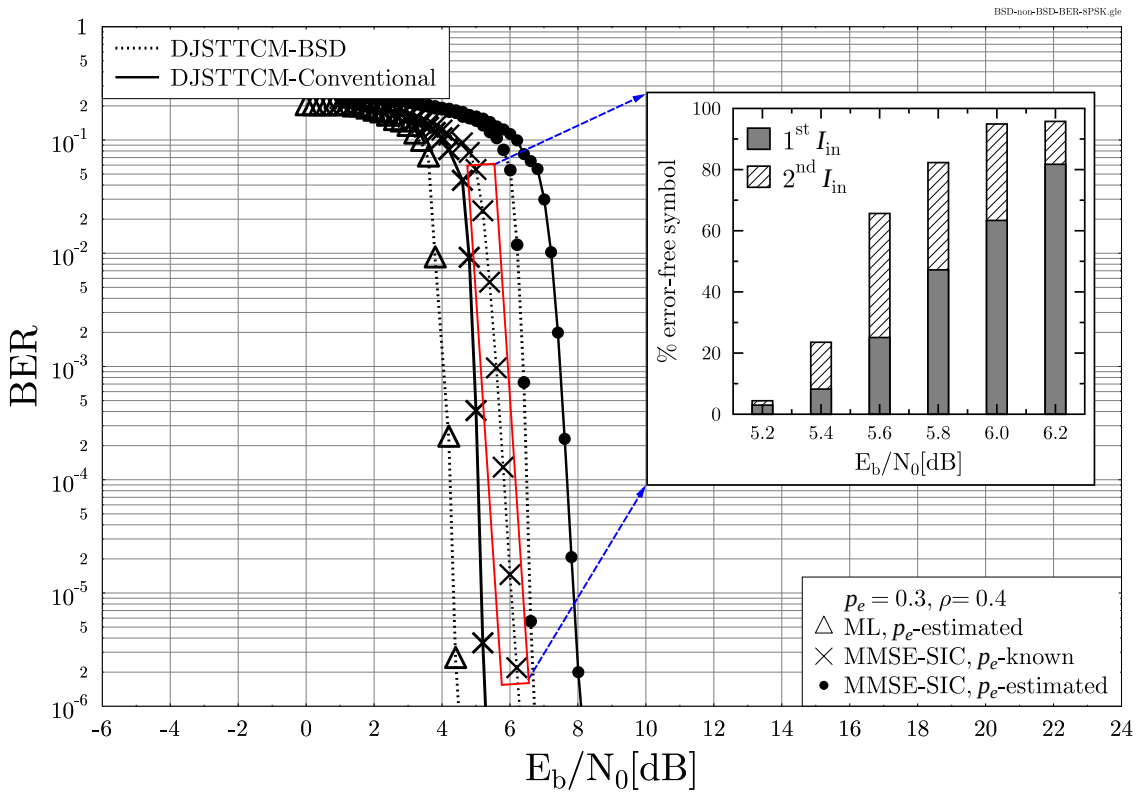

Figure 5.25: BER versus E_b/N_0 performance of the **DJSTTCM-BSD** scheme of Figure 5.3 and of the Conventional **DJSTTCM** scheme of Figure 5.21 for $\rho = 0.4$, ($p_e = 0.3$), considering **ML** and **MMSE-SIC** MUD, both for the cases when p_e is known and when it is estimated at the decoder, when communicating over a **Rayleigh fading MAC**. The parameters of Table 5.6 are used.

5.7 Chapter Conclusions

In this chapter, we have eliminated two of the idealised simplifying assumptions considered in Chapter 4. More explicitly, the chapter can divided into the following two main parts:

- In Section 5.2-Section 5.5, we have proposed the DJSTTCM scheme-aided SPM of Figure 5.2 for cooperative transmission arrangement of Figure 5.1. During Phase-I transmission, both source outputs' were TTCM encoded and then compressed before transmission through a uncorrelated Rayleigh fading MAC, rather than assuming the availability of an error-free side-information from one of the sources as in Chapter 4. Starting with Phase-I, the DJSTTCM encoder was discussed in Section 5.3.1, while the joint decoder was illustrated in Figure 5.3 of Section 5.3.2. In line with analysis of Chapter 3, we employed the EXIT chart to visualise the convergence behaviour. The EXIT curves for the outer DJSTTCM decoder were portrayed in Figure 5.4 showing the effect of the correlation. Additionally, The EXIT chart of Figure 5.5 was conceived to design the design the Phase-I transmission as follows:
  - The number of inner iterations I_{in} were determined from the stair-case trajectories.
  - The number of outer iterations I_{out} were determined from the outer and inner curves

combination that facilitate an open EXIT channel.

In Section 5.3.4, the SW/S bound of Phase-I was derived using the DCMC capacity and it was shown in Figure 5.6 that our scheme performs within 1.0 dB of the SW/S limit for $\rho = 0.4$ at a BER level of 10^{-5}, and only 0.17 bits away from the SW minimum comparison rate.

Recall from Figure 5.1 that both users were assisted by a RN that invokes the SPM scheme of Figure 5.11, during Phase-II. Different amounts of transmit power can be allocated, by means of the SPM constellation ratios, for each user's signal according to the integrity requirement. EXIT charts based investigations were used for examining the decoding convergence and for optimizing the overall system. As demonstrated in Figure 5.13, performance gains of 2.8 dB and 3.4 dB were achieved at a BER level of 10^{-5} when $\rho = 0.8$ for SPM ratios of $r_1 = 0.894$ and $r_2 = 0.447$, respectively, comparing to similar schemes dispensing with our joint decoding. Furthermore, it was demonstrated in Figure 5.15 that our cooperative DJSTTCM-SPM scheme of Figure 5.2 is capable of exploiting the source correlation for improving the attainable performance even when one of the user's sequence is heavily punctured. It is worth noting that the SNR threshold values at the target BER of 10^{-5} recorded for the various simulated schemes are summarised in Table 5.7.

- In Section 5.6, we have conceived a reduced-complexity DJSTTCM-aided BSD technique for practical DJSC applications. The iterative decoder of Figure 5.21 was shown to be capable of estimating the BSC's cross-over probability with the aid of the LLR blocks that were deemed to be error-free, as are identified by the syndrome sequence. Additionally, the decoding complexity of the schematic in Figure 5.21 was further reduced by invoking an MMSE-SIC based MUD that has a complexity which linearly proportional to both the number of users and to the constellation size. Finally, in Section 5.6.4 an accurate correlation estimation was conceived and our iterative decoder demonstrated an accurate correlation estimation for time-variant BSC cross-over probability coefficients and required about 3 dB less power for the same correlation than the conventional DJSTTCM decoder, despite its considerable complexity reduction.

The transmission of the correlated sources will be supported by a sophisticated Networks Coding (NC) schemes in the context of cooperative communications in the next chapter.

Scheme		**DJSTTCM-SPM (Phase-I and Phase-II)**		
Schematic		Figure 5.2		
Decoder		DJSTTCM decoder of Figure 5.3		
Parameters		Table 5.2 and Table 5.4		
Transmission	Figure	ρ	Scheme	SNR [dB] at BER= 10^{-5}
Phase-I	5.6	0.8	$I_{\text{out}} = 4$, $I_{\text{in}} = 4$	0.15
			$I_{\text{out}} = 1$, $I_{\text{in}} = 4$	0.52
		0.6	$I_{\text{out}} = 4$, $I_{\text{in}} = 4$	1.2
			$I_{\text{out}} = 1$, $I_{\text{in}} = 4$	1.95
		0.4	$I_{\text{out}} = 4$, $I_{\text{in}} = 4$	1.95
			$I_{\text{out}} = 1$, $I_{\text{in}} = 4$	2.8
		0.2	$I_{\text{out}} = 4$, $I_{\text{in}} = 4$	2.6
			$I_{\text{out}} = 1$, $I_{\text{in}} = 4$	3.5
Phase-II	5.13	0.8	$r_1 = 0.894$	5.2
			$r_2 = 0.447$	8.5
		0.6	$r_1 = 0.894$	6.1
			$r_2 = 0.447$	9.75
		0.4	$r_1 = 0.894$	6.8
			$r_2 = 0.447$	10.4
		0.2	$r_1 = 0.894$	7.0
			$r_2 = 0.447$	10.8

Table 5.7: SNR threshold values of various schemes when transmitting over uncorrelated Rayleigh fading channels of Phase-I and Phase-II links, where ρ denotes the correlation coefficients, while r_1 and r_2 represent the SPM weighting factor pair. The results are extracted from Figure 5.6 and Figure 5.13.

Chapter 6

TTCM-Aided Distributed Joint Source-Channel Coding-Based Adaptive Dynamic Network Coding

6.1 Introduction

In Chapter 5, the two correlated Source Nodes (SN)s were supported by a Decode-and-forward (DF)-based Relay Node (RN) that Forwards both of the received signals to a Destination Node (DN). This might be an acceptable solution when there is no direct transmission link between the SNs and DN owing to its low quality. By contrast, in this chapter we will consider the existence of direct links between the SNs and DN, where Network Coding (NC) constitutes an efficient solution. As stated in Section 1.4, NC [125] is an efficient data transport technique that is capable of increasing the overall achievable throughput of the system, while reducing both the energy required as well as the packet delay [126]. Unlike DF-based RNs cooperative schemes, the RNs of NC schemes formulate specific combinations of the received signals, rather than simply forwarding a replicate of them [129]. Motivated by its benefits, in this chapter the transmission of the correlated SNs previously investigated in Chapter 5 will be additionally supported by NC schemes in the context of cooperative communications.

Both the NC and Distributed Source Coding (DSC) schemes have to be carefully designed, when transmitting correlated sources over cooperative networks [18, 226]. More explicitly, the NC would offer multiplexing and/or diversity gains, when communicating over hostile channels, while the DSC scheme would offer source compression by exploiting the correlation between sources. The problem of multi-casting correlated sources over idealised noiseless channel was considered in [227]. Barros *et al.* generalised the problem to correlated sources communicating in a large-scale NC scenario [18]. Inspired by this theoretical contribution, several practical iterative Joint Channel-coding and Network-coding (JCN) schemes have been proposed in [228, 229, 230], where

the NC was combined with channel coding for the sake of achieving time-diversity. The JCN decoder of the schemes advocated in [228, 229, 230] was based on exchanging soft information between the channel decoder and the network decoder. More explicitly, the channel coding schemes of [228,229] invoked turbo decoder, while in [230] a Luby Transform-based decoder was employed.

When considering transmissions over a realistic noisy a environment, various Distributed Joint Source-Channel coding-aided Network-coding (DJSCN) schemes were investigated in [19, 66, 64, 231]. To elaborate further, a linear syndrome-based Slepian-Wolf code combined with random linear NC was proposed in [231]. An iterative receiver that combines a turbo equalizer, a network decoder and a source decoder was proposed in [66], when both sources are communicating over a frequency-selective fading channel. As a further development, in [64] a novel iterative turbo code-based DJSCN schemes was proposed for communicating over orthogonal block Rayleigh fading Multiple Access Relay Channels (MARC)s, where the corresponding outage probability was derived in [19].

In contrast to [66, 64], we opted for dispensing with iterative decoding between the NC decoder and the joint decoder. However, an extremely high complexity would be imposed, if we extended the scheme of [66, 64] for supporting more than two users. More explicitly, the excessive complexity is mainly imposed by the iterative decoding invoked at the receiver. Additionally, the attainable performance gain when activating such decoding iteration would be limited in our block fading channel environment [133], because the channel coding itself cannot considerably improve the BER [215].

In this chapter we intrinsically amalgamate the DJSTTCM scheme of Chapter 5 with the Dynamic Network Coding (DNC) of [133, 140, 132], resulting in systems termed as DJSTTCM-DNC. Additionally, we have also conceived the novel Adaptive Dynamic Network Coding (ADNC) design of [133] for our DJSTTCM scheme, resulting in the DJSTTCM-ADNC regime, where the RNs would adaptively transmit their corresponding frames depending on weather the signal of the sources have been successfully received at the destination or not. Hence, the scheme's overall effective throughput could be enhanced. The NC-based cooperative systems proposed in [66, 64] cannot support more than two users, because the RN signals were constructed using a simple bit-wise XOR operator. By contrast, in our NC model the RN signals are composed using non-binary linear coefficients-based equations, leading to a further scalability in our design.

The rest of the chapter is organised as follows. The proposed system model is detailed in Section 6.2, followed by our results in Section 6.3. Finally, our conclusions will be offered in Section 6.4.

6.2 System Model

The schematic of our DJSTTCM-ADNC-based cooperative transmission scheme is shown in Figure 6.1, where both the correlated SNs, namely SN_1 and SN_2 transmit their data to the DN with the

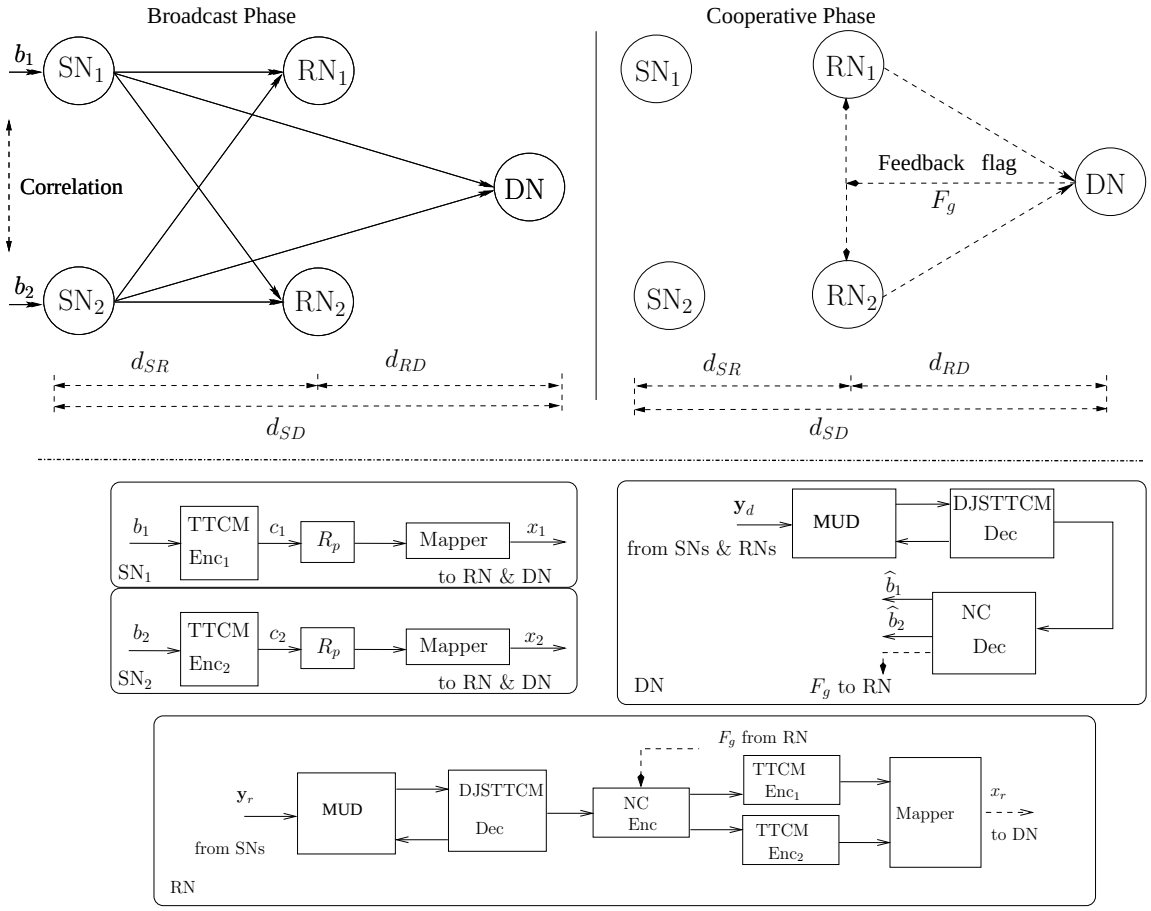

Figure 6.1: Schematic of the DJSTTCM-ADNC transmission, where d_{SD}, d_{SR} and d_{RD} are the geographical distances between $SN_{1,2}$ to DN, $SN_{1,2}$ to $RN_{1,2}$ and $RN_{1,2}$ to DN, respectively, while F_g denotes the feedback flag transmitted from the DN back to the $RN_{1,2}$. Additionally, the DJSTTCM decoder is illustrated in further details in Figure 5.3 of Section 5.3.2.

aid of the two RNs[1]. Our communication protocol might be structured into two layers, namely the NC layer and the Forward Error Correction (FEC) layer, where the NC layer is constituted by two transmission sessions, as seen at the upper part of Figure 6.1.

More explicitly, the Information Frames (IFs) are broadcast from the corresponding M number of SNs to K RNs as well as to the DN during the Broadcast Phase (BP). Next, the DN decodes the IFs received form the SNs, while the RNs decode the same IFs before encoding them into their corresponding Parity Frames (PFs). Then, PFs are transmitted to the DN during the Cooperative Phase (CP). Thus, as illustrated in Figure 6.1, the DN receives the IF that contains the original information during the BP, as well as the PF that comprises a non-binary linear combination of the IFs. The key parameters are defined in Table 6.1.

In line with the Phase-I transmission of Section 3.2.1 and of Section 5.3, the BP transmission might be viewed as an Space-Division Multiple Access (SDMA) [156] architecture, where M SNs transmit their signals to the RNs, with each RN having equipped with P receive antennas. More

[1]Our proposed scheme has a capability to support more users in a fairly straightforward manner, since both NC decoding and DJSTTCM decoding can be performed separability. Further details will be provide later in Section 6.2.2.

specifically, the signal received at the DN via the direct transmission link, namely the Source-to-Destination (SD) link, can be fully characterised using a $(P \times M)$-element channel matrix $\mathbf{H}$ as:

$$\mathbf{y}_d = \mathbf{H}_{sd}\mathbf{x}_s + \mathbf{n}\,, \tag{6.1}$$

where $\mathbf{y}_d = [y_0, y_1, \cdots, y_{P-1}]^T$ and $\mathbf{n} = [n_0, n_1, \cdots, n_{P-1}]^T$ are $(P \times 1)$-element vectors that denote the received signals and noise elements at the DN, respectively. Note that each element in $\mathbf{n}$ represents the complex-values AWGN with a variance of $N_0/2$ per dimension. Additionally, the SNs' transmitted signal $\mathbf{x}_s = [x_0, x_1, \cdots, x_{M-1}]^T$ is an $(M \times 1)$-element vector.

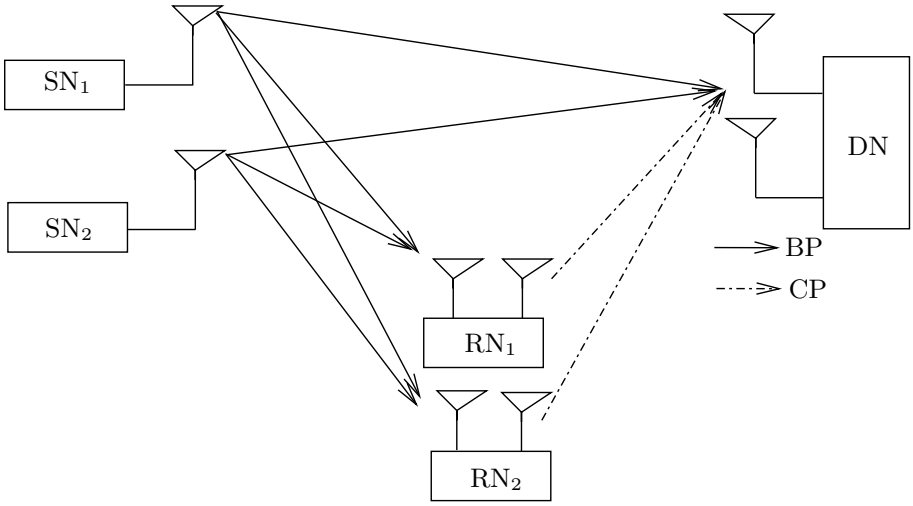

Figure 6.2: Schematic of the DJSC-aided DNC Scenario A. The simulation parameters of this scenario are detailed in Table 6.3.

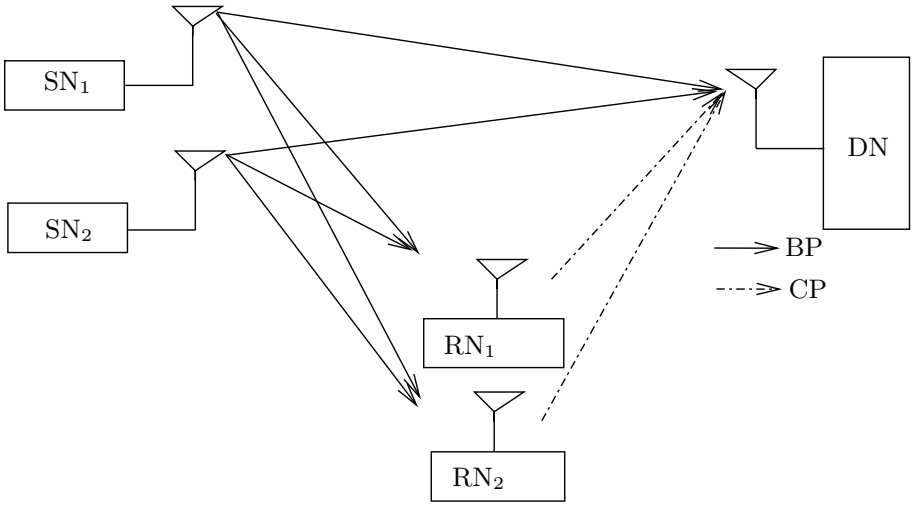

Figure 6.3: Schematic of the DJSC-aided DNC Scenario B. The simulation parameters of this scenario are detailed in Table 6.3.

This chapter considers two main configuration scenarios. The first one is portrayed in the schematic of Figure 6.2, where the channel of both phases, namely BP and CP, can be viewed as a (2×2)-elements MIMO MAC. Similar to Equation (6.1), the signal received at the j^{th} RN via the

Source-to-Relay (SR) link can be written as:

$$\mathbf{y}_{r_j} = \mathbf{H}_{sr_j}\mathbf{x}_s + \mathbf{n}\,, \tag{6.2}$$

where, we have $j \in K$ and K is the total number of RNs. Hence, for example, the channel matrix $\mathbf{H}_{sr_1}$ of Scenario A seen in Figure 6.1 for the SR link during the BP between both SNs and the RN_1 can be expressed as:

$$\mathbf{H}_{sr_1} = \begin{bmatrix} \sqrt{G_{s_1r_{1,1}}}\sqrt{P_{tx,s_1}}h_{s_1r_{1,1}} & \sqrt{G_{s_2r_{1,1}}}\sqrt{P_{tx,s_2}}h_{s_2r_{1,1}} \\ \sqrt{G_{s_1r_{1,2}}}\sqrt{P_{tx,s_1}}h_{s_1r_{1,2}} & \sqrt{G_{s_2r_{1,2}}}\sqrt{P_{tx,s_2}}h_{s_2r_{1,2}} \end{bmatrix}\,, \tag{6.3}$$

where P_{tx,s_1} and P_{tx,s_2} represent the power transmitted from SN_1 and SN_2, respectively, while $h_{s_1r_{1,l}}$ denotes the channel coefficient between SN_1 and the l^{th} receive antenna of RN_1. Similarly, $G_{s_1r_{1,l}}$ denotes the reduced-pathloss-induced geometrical gain experienced by the SN_1-RN_1 link. As suggested by Figure 6.2, the channel corresponding to CP can be expressed in a form similar to Equation (6.3), albeit, in conjunction with different channel coefficients. For example, assuming a path-loss exponent of two ($\alpha = 2$) i.e. free-space transmission, the corresponding reduced-pathloss-induced geometrical gain experienced by the SR link and RD link with respect to the SD link may be calculated, respectively, as [185, 187]:

$$G_{SR} = \left(\frac{d_{SD}}{d_{SR}}\right)^2 \;;\; G_{RD} = \left(\frac{d_{SD}}{d_{RD}}\right)^2\,, \tag{6.4}$$

where d_{SD} denotes the distance between source nodes SN_1, SN_2 and the DN. Similarly to Section 3.2.1 and Section 5.3, in our model the RNs are situated at the mid-point between the SNs and DN. Thus, we have $d_{SR} = d_{RD} = d_{SD}/2$, where $G_{SR} = G_{RD} = 2^2 = 8$.

Without loss of generality, let d_{ab} represent the distance between node a and node b. If x_a is the symbol transmitted from node a equipped with a single transmit antenna, the received Signal-to-Noise Ratio (SNR) estimated at each receive antenna of node b can be expressed as [123]:

$$\begin{aligned} \text{SNR}_r &= \frac{G_{ab}\,\text{E}\left[|h_{ab}|^2\right]\;\text{E}\left[|x_a|^2\right]}{N_0} \\ &= \frac{G_{ab}}{N_0}\,, \end{aligned} \tag{6.5}$$

where $\text{E}\left[|h_{ab}|^2\right] = 1$ and $\text{E}\left[|x_a|^2\right] = 1$. Similar to our discussions in Section 3.2.1, we define the transmit SNR[2] as a ratio of the power transmitted from node a to the noise power experienced at the receiver of node b as:

$$\text{SNR}_t = \frac{\text{E}\left[|x_a|^2\right]}{N_0} = \frac{1}{N_0}\,. \tag{6.6}$$

[2]However, the concept of transmit SNR [187] is unconventional, as it relates quantities to each other at two physically different locations, namely the transmit power to the noise power at the receiver.

Thus, we arrive at:

$$\begin{aligned} \mathrm{SNR}_r &= \mathrm{SNR}_t \; G_{ab} \\ \Gamma_R &= \Gamma_T + 10\log_{10}(G_{ab}) \; [\mathrm{dB}] \; , \end{aligned} \tag{6.7}$$

where we have $\Gamma_R = 10\log_{10}(\mathrm{SNR}_r)$ and $\Gamma_T = 10\log_{10}(\mathrm{SNR}_t)$.

As stated previously, both the BP and CP transmission channels are composed of two components, with h_s and h_f denoting the uncorrelated fast fading (small-scale Rayleigh fading) and slow fading (quasi-static Rayleigh fading) coefficients, respectively. To elaborate further, each channel coefficient $h_{s_1 r_{1,l}}$ of the channel matrix shown in Equation (6.3) might be expressed as:

$$h = h_s \cdot h_f \; , \tag{6.8}$$

where h_s in our simulations is assumed to be constant for all the symbols within a frame, while h_f fluctuates on a symbol by symbol basis within each frame. In Scenario B of Figure 6.3 both the BP and CP may be viewed as (2×1) and (1×1) SDMA channels, respectively. Thus, the channel matrices encountered during both phases can be evaluated similarly to the analysis of Scenario A.

6.2.1 DJSTTCM Encoder and Decoder

The two correlated sources are encoded using our DJSTTCM encoder and then decoded accordingly, as detailed in Sections 5.3.1 and 5.3.2, respectively. Similar to the source correlation model adopted in Section 5.3.1, the BSC is used for modelling the correlation between the source sequences $\{b_1\} = \{b_1^1, b_1^2, \cdots, b_1^i, \cdots, b_1^N\}$ and $\{b_2\} = \{b_2^1, b_2^2, \cdots, b_2^i, \cdots, b_2^N\}$, where N is the length of each source block. More explicitly, the source sequence $\{b_1\}$ is generated by an equiprobable binary symmetric i.i.d. source, while $\{b_2\}$ can be defined as $b_1^i = b_2^i \oplus e_i$, where $\oplus$ is the modulo-2 addition operation and e_i is an independent binary random variable assuming the logical value 1 with a cross-over probability of p_e and 0 with a probability of $(1 - p_e)$.

The achievable compression rate of both source is bounded by the SW rate region inequalities of Equation (5.5). Both source sequences, namely $\{b_1\}$ and $\{b_2\}$, are first encoded using TTCM encoders having a rate of $R_{cm} = \frac{m}{m+1}$. Then both encoded sequences are mapped onto the corresponding modulated symbols, namely onto $\{x_1\}$ and $\{x_2\}$, as illustrated in the lower part of Figure 6.1[3]. During the BP, both modulated signals are broadcast to all RNs and the DN through either the (2×2) or the (2×1)-element MACs according to the used scenario. Consequently, both received signals, namely $\mathbf{y}_r$ and $\mathbf{y}_d$ of Figure 6.1 are detected by the ML-based Multi-User Detector (MUD) at RN and DN, respectively. Then, both source sequences are estimated by iteratively exchanging their extrinsic information between the MUD and the DJSTTCM decoder. Accordingly, Figure 5.3 illustrates the DJSTTCM decoder, which is constituted by of two parallel

[3]To avoid repetition, while keeping the chapter readable in a stand alone fashion, we will briefly discuss the DJSTTCM encoder/decoder in this chapter, although they have been discussed in detail in Section 5.3.1 and Section 5.3.2, respectively.

Parameters	Description
R_{cm} [BPS]	TTCM coding rate
R_p [BPS]	Puncturing rate
M [user]	Number of SNs
K [relay]	Number of RNs
F	Total number of simulated frames
N	Total number of bits per simulated frame
N_s	Total number of symbols per frame
i	SN index
j	RN index
n_1 [frame]	Number Information Frames (IF)s transmitted per SN during BP within a full transmission cycle
n_2 [frame]	Number Parity Frames (PF)s transmitted per transmit antenna per RN during CP within a full transmission cycle
L [antenna]	Number of the transmit antennas of RN
P [antenna]	Number of the receive antennas of RN and DN
$\boldsymbol{G}$	Original transfer matrix that represent the Network Code
$\boldsymbol{G}'$	Modified transfer matrix that represent the Network Code
R_{NC} [BPS]	Network code information rate
R_{FEC} [BPS]	Channel code information rate
η $[BPS]$	The system overall achievable throughput
D	The diversity order
ρ	Correlation coefficient
α	Path-loss exponent

Table 6.1: Main parameters in the system schematic of Figure 6.1.

TTCM decoders, where each invokes the symbol-based MAP algorithm detailed in Section 4.2.3.

The sequences estimated at the RN will then be fed into the NC before encoding them using a pair of TTCM encoders, as shown in Figure 6.1. These TTCM-encoded streams will transmitted during the CP. Depending on the specific scenario, different mappers or receivers might be used. More explicitly, in Scenario A of Figure 6.2, a pair of TTCM-encoded sequences will mapped into two different QPSK signals. However, in Scenario B of Figure 6.3, both coded sequences are combined and mapped onto a 16QAM-SPM signal, since the RN and the DN invokes a single receive antenna, as portrayed in Figure 6.3[4].

Before embarking on our NC investigation, we first have to characterise the attainable performance of our DJSTTCM when communicating over the combined uncorrelated Rayleigh fading

[4]At the RN, although one TTCM would be enough to encode both decoded streams with complexity reduction, we decided to use a couple of TTCM encoders mainly for two reasons. First, to avoid any possible delay when encoding two sequences, second to add further coding flexibility to the design that could be utilised in future works.

Coded Modulation	**TTCM**
Code rate	$R_{cm} = 1/2$
Correlation coefficients	$\rho = \{0.8, 0.6, 0.4, 0.2\}$
Puncturing rate	$R_p = 1$
Decoding algorithm	Approximated Log-MAP
Inner Iteration	$I_{\text{in}} = 4$
Outer Iteration	$I_{\text{out}} = 4$
Number of symbol	$N_s = 120\,000$ symbols per frame
Number of frames	$F = 10\,000$
Channel	$h_s \cdot h_f$
Channel State Information (CSI)	Known
MUD Type	ML

Table 6.2: Simulation parameters for the direct link transmission.

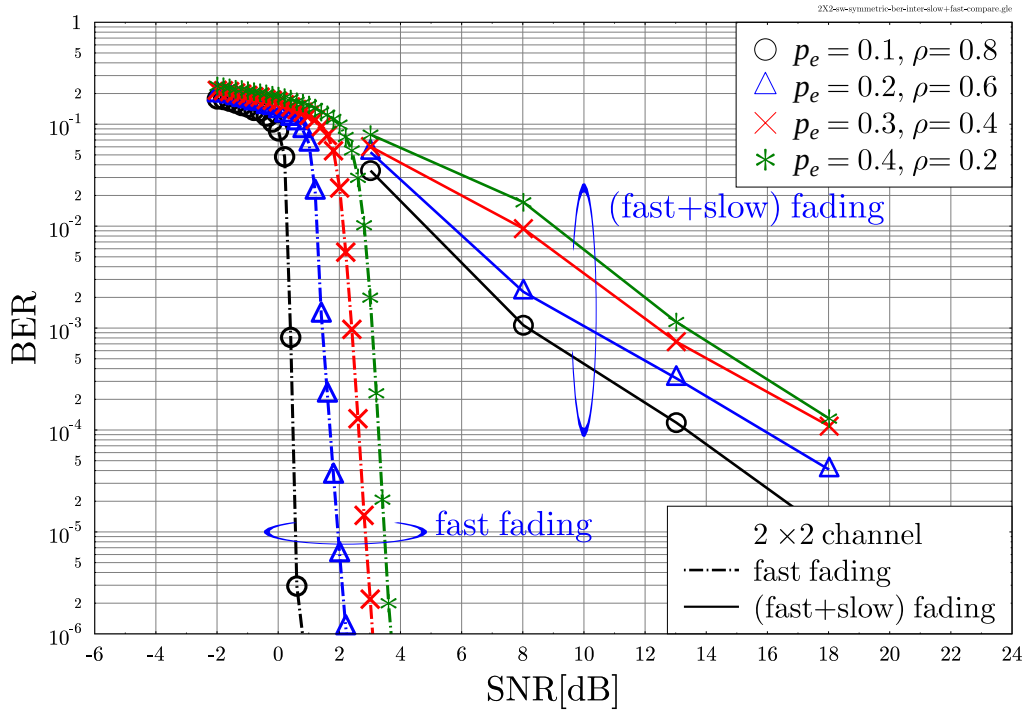

Figure 6.4: BER versus SNR performance of the proposed DJSTTCM-QPSK scheme for correlation coefficients of $\rho = \{0.8, 0.6, 0.4, 0.2\}$, when transmitting over the combined uncorrelated Rayleigh fading and quasi-static Rayleigh fading (2×2) MAC. The main parameters are defined in Table 6.2, while $R_{FEC} = 2$ BPS.

and quasi-static Rayleigh fading channels of Equation (6.8). As shown in both Figures 6.2 and 6.3, the transmission phases can be characterised in terms of three different channel combinations. In Scenario A of Figure 6.2, we have the SD, SR and RD links. More explicitly, the direct transmission might be characterised as a (2×2) MAC regime. Similarly, the SR and SD links of Scenario B of of Figure 6.3 can be viewed as a (2×1) MAC arrangement, while the RD link can be viewed as a (1×1) channel. More specially, the BER performance of the three channels recorded for various source correlation values is shown in Figure 6.4, Figure 6.5 and Figure 6.6 using the simulation parameters of Table 6.2. Note that the correlation of the pair of sources is represented by ρ, which is given by $\rho = 1 - p_e$, where p_e is the BSC's cross-over probability. As all of these three figures suggested, a substantial performance degradation is exhibited once our DJSTTCM scheme encounters a slow fading (quasi-static Rayleigh fading) channel. Quantitatively, Figure 6.4 shows the BER versus SNR performance of the DJSTTCM-QPSK scheme, when communicating over the (2×2) MAC regime. Note that the SNR is be given by:

$$\text{SNR[dB]} = E_b/N_0\text{[dB]} + 10\log_{10}(R_{FEC})\,, \tag{6.9}$$

where R_{FEC} denotes the effective channel coding rate that can be expressed as:

$$R_{FEC} = R_{cm} \cdot R_p \cdot \log_2(\mathcal{M}) \cdot M\,, \tag{6.10}$$

where $2^{m+1} = \mathcal{M}$ denotes the number of PSK/QAM modulation levels, while M is the number of SNs. As portrayed in Figure 6.4, there is an approximately 12.0 dB performance degradation, when the DJSTTCM-QPSK scheme operates over the combined channel compared to that, when transmitting over uncorrelated fading channels. More explicitly, for $\rho = 0.8$ and at a BER level of 10^{-4} an SNR gap of $13 - 0.5 = 12.5$ dB, as seen in Figure 6.4. Interestingly, our joint decoder remains capable of exploiting the correlation among the sources, even when communicating over this hostile shadow-faded and fast-faded channel. For example, at a BER of 10^{-4} a considerable 3.0 dB improvement can be attained upon comparing the system having $\rho = 0.8$ to that having $\rho = \{0.6\}$.

As expected, the BER performance was further degraded for the other two channel configurations, namely where the number of the transmit or receive antennas has been reduced to (2×1) and (1×1) channels, as seen in Figures 6.5 and 6.6, respectively. To elaborate further, upon analysing Figure 6.5 we observe that the DJSTTCM-QPSK scheme requires an excessive transmit power of SNR $= \{19, 22, 24\}$ dB for attaining a BER of 10^{-3} for $\rho = \{0.8, 0.6, 0.4\}$ when the correlated sources encounter the (2×1) channel. Additionally, as it is shown in Figure 6.6 for the (1×1) channel, even assigning a transmit power of SNR $= 30$ dB is insufficient for the DJSTTCM-16QAM-SPM scheme to attain a BER$= 10^{-3}$, despite having high correlation value of $\rho = 0.8$. It is also worth mentioning that increasing the number outer iteration $I_{\text{out}} = 4$ in the schematic of Figure 5.3[5] will only provide an insignificant performance improvement to our scheme, as depicted

[5]Similar to the discussion of Section 5.3.1, $I_{\text{out}} = 4$ denotes the iteration between the TTCM decoder and the MUD, while the inner iteration $I_{\text{in}} = 4$ represents the iterations between the two TTCM decoders.

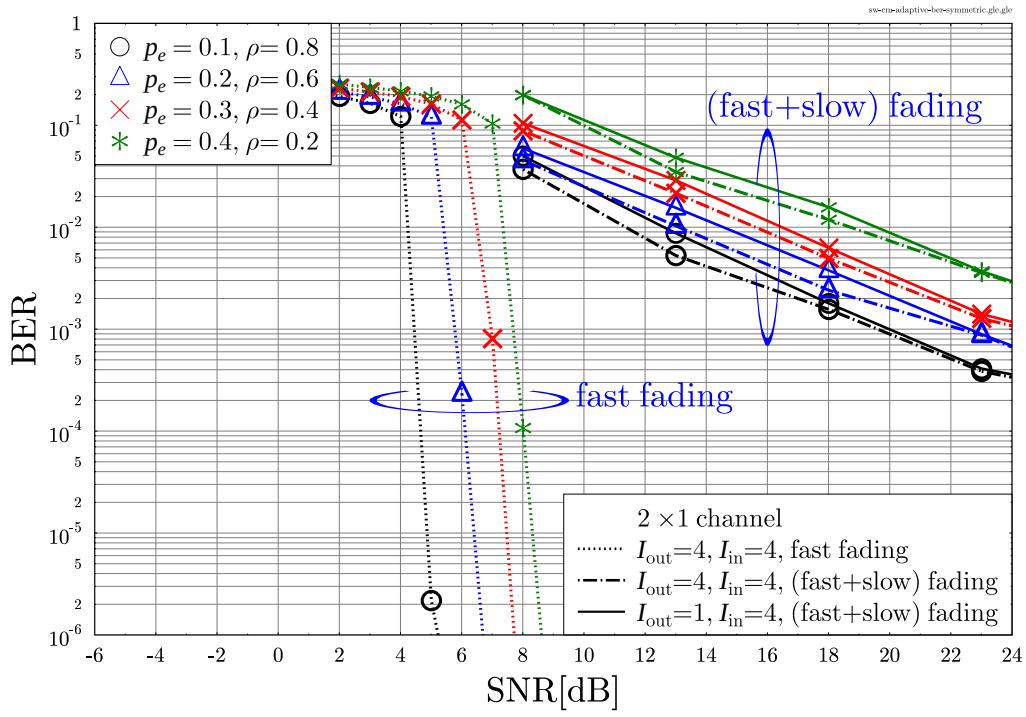

Figure 6.5: BER versus SNR performance of the proposed DJSTTCM-QPSK scheme for correlation coefficients of $\rho = \{0.8, 0.6, 0.4, 0.2\}$ when transmitting over the combined uncorrelated Rayleigh fading and quasi-static Rayleigh fading (2×1) MAC. The main parameters are defined in Table 6.2, while $R_{FEC} = 2$ BPS.

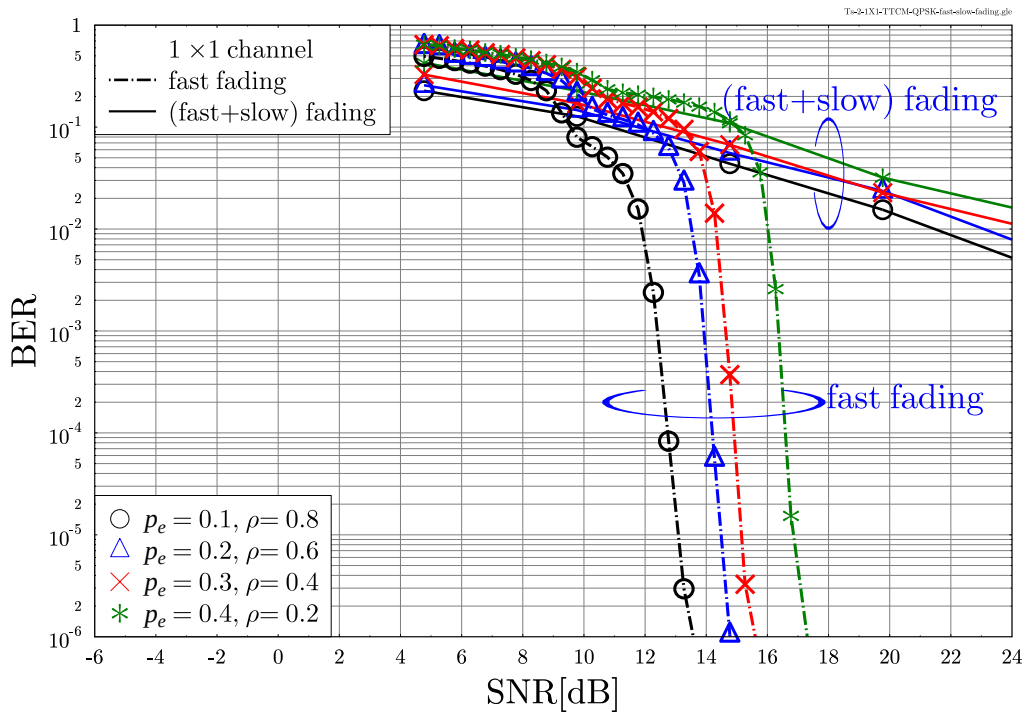

Figure 6.6: BER versus SNR performance of the proposed DJSTTCM-16QAM-SPM scheme for correlation coefficients of $\rho = \{0.8, 0.6, 0.4, 0.2\}$ when transmitting over the combined uncorrelated Rayleigh fading and quasi-static Rayleigh fading (1×1) channel. The main parameters are defined in Table 6.2, $R_{FEC} = 3$ BPS

in Figure 6.5. This is not unexpected, because it was pointed out in [215] that in the quasi-static Rayleigh fading channels, the channel coefficients remain constant during the entire transmitted frame, hence for every transmit frame the channel can be viewed as an AWGN channel, albeit, each having different SNR value. More explicitly, the frames associated with low SNRs will dominate the system's performance during the iterative detection process, hence leading to poor mutual information exchange between the constituent decoders. It was found in [19, 133, 134] that network-coded cooperative transmission constitutes an efficient remedy for such a transmission environment, as the time diversity between the frames will be utilised. Let us now discuss the NC scheme in the following sections.

6.2.2 Network Encoder

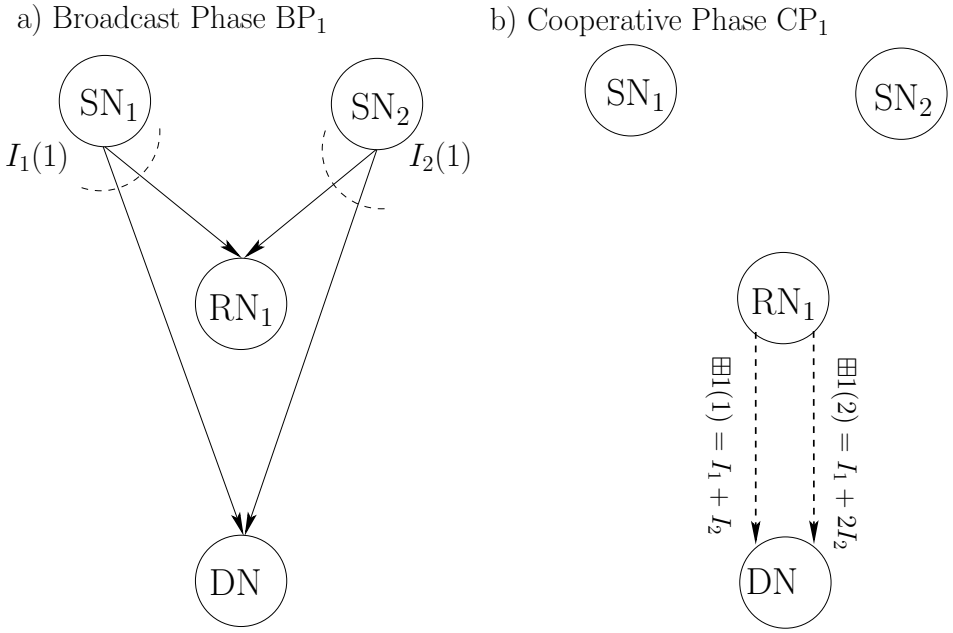

Figure 6.7: Schematic model of an NC-aided system having $M = 2$ SNs transmitting two IFs during the $n_1 = 1$ BP, where the $K = 1$ RN transmit two PFs during the $n_2 = 1$ CP. Table 6.1 defines the main parameters. The two PFs transmitted during the CP_1, namely $\boxplus 1(1)$ and $\boxplus 1(2)$, are generated according to the 3rd and 4th columns of $\boldsymbol{G}_{2\times 4}$ respectively, as specified by Equation (6.11).

Let us consider the NC transmission example illustrated in Figure 6.7, where $M = 2$ SNs aim for transmitting their information to the DN with the aid of $K = 1$ RN. In line with [133, 134, 139], NC typically adopts a TDMA-based access method, where each SN broadcasts $n_1 = 1$ IF during its corresponding BP, while each RN transmits $n_1 = 1$ PF within the CP. Thus, a total of $(n_1 \cdot M + n_2 \cdot K) = 4$ transmission phases are required for accomplishing a full transmission cycle. However, in our SDMA based method, each of the SNs broadcasts $n_1 = 1$ IFs during each BP. Then, during the CP each of the $L = 2$ transmits antennas of the RN transmit $n_2 = 1$ PF, as seen in Figure 6.7. More explicitly, both PFs are transmitted using twin-antenna-aided RN when Scenario A of Figure 6.2 is invoked. However, for Scenario B of Figure 6.3 both of the PFs are combined into a super constellation, creating a single SPM signal as illustrated in Section 5.4.1.

As stated in Section 1.4, the NC transmission protocol can be fully characterised using a transfer generator matrix $\boldsymbol{G}$, which is constructed over a Galois field GF(q), where $q = 2^b$ is the desired alphabet size and b is a non-zero integer [134, 137][6]. In this chapter, we will consider two NC systems relaying on the generator matrices of $\boldsymbol{G}_{2\times4}$ and $\boldsymbol{G}_{4\times8}$, where both matrices are generated using the software application SAGE [142]. Upon successfully decoding all of the frames during transmission sessions, $\boldsymbol{G}_{2\times4}$ used in our example of Figure 6.7 is given by [137, 232, 233]:

$$\boldsymbol{G}_{2\times4} = \left[\begin{array}{cc|cc} 1 & 0 & 1 & 1 \\ 0 & 1 & 1 & 2 \end{array}\right], \tag{6.11}$$

where the role of the elements is detailed below. Upon comparing the above transfer matrix to Figure 6.7, the transmission arrangement can be characterised by:

$$(BP_1) : SN_1 \xrightarrow[(=0 \mid 1)]{I_1(1)} DN\,,\ SN_1 \xrightarrow[(=0 \mid 1)]{I_1(1)} RN_1 \tag{6.12}$$

$$(BP_1) : SN_2 \xrightarrow[(=0 \mid 1)]{I_2(1)} DN\,,\ SN_2 \xrightarrow[(=0 \mid 1)]{I_2(1)} RN_1 \tag{6.13}$$

$$(CP_1) : RN_1^1 \xrightarrow[(=0 \mid 1)]{\boxplus 1(1)=\boldsymbol{G}(1,3)\cdot I_1(1)+\boldsymbol{G}(2,3)\cdot I_2(1)} DN,\ RN_1^2 \xrightarrow[(=0 \mid 1)]{\boxplus 1(2)=\boldsymbol{G}(1,4)\cdot I_1(1)+\boldsymbol{G}(2,4)\cdot I_2(1)} DN\,, \tag{6.14}$$

as detailed below. As seen in Equation (6.11), $\boldsymbol{G}_{2\times4}$ can divided into two main parts. The left-hand identity sub-matrix, having diagonal elements of $\boldsymbol{G}_{2\times4}(i,i) = 1,\ i \in \{1,2\}$ represents the transmission of the IFs I_i from the i^{th} SN to the DN during the BP. This phase can be interpreted using Equation (6.12) and Equation (6.13), in which the arrow's subscript $(= 0 \mid 1)$ indicates the failure or success of decoding the IFs, respectively. Additionally, the PF construction can be gleaned from the right-hand sub-matrix of $\boldsymbol{G}_{2\times4}$ in Equation (6.11). More explicitly, each of the signal $\boxplus(1)$ and $\boxplus(2)$[7] that are transmitted from the first and second antennas of RN_1 seen in Figure 6.7 are generated according to the 3rd and 4th columns of $\boldsymbol{G}_{2\times4}$, respectively, as specified by Equation (6.14).

Subsequently, a modified transfer matrix, $\boldsymbol{G}'_{2\times4}$, has to be defined at the DN as justified below. As the terminology *modified* suggests, the entries of $\boldsymbol{G}'_{2\times4}$ are modified according to the success or failure of the transmitted frame. The notation $(= \ 0)'$ (or $(= \ 1)'$) beneath the arrows of Equations (6.12) - (6.14) indicate, whether the frame was unsuccessfully (or successfully) decoded. Hence, we have $\boldsymbol{G}'_{2\times4} = \boldsymbol{G}_{2\times4}$ when all of the transmitted frames were successfully decoded during both phases. More explicitly, the elements $\boldsymbol{G'}_{2\times4}(i,i) = 1,\ i = [1,2]$ represents the successful decoding of the IFs $I_i(1)$ transmitted by SN_i at the DN during the BP_1. Meanwhile, having $\boldsymbol{G'}_{2\times4}(1,3) = \text{“}1''$ or $(\boldsymbol{G'}_{2\times4}(2,4) = \text{“}2'')$ indicates that the PFs transmitted by the RN during CP_1 are successfully decoded at the DN corresponding to linear combining coefficient of

[6]The transfer generator matrix can be derived from the appropriately selected systematic generator matrix $\boldsymbol{G}$ of an (n, k, d_{min}) linear block code [135, 136]. This linear block code should satisfied a Maximum Distance Separable (MDS) code condition for the sake of approaching the maximum minimum distance bound [141]. In our chapter, we use the systematic generator matrices $\boldsymbol{G}$ of the Reed Solomon (RS) codes constituting a well-known class of MDS codes is provided by the software application SAGE [142].

[7]$\boxplus$ denotes the non-binary linear combination of the IFs, where all operations are carried out over GF [137].

the information frame $I_1(1)$ or $(I_2(2))$. Furthermore, $\boldsymbol{G'}_{2\times4}(2,3) = \text{“1”}$ or $(\boldsymbol{G'}_{2\times4}(1,4) = \text{“1”})$ signifies that information frame $I_2(2)$ or $(I_1(1))$ is successfully decoded by RN during BP_1, and the PFs transmitted by the RN during the cooperative phase CP_1 are successfully decoded at the DN.

To elaborate further, consider the aforementioned system that might experience an actual transmission scenario, where depending on the success or the failure of each specific transmission attempt we arrive at:

$$(BP_1) : SN_1 \xrightarrow[(=0)]{I_1(1)} DN \; : \boldsymbol{G'}_{2\times4}(1,1) = 0\,; \tag{6.15}$$

$$SN_1 \xrightarrow[(=1)]{I_1(1)} RN_1 :: \boldsymbol{G'}_{2\times4}(2,3) = \boldsymbol{G}_{2\times4}(2,3)\,, \tag{6.16}$$

$$(BP_1) : SN_2 \xrightarrow[(=0)]{I_2(1)} DN \; : \boldsymbol{G'}_{2\times4}(2,2) = 0\,; \tag{6.17}$$

$$SN_2 \xrightarrow[(=1)]{I_2(1)} RN_1 : \boldsymbol{G'}_{2\times4}(1,4) = \boldsymbol{G}_{2\times4}(1,4)\,, \tag{6.18}$$

$$(CP_1) : RN_1^1 \xrightarrow[(=0)]{\boxplus1(1)} DN : \boldsymbol{G'}_{2\times4}(i,3) = 0, i = [1,2]\,; \tag{6.19}$$

$$RN_1^2 \xrightarrow[(=1)]{\boxplus1(2)} DN : \boldsymbol{G'}_{2\times4}(i,4) = \boldsymbol{G}_{2\times4}(i,4), i = [1,2]\,, \tag{6.20}$$

hence, according to the Equations (6.15) - (6.20), the modified transfer matrix can be expressed as:

$$\boldsymbol{G'}_{2\times4} = \left[\begin{array}{cc|cc} 0 & 0 & 0 & 1 \\ 0 & 0 & 0 & 2 \end{array}\right]\,, \tag{6.21}$$

Further details and in-depth mathematical description on the construction of the modified matrix construction can be found in [138, 232].

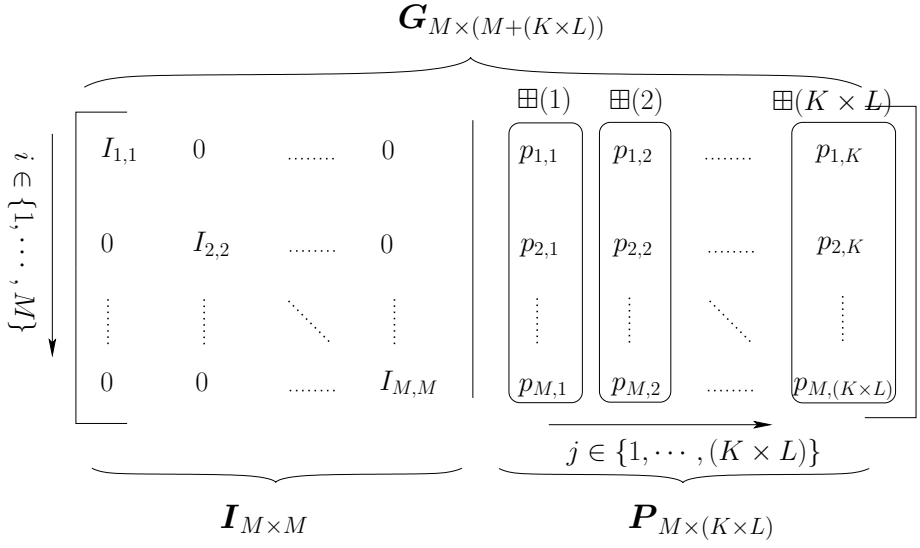

Figure 6.8: The generator matrix $\boldsymbol{G}_{M\times(M+K)}$ characterising the NC transmission, where the notations are defined in Table 6.1.

Let us now generalise the above-mentioned $\boldsymbol{G}_{2\times4}$ transfer matrix. Figure 6.8 shows the transfer

matrix $\boldsymbol{G}_{M\times(M+(K\times L))}$[8], or $\boldsymbol{G}$ for brevity, which consists of two components. The first half is constituted by the identity matrix $\boldsymbol{I}_{M\times M}$, or $\boldsymbol{I}$ for short, which models the information frames' transmission from M SNs to the DN, and each of its entries is defined as:

$$I_{i,i} = \begin{cases} 1 & \text{if } I_{i,i} \text{ successfully recovered ,} \\ 0 & \text{otherwise ,} \end{cases} \tag{6.22}$$

where we have $i \in \{1, \cdots M\}$. The second component of $\boldsymbol{G}$ is the parity matrix $\boldsymbol{P}_{M\times(K\times L)}$, or $\boldsymbol{P}$ for short, which illustrates the PFs construction process formulated as:

$$\boxplus(j) = \boxplus\, p(i,j)I(i) \ , \tag{6.23}$$

where we have $j \in \{1, \cdots (K \times L)\}$. Again, K and L denotes the number of the RNs and transmit antennas employed by each RN, respectively. Here, again ,$\boxplus$ denotes the non-binary linear combination of the IFs over finite Galois Fields (GF) [137] which can be replaced with simple modulo-2 addition operation $\oplus$ when considering binary combination. Additionally, at the j^{th} RN, the modified version of the parity matrix, namely $\boldsymbol{P'}_{n_1M\times n_2K}$ represents the IFs status of being recovered or not according to:

$$p'_{i,j} = \begin{cases} p_{i,j} & \text{if } I_{i,i} \text{ successfully recovered at RN}_j \text{ ,} \\ 0 & \text{otherwise .} \end{cases} \tag{6.24}$$

In a nutshell, the modified matrix $\boldsymbol{G}'$ is constructed by modifying the entries of the original matrix $\boldsymbol{G}$ according to Equation (6.22) and Equation (6.24).

6.2.3 Transmission Rate of the System

Before detailing our adaptive scheme, let us remind the readers of our scenarios. Figure 6.2 and Figure 6.3 defined Scenario A and Scenario B, respectively. The main simulation parameters of both scenarios were listed in Table 6.3. Again, the transmission structure employed can be divided into two layers, namely the FEC and NC layers. This section will discuss the transmission layer's rate as well as the overall system throughput. Let us commence with the NC rate, which is directly related to the multiplexing versus diversity capability and it might be expressed as:

$$R_{DNC} = \frac{\text{E}\left[\text{ number of IFs transmitted from SNs}\right]}{\text{E}\left[\text{number of IFs transmitted from SNs} + \text{number of PFs transmitted from RNs}\right]}, \tag{6.25}$$

where E[ ] represents the expectation operation over the total number of simulated frames.

Naturally, when designing any cooperative scheme, we have to aim for reducing the number of PFs transmitted from the RNs during the CPs [134], without any performance degradation. As

[8]Here we assume single BP and CP, i.e. $n_1 = n_2 = 1$. However, the more general representation $\boldsymbol{G}_{n_1M\times(n_1M+n_2(K\times L))}$ would involve further concatenation of the matrix $\boldsymbol{G}_{M\times(M+(K\times L))}$ seen in Figure 6.8.

Parameters	**Scenario A** of Figure 6.2	**Scenario B** of Figure 6.3
Channel	(fast+slow) fading	(fast+slow) fading
TTCM coding rate	$R_{cm} = 1/2$-TTCM	$R_{cm} = 1/2$-TTCM
Puncturing rate	$R_p = 1$	$R_p = 1$
Number of symbols per frame	N_s = 120 000 symbols	N_s = 120 000 symbols
Number of simulated frame	100 000 frames	100 000 frames
Modulation	QPSK(BP/CP)	QPSK(BP),16QAM-SPM(CP)
MUD types	ML	ML
Channel Access	2×2 (BP), 2×2 (CP)	2×1 (BP), 1×1 (CP)
Correlation coefficients	$\rho = \{0.8, 0.6, 0.2\}$	$\rho = \{0.8, 0.6, 0.2\}$
Number of SNs	$M = 2$ [SNs]	$M = 2$ [SNs]
Number of RNs	$K = \{1, 2\}$ [RNs]	$K = \{1, 2\}$ [RNs]
NC method	DNC/ADNC	DNC/ADNC
Transfer Matrix	$\boldsymbol{G}_{2\times4}$, $\boldsymbol{G}_{4\times8}$	$\boldsymbol{G}_{2\times4}$, $\boldsymbol{G}_{4\times8}$
Path-loss exponent	$\alpha = 2$	$\alpha = 2$

Table 6.3: Simulation parameters for both Scenario A and Scenario B where the notations are defined in Table 6.1, while the rates corresponding to the $K = 1$ and $K = 2$ RN/RNs scenarios are summarised in Tables 6.4– 6.7, respectively.

a further benefit of this reduction, the resources required, such as the time, bandwidth and power, for accomplishing a full transmission cycle might be reduced. Hence, for the same amount of available resources, the system might be able to admit more users or to transmit more IFs of the same number of users to the DN. One of the efficient techniques is to adaptively adjust the number of PFs depending on the prevalent to the channel quality. For the simplest non-adaptive case, the rate of DNC is given by:

$$R_{DNC} = \frac{n_1 \cdot M}{n_1 \cdot M + n_2 \cdot K \cdot L} \tag{6.26}$$

where M is the number of SNs and K is the number of RNs, while n_1 and n_2 represent the number of IFs and PFs, respectively. Recall that the parameters used in this chapter are defined in Table 6.1, while the simulation parameters are listed in Table 6.3. When considering a single relay-aided Scenario A transmission, for example, the $R_{DNC} = 1/2$ BPS, where we have $M = 2$ SNs and $K = 1$ RN-aided $L = 2$ transmit antennas. Regarding the FEC layer used for direct transmission, without relaying, the effective FEC transmission rate R_{FEC} can be conventionally estimated using Equation (6.10). By contrast, the overall throughput of the relaying-aided DNC can be expressed as the number of information bits transmitted delivered by the number of modulated symbols transmitted during both phases, which is similar to the two-way relaying channel scenario of Section 3.2.1.1 [139]. More explicitly, the overall throughput of cooperative DNC can be

formulated as:

$$\eta_{DNC} = \frac{n_1 \cdot M \cdot N_i}{n_1 \cdot M \cdot N_{BP} + n_2 \cdot K \cdot L \cdot N_{CP}}, \tag{6.27}$$

where N_i is the number of information bits per frame transmitted within a duration of $(N_{BP} + N_{CP})$ symbol periods and M denotes the number of users. Furthermore, N_{BP} is the number of modulated symbols per frame transmitted from the SNs during the BP, while N_{CP} is the number of modulated symbols per frame transmitted from the RNs during the CP. We have $N_{BP} = \frac{N_i}{R^{tx}_{\text{SN}}}$ and $N_{CP} = \frac{N_i}{R^{tx}_{\text{RN}}}$, where R^{tx}_{SN} and R^{tx}_{RN} denote the effective FEC transmission rates of the SN and RN, that can be estimated using Equation (6.10), respectively. Additionally, we assume having an identical number of BPs and CPs, i.e. $n_1 = n_2$. Thus, Equation (6.27) can be further simplified as:

$$\eta_{DNC} = \frac{M \cdot R^{tx}_{\text{SN}} \cdot R^{tx}_{\text{RN}}}{M \cdot R^{tx}_{\text{RN}} + R^{tx}_{\text{SN}} \cdot K \cdot L}, \tag{6.28}$$

hence, we have $\eta_{DNC} = 1$ BPS, when considering a single relay-aided Scenario A transmission associated with $M = 2$ SNs, $K = 1$ RN-aided $L = 2$ transmit antennas and FEC transmission rates of $R^{tx}_{\text{SN}} = R^{tx}_{\text{RN}} = 2$ BPS.

6.2.4 Adaptive Dynamic Network Coding

As suggested in the previous section, DNC-aided adaptive transmission is capable of enhancing the overall multiplexing or the diversity gains. Similarly to the system proposed in [133, 139], in our ADNC system we assume that the DN has the capability of sending a feedback flag F_g back to the NC encoder of the RNs, as portrayed in Figure 6.1. This flag requests the transmission of further PFs from the RNs during the BP according to the channel quality encountered. Intuitively, if the IFs were received correctly at the DN, then there is no need for any PF transmission. More explicitly, if the RNs received $F_g = 1$, this indicates that all IFs have been successfully decoded at the DN and hence the RNS become inactive. This adaptive operation may be formulated as:

$$(K_{\text{AD}} \cdot L) = \begin{cases} 0 & \text{if } F_g = 1, \\ (K \cdot L) & \text{otherwise}, \end{cases} \tag{6.29}$$

where K_{AD} denotes the number of RNs used, while n_2 represents the number of the PFs sent from each RN. Similarly to the rate-adaptive scheme of Section 4.2, the channel coding rate may also be adaptively controlled similar to [139]. However, adapting both FEC rate as well as the NC rate would impose an increased latency. In this chapter we only consider the adaptation of the NC rate. The corresponding adaptive NC rate might be expressed as:

$$R_{ADNC} = \frac{n_1 \cdot M}{n_1 \cdot M + \text{E}\left[n_2 \cdot K_{\text{AD}} \cdot L\right]}, \tag{6.30}$$

where again, the expectation $\text{E}[\,]$ is evaluated over the number of simulated frames. Upon comparing Equations (6.29) as well as (6.30). For the case, when the number of SNs equals to that of NC

the RNs, $M = K$, the adaptive NC rate of R_{ADNC} has to approach $\frac{n_1 \cdot M}{n_1 \cdot M} = 1$ for the sake of attaining the maximum achievable rate. Hence, in the high SNR region, i.e. when encountering a high channel quality or in highly correlated source scenarios, where the IFs can be recovered correctly during the BP, the term $K_{\mathrm{AD}} \cdot L$ has to be adaptively adjusted towards 0. For example, according to Equation (6.30) R_{ADNC} will assume two different values of $R_{ADNC} = 1$ BPS or $(R_{ADNC} = 1/2)$ BPS if the feedback flag received $F_g = 1$ or (otherwise), when considering a single relay-aided Scenario A transmission associated with $M = 2$ SNs, $K = 1$ RN-aided $L = 2$. Upon assuming $n_1 = n_2$, similarly to Equation (6.28), the overall throughput of our adaptive scheme can be expressed as:

$$\eta_{ADNC} = \frac{M \cdot R^{tx}_{\mathrm{SN}} \cdot R^{tx}_{\mathrm{RN}}}{M \cdot R^{tx}_{\mathrm{RN}} + R^{tx}_{\mathrm{SN}} \cdot \mathrm{E}\left[K_{\mathrm{AD}} \cdot L\right]} . \tag{6.31}$$

Similarly, $\eta_{ADNC} = 2$ BPS or $(\eta_{ADNC} = 1)$ BPS according weather the $F_g = 1$ or (otherwise), when considering a single relay-aided Scenario A transmission associated with $M = 2$ SNs, $K = 1$ RN-aided $L = 2$ transmit antennas and FEC transmission rates of $R^{tx}_{\mathrm{SN}} = R^{tx}_{\mathrm{RN}} = 2$ BPS.

6.2.5 Diversity Order of the System

In order to emphasise the scalability of our system, we consider a higher order transfer matrix of $\boldsymbol{G}_{4\times 8}$ that is constructed over GF(8), as follows [135, 136]:

$$\boldsymbol{G}_{4\times 8} = \left[\begin{array}{cccc|cccc} 1 & 0 & 0 & 0 & 3 & 7 & 3 & 6 \\ 0 & 1 & 0 & 0 & 5 & 7 & 7 & 4 \\ 0 & 0 & 1 & 0 & 2 & 4 & 6 & 1 \\ 0 & 0 & 0 & 1 & 5 & 5 & 3 & 2 \end{array}\right] . \tag{6.32}$$

As portrayed in Figure 6.8, the NC transfer matrix $\boldsymbol{G}$ is comprised of two sub-matrices, namely the identity matrix $\boldsymbol{I}$ and the parity matrix $\boldsymbol{P}$. The sub-matrices of $\boldsymbol{G}_{4\times 8}$ in Equation (6.32) have two more columns and rows compared to those of $\boldsymbol{G}_{2\times 4}$ in Equation (6.11). Intuitively, this expansion can be exploited either by adding a pair of SNs and RNs, or by doubling the number of the BPs and CPs, respectively. In Figure 6.9, we opted for the second option of increasing the number frames conveyed during the BPs and CPs, i.e. $n_1 = n_2 = 2$. For example, in Figure 6.9 SN_1 broadcasts its IF I_1 twice, namely both within the first and in the second BPs as $I_1(1)$ and $I_1(2)$, respectively. Similarly, RN_1 sends the first PF $\boxplus 1$ as $\boxplus 1(1)$ and $\boxplus 1(2)$ during first and second CPs.

The transfer matrix $\boldsymbol{G}_{4\times 8}$ can be constructed similarly to the procedure detailed in Section 6.2.2, while the decoding procedure will be detailed in Section 6.2.6. More explicitly, both the BP transmission slots can be illustrated by comparing the identity matrix of Equation (6.32) to the upper part of Figure 6.9, while the CPs can be characterised with the aid of the parity matrix of Equation (6.32) that is portrayed in the lower part of Figure 6.9. The number of transmitted IFs and PFs is identical in $\boldsymbol{G}_{2\times 4}$-based and the $\boldsymbol{G}_{4\times 8}$-based scheme, i.e. we have $n_1 = n_2$. Hence, their NC rate

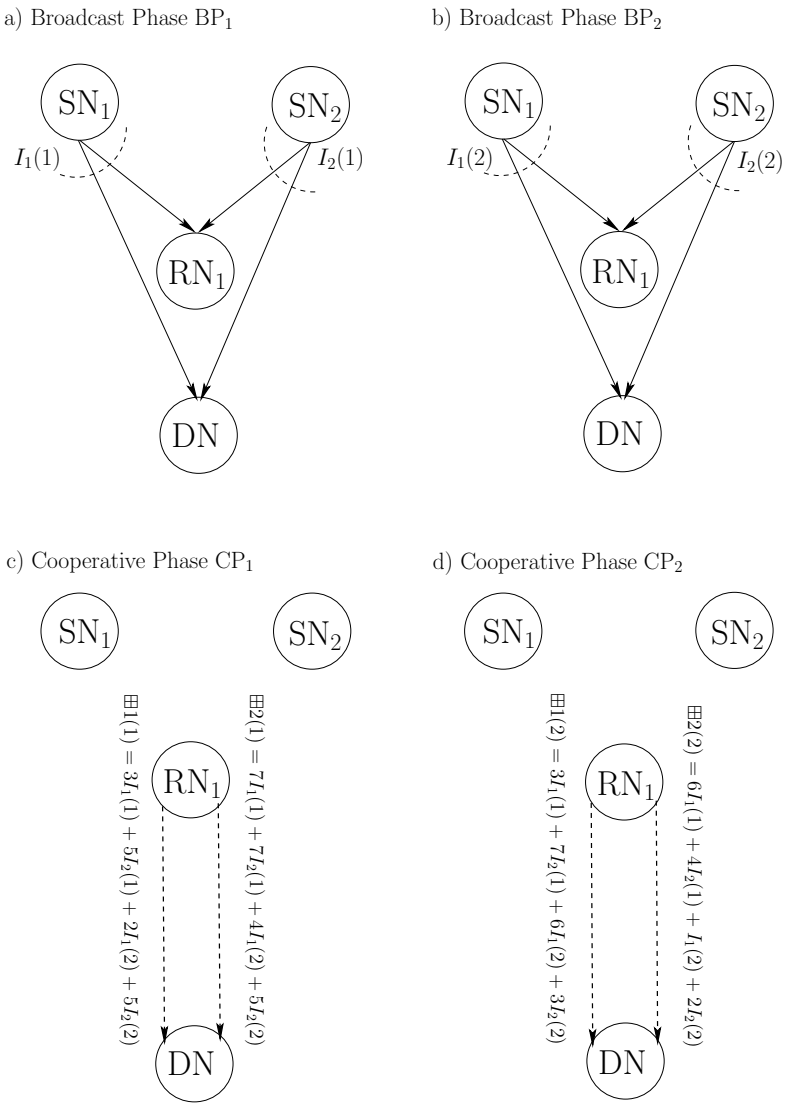

Figure 6.9: Schematic of the NC-based $\boldsymbol{G}_{4\times 8}$-based system having $M = 2$ SNs, each transmitting $n_1 = 2$ IFs, while the $K = 1$ RN is equipped with $L = 2$ antennas that transmits $n_1 = 2$ IFs. The PFs transmitted during CPs, namely $\boxplus 1(1)$, $\boxplus 2(1)$, $\boxplus 1(2)$ and $\boxplus 2(2)$ are generated according to the 3rd, 4th, 5th and 6th columns of $\boldsymbol{G}_{4\times 8}$, respectively, as specified in Equation (6.32). Table 6.1 defines the main system parameters.

will be the same as shown in Equation (6.26) Equation (6.30). However, the diversity order D_{NC} of the $\boldsymbol{G}_{4\times 8}$-based scheme will be higher than that of its $\boldsymbol{G}_{2\times 4}$-based counterpart [136]. Thus the diversity order D of the DNC-based system is bounded by [134, 136, 137, 232]:

$$(K \cdot L) + n_2 \leq D_{DNC} \leq (K \cdot L) \cdot n_2 + 1\,, \tag{6.33}$$

where K is the number of RNs and L is the number of transmit antennas per RN, while we have $n_2 = 1$ or $n_2 = 2$ for the $\boldsymbol{G}_{2\times 4}$ or $\boldsymbol{G}_{4\times 8}$ based schemes, respectively. Naturally, a higher diversity order implies having a better Frame Error Ratio (FER) performance, since a higher diversity leads to an improved signal detection reliability. We considered a number of scenarios, each of which invoked either $K = 1$ RN or $K = 2$ RNs. The corresponding rates and diversity orders are summarised according to the specific transfer matrix used in Tables 6.4– 6.7.

Parameters	Equation	Scenario A, $G_{2\times4}$	Scenario A, $G_{4\times8}$
R_{FEC} [BPS]	(6.10)	2	2
R_{DNC} [BPS]	(6.26)	1/2	1/2
R_{ADNC} [BPS]	(6.30)	$\begin{cases} 1 & \text{if } F_g = 1\,, \\ 1/2 & \text{otherwise}\,, \end{cases}$	$\begin{cases} 1 & \text{if } F_g = 1\,, \\ 1/2 & \text{otherwise}\,, \end{cases}$
η_{DNC} [BPS]	(6.27)	1	1
η_{ADNC} [BPS]	(6.31)	$\begin{cases} 2 & \text{if } F_g = 1\,, \\ 1 & \text{otherwise}\,, \end{cases}$	$\begin{cases} 2 & \text{if } F_g = 1\,, \\ 1 & \text{otherwise}\,, \end{cases}$
D_{DNC}	(6.33)	$3 \leq D_{DNC} \leq 3$	$4 \leq D_{DNC} \leq 5$
D_{ADNC}	(6.33)	$\begin{cases} 1 & \text{if } F_g = 1\,, \\ D_{DNC} & \text{otherwise}\,, \end{cases}$	$\begin{cases} 1 & \text{if } F_g = 1\,, \\ D_{DNC} & \text{otherwise}\,, \end{cases}$
n_1 [frame]	$--$	1	2
n_2 [frame]	$--$	1	2
M [user]	$--$	2	2

Table 6.4: Rates and diversity orders of the systems based on the transfer matrices $\boldsymbol{G}_{2\times4}$ and $\boldsymbol{G}_{4\times8}$, when employing Scenario A of Figure 6.2 and the number of the RNs is $K = 1$. Note that the terminologies are defined in Table 6.1, while the main parameters are listed in Table 6.3.

Parameters	Equation	Scenario B, $G_{2\times4}$	Scenario B, $G_{4\times8}$
R_{FEC} [BPS]	(6.10)	3	3
R_{DNC} [BPS]	(6.26)	1/2	1/2
R_{ADNC} [BPS]	(6.30)	$\begin{cases} 1 & \text{if } F_g = 1\,, \\ 1/2 & \text{otherwise}\,, \end{cases}$	$\begin{cases} 1 & \text{if } F_g = 1\,, \\ 1/2 & \text{otherwise}\,, \end{cases}$
η_{DNC} [BPS]	(6.27)	1.2	1.2
η_{ADNC} [BPS]	(6.31)	$\begin{cases} 2 & \text{if } F_g = 1\,, \\ 1.2 & \text{otherwise}\,, \end{cases}$	$\begin{cases} 2 & \text{if } F_g = 1\,, \\ 1.2 & \text{otherwise}\,, \end{cases}$
D_{DNC}	(6.33)	$3 \leq D_{DNC} \leq 3$	$4 \leq D_{DNC} \leq 5$
D_{ADNC}	(6.33)	$\begin{cases} 1 & \text{if } F_g = 1\,, \\ D_{DNC} & \text{otherwise}\,, \end{cases}$	$\begin{cases} 1 & \text{if } F_g = 1\,, \\ D_{DNC} & \text{otherwise}\,, \end{cases}$
n_1 [frame]	$--$	1	2
n_2 [frame]	$--$	1	2
M [user]	$--$	2	2

Table 6.5: Rates and diversity orders of the systems based on the transfer matrices $\boldsymbol{G}_{2\times4}$ and $\boldsymbol{G}_{4\times8}$, when employing Scenario B of Figure 6.3 and the number of the RNs is $K = 1$. Note that the terminologies are defined in Table 6.1, while the main parameters are listed in Table 6.3.

Parameters	Equation	Scenario A, $G_{2\times4}$	Scenario A, $G_{4\times8}$
R_{FEC} [BPS]	(6.10)	2	2
R_{DNC} [BPS]	(6.26)	$1/3$	$1/3$
R_{ADNC} [BPS]	(6.30)	$\begin{cases} 1 & \text{if } F_g = 1\,, \\ 1/3 & \text{otherwise}\,, \end{cases}$	$\begin{cases} 1 & \text{if } F_g = 1\,, \\ 1/3 & \text{otherwise}\,, \end{cases}$
η_{DNC} [BPS]	(6.27)	$2/3$	$2/3$
η_{ADNC} [BPS]	(6.31)	$\begin{cases} 2 & \text{if } F_g = 1\,, \\ 2/3 & \text{otherwise}\,, \end{cases}$	$\begin{cases} 2 & \text{if } F_g = 1\,, \\ 2/3 & \text{otherwise}\,, \end{cases}$
D_{DNC}	(6.33)	$5 \leq D_{DNC} \leq 5$	$6 \leq D_{DNC} \leq 9$
D_{ADNC}	(6.33)	$\begin{cases} 1 & \text{if } F_g = 1\,, \\ D_{DNC} & \text{otherwise}\,, \end{cases}$	$\begin{cases} 1 & \text{if } F_g = 1\,, \\ D_{DNC} & \text{otherwise}\,, \end{cases}$
n_1 [frame]	$--$	1	2
n_2 [frame]	$--$	1	2
M [user]	$--$	2	2

Table 6.6: Rates and diversity orders of the systems based on the transfer matrices $\boldsymbol{G}_{2\times4}$ and $\boldsymbol{G}_{4\times8}$, when employing Scenario A of Figure 6.2, while the number of RNs is $K = 2$. Note that the terminologies are defined in Table 6.1, while the main parameters are listed in Table 6.3.

Parameters	Equation	Scenario B, $G_{2\times4}$	Scenario B, $G_{4\times8}$
R_{FEC} [BPS]	(6.10)	3	3
R_{DNC} [BPS]	(6.26)	$1/3$	$1/3$
R_{ADNC} [BPS]	(6.30)	$\begin{cases} 1 & \text{if } F_g = 1\,, \\ 1/3 & \text{otherwise}\,, \end{cases}$	$\begin{cases} 1 & \text{if } F_g = 1\,, \\ 1/3 & \text{otherwise}\,, \end{cases}$
η_{DNC} [BPS]	(6.27)	0.86	0.86
η_{ADNC} [BPS]	(6.31)	$\begin{cases} 2 & \text{if } F_g = 1\,, \\ 0.86 & \text{otherwise}\,, \end{cases}$	$\begin{cases} 2 & \text{if } F_g = 1\,, \\ 0.86 & \text{otherwise}\,, \end{cases}$
D_{DNC}	(6.33)	$5 \leq D_{DNC} \leq 5$	$6 \leq D_{DNC} \leq 9$
D_{ADNC}	(6.33)	$\begin{cases} 1 & \text{if } F_g = 1\,, \\ D_{DNC} & \text{otherwise}\,, \end{cases}$	$\begin{cases} 1 & \text{if } F_g = 1\,, \\ D_{DNC} & \text{otherwise}\,, \end{cases}$
n_1 [frame]	$--$	1	2
n_2 [frame]	$--$	1	2
M [user]	$--$	2	2

Table 6.7: Rates and diversity orders of the systems based on the transfer matrices $\boldsymbol{G}_{2\times4}$ and $\boldsymbol{G}_{4\times8}$, when employing Scenario B of Figure 6.3 and the number of RNs is $K = 2$. Note that the terminologies are defined in Table 6.1, while the main parameters are listed in Table 6.3.

6.2.6 Network Decoder

Following our discussions on the NC encoder, this section considers at the NC decoder briefly. The motivated readers might like to refer to [138], and to the references therein for more details. Let us consider the NC-based $G_{4\times8}$ scheme depicted in Figure 6.9 relaying on the transfer matrix of Equation (6.32). Let us assume that the full transmission resulted in a modified matrix of:

$$\boldsymbol{G'}_{4\times8} = \left[\begin{array}{cccc|cccc} 0 & 0 & 0 & 0 & 0 & 0 & 3 & 0 \\ 0 & 0 & 0 & 0 & 0 & 0 & 7 & 0 \\ 0 & 0 & 1 & 0 & 0 & 0 & 6 & 1 \\ 0 & 0 & 0 & 0 & 0 & 0 & 3 & 2 \end{array}\right] . \tag{6.34}$$

As suggested by Figure 6.8, The modified transfer matrix $\boldsymbol{G}'_{4\times8}$ can be partitioned into:

$$\boldsymbol{I'}_{4\times8} = \begin{bmatrix} 0 & 0 & 0 & 0 \\ 0 & 0 & 0 & 0 \\ 0 & 0 & 1 & 0 \\ 0 & 0 & 0 & 0 \end{bmatrix} , \tag{6.35}$$

$$\boldsymbol{P'}_{4\times8} = \begin{bmatrix} 0 & 0 & 3 & 0 \\ 0 & 0 & 7 & 0 \\ 0 & 0 & 6 & 1 \\ 0 & 0 & 3 & 2 \end{bmatrix} . \tag{6.36}$$

Let us now denote the IFs transmitted from both SNs of Figure 6.9 during the two BPs as $\boldsymbol{X}_{4\times8} = \left\{ I_1^1(1), I_2^2(1), I_1^3(2), I_2^4(2) \right\}$, which can be illustrated in matrix format using:

$$\boldsymbol{X}_{4\times8} = \begin{bmatrix} I_1^1(1) & 0 & 0 & 0 \\ 0 & I_2^2(1) & 0 & 0 \\ 0 & 0 & I_1^3(2) & 0 \\ 0 & 0 & 0 & I_2^4(2) \end{bmatrix} . \tag{6.37}$$

Then the signals received at the DN during the BPs and CPs are denoted by $\boldsymbol{Z}_{I',4\times8}$ and $\boldsymbol{Z}_{P',4\times8}$, respectively and are formulated as:

$$\boldsymbol{Z}_{I',4\times8} = \boldsymbol{X}_{4\times8}\boldsymbol{I'}_{4\times8} , \tag{6.38}$$

$$\boldsymbol{Z}_{P',4\times8} = \boldsymbol{X}_{4\times8}\boldsymbol{P'}_{4\times8} , \tag{6.39}$$

Since the DN knows $\boldsymbol{G}'_{4\times8}$, both $\boldsymbol{Z}_{I',4\times8}$ and $\boldsymbol{Z}_{P',4\times8}$ can be estimated according to Equation (6.38)

and Equation (6.39) as:

$$\boldsymbol{Z}_{I',4\times 8} = \begin{bmatrix} 0 & 0 & 3 & 0 \end{bmatrix} , \tag{6.40}$$

$$\boldsymbol{Z}_{P',4\times 8} = \begin{bmatrix} 0 & 0 & 47 & 11 \end{bmatrix} . \tag{6.41}$$

More explicitly, the entries of the vector in Equation (6.40) are calculated as:

$$0 \cdot I_1^1(1) + 0 \cdot I_2^2(1) + 1 \cdot I_1^3(2) + 0 \cdot I_2^4(2) = 3 \Rightarrow I_1^3(2) = 3 . \tag{6.42}$$

Similarly, the entries of the vector in Equation (6.41) can be expressed as:

$$3 \cdot I_1^1(1) + 7 \cdot I_2^2(1) + 6 \cdot I_1^3(2) + 3 \cdot I_2^4(2) = 47 , \tag{6.43}$$

$$0 \cdot I_1^1(1) + 0 \cdot I_2^2(1) + 1 \cdot I_1^3(2) + 2 \cdot I_2^4(2) = 11 . \tag{6.44}$$

Substituting the results of Equation (6.42) into both Equation (6.43) and Equation (6.44), we arrive at:

$$3 \cdot I_1^1(1) + 7 \cdot I_2^2(1) + 3 \cdot I_2^4(2) = 29 , \tag{6.45}$$

$$2 \cdot I_2^4(2) = 8 \Rightarrow I_2^4(2) = 4 . \tag{6.46}$$

Upon substituting Equation (6.46) into Equation (6.45), we arrive at:

$$3 \cdot I_1^1(1) + 7 \cdot I_2^2(1) + 3 \cdot I_2^4(2) = 29 , \tag{6.47}$$

$$3 \cdot I_1^1(1) + 7 \cdot I_2^2(1) = 17 . \tag{6.48}$$

Observe in Equation (6.48) that we only have single equation, but two unknown variables. Hence, out of the four transmitted IFs, only two IFs namely $I_1^3(2)$ and $I_2^4(2)$ can be recovered based on Equation (6.42) and Equation (6.46), respectively.

To generalise, let us assume that $\boldsymbol{X}^s$ denotes the IFs transmitted by the SNs to both the RNs and the DN during the BP, while $\boldsymbol{X}^r$ represents the PFs transmitted from the RNs to the DN during the CP. This PF matrix is constructed using Equation (6.23). Then, upon using the modified matrices, $\boldsymbol{P}'$ and $\boldsymbol{I}'$, the frames that are successfully received at the DN can be written as [138]:

$$\boldsymbol{Z}_{I'} = \boldsymbol{X}^s \boldsymbol{I}' , \tag{6.49}$$

$$\boldsymbol{Z}_{P'} = \boldsymbol{X}^r \boldsymbol{P}' , \tag{6.50}$$

where the matrices $\boldsymbol{Z}_{I'}$ and $\boldsymbol{Z}_{P'}$ denote the IFs and PFs that are successfully received at the DN during the BP and CP, respectively. Let us now assume that the DN can successfully recovers a set $\boldsymbol{X}^s_{I'}$ that is a correct subset of $\boldsymbol{X}^s$ and since the DN knows $\boldsymbol{G}'$ [133, 134, 136], i.e. the DN is aware of how each PF was constructed, $\boldsymbol{X}^s_{I'}$ is also a subset of $\boldsymbol{X}^r$. Thus, from Equation (6.49), we arrive

at:

$$\boldsymbol{X}^s_{I'} = \boldsymbol{Z}_{I'} = \boldsymbol{Z}_{P'} \, . \tag{6.51}$$

Then, upon substituting Equation (6.51) into Equation (6.50) we arrive at [138]:

$$(\boldsymbol{X}^r - \boldsymbol{X}^s_{I'}) \, \boldsymbol{P'} = \boldsymbol{Z}_{P'} - \boldsymbol{X}^s_{I'} \boldsymbol{P'} \, . \tag{6.52}$$

Therefore, a set $\hat{\boldsymbol{X}}^s_{P'}$ of IFs may then be extracted from Equation (6.52) with the aid of the Gaussian elimination algorithm [134]. Consequently the entire set of the recorded IFs at the DN may be expressed as $\tilde{\boldsymbol{X}}^s_{P'} \cup \boldsymbol{X}^s_{I'}$ out of the full set $\boldsymbol{X}^s$ of IFs.

6.3 Performance Results

The following two sections will discuss the performance results of Scenario A of Figure 6.2 and Scenario B of Figure 6.3, respectively. The main simulation parameters of both scenarios were listed in Table 6.3.

6.3.1 Performance Results of Scenario A

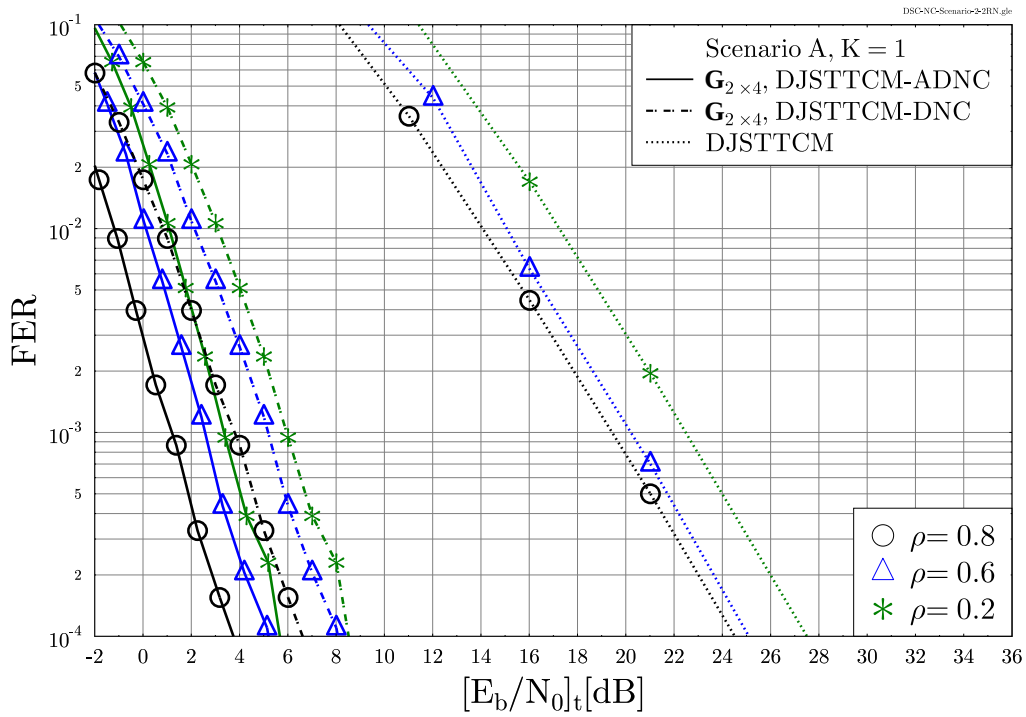

Figure 6.10: FER versus $[E_b/N_0]_t$ of the **DJSTTCM-DNC/ADNC**-aided $\boldsymbol{G}_{2\times4}$ scheme of Figure 6.1 in Scenario **A**, when $K = 1$ RN is invoked for various correlation coefficients. Note that the corresponding main simulation parameters are outlined in Table 6.3, while the associated variables are summarised in Table 6.4. The related results are summarised in Table 6.8.

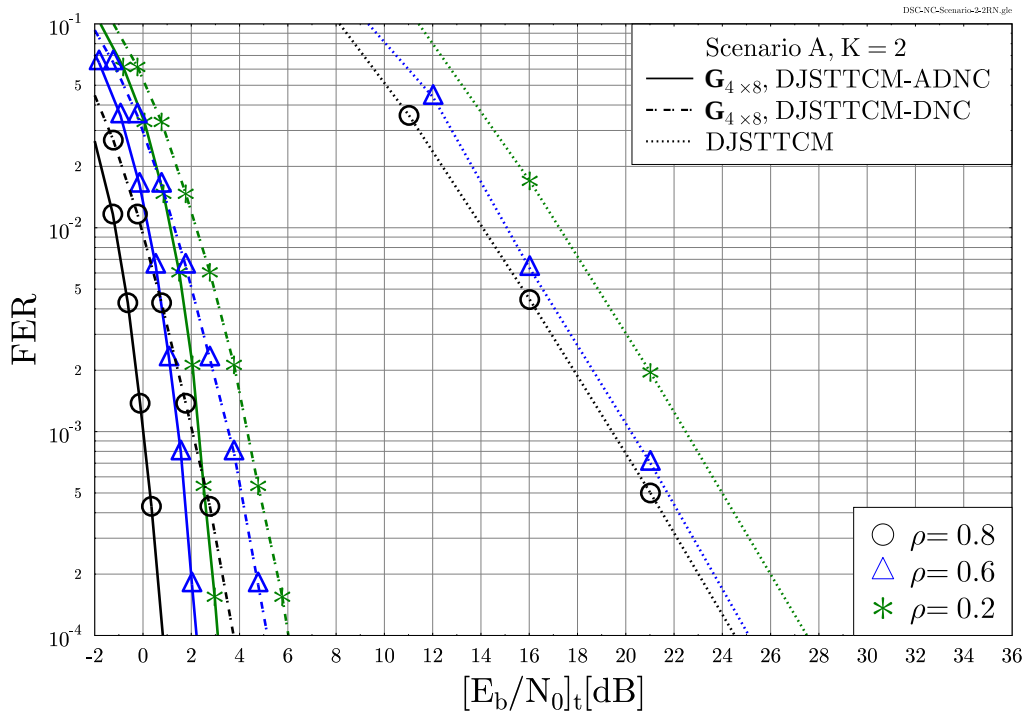

Figure 6.11: FER versus $[E_b/N_0]_t$ of the **DJSTTCM-DNC/ADNC**-aided $G_{4\times8}$ scheme of Figure 6.1 in Scenario **A**, when $K = 2$ RNs is invoked for various correlation coefficients. Note that the corresponding main simulation parameters are outlined in Table 6.3, while the associated variables are summarised in Table 6.6. The related results are summarised in Table 6.8.

The FER performance of the proposed DJSTTCM-aided DNC and ADNC schemes invoked in Scenario A is characterised in Figure 6.10 and Figure 6.11. It can be observed from all these FER performance results that our NC-aided schemes always perform better than the non-cooperative schemes, regardless of the correlation coefficient values. To elaborate further, Figure 6.10 portrays the FER performance of Scenario A, when only a single RN $(K = 1)$ is used, where the DJSTTCM-aided DNC/ADNC schemes are constructed using the transfer matrix $G_{2\times4}$ of Equation (6.11). As the figure shows, a substantial performance enhancement can be obtained, when employing our NC schemes benchmarked against its non-cooperative counterparts. More explicitly, at a FER level of 10^{-3} the DJSTTCM-ADNC scheme outperforms the DJSTTCM scheme by $[E_b/N_0]_t = 19.5 - 1.5 = 18.0$ dB for $\rho = 0.8$. This gain drops to $[E_b/N_0]_t \approx 14.7$ dB, when using the non-adaptive DJSTTCM-DNC scheme, as seen in Figure 6.10. The adaptive feedback-flag based technique of Section 6.2.4 contributed a considerable $[E_b/N_0]_t$-performance improvement in comparison to that of the system operating without the adaptive mechanism. For example, an $[E_b/N_0]_t$-performance improvement of about 1.5 dB is recorded at an FER of 10^{-3}, when applying the adaptive feedback-flag based mechanism in the context of the DJSTTCM-ADNC for the $G_{2\times4}$-based scheme relying on $\rho = 0.8$, as seen in Figure 6.10.

Figure 6.11 portrays the FER performance of our DJSTTCM-aided DNC/ADNC scheme of Figure 6.1 using $K = 2$ RNs based on the $G_{4\times8}$ transfer matrix arrangement of Equation (6.32).

As expected, employing a higher order transfer matrix improves the attainable performance further. For example, an impressive gain of about 19.5 dB is achieved when comparing the DJSTTCM-ADNC scheme to the DJSTTCM benchmark scheme for a correlation coefficient of $\rho = 0.8$. This performance improvement is an explicit benefit of the higher diversity gain offered by the $\boldsymbol{G}_{4\times8}$-based arrangements over their $\boldsymbol{G}_{2\times4}$-based counterparts. Similarly, applying our ADNC mechanism is expected to provide the scheme with a further $[E_b/N_0]_t$ gain. To elaborate, our adaptive DJSTTCM-ADNC schemes approach a FER$= 10^{-3}$ at 2 dB lower power than its non-adaptive DJSTTCM-DNC counterparts, as seen in Figure 6.11. Table 6.8 summarises the attainable performance gains of our proposed schemes, namely of the DJSTTCM-DNC and DJSTTCM-ADNC, for Scenario A in comparison to the benchmark scheme dispensing with NC at an integrity requirement of FER$= 10^{-3}$.

Scheme	p_e	ρ	$[E_b/N_0]_t(10^{-3})$ (dB)	**Gain** (dB)
DJSTTCM-DNC $\boldsymbol{G}_{2\times4}$ Figure 6.10	0.10	0.80	4.8	14.7
	0.20	0.60	5.6	14.6
	0.40	0.20	6.0	16.5
DJSTTCM-ADNC $\boldsymbol{G}_{2\times4}$ Figure 6.10	0.10	0.80	1.5	18.0
	0.20	0.60	3.0	17.4
	0.40	0.20	3.5	19.0
DJSTTCM-DNC $\boldsymbol{G}_{4\times8}$ Figure 6.11	0.10	0.80	2.0	17.5
	0.20	0.60	3.6	16.6
	0.40	0.20	4.5	18.0
DJSTTCM-ADNC $\boldsymbol{G}_{4\times8}$ Figure 6.11	0.10	0.80	0.0	19.5
	0.20	0.60	1.6	18.6
	0.40	0.20	2.5	20.0

Table 6.8: System performance of the proposed **DJSTTCM-DNC/ADNC** scheme of Figure 6.1 in Scenario A of Figure 6.2 using simulation parameters of Table 6.3. The results are extracted from Figure 6.10 and Figure 6.11 at a FER level of 10^{-3}.

Figure 6.12 quantifies the schemes' effective per user throughput against SNR$_t$ for our DJSTTCM-ADNC scheme, when employing $K = 1$ RN and $K = 2$ RNs. According to Equation (6.27) the non-adaptive schemes have an effective per user throughput of $\eta_{DNC} = 0.5$ [BPS], when a single RN is used. However this throughput is reduced to $\eta_{DNC} = 1/3$ [BPS], when adding one more RN, as shown in Figure 6.12(a) and Figure 6.12(b), respectively. As expected, upon invoking the ADNC scheme the overall normalised throughput, η_{ADNC}, increases when SNR$_t$ increases. Hence, in the high-SNR$_t$ region, more IFs may be recovered at the DN directly from the SNs, in which case $\mathrm{E}[K_{\mathrm{AD}}]$ of Equation (6.31) tends to zero. This implies that less PFs are required as SNR$_t$ increases, where η_{ADNC} might asymptotically reach 1 BPS, which simply corresponds to the direct link's rate computed from Equation (6.10). Therefore, Equation (6.31) implies that the effective throughput of the adaptive scheme, namely η_{ADNC}, exhibits a near-instantaneously time-variant nature, depend-

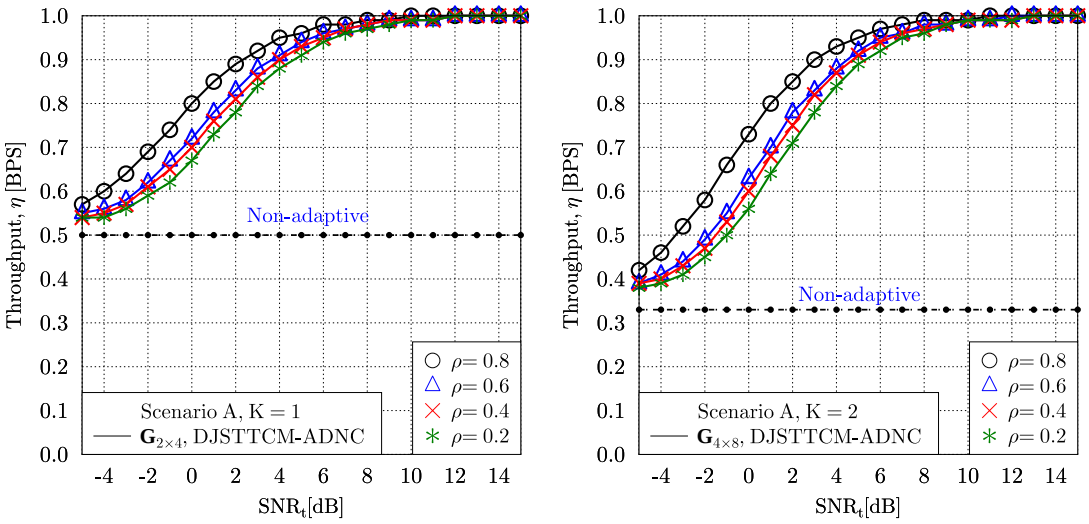

(a) $K = 1$ RN. (b) $K = 2$ RNs.

Figure 6.12: Effective per user throughput versus transmit SNR of the **DJSTTCM-ADNC** when the Scenario **A** is invoked for various correlation coefficients. Note that the corresponding main simulation parameters are outlined in Table 6.3, while the associated rates of a) $K = 1$ RN and b) $K = 2$ RNs based schemes are summarised in Table 6.4 and Table 6.6, respectively.

ing on the SNR of each transmission session. When aiming for a fair comparison, using the SNR$_t$ might be not suitable for a FER performance comparison. Thus, we have considered the transmit SNR per information bit $[E_b/N_0]_t$[dB] $=$ SNR$_t$[dB] $- 10\log_{10}(\eta_{ADNC})$, where the effect of the rate fluctuation has been eliminated.

6.3.2 Performance Results of Scenario B

As the schematic of Figure 6.3 shows, each node of our Scenario B arrangement, namely the SNs, RNs and the DN are equipped with a single transmit and/or receive antenna. This structure constitutes an attractive scheme, especially when aiming for a reduced-complexity design, where each of the RNs combines both of the received IFs during the BP into a SPM signal using the procedure introduced in Section 5.4.1.

Similar to Section 6.3.1, we will first discuss the FER performance of Scenario B, followed by its achievable throughput. As expected, the FER performance of Scenario A is better than that of Scenario B, since the MIMO structure of the former improves the system performance at the cost of a higher hardware complexity. However, our proposed scheme is still capable of outperforming the non-cooperative scheme for all the correlation values considered, as shown in Figure 6.13 and Figure 6.14. More quantitatively, our proposed DJSTTCM-ADNC-aided $\boldsymbol{G}_{2\times4}$ scheme of Figure 6.1 requires only $[E_b/N_0]_t = 5.0$ dB to attain a FER $= 10^{-3}$, while the DJSTTCM dispensing with NC requires $[E_b/N_0]_t = 31.5$ dB at $\rho = 0.8$, as seen in Figure 6.13. However, upon adding one more RN the proposed DJSTTCM-ADNC-aided $\boldsymbol{G}_{4\times8}$ only as 4.1 dB to achieve FER $= 10^{-3}$,

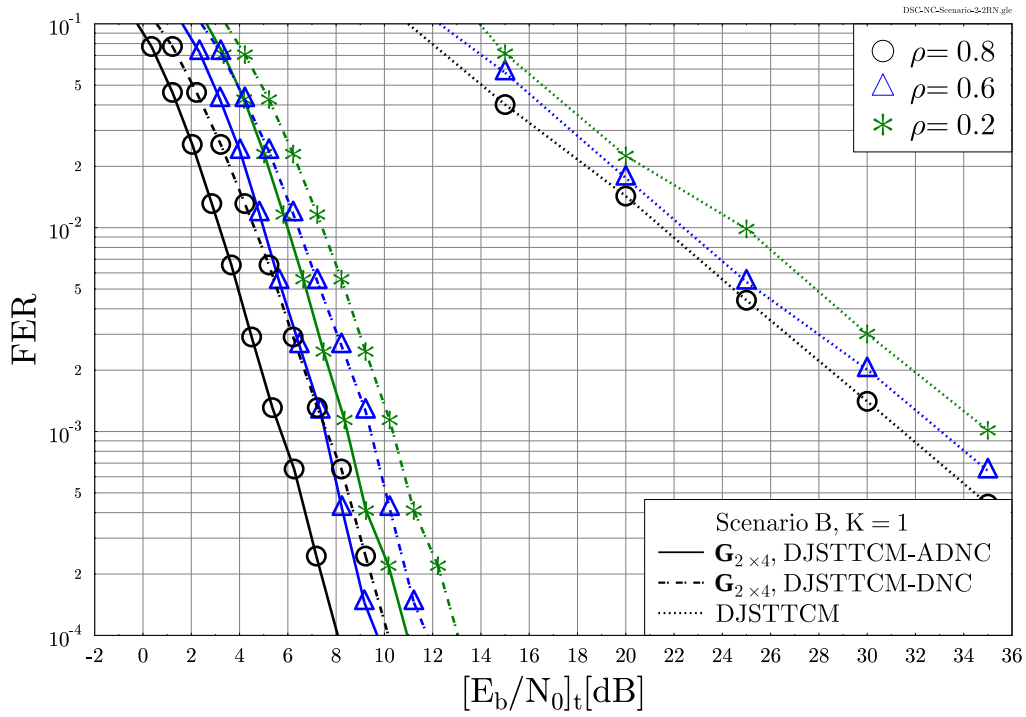

Figure 6.13: FER versus $[E_b/N_0]_t$ of the **DJSTTCM-ADNC**-aided $G_{2\times4}$ scheme of Figure 6.1 in Scenario **B**, when $K = 1$ RN is invoked for various correlation coefficients. Note that the corresponding main simulation parameters are outlined in Table 6.3, while the associated variables are summarised in Table 6.5. The related results are summarised in Table 6.9.

Scheme	p_e	ρ	$[E_b/N_0]_t(10^{-3})$ (dB)	**Gain** (dB)
DJSTTCM-DNC $G_{2\times4}$ Figure 6.13	0.10	0.80	7.8	23.7
	0.20	0.60	9.5	23.5
	0.40	0.20	10.5	24.5
DJSTTCM-ADNC $G_{2\times4}$ Figure 6.13	0.10	0.80	5.0	26.5
	0.20	0.60	7.8	25.2
	0.40	0.20	8.5	26.5
DJSTTCM-DNC $G_{4\times8}$ Figure 6.14	0.10	0.80	5.5	26.0
	0.20	0.60	7.5	25.5
	0.40	0.20	9.5	25.5
DJSTTCM-ADNC $G_{4\times8}$ Figure 6.14	0.10	0.80	4.1	27.4
	0.20	0.60	6.0	27.0
	0.40	0.20	7.8	27.2

Table 6.9: System performance of the proposed **DJSTTCM-DNC/ADNC** scheme of Figure 6.1 when the employing Scenario B of Figure 6.3 and simulation parameters of Table 6.3 are used. The results are extracted from Figure 6.13 and Figure 6.14 when aiming for FER level of $= 10^{-3}$.

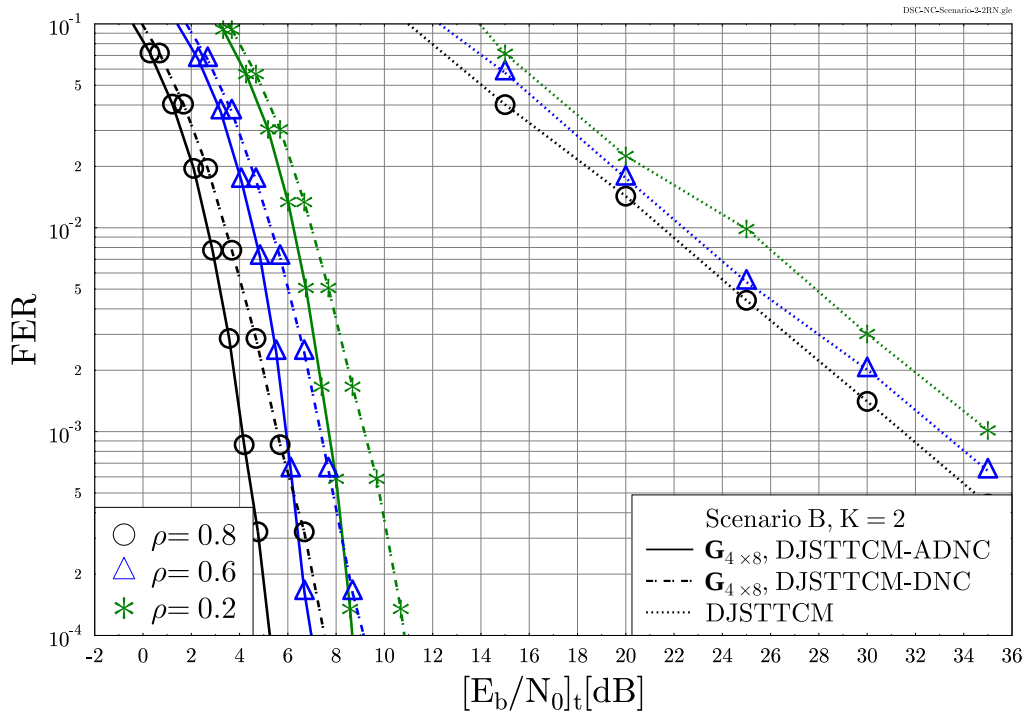

Figure 6.14: FER versus $[E_b/N_0]_t$ of the **DJSTTCM-ADNC**-aided $\boldsymbol{G}_{4\times8}$ scheme of Figure 6.1 in Scenario **B**, when $K = 2$ RNs is invoked for various correlation coefficients. Note that the corresponding main simulation parameters are outlined in Table 6.3, while the associated variables are summarised in Table 6.7. The related results are summarised in Table 6.9.

as shown in Figure 6.14. To summarise, Table 6.9 listed the FER performance of the DJSTTCM-DNC/ADNC schemes performance for Scenario B of Figure 6.3.

Figure 6.15 shows that the effective per user throughput increases as the SNR increases, when the adaptive scheme is activated. In contrast to Scenario A, the DJSTTCM-ADNC using $\boldsymbol{G}_{2\times4}$ requires almost $\text{SNR}_t = 14$ dB for asymptotically approaching a throughput of 1 BPS, as shown in Figure 6.15(a). Otherwise similar trends prevail to those discussed in Section 6.3.2.

6.4 Chapter Conclusions

In this chapter the transmission of correlated source signals was assisted by two different NC schemes, which exhibited a robust performance for transmission over hostile channels. The over all block diagram of the proposed scheme was depicted in Figure 6.1. In Section 6.2.1 the DJSTTCM encoder and decoder, that were originally introduced in Section 5.3.1 and Section 5.3.2, respectively, were revisited. Subsequently, the BER performance of our cooperative arrangements was characterised when subjected to both uncorrelated Rayleigh fading and a quasi-static Rayleigh fading channel in Figures 6.4– 6.6.

A significant performance degradation was exhibited for transmission over quasi-static Rayleigh

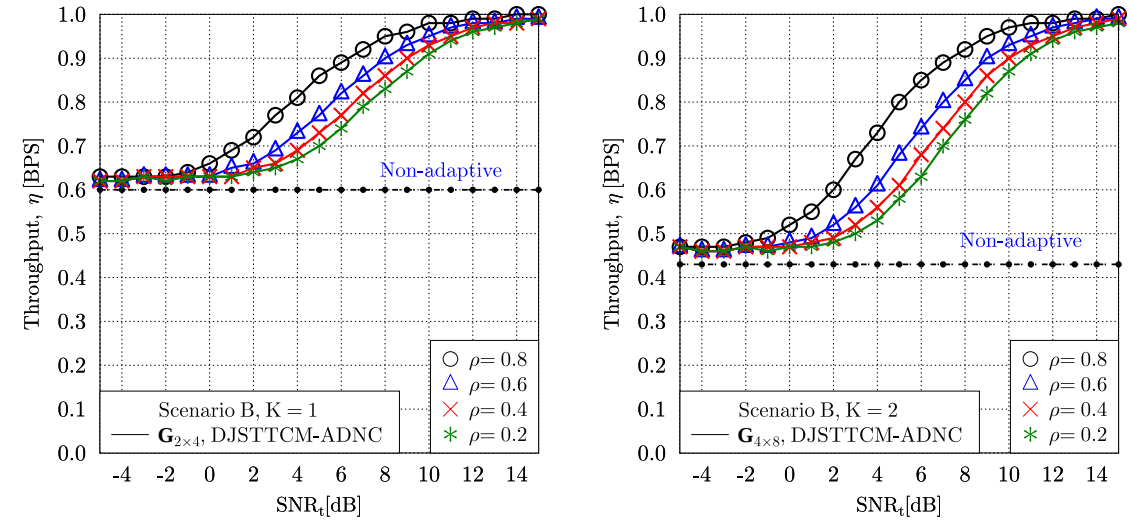

(a) $K = 1$ RN. (b) $K = 2$ RNs.

Figure 6.15: Effective per user throughput versus transmit SNR of the **DJSTTCM-ADNC** when the Scenario **B** scenario is invoked. Note that the corresponding main simulation parameters are outlined in Table 6.3, while the associated rates of a) $K = 1$ RN and b) $K = 2$ RN based schemes are summarised in Table 6.5 and Table 6.7, respectively.

fading channels. As a counter-measure, the use of both DNC and ADNC were conceived in this chapter, where the time diversity between the frames will be further exploited. A substantial gain of 19.5 dB was attained at a correlation coefficient $\rho = 0.8$ over its counterpart dispensing with NC, as evidenced by Figure 6.11. $\boldsymbol{G}_{2\times4}$ transfer matrix-based NC was introduced in Section 6.2.2 followed by $\boldsymbol{G}_{4\times8}$-based design in Section 6.2.5 of our proposed cooperative scheme. Furthermore, according to the resources availability, two scenarios were considered. In Scenario A each of the RNs and the DN were equipped with two antennas, while in Scenario B, all RNs and the DN had a single antenna. Despite having only a single antenna in Scenario B, a robust performance was attained. Quantitatively, our DJSTTCM-ADNC scheme only requires $E_b/N_0 = 5.0$ dB and $E_b/N_0 = 4.1$ dB for achieving a FER of 10^{-3} by the $\boldsymbol{G}_{2\times4}$ and $\boldsymbol{G}_{4\times8}$ based schemes, respectively, as evidenced by Figure 6.13 and Figure 6.14.

Chapter 7

Conclusions and Future Directions

In this concluding chapter, we will summarise our main findings in Section 7.1, while various future research avenues will be discussed in Section 7.2.

7.1 Summary and Conclusions

Distributed Source Coding (DSC) refers to the problem of transmitting several correlated, but physically separated sources, where the receiver has the capability of joint decoding. The correlation between sources can be characterised using an abstraction constituted by the Binary Symmetric Channel (BSC). Based on this abstraction, channel codes can be invoked for resolving the associated Distributed Joint Source-Channel coding (DJSC) problem. Hence our goal was to design a channel code for DJSC problems and to investigate it in the context of cooperative communication transmission arrangements.

- **Chapter 1**: We commenced by outlining the motivation of using DSC schemes in the real-based application of a hyperspectral image transmission scenario in Section 1.1. The main principles as well as the historical background concerning both the theory and practice of DSC were presented in Section 1.2. Next in Section 1.3, Joint Source-coding and Channel-coding (JSCC) techniques were designed for jointly exploiting the residual redundancy that the source-code fails to remove. We then continued in Section 1.5.1 with the thesis' outline, followed by its novel contributions in Section 1.5.2.

- **Chapter 2**: We provided a rudimentary introduction to both Coded Modulation (CM) and EXtrinsic Information Transfer (EXIT charts). CM constitutes a bandwidth-efficient scheme, where the coding and modulation functions are intrinsically integrated by absorbing the parity bit upon doubling the constellation size. The EXIT chart technique constitutes a powerful semi-analytical tool conceived for characterising the convergence behaviour of iterative decoding schemes. Accordingly, this chapter can be divided into two main parts, as follows:

– The first part commenced with presenting the historical background of CM in Section 2.2, while Trellis-Coded Modulation (TCM) and Turbo TCM (TTCM) were analysed and investigated in Section 2.3 and Section 2.4, respectively. The TCM schematic was portrayed in Figure 2.1, where a Recursive Systematic Code (RSC) is combined with Set Partitioning (SP)-assisted signal labelling. The SP labelling technique, which was proposed for attaining an increased Free Euclidean Distance (FED) between the unprotected bits of the constellation, was reviewed in Section 2.3.1. The associated non-binary Maximum A-Posteriori (MAP) TCM decoder was detailed in Section 2.3.2, which was summarised in Figure 2.4.

  Section 2.4.1 detailed the TTCM encoder constituted by a pair of parallel concatenated TCM encoders connected by a symbol-based interleaver. Subsequently, TTCM decoding was detailed in Section 2.4.2, where the inseparable nature of the information passed from one decoder to the other was described. The TTCM decoding procedure was depicted in Figure 2.8.

  The performance of QPSK, 8PSK, 16QAM and 64QAM-aided TCM and TTCM was evaluated for transmission over both AWGN and uncorrelated Rayleigh fading channels in Section 2.4.3. The superiority of TTCM was demonstrated by our Bit Error Ratio (BER) performance curves. To elaborate, it was found in Figure 2.9 and Figure 2.10 that TTCM-QPSK needs an SNR$=$ 1.8 dB for achieving a BER level of 10^{-6}, while SNR$=$ 6.4 dB was required by the TCM scheme, when communicating over AWGN channels. Similarly, when uncorrelated Rayleigh fading channels were considered, TTCM-QPSK outperformed TCM-QPSK by a significant power-difference of 11.8 dB at a BER level of 10^{-6}. Both the TCM and TTCM performances were summarised in Table 2.4 and Table 2.5 for transmission over both AWGN as well as uncorrelated Rayleigh fading channels, respectively. Additionally, the number of required iterations, I, between the parallel TCM decoders was quantified using the BER curves of Figure 2.13, which suggested that four iterations exhibited a good trade-off between the performance attained and the decoding complexity imposed. As many as $N_s = 12\,000$ symbols per frame were required for the TTCM scheme for avoiding the formation of an error-floor up to a BER level of 10^{-6}, as documented in Figure 2.14

– The powerful semi-analytical EXIT chart technique is capable of visualising the convergence behaviour of iterative decoding schemes by exploiting the relationship between the Mutual Information (MI) of the input and output probabilities of each constituent decoder. These MI averages were quantified for our non-binary EXIT charts in Section 2.5.1, which was followed by an insightful example on how the EXIT charts can be utilised for optimising the two-stage coding scheme of Figure 2.17. More specifically, our detector comprises an inner Maximum Likelihood (ML) based Multi-User Detector (MUD) and an outer TTCM decoder. The EXIT charts were used for designing and optimising our scheme as follows:

  * Figure 2.18 determined the minimum transmit SNR required for facilitating an

open EXIT tunnel, which was necessitated for attaining a vanishingly low BER.

- The required number of the iterations between the inner and outer decoders was evaluated with the aid of the stair-case-shaped trajectory of Figure 2.18. The EXIT chart predictions were also confirmed by our Monte-Carlo simulation based BER curves.

- **Chapter 3** This chapter proposed and investigated an attractive Joint Source-coding, Channel-coding and Modulation (JSCM) scheme conceived for a two-way relaying system. More specifically, Variable Length Code (VLC) were uniquely amalgamated with TTCM for creating a JSCM scheme. This scheme was conceived for two-way relaying channels and the resultant system was referred to as the TTCM-VLC-2Way arrangement. The chapter commenced with the description of the resultant spectral-efficient two-way relaying arrangement in Section 3.2, where only two time slots are needed for achieving full-duplex information exchange between two users, compared to the four time slots of the conventional one-way relaying scheme. The schematic of both phases, namely of Phase-I and Phase-II was portrayed in Figure 3.2. Additionally, the achievable Discrete-input Continuous-output Memoryless Channel (DCMC) capacity of the corresponding two-way relaying channel was quantified in Section 3.2.2. Furthermore, a novel Power Sharing (PS) technique was proposed in Section 3.2.2 for allocating the transmission power appropriately between the Source Node (SN) and the Relay Node (RN).

  Section 3.3 detailed our EXIT chart-aided design, where the minimum number of inner iterations I_{in} within the outer block of Figure 3.2 constituted by the TTCM and VLC decoder was optimised based on the outer decoder EXIT curves in Figure 3.5. More explicitly, $I_{\text{in}} = 4$ facilitated an open EXIT tunnel, while employing $I_{\text{in}} < 4$ may lead to a closed EXIT chart tunnel, hence resulting in a high residual BER. Doubling the number inner iterations to $I_{\text{in}} = 8$ would only provide a diminishing return, despite its higher decoding complexity, as illustrated on Figure 3.5. Additionally, the minimum SNRs required for both phases for the case of facilitating open EXIT tunnels leading to the right-hand axis were evaluated for both phases in Figure 3.5. Explicitly, SNR$=$ 8.6 dB and SNR$=$ 15.8 dB were required for the Phase-I and Phase-II transmissions, respectively. Our EXIT charts predictions were authenticated by the BER simulation results of Figure 3.6. The BER performance of our proposed TTCM-VLC-2Way scheme was depicted in Figure 3.7, where our scheme operated within 2.92 dB of the DCMC capacity bound, while attaining a combined coding and relaying gain of 11.4 dB over the conventional non-cooperative benchmarker.

  A novel reduced-complexity method was introduced in Section 3.3.2 for representing the pixel values with a reduced number of codewords. According to our bit-based trellis VLC, 965 states were needed if each of the 8-bit pixel were mapped into a VLC source symbol, hence resulting into an excessive decoding complexity. Our reduced-complexity source encoder, which was depicted in Figure 3.10, was capable of significantly reducing the number of states form 965 to 12 states. Our joint iterative scheme proposed in Section 3.2 was inves-

tigated in the context of robust image and video transmissions in Section 3.4. Our still image performance results were analysed in Section 3.4.1, while the video-based performance was analysed in Section 3.4.2.

- **Chapter 4** Motivated by the example presented in Section 1.1 and by the reliable performance associated with the high bandwidth-efficiency offered by the TTCM schemes discussed in Section 2.4, this chapter conceived a TTCM-aided relying on perfect side-information DJSC scheme, which was termed as DJSTTCM. To elaborate further, the first source sequence it was TTCM encoded and it was further compressed before its transmission, while the second source signal was assumed to be perfectly decoded and hence it was flawlessly available at the destination for exploitation as side-information for improving the decoding performance of the first source. The proposed scheme was capable of supporting reliable communications near the Slepian-Wolf Shannon (SW/S) theoretical limit for both uncorrelated Rayleigh and Nakagami-m fading channels. Furthermore, the DJSTTCM scheme was assisted by our adaptive mechanism, where the encoder was capable of accommodating the near-instantaneously time-varying nature of the wireless channel. We refer to this scheme as A-DJSTTCM.

  The non-binary MAP decoding algorithm was modified in Section 4.2.3 in order to exploit the side-information available at the receiver. The benefits of the side-information at the decoder were demonstrated by the BER results of Figures 4.3– 4.5, where for example our DJSTTCM-QPSK scheme had a significant gain of 5.6 dB compared to its separate-processing based counterpart at a BER level of 10^{-5} for a correlation coefficient of $\rho = 0.9$. The rate regions of our schemes were analysed in Section 4.3, where the SW/S bounds were evaluated. In order to examine the capability of our proposed scheme to beneficially exploit the side-information, one bit from each TTCM coded symbol was punctured. The minimum SNR required for approaching the SW/S bounds was determined by inferring the minimum achievable compression rate from the DCMC capacity curve of Figure 4.9. The proposed scheme was shown to operate within 2 dB from the SW/S bound, for $\rho = 0.93$ at a BER of 10^{-5}, when employing DJSTTCM-QPSK/BPSK scheme. In Section 4.3.2, we further extended our DJSTTCM scheme into a wide range of realistic Nakagami-m fading channels, where the DCMC capacity was formulated and plotted in Figure 4.10.

  Our rate adaptive scheme was introduced in Section 4.4 which was described by the flow chart of Figure 4.14. Explicitly, a specific modulation scheme is activated according to the near-instantaneous quality of the wireless channel as well as based on the particular time-variant correlations between the two sources.

- **Chapter 5** Based on the design of Chapter 4, the relying on perfect side-information DJSC arrangement of Figure 4.1 was extended to a more realistic cooperative scenario of Figure 5.1. More explicitly, the two correlated sources were transmitted to a Destination Node (DN) with the aid of an RN, where both source outputs were TTCM encoded and then compressed before transmission through a Rayleigh fading Multiple Access Channel (MAC). The RN then

transmitted both user signals with the aid of the powerful SuperPosition Modulation (SPM) technique of Figure 5.11 that appropriately allocated the transmit power between the two signals. The resultant scheme of Figure 5.2 in this part was referred to as the DJSTTCM-SPM regime. Later a reduced-complexity Block Syndrome Decoding (BSD) based DJSTTCM arrangement was introduced in Figure 5.20 where the scheme was capable for providing an accurate correlation estimation at the receiver. Accordingly, this chapter can be divided into two main parts as follows:

- Our cooperative system model was illustrated in Section 5.2, where the overall transmission regime relies on a pair of phases, namely on Phase-I and Phase-II. Section 5.3.3 evaluated the performance of our joint DJSTTCM scheme, where we employed EXIT charts to visualise the convergence behaviour of our decoder of Figure 5.3. The BER performance of Figure 5.6 confirmed our EXIT chart predictions. Our DJSTTCM-QPSK scheme was capable of operating within 0.55 dB from the SW/S limit for a correlation coefficient value $\rho = 0.8$, which was within 0.07 bits of the SW minimum comparison rate.

  The Phase-II transmission was discussed in Section 5.4 where the SPM invoked was introduced in Section 5.4.1. Similarly, EXIT charts were utilised for designing the transceiver for this phase. Performance gains of 2.8 dB and 3.4 dB were achieved at a BER level of 10^{-5} when $\rho = 0.8$ for $r_1 = 0.894$ and $r_2 = 0.447$, respectively, compared to the similar benchmarker schemes dispensing with joint decoding. The overall cooperative scheme was investigated in Section 5.5. The RN-aided SPM scheme allowed us to prioritise the protection of the source signals according to the targeted application, thus two different cases were introduced and simulated in Section 5.5.

- In Chapter 4, the correlation coefficient ρ was assumed to be known at the decoder. However, this assumption is not practical. Hence, Section 5.6 introduced our reduced-complexity BSD-based DJSTTCM (DJSTTCM-BSD) for estimating the correlation coefficient ρ at the receiver. Therefore, the BSD-based decoder was capable of separating the received sequence into error-free and erroneous sub-blocks, where only the erroneous blocks were actively decoded, while the error-free blocks were used for providing an accurate correlation coefficient estimate. Figure 5.24 demonstrated the accuracy of our BSD-based estimator that only required $E_b/N_0 = 6.0$ dB for attaining an accurate correlation coefficient estimation, in comparison to the conventional TTCM scheme that requires a higher value of $E_b/N_0 = 9.0$ dB.

- **Chapter 6** In this chapter, a pair of correlated source transmissions were supported by a relaying-aided Network Coding (NC). More explicitly, the bandwidth-efficient DJSTTCM scheme introduced in Chapter 5 was assisted by an active Dynamic NC (DNC), which was referred to as DJSTTCM-DNC. An Adaptive DNC (ADNC) design was conceived, resulting in a system termed as DJSTTCM-ADNC in which the RNs adaptively transmitted their frames according to the near-instantaneous channel conditions. Moreover, according to the

available resources, two different scenarios, namely Scenario A and Scenario B, were considered. The first assumed twin-antenna-aided RNs and DN, while the second assumed single-antenna based RNs and DN. In both scenarios, a Space-Division Multiple Access (SDMA) system was employed which requires only two slots for accomplishing a full transmission cycle.

Section 6.2 detailed our cooperative system model, where the transmissions are divided into two different phases, namely the Broadcast Phase (BP)s in which the Source Nodes (SNs) broadcast their Information Frames (IFs) and the Cooperative Phase (CP)s, where the Parity Frames (PFs) are transmitted from the RNs to the DN. Substantial performance degradations were observed once our DJSTTCM schemes encountered slow fading or quasi-static fading channel. For example, an approximately 12.0 dB of SNR loss was incurred when the DJSTTCM-QPSK scheme experienced slow fading. As a remedy to this problem, the employment of NC was considered.

The NC encoder was briefly introduced with the aid of the $\boldsymbol{G}_{2\times4}$-based NC example of Section 6.2.2, where $\boldsymbol{G}$ is a transfer matrix that fully characterises the NC transmission regime. The transfer matrix was further generalised, as shown in Figure 6.8. The NC decoder was detailed in Section 6.2.6, where an example using a $\boldsymbol{G}_{4\times8}$-based NC was considered. The overall attainable transmission rate was determined in Section 6.2.3, while the diversity order was studied in Section 6.2.3. Finally, the benefits of employing the proposed NC-based cooperative arrangements were demonstrated in terms of the attainable Frame Error Ratio (FER) performance in Section 6.3.

7.2 Suggestions for Future Research

In this section, we briefly discuss some promising future research directions.

7.2.1 Reduced-Complexity Near-Capacity Joint Source-Coding Channel-Coding

As shown in Figure 3.5, the area between the inner and outer decoders' EXIT curves was wide for both transmission phases. Hence, the schemes were not capable of attaining a near-capacity performance, as it was documented in the BER results of Figure 3.6. It is possible to further minimize this gap with regard to the capacity limit by using irregular code designs [114, 185] at the cost of a higher decoding complexity. However, a reduced-complexity near-capacity scheme using doping [49] and puncturing [234] based joint Unity Rate Coding (URC) and a VLC scheme is also a promising future research topic. The schematic of the system is illustrated in Figure 7.1, where Φ represents the doping process implementing that capability selected information bits will be inserted into the URC-coded sequence. The inner curves of the EXIT chart can be matched to that of the outer EXIT curve by changing both the doping rate R_Φ and the puncturing rate R_Γ. Observe in Figure 7.2 that changing the doping rate R_Φ, the shape of the inner EXIT curves

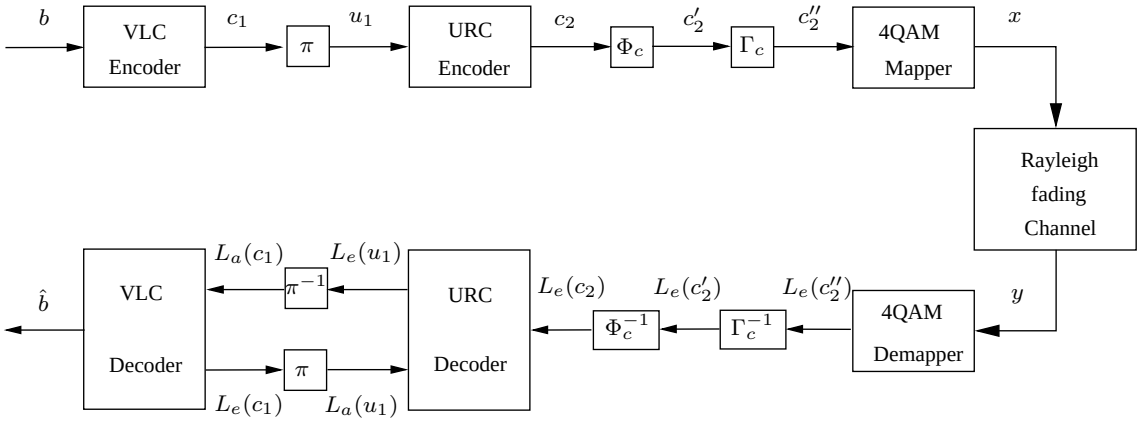

Figure 7.1: Schematic of the proposed transmission system, where Φ_c and Γ_c denotes the doping and puncturing process, respectively.

can be changed, while maintaining the same areas under the curves. Modifying the puncturing rate, however, will change the starting point of the inner EXIT curve. Hence, the area under the curve will not be the same for all rates, as suggested by Figure 7.3, where the hitherto best match was achieved, as seen in Figure 7.4. Therefore, further investigations may conducted, aiming for designing reduced-complexity near-capacity JSCC schemes.

7.2.2 Non-Coherent Coded Modulation for Distributed Joint Source-Channel coding

In all the schemes considered, we have assumed that the receiver has perfect knowledge of the channel information, i.e. the receiver knows the Channel State Information (CSI). In realistic applications the receiver has to estimate the CSI either blindly or using training symbols [235]. For example, in the Pilot Symbol Assisted Modulation (PSAM) scheme known pilot symbols are inserted into the transmitted data streams for helping the receiver to estimate the CSI. This comes at the expense of an unavoidable effective throughput loss due to the associated pilot overhead. Alternatively, differentially encoded transmission and non-coherent detection constitute attractive design alternatives that do not require the knowledge of the CSI [236]. More explicitly, non-coherent schemes should also be investigated. However, non-coherent detectors generally exhibit a 3.0 dB performance loss in comparison to coherent detection having perfect channel knowledge at the receiver [236]. Thus, we should also consider the employment of non-coherent schemes, such as soft-decision-aided Differential Amplitude and Phase-Shift Keying (DAPSK) [237, 238] for low-complexity wireless communications, since it dispenses with high-complexity channel estimation.

7.2.3 Hidden Markov Correlation Modelling

The correlation between sources may be modelled using a BSC, which is suitable for modelling the correlation of memoryless sources. However, most practical sources exhibit memory [239], where similar to [240] a hidden Markov model can be used for modelling the source correlation. Thus,

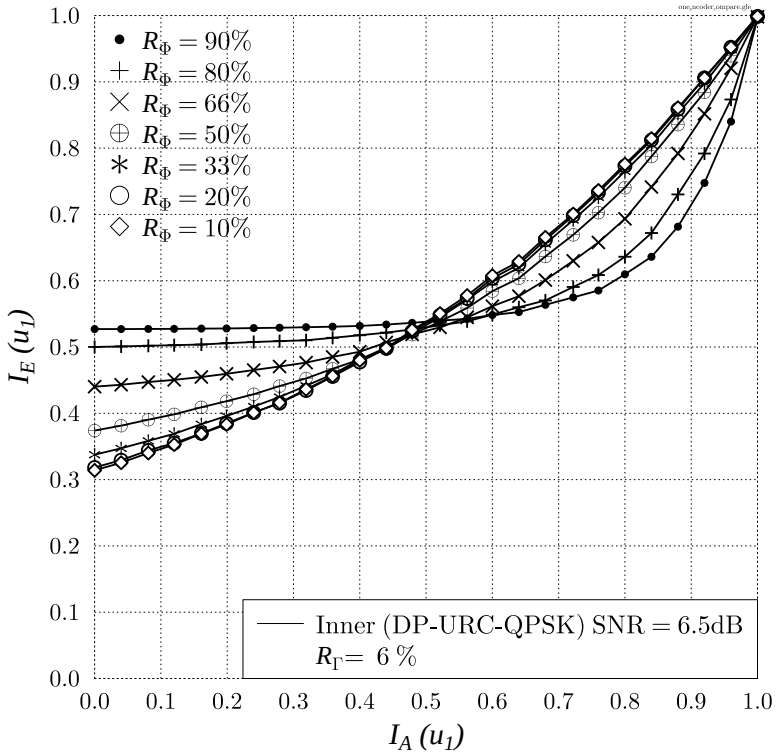

Figure 7.2: EXIT chart for doped URC with different doping percentages, when puncturing $R_\Gamma = 6\%$ is invoked.

our next contribution will assume hidden Markov correlation models by exploring the modification needed in both the DJSTTCM encoder and decoder.

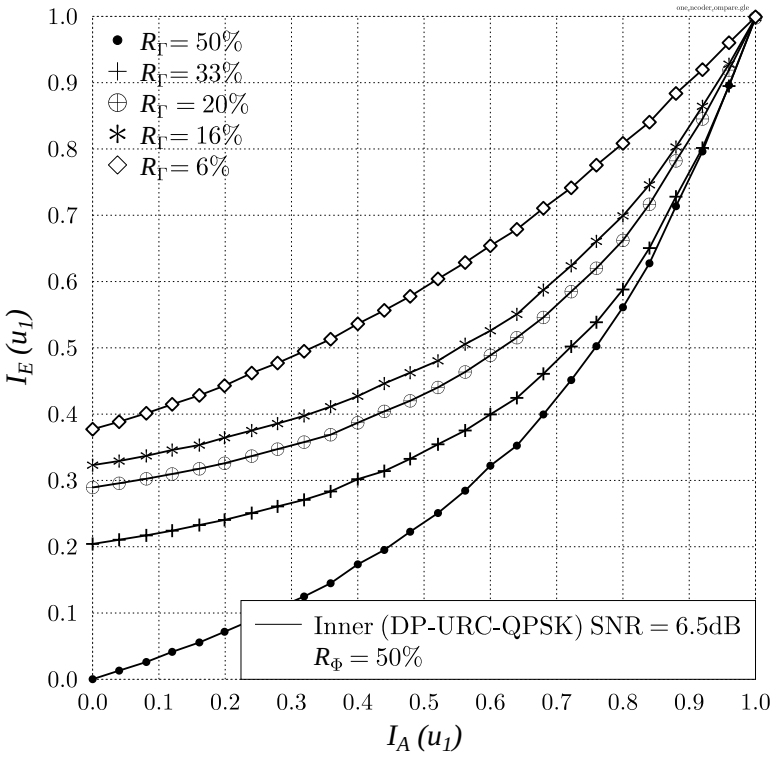

Figure 7.3: EXIT chart for doped URC with different puncturing percentages R_Γ, when using doping ratio of $R_\Phi = 50\%$.

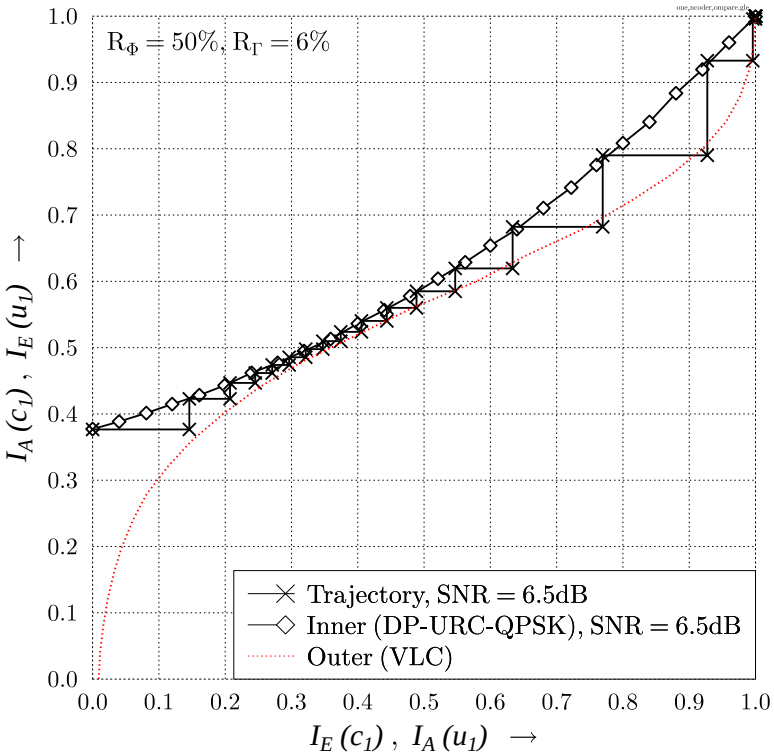

Figure 7.4: EXIT chart for doped joint URC-VLC scheme of Figure 7.1 with a doping ratio of $R_\Phi = 50\%$ and puncturing ratio of $R_\Gamma = 16\%$.

Appendix A

This appendix details the construction of the Reversible Variable Length Code (RVLC) which was invoked in our Joint Source-coding Channel-coding and Modulation (JSCM) scheme of Chapter 3. More explicitly, a brief source coding background is presented in Section A.1, while the RVLC trellis construction is detailed in Section A.1.2.

A.1 Source Coding

Generally, sources can be grouped into two main categories namely into *Memoryless* sources and sources exhibiting *Memory*. Consider a source emitting a symbol sequence of N symbols, from the alphabet $\Lambda = \{a_1, a_2, \ldots a_i, \ldots a_s\}$ with symbol occurrence probabilities of p_i, for $i = \{1, 2, \ldots, N_s\}$, where the probabilities for any symbol are assumed to be independent of any previously transmitted one. The information carried by a_i is given by $I_i = (p_i.N).\log_2(1/p_i)$ [bits], where the overall contributed information per symbol is:

$$I_{total} = \sum_{i=1}^{N_s} I_i = \sum_{i=1}^{N_s} p_i.N.\log_2\left(\frac{1}{p_i}\right) \text{ [bits]} . \tag{A.1}$$

The average information per source symbol can be expressed as:

$$H = \frac{I_{total}}{N} = \sum_{i=1}^{N_s} p_i.\log_2\left(\frac{1}{p_i}\right) \text{ [bits/symbols]} . \tag{A.2}$$

The coding efficiency (CE) of such a source can be given as:

$$CE = \frac{\text{source information rate}}{\text{average source output rate}} . \tag{A.3}$$

Thus, for a given source that has an emission rate of R_s[symbols/sec], the corresponding information rate can be calculated as $R = R_s.H$ [bits/sec], given that for an q-ary source, the entropy H is bounded by: $0 \leq H \leq \log_2(q)$.

A.1.1 Reversible Variable Length Code

Similar to VLCs, RVLCs aim for removing the redundancy from the source by exploiting the source correlation. The RVLC concept was proposed in [189] for enabling both backward and forward decoding, in order facilitate decoding also from the end of a codeword aiming to mitigate the effect of synchronization loss, routinely experienced by conventional VLC schemes. To elaborate a little further, a decoder can start decoding the received symbol from the first bit and once an error is detected, the decoder will start decoding from the codeword's end in the backward direction, because the bit-patterns at both ends of the codeword are identical. This allows instantaneous forward and backward decoding, where the transmitted data can be recovered with a higher probability, when there is potential error propagation [120]. In order to achieve unique and unambiguous decoding, RVLC construction should satisfy the condition that no codeword to be formed as a prefix or suffix of any other codeword.

A more efficient so called Asymmetric RVLC was proposed in [241], which requires a lower average codeword length than its perfectly symmetric counterpart for a given source, hence leading to a higher coding efficiency. However, in terms of complexity and memory requirement symmetric RVLCs are more efficient, because the Asymmetric RVLC requires two different tables for decoding at both ends. More details can be found in [120]. Several algorithms have been proposed for RVLC construction which were reviewed quite extensively in [189, 242, 243, 120]. Typically, the RVLC construction starts from a Huffman code table for the given source and then each codeword is replaced by identical-length codewords that satisfy the above-mentioned prefix and suffix conditions. If the number of legitimate RVLC codewords is not adequate, longer codewords will be generated, leading to an increased redundancy.

A.1.2 RVLCs Trellis Representation

In our simulations we invoked a Trellis-based RVLC code, which was originally introduced in [105] for the sake of improving the VLC decoding process. The trellis is derived by allocating its states to the nodes of the VLC code tree. The tree nodes of the bit-level structure consist of single Root node (R), several Internal nodes (I) and several Termination nodes (T). For example, the tree structure of the RVLC having the code table of $C = \{00,\ 11,\ 010,\ 101,\ 0110\}$ is illustrated on the left of Figure A.1. Moreover, the corresponding trellis diagram representing the pair of bit time instances n and $n+1$ is shown on the right of Figure A.1. The trellis created from the code tree comprises a single root state, which is related both to the root node R of the code tree and to several further states corresponding to the internal nodes of the same tree. It can be seen from Figure A.1 that all terminal nodes lead back to the root state $R = T$. The internal nodes and the root node are assigned an upward pointing branch, when the input bit is zero, and a downward pointing branch, when it equals to one. Furthermore, the number of trellis states is equivalent to the number of internal nodes plus one. Finally, for a sequence of N bits, the trellis terminates after N sections. Thus, the trellis defines the RVLC source code explicitly. Hence, this trellis can be used to decode the RVLC just

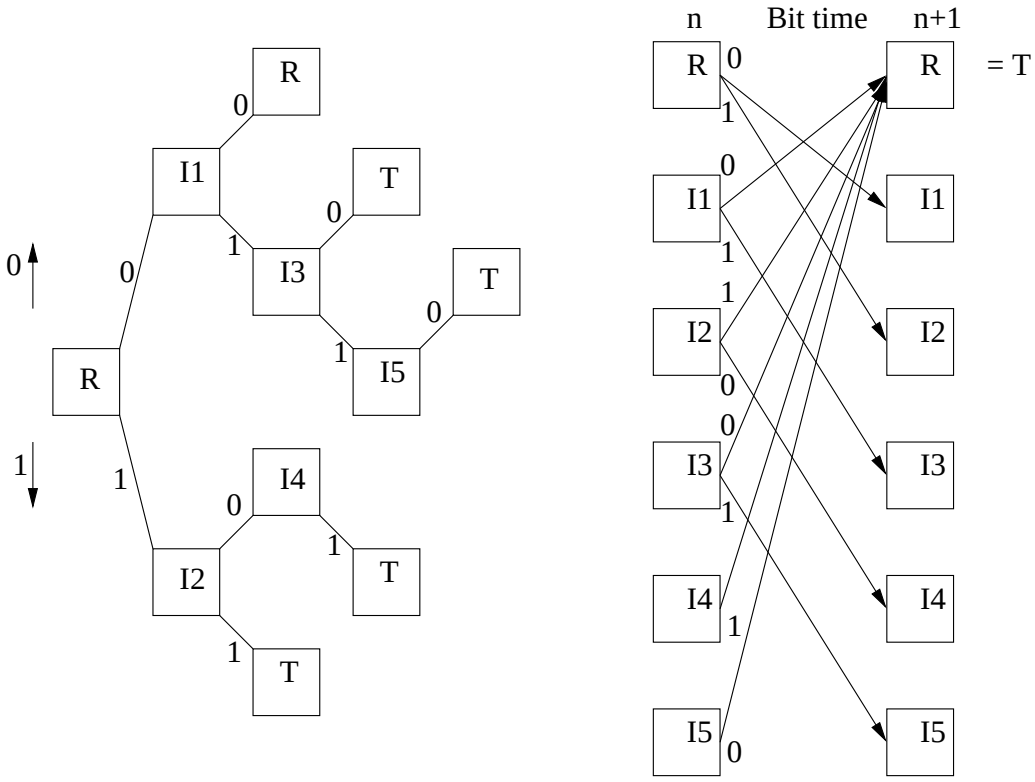

Figure A.1: Code-tree and trellis diagram for RVLC for $C = \{00, 11, 010, 101, 0110\}$ [108].

simply as in Viterbi or MAP decoding techniques.

Appendix B

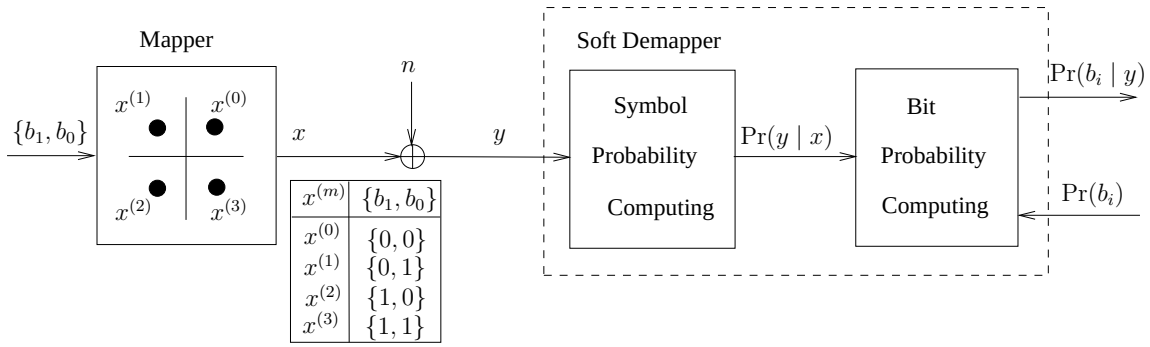

Figure B.1: Schematic diagram of mapper and demapper, where the transmitted signal is mapped using QPSK-based Set-Partition labelled mapping.

This appendix details the conversion between Log-Likelihood Ratio (LLR) and Probability, which is used in both Chapter 4 and Chapter 5. This appendix is mainly based on [156], where readers might like to refer to this source for further details. Consider the transmission schematic shown in Figure B.1, where the input sequence $\{b_1, b_0\}$ is mapped to the QPSK signal before its transmission. Denoting the binary "one" as $+1$ and binary "zero" as -1, the LLR for a bit b_t may be expressed as:

$$L(b_t) = \ln\left(\frac{\Pr(b_t = +1)}{\Pr(b_t = -1)}\right) , \tag{B.1}$$

where it is shown in [156] that the bit probability for b_t can be estimated using:

$$\Pr(b_t) = \left(\frac{\exp(-L(b_t)/2)}{1 + \exp(-L(b_t))}\right) \cdot \exp\left(b_t \, L(b_t)/2\right) , \tag{B.2}$$

$$= C \cdot \exp\left(b_t \, L(b_t)/2\right) . \tag{B.3}$$

The term $C = \left(\frac{\exp(-L(b_t)/2)}{1+\exp(-L(b_t))}\right)$ is constant, since it is independent of the b_t value.

Returning to our example of Figure B.1, the channel probability of receiving y given $x = x^{(m)}$ was transmitted over an AWGN channel having a variance of $N_0/2$ per dimension can be written

as:

$$\Pr\left(y \mid x = x^{(m)}\right) = \frac{1}{\pi N_0} \exp\left(-\frac{\left|y - x^{(m)}\right|^2}{N_0}\right) , \tag{B.4}$$

where $m \in \{0, 1, 2, 3\}$, as shown in the table of Figure B.1. Accordingly, the probability $\Pr\left(x = x^{(m)} \mid y\right)$ can be further expressed using Bayes' theorem as [156]:

$$\Pr\left(x = x^{(m)} \mid y\right) = \Pr\left(y \mid x = x^{(m)}\right) \Pr\left(x = x^{(m)}\right) \tag{B.5}$$

$$= \Pr\left(y \mid x = x^{(m)}\right) \prod_{j=1}^{N_b} \Pr\left(b_j = b_j^{(m)}\right) . \tag{B.6}$$

Given Equation (B.6), the probability that the i^{th} bit equals to B, where $B \in \{0, 1\}$, given that y was received can be expressed as:

$$\Pr\left(b_i = B \mid y\right) = \sum_{x^{(m)} \in \mho(i,B)} \Pr\left(x^{(m)} \mid y\right) , \tag{B.7}$$

where $x^{(m)}$ belongs to the subset $\mho(i, B)$ which indicates that the i^{th} bit of $x^{(m)}$ equals to B. More explicitly, Equation (B.7) can be further expanded using:

$$\Pr\left(b_i = B \mid y\right) = \sum_{x^{(m)} \in \mho(i,B)} \left(\Pr\left(y \mid x^{(m)}\right) \prod_{j \neq i}^{\text{all } j} (\Pr\left(b_j^{(m)}\right)\right) . \tag{B.8}$$

For example, given $x^{(m)}$ that is defined using the table in Figure B.1, the probability of $b_1 = 0$ can be written as:

$$\Pr\left(b_1 = 0 \mid y\right) = \sum_{x^{(m)} \in \mho(1,\,0)} \left(\Pr\left(y \mid x^{(m)}\right) \prod_{j \neq 1}^{\text{all } j} \Pr\left(b_j^{(m)}\right)\right) \tag{B.9}$$

$$= \Pr\left(y \mid x = x^{(0)}\right) \Pr\left(b_0 = 0\right) + \Pr\left(y \mid x = x^{(1)}\right) \Pr\left(b_0 = 1\right) . \tag{B.10}$$

Upon using Equation (B.10) for calculating $\Pr\left(b_1 = 1 \mid y\right)$, the LLR of b_1, $L(b_1)$, can be simply estimated using Equation (B.1).

Appendix C

This appendix discuss the the construction of the syndrome former, that was employed in Section 5.6. Particularly, the Convolutional Codes (CC) syndrome former is derived in Section C.1, while the Turbo Trellis-Coded Modulation (TTCM) former is constructed in Section C.2.

C.1 Convolutional Codes Syndrome Former

Following the example presented in Section 5.6.1, where the generator matrix $\mathbf{G}(D)$ was given by:

$$\mathbf{G}(D) = \begin{pmatrix} 1+D & D & 1+D \\ D & 1 & 1 \end{pmatrix} . \tag{C.1}$$

The corresponding syndrome former can be computed using elementary row operations to Equation (C.1) as follows:

- Divide the 1st row of Equation (C.1) by $1+D$:

$$\mathbf{G}(D) = \begin{pmatrix} 1 & D/(1+D) & 1 \\ D & 1 & 1 \end{pmatrix} . \tag{C.2}$$

- Add $D \times$ 1st row of Equation (C.2) to the 2nd row:

$$\mathbf{G}(D) = \begin{pmatrix} 1 & D/(1+D) & 1 \\ 0 & (1+D+D^2)/(1+D) & (1+D) \end{pmatrix} . \tag{C.3}$$

- Multiply 2nd row of Equation (C.3) by $(1+D)/(1+D+D^2)$:

$$\mathbf{G}(D) = \begin{pmatrix} 1 & D/(1+D) & 1 \\ 0 & 1 & (1+D^2)/(1+D+D^2) \end{pmatrix} . \tag{C.4}$$

- Add $(D/(1+D) \times 2^{\text{nd}}$ row$)$ to 1^{st} row of Equation (C.4):

$$\mathbf{G}(D) = \begin{pmatrix} 1 & 0 & 1/(1+D+D^2) \\ 0 & 1 & (1+D^2)/(1+D+D^2) \end{pmatrix} . \tag{C.5}$$

From Equation (C.5), the parity check matrix H can be deduced as [225]:

$$\mathbb{H}(D) = \begin{pmatrix} 1/(1+D+D^2) & (1+D^2)/(1+D+D^2) & 1 \end{pmatrix} . \tag{C.6}$$

Upon multiplying Equation (C.6) by $(1+D+D^2)$ and taking the transpose the syndrome former is given by:

$$\mathbb{H}^{\text{T}}(D) = \begin{pmatrix} 1 \\ 1+D^2 \\ 1+D+D^2 \end{pmatrix} . \tag{C.7}$$

C.2 Turbo Trellis-Coded Modulation Syndrome Former

Our Block Syndrome Decoder (BSD) of Section 5.6.3 employs an $2/3$-rate TTCM-8PSK scheme. Additionally, as stated in Section 2.3 TTCM scheme consists of two parallel concatenated TCM codes whose Recursive Systematic Code (RSC) is shown in Figure C.1. The associated generator

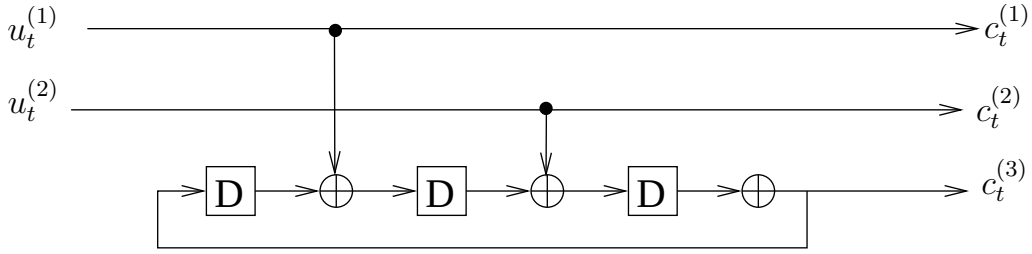

Figure C.1: The Ungerböck's RSC encoder of the TCM-8PSK encoder [158].

matrix is expressed as:

$$\mathbf{G}(D) = \begin{pmatrix} 1 & 0 & D^2/(1+D^3) \\ 0 & 1 & D/(1+D^3) \end{pmatrix} . \tag{C.8}$$

The corresponding parity check matrix $\mathbb{H}^{\text{T}}$ is given by:

$$\mathbb{H}^{\text{T}}(D) = \begin{pmatrix} D^2 \\ D \\ 1+D^3 \end{pmatrix} . \tag{C.9}$$

Finally, the syndrome former circuit of Equation (C.9) is shown in Figure C.2.

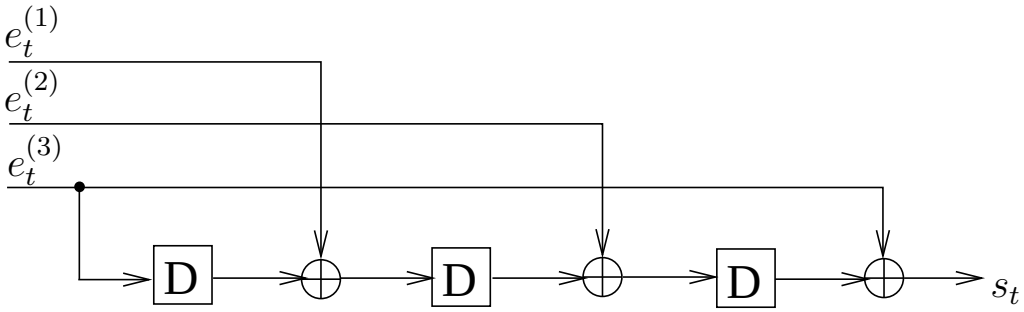

Figure C.2: The syndrome former of the TCM-8PSK encoder of Figure C.1.

Bibliography

[1] "NASA,." NASA STEREO MISSION, Accessed: 2015-09-21. Available :http://www.nasa.gov/stereo/.

[2] S. Wang, L. Cui, S. Cheng, L. Stanković, and V. Stanković, "Onboard low-complexity compression of solar stereo images," *IEEE Transactions on Image Processing*, vol. 21, pp. 3114–3118, June 2012.

[3] D. Varodayan, *Adaptive distributed source coding*. PhD thesis, Stanford University, 2010.

[4] D. Slepian and J. K. Wolf, "Noiseless coding of correlated information sources," *IEEE Transactions on Information Theory*, vol. 19, pp. 471–480, July 1973.

[5] A. D. Wyner and J. Ziv, "The rate-distortion function for source coding with side information at the decoder," *IEEE Transactions on Information Theory*, vol. 22, pp. 1–10, January 1976.

[6] S. S. Pradhan and K. Ramchandran, "Distributed source coding using syndromes (DISCUS): Design and construction," *IEEE Transactions on Information Theory*, vol. 49, pp. 626–643, March 2003.

[7] Z. Xiong, A. D. Liveris, and S. Cheng, "Distributed source coding for sensor networks," *IEEE Signal Processing Magazine*, vol. 21, pp. 80–94, September 2004.

[8] J. Garcia-Frias, Y. Zhao, and W. Zhong, "Turbo-like codes for transmission of correlated sources over noisy channels," *IEEE Signal Processing Magazine*, vol. 24, pp. 58–66, September 2007.

[9] A. Aaron and B. Girod, "Compression with side information using turbo codes," in *Data Compression Conference (DCC'02)*, (Snowbird, UT, USA), pp. 252–261, April 2002.

[10] J. Garcia-Frias and Z. Xiong, "Distributed source and joint source-channel coding: From theory to practice," in *IEEE International Conference on Acoustics, Speech, and Signal Processing (ICASSP'05)*, vol. 5, (Philadelphia, PA), pp. 1093–1096, March 2005.

[11] J. Garcia-Frias and Y. Zhao, "Near-Shannon/Slepian-Wolf performance for unknown correlated sources over AWGN channels," *IEEE Transactions on Communicatons*, vol. 53, pp. 555–559, April 2005.

[12] D. Varodayan, Y.-C. Lin, and B. Girod, "Adaptive distributed source coding," *IEEE Transactions on Image Processing*, vol. 21, pp. 2630–2640, May 2012.

[13] P. L. Dragotti and M. Gastpar, *Distributed Source Coding: Theory, Algorithms and Applications*. Academic Press, 2009.

[14] T. M. Cover, "A proof of the data compression theorem of Slepian and Wolf for ergodic sources (corresp.)," *IEEE Transactions on Information Theory*, vol. 21, pp. 226–228, March 1975.

[15] R. Ahlswede and J. Korner, "Source coding with side information and a converse for degraded broadcast channels," *IEEE Transactions on Information Theory*, vol. 21, pp. 629–637, November 1975.

[16] T. M. Cover, A. E. Gamal, and M. Salehi, "Multiple access channels with arbitrarily correlated sources," *IEEE Transactions on Information Theory*, vol. 26, pp. 648–657, November 1980.

[17] R. Cristescu, B. Beferull-Lozano, and M. Vetterli, "Networked Slepian-Wolf: Theory, algorithms, and scaling laws," *IEEE Transactions on Information Theory*, vol. 51, pp. 4057–4073, December 2005.

[18] J. Barros and S. D. Servetto, "Network information flow with correlated sources," *IEEE Transactions on Information Theory*, vol. 52, pp. 155–170, January 2006.

[19] P. Lu, X. Zhou, and T. Matsumoto, "Outage probabilities of orthogonal multiple-access relaying techniques with imperfect source-relay links," *IEEE Transactions on Wireless Communications*, vol. 14, pp. 2269–2280, April 2015.

[20] C. Heegard and T. Berger, "Rate distortion when side information may be absent," *IEEE Transactions on Information Theory*, vol. 31, pp. 727–734, November 1985.

[21] R. Zamir, S. Shamai, and U. Erez, "Nested linear/lattice codes for structured multiterminal binning," *IEEE Transactions on Information Theory*, vol. 48, pp. 1250–1276, June 2002.

[22] V. Stanković, L. Stanković, and S. Cheng, "Distributed source coding: Theory, code designs and applications," in *IEEE International Conference on Acoustics, Speech and Signal Processing*, (Taipei, Taiwan), April 2009.

[23] Y. Oohama, "Gaussian multiterminal source coding," *IEEE Transactions on Information Theory*, vol. 43, pp. 1912–1923, November 1997.

[24] Y. Yang, V. Stanković, Z. Xiong, and W. Zhao, "On multiterminal source code design," *IEEE Transactions on Information Theory*, vol. 54, pp. 2278–2302, May 2008.

[25] T. Flynn and R. M. Gray, "Encoding of correlated observations," *IEEE Transactions on Information Theory*, vol. 33, pp. 773–787, November 1987.

[26] Y. Oohama, "Rate-distortion theory for Gaussian multiterminal source coding systems with several side informations at the decoder," *IEEE Transactions on Information Theory*, vol. 51, pp. 2577–2593, July 2005.

[27] H. Viswanathan and T. Berger, "The quadratic Gaussian CEO problem," *IEEE Transactions on Information Theory*, vol. 43, pp. 1549–1559, September 1997.

[28] T. Berger, "Multiterminal source coding," in *The Information Theory Approach to Communications*, G. Longo, Ed. New York: Springer-Verlag, 1977.

[29] R. Zamir, "The rate loss in the Wyner-Ziv problem," *IEEE Transactions on Information Theory*, vol. 42, pp. 2073–2084, November 1996.

[30] Y. Oohama, "Indirect and direct Gaussian distributed source coding problems," *IEEE Transactions on Information Theory*, vol. 60, pp. 7506–7539, December 2014.

[31] V. Stanković, L. Stanković, and S. Cheng, "Distributed source coding: Theory, code designs and applications," in *Proceedings of the 15th European Signal Processing Conference (EUSIPCO'10)*, (Aalborg, Denmark), August 2010.

[32] S. S. Pradhan and K. Ramchandran, "Distributed source coding using syndromes (DISCUS): Design and construction," in *Data Compression Conference (DCC'99)*, (Snowbird, UT, USA), pp. 158–167, March 1999.

[33] V. Stanković, A. D. Liveris, Z. Xiong, and C. N. Georghiades, "Design of Slepian-Wolf codes by channel code partitioning," in *Data Compression Conference (DCC'04)*, (Snowbird, UT, USA), pp. 302–311, March 2004.

[34] C. Berrou, A. Glavieux, and P. Thitimajshima, "Near Shannon limit error-correcting coding and decoding: Turbo-codes. 1," in *IEEE International Conference on Communications (ICC'93)*, vol. 2, (Geneva), pp. 1064–1070, May 1993.

[35] R. G. Gallager, "Low-density parity-check codes," *IRE Transactions on Information Theory*, vol. 8, pp. 21–28, January 1962.

[36] A. D. Liveris, Z. Xiong, and C. N. Georghiades, "Compression of binary sources with side information at the decoder using LDPC codes," *IEEE Communications Letters*, vol. 6, pp. 440–442, October 2002.

[37] Y. Zhao, W. Zhong, and J. Garcia-Frias, "Transmission of correlated senders over a Rayleigh fading multiple access channel," *Elsevier Signal Processing*, vol. 86, pp. 3150–3159, April 2006.

[38] D. Varodayan, A. Aaron, and B. Girod, "Rate-adaptive codes for distributed source coding," *Elsevier Signal Processing*, vol. 86, pp. 3123–3130, November 2006.

[39] M. Sartipi and F. Fekri, "Distributed source coding using short to moderate length rate-compatible LDPC codes: The entire Slepian-Wolf rate region," *IEEE Transactions on Communications*, vol. 56, pp. 400–411, March 2008.

[40] D. Schonberg, K. Ramchandran, and S. S. Pradhan, "Distributed code constructions for the entire Slepian-Wolf rate region for arbitrarily correlated sources," in *Data Compression Conference (DCC'04)*, (Snowbird, UT, USA), pp. 292–301, March 2004.

[41] J. Garcia-Frias, "Joint source-channel decoding of correlated sources over noisy channels," in *Data Compression Conference (DCC'01)*, pp. 283–292, March 2001.

[42] S. Shamai and S. Verdú, "Capacity of channels with uncoded side information," *European Transactions on Telecommunications*, vol. 6, pp. 587–600, September 1995.

[43] J. D. Ser, P. Crespo, and A. Munoz, "Joint source-channel decoding of correlated sources over ISI channels," in *IEEE 61th Vehicular Technology Conference (VTC'05)*, vol. 1, (Stockholm), pp. 625–629, June 2005.

[44] A. J. Aljohani, S. X. Ng, and L. Hanzo, "TTCM-aided rate-adaptive distributed source coding for Rayleigh fading channels," *IEEE Transactions on Vehicular Technology*, vol. 63, pp. 1126–1134, March 2014.

[45] A. D. Liveris, Z. Xiong, and C. N. Georghiades, "Joint source-channel coding of binary sources with side information at the decoder using IRA codes," in *IEEE Workshop on Multimedia Signal Processing*, (St.Thomas, VI, USA), pp. 53–56, December 2002.

[46] A. R. Gopala, P. K. Gopala, and H. E. Gamal, "Correlated sources over wireless channels: Cooperative source-channel coding," *IEEE JOURNAL ON SELECTED AREAS IN COMMUNICATIONS*, vol. 22, pp. 988–998, August 2004.

[47] Y. Zhao and J. Garcia-Frias, "Joint estimation and compression of correlated nonbinary sources using punctured turbo codes," *IEEE Transactions on Communications*, vol. 53, pp. 385–390, March 2005.

[48] K. Anwar and T. Matsumoto, "Spatially concatenated codes with turbo equalization for correlated sources," *IEEE Transactions on Signal Processing*, vol. 60, pp. 5572–5577, October 2012.

[49] K. Anwar and T. Matsumoto, "Accumulator-assisted distributed turbo codes for relay systems exploiting source-relay correlation," *IEEE Communications Letters*, vol. 16, pp. 1114–1117, July 2012.

[50] K. Anwar and T. Matsumoto, "Iterative spatial demapping for two correlated sources with power control over fading MAC," in *IEEE 75th Vehicular Technology Conference (VTC'12)*, (Yokohama, Japan), May 2012.

[51] Y. Fang, "Asymmetric Slepian-Wolf coding of nonstationarily-correlated M-ary sources with sliding-window belief propagation," *IEEE Transactions on Communications*, vol. 61, pp. 5114–5124, December 2013.

[52] Y. Fang, "Crossover probability estimation using mean-intrinsic-LLR of LDPC syndrome," *IEEE Communications Letters*, vol. 13, pp. 679–681, September 2009.

[53] Y. Fang, "Joint source-channel estimation using accumulated LDPC syndrome," *IEEE Communications Letters*, vol. 14, pp. 1044–1046, November 2010.

[54] L. Cui, S. Wang, and S. Cheng, "Adaptive Slepian-Wolf decoding based on expectation propagation," *IEEE Communications Letters*, vol. 16, pp. 252–255, February 2012.

[55] L. Cui, S. Wang, S. Cheng, and M. Yeary, "Adaptive binary Slepian-Wolf decoding using particle based belief propagation," *IEEE Transactions on Communications*, vol. 59, pp. 2337–2342, September 2011.

[56] C. Tang, N.-M. Cheung, A. Ortega, and C. S. Raghavendra, "Efficient inter-band prediction and wavelet based compression for hyperspectral imagery: A distributed source coding approach," in *Data Compression Conference (DCC'05)*, (Snowbird, USA), pp. 437–446, March 2005.

[57] J. Zhang, H. Li, and C. W. Chen, "Distributed lossless coding techniques for hyperspectral images," *IEEE Journal of Selected Topics in Signal Processing*, vol. 9, pp. 977–989, September 2015.

[58] X. Lv, R. Liu, and R. Wang, "A novel rate-adaptive distributed source coding scheme using polar codes," *IEEE Communications Letters*, vol. 17, pp. 143–146, January 2013.

[59] M. Vaezi and F. Labeau, "Distributed source-channel coding based on real-field BCH codes," *IEEE Transactions on Signal Processing*, vol. 62, pp. 1171–1184, March 2014.

[60] L. Hanzo, O. R. Alamri, M. El-Hajjar, and N. Wu, *Near-capacity multi functional MIMO systems*. John Wiley & Sons, Ltd, 2009.

[61] L. Hanzo, Y. Akhtman, L. Wang, and M. Jiang, *MIMO-OFDM for LTE, WiFi and WiMAX: Coherent versus non-coherent and cooperative turbo transceivers*. John Wiley & Sons, Ltd, 2010.

[62] K. J. R. Liu, A. K. Sadek, W. Su, and A. Kwasinski, *Cooperative communications and networking*. Cambridge University Press, 2009.

[63] M. Uppal, G. Yue, X. Wang, and Z. Xiong, "A rateless coded protocol for half-duplex wireless relay channels," *IEEE Transactions on Signal Processing*, vol. 59, pp. 209–222, January 2011.

[64] X. Zhou, P. Lu, K. Anwar, and T. Matsumoto, "Correlated sources transmission in orthogonal multiple access relay channel: Theoretical analysis and performance evaluation," *IEEE Transactions on Wireless Communications*, vol. 13, pp. 1424–1435, March 2014.

[65] V. Stanković, A. Høst-Madsen, and Z. Xiong, "Cooperative diversity for wireless ad hoc networks," *IEEE Signal Processing Magazine*, vol. 23, pp. 37–49, September 2006.

[66] J. D. Ser, P. M. Crespo, B. H. Khalaj, and J. Gutierrez-Gutierrez, "On combining distributed joint source-channel-network coding and turbo equalization in multiple access relay networks," in *Third IEEE International Conference on Wireless and Mobile Computing, Networking and Communications (WiMOB'07)*, (White Plains, NY), p. 18, October 2007.

[67] X. Zhou, A. O. Lim, K. Anwar, and T. Matsumoto, "Distributed joint source-channel-network coding exploiting source correlation for multiple access relay channel," in *Proceedings of the 2013 19th European Wireless Conference (EW)*, pp. 1–6, April 2013.

[68] M. Uppal, Z. Liu, V. Stanković, and Z. Xiong, "Compress-forward coding with BPSK modulation for the half-duplex Gaussian relay channel," *IEEE Transactions on Signal Processing*, vol. 57, pp. 4467–4481, November 2009.

[69] A. Aaron, R. Zhang, and B. Girod, "Wyner-Ziv coding of motion video," in *Thirty-Sixth Asilomar Conference on Signals, Systems and Computers*, vol. 1, (Pacific Grove, CA, USA), pp. 240–244, November 2002.

[70] B. Girod, A. Aaron, S. Rane, and D. Rebollo-Monedero, "Distributed video coding," *Proceedings of the IEEE*, vol. 93, pp. 71–83, January 2005.

[71] L. Hanzo, P. Cherriman, and J. Streit, *Video Compression and Communications: From Basics to H.261, H.263, H.264, MPEG4 for DVB and HSDPA-Style Adaptive Turbo-Transceivers*. Wiley-IEEE Press, 2007.

[72] Y. Yang, V. Stanković, Z. Xiong, and W. Zhao, "Two-terminal video coding," *Image Processing, IEEE Transactions on*, vol. 18, pp. 534–551, March 2009.

[73] R. Puri and K. Ramchandran, "PRISM: A video coding architecture based on distributed compression principles," Tech. Rep. UCB/ERL M03/6, EECS Department, University of California, Berkeley, 2003.

[74] X. A. Artigas, J. Ascenso, M. Dalai, D. K. Kubasov, and M. O. Ouaret, "The DISCOVER codec: Architecture, techniques and evaluation," in *Picture Coding Symposium (PCS'07)*, (Lisbon, Portugal), November 2007.

[75] J. Ascenso, C. Brites, and F. Pereira, "Content adaptive Wyner-Ziv video coding driven by motion activity," in *IEEE International Conference on Image Processing (ICIP'06)*, (Atlanta, GA), pp. 605–608, October 2006.

[76] M. Dalai, R. Leonardi, and F. Pereira, "Improving turbo codec integration in pixel-domain distributed video coding," in *IEEE International Conference on Acoustics, Speech and Signal Processing (ICASSP'06)*, vol. 2, (Toulouse), p. II, May 2006.

[77] J. Ascenso and F. Pereira, "Adaptive hash-based side information exploitation for efficient Wyner-Ziv video coding," in *IEEE International Conference on Image Processing (ICIP'07)*, vol. 3, (San Antonio, TX), pp. 29–32, September 2007.

[78] C. Brites and F. Pereira, "Correlation noise modeling for efficient pixel and transform domain Wyner-Ziv video coding," *IEEE Transactions on Circuits and Systems for Video Technology*, vol. 18, pp. 1177–1190, September 2008.

[79] C. Brites, J. Ascenso, and F. Pereira, "Studying temporal correlation noise modeling for pixel based Wyner-Ziv video coding," in *IEEE International Conference on Image Processing*, (Atlanta, GA), pp. 273–276, October 2006.

[80] H. S. Witsenhausen and A. D. Wyner, "Interframe coder for video signals," March 1980. US Patent 4,191,970.

[81] R. Puri and K. Ramchandran, "PRISM: A new robust video coding architecture based on distributed compression principles," in *Allerton Conference on Communication, Control, and Computing*, (Monticello, Illinois), 2002.

[82] R. Martins, C. Brites, J. Ascenso, and F. Pereira, "Refining side information for improved transform domain Wyner-Ziv video coding," *IEEE Transactions on Circuits and Systems for Video Technology*, vol. 19, pp. 1327–1341, September 2009.

[83] S. Wang, L. Cui, L. Stanković, V. Stanković, and S. Cheng, "Adaptive correlation estimation with particle filtering for distributed video coding," *IEEE Transactions on Circuits and Systems for Video Technology*, vol. 22, pp. 649–658, May 2012.

[84] J. Skorupa, J. Slowack, S. Mys, N. Deligiannis, J. D. Cock, P. Lambert, C. Grecos, A. Munteanu, and R. V. de Walle, "Efficient low-delay distributed video coding," *IEEE Transactions on Circuits and Systems for Video Technology*, vol. 22, pp. 530–544, April 2012.

[85] A. Abou-Elailah, F. Dufaux, J. Farah, M. Cagnazzo, and B. Pesquet-Popescu, "Fusion of global and local motion estimation for distributed video coding," *IEEE Transactions on Circuits and Systems for Video Technology*, vol. 23, pp. 158–172, January 2013.

[86] A. Majumdar, K. Ramchandran, and I. Kozintsev, "Distributed coding for wireless audio sensors," in *IEEE Workshop on Applications of Signal Processing to Audio and Acoustics*, (New Paltz, NY, USA), pp. 209–212, October 2003.

[87] H. Dong, J. Lu, and Y. Sun, "Distributed audio coding in wireless sensor networks," in *International Conference on Computational Intelligence and Security*, vol. 2, (Guangzhou), pp. 1695–1699, November 2006.

[88] A. J. Berkhout, D. de Vries, and P. Vogel, "Acoustic control by wave field synthesis," *The Journal of the Acoustical Society of America*, vol. 93, no. 5, pp. 2764–2778, 1993.

[89] O. Roy and M. Vetterli, "Distributed spatial audio coding in wireless hearing aids," in *IEEE Workshop on Applications of Signal Processing to Audio and Acoustics*, (New Paltz, NY, USA), pp. 227–230, October 2007.

[90] O. Roy and M. Vetterli, "Rate-constrained collaborative noise reduction for wireless hearing aids," *IEEE Transactions on Signal Processing*, vol. 57, pp. 645–657, February 2009.

[91] X. Li, "Distributed coding of multispectral images: A set theoretic approach," in *International Conference on Image Processing (ICIP'04)*, vol. 5, (Singapore), pp. 3105–3108, October 2004.

[92] N.-M. Cheung and A. Ortega, "An efficient and highly parallel hyperspectral imagery compression scheme based on distributed source coding," in *Fortieth Asilomar Conference on Signals, Systems and Computers (ACSSC'06)*, (Pacific Grove, CA), pp. 1892–1896, October 2006.

[93] N.-M. Cheung, C. Tang, A. Ortega, and C. S. Raghavendra, "Efficient wavelet-based predictive Slepian-Wolf coding for hyperspectral imagery," *EURASIP Signal Processing Journal*, vol. 86, pp. 3180–3195, November 2006.

[94] Z. Qian and X. Zhang, "Reversible data hiding in encrypted image with distributed source encoding," *IEEE Transactions on Circuits and Systems for Video Technology*, vol. PP, p. 1, April 2015.

[95] Y. Lin, D. Varodayan, and B. Girod, "Image authentication based on distributed source coding," in *IEEE International Conference on Image Processing (ICIP'07)*, vol. 3, (San Antonio, TX), pp. III–5 – III–8, September 2007.

[96] Y. Lin, D. Varodayan, and B. Girod, "Image authentication and tampering localization using distributed source coding," in *IEEE 9th Workshop on Multimedia Signal Processing (MMSP'07)*, (Crete), pp. 393–396, October 2007.

[97] Y. Lin, D. Varodayan, and B. Girod, "Distributed source coding authentication of images with contrast and brightness adjustment and affine warping," in *Picture Coding Symposium (PCS'09)*, (Chicago, IL), May 2009.

[98] G. Valenzise, G. Prandi, M. Tagliasacchi, and A. Sarti, "Identification of sparse audio tampering using distributed source coding and compressive sensing techniques," *Journal on Image Video Processing*, vol. 2009, February 2009.

[99] E. Martinian, S. Yekhanin, and J. S. Yedidia, "Secure biometrics via syndromes," in *43rd Annual Allerton Conference on Communications, Control, and Computing*, November 2005.

[100] Y. Sutcu, S. Rane, J. S. Yedidia, S. C. Draper, and A. Vetro, "Feature extraction for a Slepian-Wolf biometric system using LDPC codes," in *IEEE International Symposium on Information Theory (ISIT'08)*, (Toronto, ON), pp. 2297–2301, July 2008.

[101] S. C. Draper, A. Khisti, E. Martinian, A. Vetro, and J. S. Yedidia, "Using distributed source coding to secure fingerprint biometrics," in *IEEE International Conference on Acoustics, Speech and Signal Processing (ICASSP'07)*, vol. 2, (Honolulu, HI), pp. 129–132, April 2007.

[102] S. C. Draper, A. Khisti, E. Martinian, and A. Vetro, "Secure storage of fingerprint biometrics using Slepian-Wolf codes," in *IEEE Information Theory and Applications Workshop*, (San Diego, California), 2007.

[103] K. Sayood and J. C. Borkenhagen, "Use of residual redundancy in the design of joint source/channel coders," *IEEE Transactions on Communications*, vol. 39, pp. 838–846, June 1991.

[104] J. Hagenauer, "Source-controlled channel decoding," *IEEE Transactions on Communications*, vol. 43, pp. 2449–2457, September 1995.

[105] V. B. Balakirsky, "Joint source-channel coding with variable length codes," in *IEEE International Symposium on Information Theory*, (Ulm, Germany), June 1997.

[106] Z. Peng, Y.-F. Huang, and D. J. Costello, "Turbo codes for image transmission-a joint channel and source decoding approach," *IEEE Journal on Selected Areas in Communications*, vol. 18, pp. 868–879, June 2000.

[107] N. Görtz, "On the iterative approximation of optimal joint source-channel decoding," *IEEE Journal on Selected Areas in Communications*, vol. 19, pp. 1662–1670, September 2001.

[108] R. Bauer and J. Hagenauer, "On variable length codes for iterative source/channel decoding," in *IEEE Data Compression Conference (DCC'01)*, (UT, USA), pp. 273–282, March 2001.

[109] J. Garcia-Frias and J. D. Villasenor, "Joint turbo decoding and estimation of hidden Markov sources," *IEEE Journal on Selected Areas in Communications*, vol. 19, pp. 1671–1679, September 2001.

[110] J. Kliewer and R. Thobaben, "Combining FEC and optimal soft-input source decoding for the reliable transmission of correlated variable-length encoded signals," in *Data Compression Conference (DCC'02)*, (Snowbird, UT, USA), pp. 83–91, April 2002.

[111] R. Thobaben and J. Kliewer, "Low-complexity iterative joint source-channel decoding for variable-length encoded markov sources," *IEEE Transactions on Communications*, vol. 53, pp. 2054–2064, December 2005.

[112] J. Kliewer, S. X. Ng, and L. Hanzo, "Efficient computation of EXIT functions for non-binary iterative decoding," *IEEE Transactions on Communications*, vol. 54, pp. 2133–2136, December 2006.

[113] S. X. Ng, J. Wang, M. Tao, L.-L. Yang, and L. Hanzo, "Iteratively decoded variable length space-time coded modulation: Code construction and convergence analysis," *IEEE Transactions on Wireless Communications*, vol. 6, pp. 1953–1963, May 2007.

[114] R. G. Maunder, J. Wang, S. X. Ng, and L. Hanzo, "On the performance and complexity of irregular variable length codes for near-capacity joint source and channel coding," *IEEE Transactions on Wireless Communications*, vol. 7, pp. 1338–1347, April 2008.

[115] Y. Zhang, C. Zhu, and K.-H. Yap, "A joint source-channel video coding scheme based on distributed source coding," *IEEE Transactions on Multimedia*, vol. 10, pp. 1648–1656, December 2008.

[116] T. Wang, W. Zhang, R. G. Maunder, and L. Hanzo, "Near-capacity joint source and channel coding of symbol values from an infinite source set using Elias gamma error correction codes," *IEEE Transactions on Communications*, vol. 62, pp. 280–292, January 2014.

[117] W. Zhang, Y. Jia, X. Meng, M. F. Brejza, R. G. Maunder, and L. Hanzo, "Adaptive iterative decoding for expediting the convergence of unary error correction codes," *IEEE Transactions on Vehicular Technology*, vol. 64, pp. 621–635, February 2015.

[118] C. E. Shannon, "A mathematical theory of communication," *The Bell system technical journal*, vol. 27, pp. 379–423, July 1948.

[119] L. Hanzo, R. G. Maunder, J. Wang, and L.-L. Yang, *Near-capacity variable-length coding: Regular and EXIT-chart-aided irregular designs*. Wiley-IEEE Press, 2010.

[120] J. Wang, *Iterative Source Decoding, Channel Decoding and Channel Equalisation*. PhD thesis, University of Southampton, UK, 2006.

[121] M. Park and D. J. Miller, "Joint source-channel decoding for variable-length encoded data by exact and approximate MAP sequence estimation," *IEEE Transactions on Communications*, vol. 48, pp. 1–6, January 2000.

[122] S. X. Ng, F. Guo, J. Wang, L.-L. Yang, and L. Hanzo, "Jointly optimised iterative source-coding, channel-coding and modulation for transmission over wireless channels," in *IEEE Vehicular Technology Conference (VTC'04)*, vol. 1, (Milan, Italy), pp. 313–317, May 2004.

[123] A. J. Aljohani, S. X. Ng, R. G. Maunder, and L. Hanzo, "EXIT-chart aided joint source-coding, channel-coding and modulation design for two-way relaying," *IEEE Transactions on Vehicular Technology*, vol. 62, pp. 2496–2506, July 2013.

[124] R. G. Maunder and L. Hanzo, "Near-capacity irregular variable length coding and irregular unity rate coding," *IEEE Transactions on Wireless Communications*, vol. 8, pp. 5500–5507, November 2009.

[125] R. Ahlswede, N. Cai, S.-Y. Li, and R. Yeung, "Network information flow," *IEEE Transactions on Information Theory*, vol. 46, pp. 1204–1216, July 2000.

[126] R. W. Yeung, "Network coding: A historical perspective," *Proceedings of the IEEE*, vol. 99, pp. 366–371, March 2011.

[127] P. Chou and Y. Wu, "Network coding for the internet and wireless networks," *IEEE Signal Processing Magazine*, vol. 24, pp. 77–85, September 2007.

[128] S.-Y. Li, Q. T. Sun, and Z. Shao, "Linear network coding: Theory and algorithms," *Proceedings of the IEEE*, vol. 99, pp. 372–387, March 2011.

[129] A. Ramamoorthy, K. Jain, P. A. Chou, and M. Effros, "Separating distributed source coding from network coding," *IEEE Transactions on Information Theory*, vol. 52, pp. 2785–2795, June 2006.

[130] Y. Chen and S. Kishore, "On the tradeoffs of implementing randomized network coding in multicast networks," *IEEE Transactions on Communications*, vol. 58, pp. 2107–2115, July 2010.

[131] R. Koetter and M. Médard, "An algebraic approach to network coding," *IEEE/ACM Transactions on Networking*, vol. 11, pp. 782–795, October 2003.

[132] T. Ho, M. Médard, R. Koetter, D. R. Karger, M. Effros, J. Shi, and B. Leong, "A random linear network coding approach to multicast," *IEEE Transactions on Information Theory*, vol. 52, pp. 4413–4430, October 2006.

[133] H. V. Nguyen, S. X. Ng, and L. Hanzo, "Irregular convolution and unity-rate coded network-coding for cooperative multi-user communications," *IEEE Transactions on Wireless Communications*, vol. 12, pp. 1231–1243, March 2013.

[134] H. V. Nguyen, C. Xu, S. X. Ng, and L. Hanzo, "Non-coherent near-capacity network coding for cooperative multi-user communications," *IEEE Transactions on Communications*, vol. 60, pp. 3059–3070, October 2012.

[135] J. L. Rebelatto, B. F. Uchôa-Filho, Y. Li, and B. Vucetic, "Generalized distributed network coding based on nonbinary linear block codes for multi-user cooperative communications," in *IEEE International Symposium on Information Theory Proceedings (ISIT'10)*, (Austin, TX), pp. 943–947, June 2010.

[136] J. L. Rebelatto, B. F. Uchôa-Filho, Y. Li, and B. Vucetic, "Multiuser cooperative diversity through network coding based on classical coding theory," *IEEE Transactions on Signal Processing*, vol. 60, pp. 916–926, February 2012.

[137] M. Xiao and M. Skoglund, "M-user cooperative wireless communications based on nonbinary network codes," in *IEEE Information Theory Workshop on Networking and Information Theory (ITW'09)*, (Volos), pp. 316–320, June 2009.

[138] H. V. Nguyen, S. X. Ng, and L. Hanzo, "Performance bounds of network coding aided cooperative multiuser systems," *IEEE Signal Processing Letters*, vol. 18, pp. 435–438, July 2011.

[139] W. Liang, H. Nguyen, S. X. Ng, and L. Hanzo, "Adaptive TTCM aided near-instantaneously dynamic network coding for cooperative cognitive radio networks," *IEEE Transactions on Vehicular Technology*, vol. PP, p. 1, March 2015.

[140] J. L. Rebelatto, B. F. Uchôa-Filho, Y. Li, and B. Vucetic, "Adaptive distributed network-channel coding," *IEEE Transactions on Wireless Communications*, vol. 10, pp. 2818–2822, September 2011.

[141] C. Hausl and P. Dupraz, "Joint network-channel coding for the multiple-access relay channel," in *3rd Annual IEEE Communications Society on Sensor and Ad Hoc Communications and Networks (SECON'06)*, vol. 3, (Reston, VA), pp. 817–822, September 2006.

[142] "SAGE,." Open source mathematics software, Accessed: 2015-09-08. Available :http://www.sagemath.org/.

[143] A. J. Aljohani, H. Sun, S. X. Ng, and L. Hanzo, "Distributed source and turbo trellis coded modulation aided superposition modulation based relaying for cooperative communication," Yet to be published.

[144] A. J. Aljohani, Z. Babar, S. X. Ng, and L. Hanzo, "Distributed source-channel coding using reduced-complexity syndrome-based TTCM," Yet to be published.

[145] A. J. Aljohani, H. Sun, S. X. Ng, and L. Hanzo, "Distributed source and turbo trellis coded modulation aided adaptive network coding," Yet to be published.

[146] A. J. Aljohani, S. X. Ng, R. G. Maunder, and L. Hanzo, "Joint TTCM-VLC-Aided SDMA for two-way relaying aided wireless video transmission," in *IEEE 78th Vehicular Technology Conference (VTC'13)*, (Las Vegas, NV), September 2013.

[147] A. J. Aljohani, S. X. Ng, and L. Hanzo, "TTCM-assisted distributed source-channel coding for Nakagami-m fading channels," in *IEEE 80th Vehicular Technology Conference (VTC'14)*, (Vancouver, BC), September 2014.

[148] S. X. Ng, K. Zhu, and L. Hanzo, "Distributed source-coding, channel-coding and modulation for cooperative communications," in *IEEE Vehicular Technology Conference (VTC'10)*, (Ottawa, Canada), September 2010.

[149] A. Roumy, K. Lajnef, and C. Guillemot, "Rate-adaptive turbo-syndrome scheme for Slepian-Wolf coding," in *Asilomar Conference on Signals, Systems and Computers (ACSSC'07)*, (Pacific Grove, CA), pp. 545–549, November 2007.

[150] V. Toto-Zarasoa, A. Roumy, and C. Guillemot, "Rate-adaptive codes for the entire Slepian-Wolf region and arbitrarily correlated sources," in *IEEE International Conference on Acoustics, Speech and Signal Processing (ICASSP'08)*, (Las Vegas, NV), pp. 2965–2968, March 2008.

[151] G. Ungerböeck, "Channel coding with multilevel/phase signals," *IEEE Transactions on Information Theory*, vol. 28, pp. 55–67, January 1982.

[152] P. Robertson and T. Wörz, "Bandwidth-efficient turbo trellis-coded modulation using punctured component codes," *IEEE Journal on Selected Areas in Communications*, vol. 16, pp. 206–218, February 1998.

[153] E. Zehavi, "8-PSK trellis codes for a Rayleigh channel," *IEEE Transactions on Communications*, vol. 40, pp. 873–884, May 1992.

[154] X. Li and J. A. Ritcey, "Bit-interleaved coded modulation with iterative decoding," *IEEE Communications Letters*, vol. 1, pp. 169–171, November 1997.

[155] S. X. Ng, T. H. Liew, L.-L. Yang, and L. Hanzo, "Comparative study of TCM, TTCM, BICM and BICM-ID schemes," in *IEEE Vehicular Technology Conference (VTC'01)*, vol. 4, (Rhodes), pp. 2450–2454, May 2001.

[156] L. Hanzo, T. H. Liew, B. L. Yeap, R. Y. S. Tee, and S. X. Ng, *Turbo Coding, Turbo Equalisation and Space-Time Coding: EXIT-Chart Aided Near-Capacity Designs for Wireless Channels*. John Wiley & Sons, 2nd ed., 2011.

[157] S. T. Brink, "Convergence behaviour of iteratively decoded parallel concatenated codes," *IEEE Transactions on Communications*, vol. 49, pp. 1727–1737, October 2001.

[158] G. Ungerböck, *Trellis-coded modulation with redundant signal sets Part 1 and Part 2*, vol. 25. IEEE Communications Magazine, February 1987.

[159] L. Hanzo, S. X. Ng, T. Keller, and W. T. Webb, *Quadrature amplitude modulation: From basics to adaptive trellis-coded, turbo-equalised and space-time coded OFDM, CDMA and MC-CDMA systems*. Hardcover, Wiley-IEEE Press, 2004.

[160] P. Elias, "Coding for noisy channels," *IRE Convention Record, Part 4*, pp. 37–47, 1955.

[161] L. Bahl, C. Cullum, W. Frazer, and F. Jelinek, "An efficient algorithm for computing free distance (corresp.)," *IEEE Transactions on Information Theory*, vol. 18, pp. 437–439, May 1972.

[162] L. Bahl, J. Cocke, F. Jelinek, and J. Raviv, "Optimal decoding of linear codes for minimizing symbol error rate (corresp.)," *IEEE Transactions on Information Theory*, vol. 20, pp. 284–287, March 1974.

[163] J. Hagenauer and P. Hoeher, "A Viterbi algorithm with soft-decision outputs and its applications," in *IEEE Global Telecommunications Conference*, vol. 3, (Dallas, TX), pp. 1680–1686, November 1989.

[164] Y. Kofman, E. Zehavi, and S. Shamai, "Performance analysis of a multilevel coded modulation system," *IEEE Transactions on Communications*, vol. 42, pp. 299–312, February 1994.

[165] S. L. Goff, A. Glavieux, and C. Berrou, "Turbo-codes and high spectral efficiency modulation," in *IEEE International Conference on Communications (ICC'94)*, vol. 2, (New Orleans, LA), pp. 645–649, May 1994.

[166] P. Robertson, E. Villebrun, and P. Hoeher, "A comparison of optimal and sub-optimal MAP decoding algorithms operating in the log domain," in *IEEE International Conference on Communications*, vol. 2, (Seattle, WA), pp. 1009–1013, June 1995.

[167] Y. Nana, E. Sharon, and S. Litsyn, "Improved decoding of LDPC coded modulations," *IEEE Communications Letters*, vol. 10, pp. 375–377, May 2006.

[168] S. X. Ng, O. R. Alamri, Y. Li, J. Kliewer, and L. Hanzo, "Near-capacity turbo trellis coded modulation design based on EXIT charts and union bounds," *IEEE Transactions on Communications*, vol. 56, pp. 2030–2039, December 2008.

[169] S. X. Ng, Y. Li, and L. Hanzo, "Distributed turbo trellis coded modulation for cooperative communications," in *International Conference on Communications (ICC'09)*, (Dresden, Germany), June 2009.

[170] T. Islam, R. Schober, R. K. Mallik, and V. K. Bhargava, "Analysis and design of cooperative BICM-OFDM systems," *IEEE Transactions on Communications*, vol. 59, pp. 1742–1751, June 2011.

[171] M. El-Hajjar and L. Hanzo, "EXIT charts for system design and analysis," *IEEE Communications Surveys Tutorials*, vol. 16, pp. 127–153, February 2014.

[172] S. X. Ng, J. Kliewer, O. R. Alamri, and L. Hanzo, "On the design of turbo trellis coded modulation schemes using symbol-based EXIT charts," in *IEEE Vehicular Technology Conference (VTC'06)*, (Montreal, Canada), September 2006.

[173] S. X. Ng, J. Wang, and L. Hanzo, "Unveiling near-capacity code design: The realization of Shannon's communication theory for MIMO channels," in *IEEE International Conference on Communications (ICC'08)*, (Beijing), pp. 1415–1419, May 2008.

[174] R. G. Maunder, J. Kliewer, S. X. Ng, J. Wang, L.-L. Yang, and L. Hanzo, "Joint iterative decoding of trellis-based VQ and TCM," *IEEE Transactions on Wireless Communications*, vol. 6, pp. 1327–1336, April 2007.

[175] S. X. Ng, F. Guo, J. Wang, L.-L. Yang, and L. Hanzo, "Joint source-coding, channel-coding and modulation schemes for AWGN and Rayleigh fading channels," *Electronics Letters*, vol. 39, pp. 1259–1261, August 2003.

[176] A. Sendonaris, E. Erkip, and B. Aazhang, "User cooperation diversity part I: System description," *IEEE Transactions on Communications*, vol. 51, pp. 1927–1938, November 2003.

[177] J. N. Laneman, D. N. C. Tse, and G. W. Wornell, "Cooperative diversity in wireless networks: Efficient protocols and outage behavior," *IEEE Transactions on Information Theory*, vol. 50, pp. 3062–3080, December 2004.

[178] K. J. Lee, H. J. Sung, E. S. Park, and I. K. Lee, "Joint optimization for one and two-way MIMO AF multiple-relay systems," *IEEE Transactions on Wireless Communications*, vol. 9, pp. 3671–3681, December 2010.

[179] R. Vaze and R. W. Heath, "On the capacity and diversity-multiplexing tradeoff of the two-way relay channel," *IEEE Transactions on Information Theory*, vol. 57, pp. 4219–4234, July 2011.

[180] A. Papadogiannis, A. G. Burr, and M. Tao, "On the maximum achievable sum-rate of interfering two-way relay channels," *IEEE Communications Letters*, vol. 16, pp. 72–75, January 2012.

[181] W. Liang, S. X. Ng, and L. Hanzo, "TTCM-aided SDMA-based two-way relaying," in *IEEE Vehicular Technology Conference (VTC'11)*, (San Francisco, USA), September 2011.

[182] S. X. Ng, F. Guo, J. Wang, L.-L. Yang, and L. Hanzo, "Joint source-coding, channel-coding and modulation schemes for AWGN and Rayleigh fading channels," *Electronic Letters*, vol. 39, pp. 1259–1261, August 2003.

[183] X. Zuo, R. G. Maunder, and L. Hanzo, "Design of fixed-point processing based LDPC codes using EXIT charts," in *IEEE Vehicular Technology Conference (VTC'11)*, (San Francisco, USA), September 2011.

[184] J. Wang, S. X. Ng, L.-L. Yang, and L. Hanzo, "Combined serially concatenated codes and MMSE equalization: An EXITchart aided perspective," in *IEEE Vehicular Technology Conference (VTC'06)*, (Montreal, Canada), September 2006.

[185] L. Kong, S. X. Ng, R. G. Maunder, and L. Hanzo, "Maximum-throughput irregular distributed space-time code for near-capacity cooperative communications," *IEEE Transactions on Wireless Communications*, vol. 59, pp. 1511–1517, March 2010.

[186] A. F. Tobagi and M. M. Hira, "Joint optimization of physical layer parameters and routing in wireless mesh networks," in *9th IFIP Annual Mediterranean, Ad Hoc Networking Workshop (Med-Hoc-Net)*, (Juan Les Pins, France), June 2010.

[187] H. Ochiai, P. Mitran, and V. Tarokh, "Design and analysis of collaborative diversity protocols for wireless sensor networks," in *IEEE 60th Vehicular Technology Conference (VTC'04)*, (Los Angeles, USA), pp. 4645–4649, September 2004.

[188] L. Hanzo, M. Münster, B. Choi, and T. Keller, *OFDM and MC-CDMA for Broadband Multi-user Communications, WLANs and Broadcasting*. John Wiley & Sons, May 2003.

[189] Y. Takishima, M. Wada, and H. Murakami, "Reversible variable length codes," *IEEE Transactions on Communications*, vol. 43, pp. 158–162, February 1995.

[190] J. G. Proakis, *Digital Communications*. New York: Mc-Graw Hill International Editions, 3rd ed., 1995.

[191] S. X. Ng and L. Hanzo, "On the MIMO channel capacity of multi-dimensional signal sets," *IEEE Transactions on Vehicular Technology*, vol. 55, pp. 528–536, March 2006.

[192] R. Ahlswede, N. Cai, S.-Y. R. Li, and R. W. Yeung, "Network information flow," *IEEE Transactions on Information Theory*, vol. 46, pp. 1204–1216, July 2000.

[193] L. Li and A. J. Goldsmith, "Capacity and optimal resource allocation for fading broadcast channels–Part II: Outage capacity," *IEEE Transactions on Communications*, vol. 4, pp. 1083–1102, March 2001.

[194] L. Hanzo, P. Cherriman, and J. Streit, *Wireless Video Communications: From Second to Third Generation Systems, WLANs and Beyond*. Wiley-IEEE Press, 2001.

[195] A. D. Wyner, "Recent results in the shannon theory," *IEEE Transactions on Information Theory*, vol. 20, pp. 2–10, January 1974.

[196] J. Bajcsy and P. Mitran, "Coding for the Slepian-Wolf problem with turbo codes," in *IEEE Global Telecommunications Conference (GLOBECOM'01)*, vol. 2, (San Antonio, TX), pp. 1400–1404, November 2001.

[197] J. Garcia-Frias, "Compression of correlated binary sources using turbo codes," *IEEE Communications Letters*, vol. 5, pp. 417–419, October 2001.

[198] S. X. Ng, J. Y. Chung, P. Cherriman, and L. Hanzo, "Burst-by-burst adaptive decision feedback equalised TCM, TTCM and BICM for H.263-assisted wireless video telephony," *IEEE Transactions on Circuits and Systems for Video Technology*, vol. 16, pp. 363–374, March 2006.

[199] A. Goldsmith and S. Chua, "Adaptive coded modulation for fading channels," *IEEE Transactions on Communications*, vol. 46, pp. 595–602, May 1998.

[200] S. X. Ng, C. Y. Qian, D. Liang, and L. Hanzo, "Adaptive turbo trellis coded modulation aided distributed space-time trellis coding for cooperative communications," in *IEEE Vehicular Technology Conference (VTC'10)*, (Taipei, Taiwan), May 2010.

[201] A. Goldsmith, *Wireless communications*. Cambridge University Press, 2005.

[202] J. Proakis, *Digital Communications*. New York, USA: McGraw-Hill, 4 th ed., 2000.

[203] M. Nakagami, *The M-distribution - A General Formula of Intensity Distribution of Rapid Fading*. Pergamon Press, 1960.

[204] L.-L. Yang and L. Hanzo, "Performance of generalized multicarrier DS-CDMA over Nakagami-m fading channels," *IEEE Transactions on Communications*, vol. 50, pp. 956–966, June 2002.

[205] M. Campanella and G. Mamola, "On the channel capacity for constant envelope signals with effective bandwidth constraint," *IEEE Transactions on Communications*, vol. 38, pp. 1164–1172, August 1990.

[206] R. G. Gallager, *Information theory and reliable communication*. John Wiley and Sons, 1968.

[207] E. G. Larsson and B. R. Vojcic, "Cooperative transmit diversity based on superposition modulation," *IEEE Communications Letters*, vol. 9, pp. 778–780, September 2005.

[208] L. Huang, Z. Fei, and J. Kuang, "A decode-and-forward relaying scheme based on orthogonal superposition modulation," in *IEEE International Conference on Communication Technology (ICCT'08)*, (Hangzhou), pp. 241–244, November 2008.

[209] V. Toto-Zarasoa, A. Roumy, and C. Guillemot, "Maximum likelihood BSC parameter estimation for the Slepian-Wolf problem," *IEEE Communications Letters*, vol. 15, pp. 232–234, February 2011.

[210] Y. Li, B. Vucetic, T. Wong, and M. Dohler, "Distributed turbo coding with soft information relaying in multihop relay networks," *IEEE Journal on Selected Areas in Communications*, vol. 24, pp. 2040–2050, November 2006.

[211] J. N. Laneman, G. W. Wornell, and D. N. C. Tse, "An efficient protocol for realizing cooperative diversity in wireless networks," in *IEEE International Symposium on Information Theory*, (Washington, DC), June 2001.

[212] A. Sendonaris, E. Erkip, and B. Aazhang, "User cooperation diversity part II: Implementation aspects and performance analysis," *IEEE Transactions on Communications*, vol. 51, pp. 1939–1948, November 2003.

[213] T. M. Cover and A. E. Gamal, "Capacity theorems for the relay channel," *IEEE Transactions on Information Theory*, vol. 25, pp. 572–584, September 1979.

[214] T. E. Hunter and A. Nosratinia, "Cooperation diversity through coding," in *IEEE International Symposium on Information Theory*, (Lausanne, Switzerland), June 2002.

[215] D. N. C. Tse and P. Viswanath, *Fundamentals of Wireless Communication*. New York, NY, USA: Cambridge University Press, 2005.

[216] S. Gadkari and K. Rose, "Time-division versus superposition coded modulation schemes for unequal error protection," *IEEE Transactions on Communications*, vol. 47, pp. 370–379, March 1999.

[217] J. Hossain, M. S. Alouini, and V. K. Bhargava, "Rate adaptive hierarchical modulation-assisted two-user opportunistic scheduling," *IEEE Transactions on Wireless Communications*, vol. 6, pp. 2076–2085, June 2007.

[218] P. A. Hoeher and T. Wo, "Superposition modulation: Myths and facts," *IEEE Communications Magazine*, vol. 49, pp. 110–116, December 2011.

[219] I. Krikidis, "Analysis and optimization issues for superposition modulation in cooperative networks," *IEEE Transactions on Vehicular Technology*, vol. 58, pp. 4837–4847, November 2009.

[220] H. Sun, S. X. Ng, and L. Hanzo, "Superposition coded modulation for cooperative communications," in *IEEE Vehicular Technology Conference (VTC'12)*, (Quebec City, QC), September 2012.

[221] J. Geldmacher, K. Hueske, and J. Götze, "Syndrome based block decoding of convolutional codes," in *IEEE International Symposium on Wireless Communication Systems (ISWCS'08)*, (Reykjavik, Iceland), pp. 542–546, October 2008.

[222] K. Hueske, J. Geldmacher, and J. Götze, "Adaptive decoding of convolutional codes," *Advances in Radio Science*, vol. 5, pp. 209–214, June 2007.

[223] Z. Babar, S. X. Ng, and L. Hanzo, "Reduced-complexity syndrome-based TTCM decoding," *IEEE Communications Letters*, vol. 17, pp. 1220–1223, June 2013.

[224] J. Geldmacher, K. Hueske, J. Götze, and M. Kosakowski, "Low complexity syndrome based decoding of turbo codes," in *IEEE International Symposium on Information Theory Proceedings (ISIT'12)*, (Cambridge, MA), pp. 2371–2375, July 2012.

[225] M. Tajima, K. Shibata, and Z. Kawasaki, "Relation between encoder and syndrome former variables and symbol reliability estimation using a syndrome trellis," *IEEE Transactions on Communications*, vol. 51, pp. 1474–1484, September 2003.

[226] S. Gao, "Joint distributed source and network coding for correlated information multicasting," in *6th International ICST Conference on Communications and Networking in China (CHINACOM'11)*, (Harbin), pp. 698–702, August 2011.

[227] T. Ho, M. Médard, M. Effros, and R. Koetter, "Network coding for correlated sources," in *in CISS*, 2004.

[228] O. Iscan, I. Latif, and C. Hausl, "Network coded multi-way relaying with iterative decoding," in *IEEE 21st International Symposium on Personal Indoor and Mobile Radio Communications (PIMRC'10)*, (Istanbul, Turkey), pp. 482–487, September 2010.

[229] O. Iscan and C. Hausl, "Iterative network and channel decoding for the relay channel with multiple sources," in *IEEE Vehicular Technology Conference (VTC'11)*, (San Francisco, CA), September 2011.

[230] F. P. S. Luus and B. T. Maharaj, "Joint source-channel-network coding for bidirectional wireless relays," in *IEEE International Conference on Acoustics, Speech and Signal Processing (ICASSP'11)*, (Prague), pp. 3156–3159, May 2011.

[231] Y. Wu, V. Stanković, Z. Xiong, and S.-Y. Kung, "On practical design for joint distributed source and network coding," *IEEE Transactions on Information Theory*, vol. 55, pp. 1709–1720, April 2009.

[232] M. Xiao and M. Skoglund, "Multiple-user cooperative communications based on linear network coding," *IEEE Transactions on Communications*, vol. 58, pp. 3345–3351, December 2010.

[233] M. Xiao, J. Kliewer, and M. Skoglund, "Design of network codes for multiple-user multiple-relay wireless networks," *IEEE Transactions on Communications*, vol. 60, pp. 3755–3766, December 2012.

[234] F. Brannstrom, L. K. Rasmussen, and A. J. Grant, "Optimal puncturing ratios and energy allocation for multiple parallel concatenated codes," *IEEE Transactions on Information Theory*, vol. 55, pp. 2062–2077, May 2009.

[235] N. Bonello, S. Chen, and L. Hanzo, "Pilot symbol assisted coding," *Electronics Letters*, vol. 45, pp. 518–519, May 2009.

[236] M. El-Hajjar and L. Hanzo, "Dispensing with channel estimation," *IEEE Vehicular Technology Magazine*, vol. 5, pp. 42–48, June 2010.

[237] C. Xu, D. Liang, S. X. Ng, and L. Hanzo, "Reduced-complexity non-coherent soft-decision-aided M-DAPSK dispensing with channel estimation," *IEEE Transactions on Vehicular Technology*, vol. 62, pp. 2633–2643, July 2013.

[238] D. Liang, S. X. Ng, and L. Hanzo, "Near-capacity turbo coded soft-decision aided DAPSK/star-QAM," in *IEEE Vehicular Technology Conference (VTC'11)*, (San Francisco, CA), September 2011.

[239] Y. Zhao and J. Garcia-Frias, "Turbo compression/joint source-channel coding of correlated binary sources with hidden markov correlation," *Signal Processing*, vol. 86, pp. 3115–3122, November 2006.

[240] J. Garcia-Frias and W. Zhong, "LDPC codes for compression of multi-terminal sources with hidden Markov correlation," *IEEE Communications Letters*, vol. 7, pp. 115–117, March 2003.

[241] J. Wen and J. D. Villasenor, "Reversible variable length codes for efficient and robust image and video coding," in *Data Compression Conference (DCC'98)*, (Snowbird, UT, USA), pp. 471–480, March 1998.

[242] C. Lin, Y. Chuang, and J. Wu, "Generic construction algorithms for symmetric and asymmetric RVLCs," in *IEEE International Conference on Computational Science (ICCS'02)*, vol. 2, (Singapore), pp. 968–972, November 2002.

[243] J. Wen and J. D. Villasenor, "A class of reversible variable length codes for robust image and video coding," in *IEEE International Conference on Image Processing*, vol. 2, (Santa Barbara, CA), pp. 65–68, October 1997.

Subject Index

O

P

Q

R

S

Author Index

H

N

O

Z